UNIVERSITY OF OXFORD

DEPARTMENT OF CHEMISTRY

Bimetallic Alloy Catalysts for Green Methanol Production via CO_2 and Renewable Hydrogen

BY

MOLLY MENG-JUNG LI

UNIVERSITY COLLEGE

SUPERVISOR: PROF. S. C. EDMAN TSANG

A THESIS SUBMITTED FOR THE DEGREE

DOCTOR OF PHILOSOPHY

2018

Declaration

I confirm that this is my own work and the use of all materials from other sources has been properly and fully acknowledged.

Molly Meng-Jung Li

Dedication

To my parents and Jacob

Acknowledgements

First and foremost, I like to offer my gratitude to my supervisor Prof. Shik Chi Edman Tsang, for giving me the opportunity to pursue my DPhil study here at Oxford. Under his guidance, I have learned a lot in the field of heterogeneous catalysts for renewable applications, and I have been motivated to become a good scientist like him. Without his patience to guide me through various challenges, this thesis would not be completed on the schedule.

I would also like to thank the Swire Educational Trust for the four-year full funding on my DPhil study and the financial support on my conference trips.

Over the four good years, I have had the pleasure to work with some very smart and nice people in Oxford. I would like to thank Dr. Fenglin Liao and Dr. Cheng-Tar Wu for their guidance on the synthesis, characterisation and everything on the research skills; Prof. Hanbo Zou for her assistance in the characterisation and testing of the catalysts as well as reactor design and modifications; Dr. Tuğçe Ayvalı for helping me on the AMO-LDH projects and working with me when the GC/reactor was broken and needed to be fixed; Dr. Chunping Chen and Dr. Hongri Suo for the synthesis and structural investigation of the AMO-LDH catalysts; Dr. Jianwei Zheng for lots of catalyst characterisations and data interpretation; Dr. Yung-Kang Peng for his helps on the synthesis of CdS-based photocatalysts; Dr. Jin Qu for theoretical calculations; Dr. Ivo F. Teixeira and Dr. Alex Robertson for TEM investigation; Dr. Ian McPherson for FTIR experiments and helps on fixing many lab instruments; Dr. Anna Kroner for XAFS experiment at Diamond B18; Dr. Ashley Shepherd for performing XPS experiments; all the Tsang group member of past and present: Dr. Pu Zhao, Dr. Ye Lin, Dr. Xinping Duan, Dr. Haohong Duan, Dr. Keizo Nakagawa, Dr. Enna Ha, Dr. Zhenyu Sun, Dr. Weiran Zheng, Dr. Feng Xu, Dr. Qineng Xia,

Dr. Guoliang Liu, Dr. Simantini Nayak, Dr. Bozhidar Stefanov, Dr. Simon Fairclough, Dr. Simon Jones, Dr. Steven Zhou, Mr. Aniwat Pengsawang, Dr. Abdullah Khan, Dr. Amy Kolpin, Dr. Clive Eley, Dr. Tiantian Jia, Dr. Aaron Lau, Dr. Hanif Mahadi, Dr. Ieuan Ellis, Dr. Benedict Lo, Dr. Hannah Kreissl, Dr. Bin Yu, Ms. Elizabeth Raine, Mr. Sultan Alshuhri, Mr. Josh Fellowes, Mr. Thomas Lau, Mr. Tim Sudmeier, Mr. Jiri Kulhavy, Mr. Linus Lin, Mr. Simson Wu, Ms. Kirsty Purchase, Ms. Tatchamapan Yoskamtorn, Ms. Tianyi Chen, Ms. Jiaying Mo.

I would like to thank my collaborators: Dr. Tai-Sing Wu, Dr. Ting-Shan Chan and Prof. Yun-Liang Soo (NSRRC Taiwan) for the XAFS experiments and useful advices on data interpretation; Dr. C. Nie and Prof. Emmanuel Flahaut (Université Paul Sabatier) for providing me high-quality carbon nanotube samples; Dr. Winson C. H. Kuo (Johnson Matthey), Dr. Shei Sia Su and Dr. Pang Po (University of Birmingham) for their assistance with HR-STEM images collection and structure analysis; Prof. Youzhu Yuan (Xiamen University), Dr. Ziyan Zeng and Prof. Xinlin Hong (Wuhan University) for their helps on the CuZn catalyst project.

List of Publications

CO_2 hydrogenation to renewable methanol

1. Molly Meng-Jung Li, Ziyan Zeng, Fenglin Liao, Xinlin Hong, Shik Chi Edman Tsang, *Enhanced CO_2 Hydrogenation to Methanol over CuZn Nanoalloy in Ga Modified Cu/ZnO Catalysts.* **Journal of Catalysis**, 2016, 343, p. 157-167.
2. Fenglin Liao, Xin-Ping Wu, Jianwei Zheng, Meng-Jung Li, Ziyan Zeng, Xinling Hong, Anna Kroner, Youzhu Yuan, Xue-Qing Gong, Shik Chi Edman Tsang, *Pd@ Zn core–shell nanoparticles of controllable shell thickness for catalytic methanol production*. **Catalysis Science & Technology**, 2016, 6, p.7698-7702.
3. Fenglin Liao, Xin-Ping Wu, Jianwei Zheng, Molly Meng-Jung Li, Anna Kroner, Ziyan Zeng, Xinlin Hong, Youzhu Yuan, Xue-Qing Gong, Shik Chi Edman Tsang, *A Promising Low Pressure Methanol Synthesis Route From CO_2 Hydrogenation Over Pd@Zn Core–Shell Catalysts*. **Green Chemistry**, 2017, 19, p. 270-280.
4. Molly Meng-Jung Li, Chunping Chen, Tuğçe Ayvalı, Hongri Suo, Jianwei Zheng, Ivo F. Teixeira, Lin Ye, Hanbo Zou, Dermot O'Hare, Shik Chi Edman Tsang, *CO_2 Hydrogenation to Methanol over Nanosheets Derived from Single Cationic Layer CuZnGa LDH Precursors*. **Accepted by ACS Catalysis with revisions**.
5. Molly Meng-Jung Li, Hanbo Zou, Alex Robertson, Tai-Sing Wu, Ian McPherson, Jianwei Zheng, Ting-Shan Chan, Yun-Liang Soo, Shik Chi Edman Tsang, *Convenient methanol synthesis at low H_2/CO_2 over Rh-In bimetallic catalyst*. **Submitted**.

Renewable H_2 generation

1. Molly Meng-Jung Li, Poppy Mills, Simon M Fairclough, Alex Robertson, Yung-Kang Peng, Jamie Warner, Chunyang Nie, Emmanuel Flahaut, Shik Chi Edman Tsang, *Importance of the structural integrity of a carbon conjugated mediator for photocatalytic hydrogen generation from water over a CdS–carbon nanotube–MoS_2 composite.* **Chemical Communications**, 2016, 52, p. 13596-13599.
2. Tiantian Jia, Molly Meng-Jung Li, Lin Ye, Sam Wiseman, Guoliang Liu, Jin Qu, Keizo Nakagawa, Shik Chi Edman Tsang, *The remarkable activity and stability of a dye-sensitized single molecular layer MoS_2 ensemble for photocatalytic hydrogen production*. **Chemical Communications**, 2015, 51, p. 13496-13499.

Dimethyl oxalate hydrogenation

1. Molly Meng-Jung Li, Jianwei Zheng, Jin Qu, Fenglin Liao, Elizabeth Raine, Winson C. H. Kuo, Shei Sia Su, Pang Po, Youzhu Yuan, Shik Chi Edman, *The remarkable activity and stability of a highly dispersive beta-brass Cu-Zn catalyst for the production of ethylene glycol*. **Scientific Reports**, 2016, 6, p. 20527.
2. Molly Meng-Jung Li, Linmin Ye, Jianwei Zheng, Huihuang Fang, Anna Kroner, Youzhu Yuan, Shik Chi Edman Tsang, Surfactant-free nickel–silver core@ shell nanoparticles in mesoporous SBA-15 for chemoselective hydrogenation of dimethyl oxalate. **Chemical Communications**, 2016, 52, p. 2569-2572.
3. Junfu Zhou, Xinping Duan, Linmin Ye, Jianwei Zheng, Molly Meng-Jung Li, Shik Chi Edman Tsang, Youzhu Yuan. *Enhanced chemoselective hydrogenation*

of dimethyl oxalate to methyl glycolate over bimetallic Ag–Ni/SBA-15 catalysts. **Applied Catalysis A: General,** 2015, 505, p. 344-353.

Other Collaborations

1. Hannah T Kreissl, Molly Meng-Jung Li, Yung-Kang Peng, Keizo Nakagawa, Thomas JN Hooper, John V Hanna, Ashley Shepherd, Tai-Sing Wu, Yun-Liang Soo, Shik Chi Edman Tsang. *Structural Studies of Bulk to Nanosize Niobium Oxides with Correlation to Their Acidity.* **Journal of the American Chemical Society**, 2017, 139, p. 12670-12680.
2. Guoliang Liu, Alex W Robertson, Molly Meng-Jung Li, Winson CH Kuo, Matthew T Darby, Mohamad H Muhieddine, Yung-Chang Lin, Kazu Suenaga, Michail Stamatakis, Jamie H Warner, Shik Chi Edman Tsang, MoS_2 monolayer catalyst doped with isolated Co atoms for the hydrodeoxygenation reaction. **Nature Chemistry**, 2017, 9, p.810-816.
3. Y. Koito, G. J. Rees, J. V. Hanna, Molly Meng-Jung Li, Y. K. Peng, T. Puchtler, R. Taylor, T. Wang, H. Kobayashi, I. F. Teixeira, M. A. Khan, H. T. Kreissl and S. C. E. Tsang, *Structure–Activity Correlations for Brønsted Acid, Lewis Acid, and Photocatalyzed Reactions of Exfoliated Crystalline Niobium Oxides*. **ChemCatChem**, 2017, 9, p. 144-154.
4. Ieuan T Ellis, Elisabeth H Wolf, Glenn Jones, Ben Lo, Molly Meng-Jung Li, Andrew PE York, Shik Chi Edman Tsang. *Lithium and boron as interstitial palladium dopants for catalytic partial hydrogenation of acetylene.* **Chemical Communications**, 2017, 53, p. 601-604.
5. M Abdullah Khan, Ivo F Teixeira, Molly Meng-Jung Li, Yusuke Koito, Shik Chi Edman Tsang. *Graphitic carbon nitride catalysed photoacetalization of*

aldehydes/ketones under ambient conditions. **Chemical Communications**, 2016, 52, p. 2772-2775.

6. Qineng Xia, Xiaojing Zhuang, Molly Meng-Jung Li, Yung-Kang Peng, Guoliang Liu, Tai-Sing Wu, Yun-Liang Soo, Xue-Qing Gong, Yanqin Wang, Shik Chi Edman Tsang. *Cooperative catalysis for the direct hydrodeoxygenation of vegetable oils into diesel-range alkanes over Pd/$NbOPO_4$.* **Chemical Communications**, 2016, 52, p. 5160-5163.

7. Chun Wong Aaron Chan, Abdul Hanif Mahadi, Molly Meng-Jung Li, Elena Cristina Corbos, Chiu Tang, Glenn Jones, Winson Chun Hsin Kuo, James Cookson, Christopher Michael Brown, Peter Trenton Bishop, Shik Chi Edman Tsang, *Interstitial modification of palladium nanoparticles with boron atoms as a green catalyst for selective hydrogenation*. **Nature Communications**, 2014, 5, p. 5787.

Abstract

Recently, the increasing level of atmospheric CO_2 has been widely noticed due to its association with global warming, provoking a growth in environmental concerns toward the continued use of fossil fuels. According to the World Meteorological Organisation (WMO), the concentration of CO_2 in the Earth's atmosphere surged to a record high, hitting 403.3 ppm in 2016. Researchers suggested that a combination of human activities and the El Niño weather phenomenon drove CO_2 to a level not seen in 800,000 years. Green methanol synthesis that consists of CO_2 recycling together with renewable hydrogen production seems to be a promising way to achieve carbon neutral process and sustainable development. This thesis is therefore intended to provide some research advancements on methanol synthesis from CO_2 hydrogenation over promising bimetallic materials and green hydrogen synthesis over nanocomposite materials.

Since the prevailing of the highly active and economic $Cu/ZnO/Al_2O_3$ catalyst for CO_2 hydrogenation to methanol, the Cu/ZnO based catalysts have attracted increasing attention and many systematic studies have focused on elucidating the structure of active sites. Although the active sites of methanol synthesis over commercial $Cu/ZnO/Al_2O_3$ catalysts have recently been the subject of intense debate, many studies over the past 20 years have shown that the good performance of Cu/ZnO based catalysts is attributed to the active Zn-Cu bimetallic sites. In this thesis, we present a novel and simple method for the preparation of active bimetallic Cu-Zn nanoparticles. Through the establishment of a type-II heterojunction in the support, Zn-rich Cu-Zn bimetallic alloys can be derived from the reduction of the mixed metal (Cu, Zn, Ga) oxides support synthesised via co-precipitation method. The catalytic performance of the catalysts shows CO_2 conversion and methanol selectivity can be significantly improved by increasing the Zn^0 content in the Cu-Zn

nanoparticles under the facilitation of the metal oxides heterojunction. Moreover, the number of the Cu-Zn active species can be further increased by introducing an ultra-thin (1-3 cationic-layers) $(CuZn)_{1-x}Ga_x$-CO_3 layered double hydroxides nanosheets as catalyst precursors synthesised following the recently reported aqueous miscible organic solvent method. Owing to the distinctive local steric and electrostatic stabilisation of the ultra-thin nanosheets, the newly formed Cu-Zn alloys can be stabilised by the cationic layers upon reduction, exerting a great enhancement to the catalytic reaction of methanol production from CO_2 and H_2. On the other hand, a new class of Rh-In bimetallic catalysts were synthesised and applied as catalysts for renewable methanol production. The fine-tuning of product specificity, owing to strong synergies that contribute to the electronic or geometric alterations of the monometallic surfaces, is clearly demonstrated in this bimetallic system: An unmodified Rh surface catalyses CO_2 and H_2 to methane, while the bimetallic Rh-In system presents excellent methanol production rate of CO_2 hydrogenation. In addition, the supported Rh-In nanoparticles show the ability to inhibit the reverse water-gas shift reaction such that to minimise the formation of CO. Therefore, high methanol yield and methanol selectivity under thermodynamically unfavourable methanol synthesis conditions can be achieved over this novel and promising bimetallic system.

For the renewable methanol production from H_2 and CO_2, it needs to be emphasised that the hydrogen sources must come from the green production routes. Therefore, an in-depth study of a nanocomposite system, CdS-carbon nanotubes-MoS_2, for photocatalytic hydrogen production from water has been demonstrated. The hydrogen evolution rate of this nanocomposite is found critically dependent on the content and structural integrity of carbon nanotube, and the study depicts the importance of fabrication of intimate heterojunctions demonstrating the benefits of nano-ensembles of functional units for light capture, carrier

transfer and catalysis in synergy for efficient solar photo-production of hydrogen from water.

Keywords: Methanol synthesis, carbon dioxide, renewable hydrogen, bimetallic alloy, heterogeneous catalysts, nanocomposite photocatalysts, sustainable development.

Thesis Contents

List of Abbreviations

AFM	Atomic force microscopy
AMOST	Aqueous miscible organic solvent method
APR	Aqueous-phase reforming
ATR	Attenuated total reflection
BET	Brunauer-Emmett-Teller
bcc	Body-centred cubic
CB	Conduction band
CCD	Charge-coupled device
CCS	Carbon capture and storage
CCU	Carbon capture and utilisation
CCVD	Catalytic chemical vapour deposition
CNTs	Carbon nanotubes
DFT	Density function theory
DWNTs	Double-walled carbon nanotubes
EB	Binding energy
EELS	Electron energy loss spectroscopy
Ek	Kinetic energy
EOR	Enhanced oil recovery
ESCA	Electron spectroscopy for chemical analysis
EXAFS	Extended x-ray absorption fine structure
fcc	Face-centred cubic
FFT	Fast-Fourier transform
FID	Flame ionisation detector
FTIR	Fourier transform infrared
FWHM	Full width half maximum
GHSV	Gas hourly space velocity
gof	Goodness-of-fit factor
HR-TEM	High-resolution transmission electron microscopy
HS-LEIS	High sensitivity-low energy ion scattering
ICP-MS	Inductively coupled plasma mass spectrometry
IEA	International Energy Agency

LDHs	Layered double hydroxides
MOFs	Metal-organic frameworks
MWNTs	Multi-walled carbon nanotubes
PEM	Polymer electrolyte membranes
PL	Photoluminescence
PXRD	Powder X-ray diffraction
R_{exp}	Expected error
R_p	Residual of least-squares refinement
R_{wp}	Weighted profile factor
RWGS	Reverse water-gas shift
SAS	Supercritical antisolvent precipitation
SCW	Supercritical water gasification
SMSI	Strong metal-support interactions
SOEC	Solid oxide electrolysers
STEM	Scanning transmission electron microscope
SWNTs	Single-walled carbon nanotubes
SXRD	Synchrotron X-ray diffraction
TCSPC	Time-correlated single photon counting
TCD	Thermal conductivity detector
TEM	Transmission electron microscopy
TGA	Thermogravimetric analysis
TOF	Turnover frequency
TPR	Temperature programmed reduction
TRPL	Time-resolved photoluminescence
VB	Valence band
WHSV	Weight Hourly Space velocity
WMO	World Meteorological Organisation
XAFS	X-ray absorption fine structure
XANES	X-ray absorption near-edge structure
XAS	X-ray absorption spectroscopy
XPS	X-ray photoelectron spectroscopy
XRD	X-ray diffraction

Chapter 1: Introduction

1.1 Background and aims of the thesis

Along with the benefits brought by the advance of industrialisation, more and more problems of greenhouse gas emissions have emerged, which result in global warming and lead to extreme weather change[1,2]. Although it is well-known that burning of fossil fuels accounts for the major greenhouse gas production, the world energy supply is still strongly dependent on this limited and non-environmentally friendly source[3] as shown in Figure 1-1a. According to the World Meteorological Organisation (WMO), the concentration of CO_2 in the Earth's atmosphere surged to a record high, hitting 403.3 ppm in 2016. Researchers suggested that a combination of human activities and the El Niño weather phenomenon drove CO_2 to a level not seen in 800,000 years[4]. This has become an international concern where increasing efforts are being made to end this carbon emission problem.

Carbon capture and storage (CCS) is one of the options that could help towards meeting the target of climate change mitigation. The International Energy Agency (IEA) reported in 2017 that among the many human activities, the use of energy represents by far the largest source of emissions[5]. It can be seen from Figure1-1b that c.a. 42% of the global CO_2 emissions from fuel combustion are related to electricity and heat generation, indicating that CO_2 capture technologies could effectively alleviate the current carbon emission problem if it was applied at large point sources, i.e., power plants. However, the main economic obstacle for CCS today is that it requires large capital investment which yet to be profitable[6]. Therefore, an alternative, carbon capture and utilisation (CCU), has started to attract people's attention, as it can turn waste CO_2 into valuable products such as chemical

feedstocks and fuels. In addition, its application for enhanced oil recovery (EOR) has also attracted commercial interests since 1970s[7]. By storing CO_2 in oil fields, EOR has the advantages of the enhanced oil production and reduced carbon emissions, that may offset the cost of the CO_2 capture process. With the development of the CCU technologies, CO_2 is no longer considered as a waste but as an alternative carbon feedstock. Chemical fixation of CO_2 using renewable hydrogen from biomass or decomposition of water from solar, tidal wave, and wind powers through its hydrogenation to methanol, as suggested in the "Methanol economy" strategy[8], has prompted intense research activities because methanol not only can be a platform chemical for many chemical products manufacture but also act as a high energy density and easy storable/transportable liquid hence it is suitable for replacing fossil fuels.

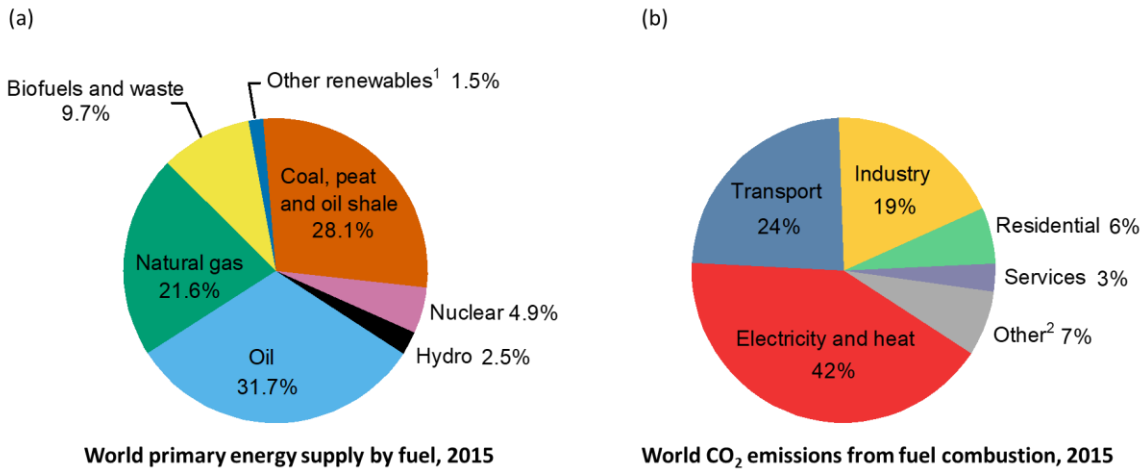

Figure 1-1. The sources of (a) the global primary energy supply by fuel, and (b) the global CO_2 emissions from fuel combustion by sector; data retrieved from the reports of IEA Statistics[3,5], 2017. *[1]Includes geothermal, solar, wind, tide/wave/ocean, heat and other renewables; [2]Includes agriculture/forestry, fishing, energy industries other than electricity and heat generation.*

The rapid advancement in the development of heterogeneous catalysts for methanol synthesis from CO_2 and hydrogen reflects the fact that heterogeneous catalysts are preferable than the homogeneous systems owing to their high stability, easier handling, and reusability that help to fulfil large-scale productions with lower costs[9]. Over the years, a great amount of effort has been put into the development of active and stable heterogeneous catalysts for CO_2 hydrogenation to methanol with several important review articles published. Liu *et al*.[10] summarised the catalyst innovation for methanol synthesis via CO_2 and CO through the detailed aspects including active site, support effect, promoter, synthesis and pre-treatment effect. However, this report was published 15 years ago hence an update of recent studies is desirable. In a review of recent advances in catalytic hydrogenation of CO_2, various catalyst systems such as Cu-based catalysts, Pd-based catalysts, and other novel catalysts are discussed in detail[11]. Álvarez *et al*.[12] provided a statistical result on types of catalyst reported for methanol synthesis from CO_2 hydrogenation published in the past 10 years, which shows that 79% of the reports described catalysts based on Cu, followed by 11.5% based on Pd, and 9.5% on bimetallic systems. It can recently be seen that CO_2 hydrogenation to methanol over bimetallic catalysts has emerged as an important subject in this area. In many cases, there is a great enhancement in their specific physical and chemical properties owing to a synergistic effect over the monometallic counterparts, therefore leading to a desirable catalytic performance toward methanol production.

So far, numerous solutions have been proposed to alleviate the problems associated with the emission of CO_2. Among all the options, green methanol synthesis that consists of CO_2 capturing/recycling together with renewable hydrogen production seems to be a promising way to achieve carbon neutral process and sustainable development. To make the green methanol production become economically attractive, from the feedstock side, the efficient

and economical CO_2 capture, as well as hydrogen production technologies, need to be available. As for the catalyst systems for CO_2 hydrogenation to methanol, at present the commonly used Cu-based catalyst, especially Cu-Zn based catalysts, still at the benchmark position due to their superior activity and economic advantages. However, the catalytic performance of the conventional Cu-based catalysts is often governed by thermodynamics which shows low methanol selectivity under low reaction pressure or low H_2/CO_2 conditions, presumably due to the poor intrinsic H_2 activation capability of Cu. Therefore, the advancement of Cu-based catalysts with new synthesis approaches as well as the development of new non-Cu based catalysts with good performance, and most importantly, can be effectively coupling with the above-mentioned feedstocks generation processes are highly desirable. In this context, rational design of novel bimetallic alloy systems as well as developing new synthesis methods that can lead to unique structural properties and enhanced activities toward methanol synthesis are required. This thesis is therefore intended to provide the studies on methanol synthesis from CO_2 hydrogenation over promising Cu and non-Cu based bimetallic materials, and a green hydrogen synthesis route from the photocatalytic way over nanocomposite materials.

1.2. Renewable CO_2/H_2 sources

1.2.1 CO_2 sources

Carbon dioxide capture and storage (CCS) is an emerging combination of technologies which can help to reduce CO_2 emissions from the use of fossil fuels. However, CCS faces many economic and technical barriers, such as the shortage of capital investment, the uncertain CO_2 leakage rate, and the geological incapability in certain areas, that must be overcome before it can be applied on a large scale[13]. More recently, carbon capture and utilisation (CCU) has started to attract attention because it can turn waste CO_2 into valuable

products, such as methanol and many other chemicals. Utilisation of CO_2 has the advantage of being a renewable, low cost, and non-toxic process. In addition, the CCU is generally a profitable activity as the produced chemicals or fuels can be sold, which makes it a promising way to help with the climate change mitigation[6].

Elimination of CO_2 from the flue gases of power plants would greatly reduce the global annual emissions, as the CO_2 produced from the electric power industry represents almost half of the global greenhouse gas emissions[14]. There are three CO_2 capture strategies that have been considered to possess the greatest possibility of reducing the emissions of CO_2 from fossil fuel-based power plants, namely, post-combustion, pre-combustion, and oxy-fuel capture[12]. In the post-combustion strategy, CO_2 is separated from the flue gas stream which allows for an easy adaptation to use with an existing power plant. As for the pre-combustion strategy, the fossil fuel is gasified under certain temperature and pressure for the removal of carbon prior to combustion. Given the higher partial pressure of CO_2 in this stream, an easy separation by utilising a variety of solvents can be achieved. In the last scenario of CO_2 capture, the oxy-fuel capture, pure oxygen is used for the combustion, resulting in a flue gas containing mainly water vapour and CO_2 so that the process can be easily recovered through a simple condensation method.

Presently, the biggest challenge for the implementation of CO_2 capture within power plants is the development of new materials. Many researchers are devoted to finding a material that displays suitable physical and chemical properties, and can reduce the large energy requirements when conducting the capture process[15]. The aqueous amine solutions such as monoethanolamine (MEA), diethanolamine (DEA) methyl diethanolamine (MDEA), as well as the amine blends solutions, show highly selective for acid gases[16,17]. Those amine

scrubbers have been commonly employed industrially for post-combustion CO_2 capture because of their rapid reaction rate and low cost[16]. However, due to the considerable energy penalty for desorbing CO_2 from the liquids, other materials with lower heat capacities are frequently proposed as alternatives. For example, ammonia-based solvents for CO_2 separation has been applied to overcome the drawbacks of amine-based capture technologies[18]. Ionic liquids show the advantages of high CO_2 solubility, good thermal stability and tuneable structures, hence they have also been proposed as promising solvents to replace the existing amine-based solvents[19]. On the other hand, solid sorbents such as zeolites[20,21], carbon-based adsorbents (activated carbons[21], carbon nanotubes[22], and graphenes[23]), layered double hydroxides (LDHs), and metal-organic frameworks (MOFs)[24] are considered to be good candidates for CO_2 capture owing to their promising adsorption capacity, CO_2 selectivity, stability and regenerability[21]. The high costs in the syntheses for some of these solid absorbers are presently the prime concerns.

More recently, another method using a membrane system has been introduced for CO_2 separation. The advantages of using membranes are simple, flexible, and less space-demanding. Most importantly, the potential to perform separations at low energy penalties makes the membrane strategies attractive for the practical CO_2 removal applications[25]. Apart from the polymer-based membranes, the inorganic solid sorbents mentioned above can also be used as inorganic fillers to form mixed-matrix membranes, which were found to improve both the permeability and selectivity of the membranes compared to the base polymer when applying for CO_2 capture[26].

Overall, current CO_2 capture technologies still require a substantial energy input, therefore it is unlikely that CO_2 capture will become profitable in the near future. If the government

can develop policies that help the development of CO_2 capture projects, for example, including CO_2 capture costs into the electricity bill[12], allowing tax-exempt financing for the acquisition of capital equipment that is used to capture CO_2, etc., then the implementation of CO_2 capture and the subsequent CO_2 mitigation may be able to take effect in a shorter timescale.

1.2.2 Hydrogen sources

In the current industrial production, hydrogen is commercially produced by steam methane reforming, coal gasification, and partial oxidation of light oil residues, which accelerates the depletion of fossil fuels and lead to an increasing CO_2 level in the atmosphere[27,28]. For the renewable methanol production from H_2 and CO_2, it must be pointed out that the consumed CO_2 in this process has to be more than that produced in hydrogen manufacturing, which means hydrogen sources must come from the green production routes. Water electrolysis with the electricity generated from green energy, i.e., photovoltaic power plant, wind power plant, and ocean energy converted into electricity[29], is considered to be one of the potential options for green hydrogen productions. Today, the most common electrolysis technology is alkaline-based water electrolysis[30]. Alkaline electrolysers operate by having two electrodes in a liquid alkaline electrolyte solution that transports hydroxide ions (OH^-) from the cathode to the anode with hydrogen being generated on the cathode side. State-of-the-art nickel-based cathode materials show good corrosion resistance in an alkaline solution water thus attracting extensive research efforts[30]. Although alkaline systems are the most developed electrolysis technologies with the lowest in capital cost, they have the lowest efficiency which leads to the highest electrical energy costs. Other ways toward green water electrolysis such as polymer electrolyte membranes (PEM) and solid oxide electrolysers (SOEC) are the developing technologies[28]. PEM electrolysers have no corrosion and seals

issues, and they are more efficient than alkaline systems but more expensive. SOEC technology has a huge potential for industrial application because it can produce hydrogen while achieving 100% Faradaic efficiency[12]. However, it has problems with corrosion, seals, thermal cycling, and chromium migration[27].

In addition to the above-mentioned processes, photocatalytic water splitting has a high potential for application as a clean and renewable way to generate hydrogen, because it is a process with negligible CO_2 emission: Decomposition of water directly into hydrogen and oxygen under sunlight irradiation with semiconductor materials (photocatalysts) are investigated. To efficiently exploit solar energy, myriad efforts have been made to develop photocatalysts that can be used not only under UV light but also under visible light[31]. Up to now, TiO_2 has been a widely used catalyst for photocatalytic water splitting, due to the fact that it is environmentally benign, stable, abundant and economical. However, the main obstacles of TiO_2-based photocatalysts are the rapid recombination of electrons and holes of photo-generated excitons, fast backward reaction, and its poor activation by sunlight[32]. In response to these weaknesses, modification of its structure through the introduction of surface oxygen vacancies by controlled reduction (blue or black TiO_2) and incorporation of dopers (N, F) to alter surface defects concentration are the common strategy. Employing composite photocatalysts is also an up-and-coming approach to increase the photocatalytic performance. For example, the composites are prepared by combining non-oxide materials with oxides or other non-oxides to form heterojunctions such as CdS-TiO_2, CdS-ZnO, CdS-MoS_2, CdS-AgI, etc.,[31,33,34] which lead to new photocatalysts with more efficient charge separation and widened absorption spectrum.

So far, a tremendous amount of research has been pursued in developing the hydrogen production via green routes. Among all the strategies, water electrolysis coupled with renewable resources should be at this moment the preferable option for low CO_2 emission hydrogen synthesis technology in short term. The availability of inexpensive electric power generated by wind, photovoltaic, tidal, or ground heat in special locations or countries may justify the implantation of this technology. It is, however, for most industrial areas of major CO_2 emission sources, the high installation and operational cost are still the major hindrances. Further research to address the cost issues is urgently needed. For photocatalytic generation of H_2, with the rapid development of new photocatalytic materials that overcoming the current deficiencies such as low stability of the catalysts and low energy efficiencies, it is anticipated that the low cost, environmentally friendly photocatalytic water-splitting for hydrogen production can contribute more significantly to the green hydrogen economy in further future. Particularly, the direct conversion of light energy to H_2 over the indirect conversion via photovoltaic and electrolysis would in principle offer lesser energy losts for the stepwise conversions.

1.2.3 CO_2/H_2 mixtures from biomass

Biomass is currently considered as one of the potential alternatives to produce renewable methanol. It can be obtained from various sources, including agricultural and forest residues, animal wastes, municipal paper wastes, sawdust, aquatic plants, and many more[28]. The currently accepted procedure to catalytically convert biomass into methanol is first via biomass conversion to syngas (CO, CO_2 and H_2), followed by water-gas shift reaction ($CO + H_2O \rightarrow CO_2 + H_2$), and ultimately by hydrogenation of CO_2 to methanol ($CO_2 + 3H_2 \rightarrow CH_3OH + H_2O$). Among the various gasification options, supercritical water (SCW) gasification[35] has received a great deal of attention as a promising method for utilising high

moisture content biomass and allowing maximum conversion. In addition, SCW gasification is non-toxic, safe, readily available, economically feasible and environmentally friendly[36]. However, high temperature and pressure (T > 500 °C and P > 23 MPa) are usually required to satisfy the SCW operating condition, which are very energy intensive[35]. On the other hand, aqueous-phase reforming (APR) of biomass-derivatives is a recently developed process and is preferable over other methods owing to its wide renewable resource, mild reaction conditions (T = 230 °C and P = 2 MPa), and low processing cost[37]. These biomass conversion technologies have been found promising in generating a CO_2/H_2 mixture that can incorporate with the downstream CO_2 hydrogenation reaction. However, most biomasses and their derived molecules generally contain lower hydrogen to carbon ratios. As a result, the utilisation of biomass for methanol production faces the main problem in producing reformate gas of large excess CO_2 to H_2, while in practice $H_2/CO_2 \geq 3$ is preferable for methanol synthesis over most catalyst formulations. Therefore, the stoichiometric adjustment has to be introduced either by adding hydrogen gas or applying a CO_2 removal step, which requires burdensome equipment and increases cost[38]. Alternatively, developing a new catalyst that can efficiently catalyse CO_2 hydrogenation to methanol under excess CO_2 but H_2-deficient conditions would be highly desirable.

1.3 Bimetallic catalysts on CO_2 hydrogenation to methanol

Bimetallic catalysts have emerged as an important class of catalysts due to their unique properties that are combined with two constituent metals. In many cases, bimetallic surfaces have enhanced catalytic properties owing to strong synergies to contribute the electronic or geometric alterations to monometallic counterparts. For the studies on CO_2 hydrogenation to methanol, Cu-Zn based system is prominently chosen. Other bimetallic catalysts such as Pd-Zn, Pd-Ga, Cu-Ni and Ni-Ga have also been investigated. In this part, we survey the

research progress on CO_2 hydrogenation reaction to methanol over many of diversified bimetallic catalysts in the literature. This section will start with a brief introduction of thermodynamic equilibrium of the methanol synthesis reactions, followed by a discussion of the possible reaction pathways and reaction intermediates. The correlation between reaction products and the adsorption properties of the metallic surfaces will also be addressed. Then the review of different synthesis methods of the selected bimetallic systems and their catalytic performance toward methanol synthesis will be illustrated.

1.3.1 Methanol synthesis mechanism

Due to the increasing focuses and interests in the methanol synthesis processes, numerous studies on the mechanism of CO_2 hydrogenation have been conducted. To fully understand the catalytic performance of CO_2 hydrogenation to methanol, the kinetics and thermodynamics of the catalytic system need to be considered. This section reviews the existing literature that provides information on the thermodynamic aspects and the possible reaction pathways. The influences of adding foreign metals (to form bimetallic system) on the reaction mechanism will also be discussed.

1.3.1.1 Thermodynamic equilibrium

In general, direct CO_2 hydrogenation to methanol contains two major competing reactions[39]. The first reaction is the synthesis of methanol from CO_2 and hydrogen:

$CO_2 + 3H_2 \rightarrow CH_3OH + H_2O$. $\Delta H^0 = -49.5$ kJ mol^{-1}; $\Delta G^0 = -10.7$ kJ mol^{-1} (1)

The second reaction is the reverse water-gas shift (RWGS) reaction that produces CO:

$CO_2 + H_2 \rightarrow CO + H_2O$. $\Delta H^0 = 41.2$ kJ mol^{-1}; $\Delta G^0 = 28.5$ kJ mol^{-1} (2)

Moreover, the catalytic hydrogenation of CO_2 to methanol can also occur indirectly from CO formed through the RWGS reaction[39]:

$CO + 2H_2 \rightarrow CH_3OH$. $\Delta H^0 = -90.6$ kJ mol^{-1}; $\Delta G^0 = -29.6$ kJ mol^{-1} (3)

It can be seen from equations (1) and (3) that, according to Le Chatelier's principle, increasing pressures and decreasing temperatures will cause the reaction to shift toward the products to produce more methanol over the CO production from RWGS (equation 2). In addition, using a high molar ratio of H_2/CO_2 is also thermodynamically as well as kinetically favourable in methanol synthesis with taking the two equilibria into account[40]. Early studies have demonstrated the necessity of using extremely high-pressure conditions in the synthesis of methanol from syngas with CO_2 as reactants[41–43]. Thanks to the development of active Cu-Zn based catalysts, the reaction pressure of methanol synthesis has been substantially reduced to 5-10 MPa while a satisfactory methanol selectivity of 50% can be attained compared to previous catalyst formulations[44]. Nevertheless, due to the advantages of applying high-pressure conditions in CO_2 hydrogenation to methanol such as boosting methanol yield, handling hydrogen more safely, reduction in reactor volume and plant area thus decreasing capital costs, etc., high-pressure methanol synthesis over Cu based catalysts have been explored and documented by some research groups. Ipatieff *et al.*[45] conducted a high-pressure study up to 41.4 MPa over Cu/Al_2O_3 catalysts in a fixed-bed reactor, which showed remarkable conversion (94%) from CO_2 to methanol. By using co-precipitated $Cu/ZnO/Al_2O_3$ catalysts, Bansode *et al.*[46] demonstrated that one-pass CO_2 conversion (>95%) and methanol selectivity (>98%) were achieved under the reaction conditions of $H_2/CO_2 = 10$, reaction temperature of 260 ^oC, reactant pressure of 33.1 MPa, and gas hourly space velocity (GHSV) of 10,471 h^{-1}. Gaikwad *et al.*[47] also showed that at the stoichiometric molar ratio of $H_2/CO_2 = 3$, ca. 90% CO_2 conversion and > 95% methanol selectivity could be achieved at 44.2 MPa. In contrast, some researchers devoted to the development of catalysts that can work under low reaction pressures. It is mainly because the low-pressure CO_2 hydrogenation processes are more economically attractive with lower installation and

operation (pumping) costs. Moreover, they have the advantages of safer operation and can be readily coupling with the upstream feedstocks generation processes. For example, hydrogen production from standard alkaline electrolyser is typically operated at ambient pressure or less than 3 MPa[48], and some low-pressure biomass conversion processes (e.g., APR) to form CO_2/H_2 mixture are operated at around 2 MPa[37]. However, the conversion of CO_2/H_2 to methanol by using low-pressure technologies is limited by thermodynamic and kinetic considerations. It has to be emphasised that obtaining satisfactory single-pass CO_2 conversion and methanol selectivity is important for practical catalytic application since recycling processes are costly and require cumbersome facilities. So far, very little research has demonstrated high methanol production rate at the pressure lower than 2 MPa. In fact, most of the reported catalysts perform poorly at low-pressure conditions. Taking Cu-Zn system as an example, when the reaction pressures are applied at less than 2 MPa, the rate of RWGS is generally 1–3 orders of magnitude higher than that of methanol production over the Cu-Zn surface[49], thus resulting very poor selectivity toward methanol. It was reported previously by Toyir *et al*.[50] that under pressure of 2 MPa, silica-supported Cu/ZnO based catalysts showed methanol selectivity around 99%. In addition, In_2O_3/ZrO_2 catalyst reported more recently by Martin *et al*.[51] also achieved nearly 100% methanol selectivity under relatively low pressure (5 MPa). Although these catalysts presented unexpectedly high selectivity toward methanol, they showed very low CO_2 conversion (2% to 5%) hence leading to an overall low methanol production yield. Other Cu-based systems and novel catalyst materials such as the catalysts with copper-ceria interface[52] as well as Ni-Ga/SiO_2 system[53] have proven their potential on highly efficient methanol synthesis. However, those systems were evaluated for CO_2 to methanol at the pressure around ambient pressure where the obtained methanol yield is not very impressive, hence little information on their realistic application of CO_2 hydrogenation is known from the results provided by the authors.

Nevertheless, it has been recently reported that the PdZn site from Pd-Zn bimetallic catalyst appeared to alter the overall thermodynamic equilibria between methanol production and RWGS reaction by offering an unusually high kinetic barrier for the latter reaction, and thus effectively enhancing methanol production under low pressure (2 MPa) conditions without catalysing RWGS reaction to equilibrium position[54]. This catalyst system apparently opens up a promising possibility for low-pressure CO_2 hydrogenation application.

1.3.1.2 Reaction pathways and intermediates of methanol production

As stated, the catalytic hydrogenation of CO_2 to methanol can happen directly or indirectly. In the former, two different mechanistic routes have been proposed according to their key reaction intermediates: The formate (HCOO) pathway or the hydrocarboxyl (COOH) pathway. Methanol synthesis via the HCOO-mediated mechanism has been proposed by many studies due to the fact that the formation barrier of the HCOO is considerably lower than the formation barrier of the COOH[49,55–57]. In addition, formate species were found to be the most abundant surface intermediates during CO_2 hydrogenation reaction from the experimental observations[58–62]. Grabow *et al*.[55] found that under typical methanol synthesis conditions, CO_2 hydrogenation is responsible for ~2/3 of the methanol produced, and the intermediates of the formate pathway for methanol production include HCOO*, HCOOH*, CH_3O_2*, CH_2O*, and CH_3O*, see Figure 1-2. Another example of the formate pathway, calculated by Yang *et al*.[49], showed that methanol synthesis on Cu surfaces followed the formate pathway via HCOO, H_2COO, H_2CO and H_3CO intermediates, which were considered to be less stable from the above-mentioned calculations done by Grabow *et al*.[55]. But the authors indicated that the presence of the active low-coordinated Cu sites in the Cu nanoparticle could stabilise the key intermediates (HCOO and H_2COO) therefore lowered the barrier for the rate-limiting hydrogenation process. On the contrary, other researchers

proposed that the H_2O-promoted hydrocarboxyl (COOH) mediated mechanism, following the sequence of COOH → HCOOH → HCO → HCOH → CH_2OH → CH_3OH, is kinetically more favourable than the formate pathway for the hydrogenation of CO_2 to methanol on Cu(111)[63]. In this proposed COOH pathway, it has been suggested that the formate species only plays a spectator co-adsorbate role[64], and the direct HCOO hydrogenation is even believed to be a "dead end" for methanol production[63]. For an easy comparison, the above-mentioned pathways for CO_2 hydrogenation to methanol and the intermediates are displayed in Figure 1-2. On the other hand, it is also believed that hydrocarboxyl (COOH) is the chemical precursor of CO from RWGS reaction[54,65]. Hence, an indirect CO_2 hydrogenation mechanism has also been suggested, which involves the formation of CO from the RWGS reaction as the first step, then methanol is formed by the hydrogenation of CO. However, this claim is not as widely accepted as the other two. Moreover, the recently reported isotope labelling experiments indicate that CO_2, rather than CO, is the preferred carbon source for methanol production[66,67].

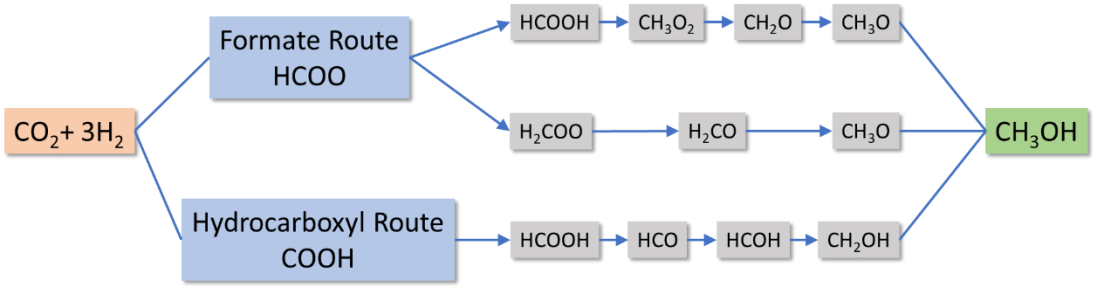

Figure 1-2. CO_2 hydrogenation to methanol through formate route and hydrocarboxyl route and the intermediates[49,55,63] discussed in this Chapter.

1.3.1.3 Synergistic enhancement in bimetallic catalysts

Adding foreign atoms to an existing metal system is used frequently to modify the chemical properties of metal surfaces. In catalysis, bimetallic alloys usually have different catalytic properties from their primary mono-metallic surfaces, which depend strongly on their electronic or geometric structures. Figure 1-3 illustrates the main types of mixing patterns and structures of bimetallic, namely, mixed, core-shell or Janus alloys[68,69]. For the transition metals, the d-band model is often employed in understanding bond formation at the surface and their catalytic trends. Nørskov and co-workers have illustrated the correlation between the adsorption energy and the d-band structure on the surface metal atoms that the adsorbate binds to[70,71]. By forming a bimetallic alloy, the structure of the surface d-electron bands and filling could change substantially owing to the modification of the electronic properties driven by i) the formation of heteroatomic bonds that leads to the electronic interaction between the two metals. This can alter the electronic environment of the primary metal, giving rise to modifications in the electronic configuration of it, and consequently, change its chemical properties. This is so-called electronic (or ligand) effect[72,73]; ii) geometric irregularity, that is, lattice distortion induced by alloying of two metals with different sizes, and lattice compression or expansion occurs often in the core-shell (see Figure 1-3) bimetallic structure. Those geometric differences can cause the changes in surface bond lengths and bond angles, giving rise to the so-called geometrical (or ensemble) effect that modifies the electronic properties of the parent metal atoms[72–74]. According to theoretical calculations[53,65,75–77], catalytic activity and selectivity of CO_2 hydrogenation to methanol is critically dependent on the overall adsorptivity of the active surfaces. For a better understanding on the differences in product specificity and methanol production rate caused by the alteration of molecule adsorption through forming bimetallic alloys, we have surveyed the reported CO_2 hydrogenation studies and some examples are given as below.

In the literature, it has been suggested that Cu/Zn interface plays a significant role in methanol synthesis from CO_2 hydrogenation as these two species (Cu and Zn) work synergistically. Indeed, placing Zn in a proximity to Cu showed enhanced methanol production has been demonstrated by many researchers[78–80]. Behrens *et al*.[79] have reported the stabilisation of adsorbed intermediates with decreased energy barriers when Zn atoms were introduced on Cu step sites, which significantly increased the methanol production rate of Cu-Zn surface compared to the unmodified Cu surface. Moreover, catalysts containing Cu/ZnO were recently found to show 10 times higher activity than Cu catalysts of the same sizes but without in contact with ZnO[81]. Another non-precious bimetallic system, discovered by Studt *et al*.[53], showed that by alloying of Ga into Ni, the adsorption strength of Ni surface was modified hence accelerated methanol formation. In contrast, Ni alone binds oxygen too strongly that would result in surface poisoning by formate or the surface would mainly perform methanation in CO_2 hydrogenation reaction[53]. Kusama *et al*. found that the formation of bimetallic alloys on the catalyst surface could change the electronic states of rhodium and lead to different adsorption properties: Rhodium-based catalysts are known to effectively catalyse CO_2 hydrogenation to CH_4 or CO, but alloying with Fe to form Fe-Rh catalysts could improve the ethanol selectivity remarkably[82], while alloying with Co and Rh resulted in promotion of methanol formation[83]. The authors concluded that the changes of product specificity could be correlated with the electronic state of rhodium changed with the foreign atom addition. The changes of the adsorptivity of the active surfaces can also be illustrated in the Pd-Zn bimetallic system. Liao *et al*.[54] found that alloying of Pd with Zn to form Pd core-Zn shell (Pd@Zn) structure could increase the adsorption strength of the bidentate formate species (the key intermediate to methanol). From density function theory (DFT) calculation, a strong electronic charge transfer from Zn to Pd was revealed. The Zn-rich Pd-Zn bimetallic surfaces showed more selective and active for the formation of surface

HCOO rather than COOH species in the first step of CO_2 hydrogenation, leading to a higher selectivity towards methanol production. Overall, from the above-mentioned examples, it can be seen that the changes in the adsorption properties of the primary mono-metallic surface are obvious when forming bimetallic system, giving rise to a different catalytic behaviour.

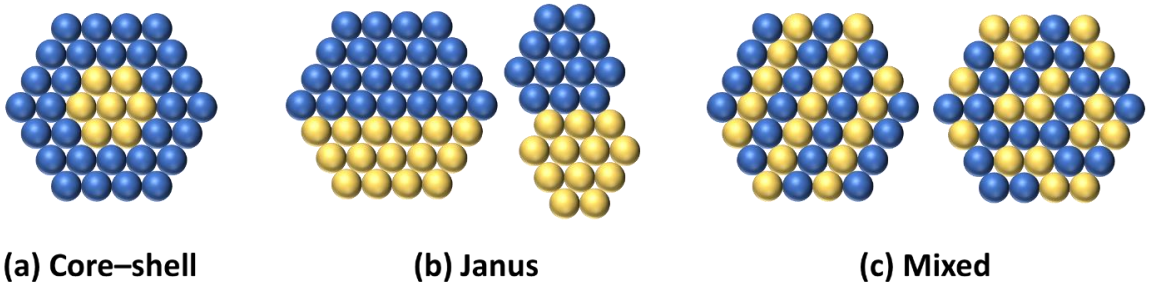

Figure 1-3. Schematic representation of the types of structures of bimetallic alloy nanoparticles (based on Ref. [68, 69]).

1.3.2 Bimetallic catalysts made by different methods and their catalytic performances

The high-pressure methanol synthesis process from CO/CO_2 and H_2 mixture using mixed metals and metal oxides was firstly investigated in the early 20th century[41–43]. In the 1960s, the highly active and economic $Cu/ZnO/Al_2O_3$ catalyst was developed and it is still currently the industrial preferred catalyst for methanol synthesis operated at 240 °C – 260 °C and 50 –100 bar[44]. At present, the major challenges for catalyst development to methanol synthesis from CO_2 are to develop the most efficient catalyst, thus the academic research efforts on catalyst development using different catalyst compositions and preparation methods are continuously shared and built. Recently, bimetallic nanoparticles/alloys have emerged as an

important class of catalysts because they show the intimate contacts of the two elements which can modify their electronic properties and change the adsorption properties of the metal surfaces. It is well-known that catalytic conversion of CO_2 to methanol is a structural-sensitive reaction[81]. Therefore, the differences in synthesis methods can influence the structure of the catalysts and then lead to a different catalytic performance. This section will focus on the review of synthesis methods of those bimetallic catalysts that showed enhanced ability to catalyse CO_2 hydrogenation to methanol than their monometallic counterparts. The catalytic performance of the selected catalysts is compared in Table 1-1.

Table 1-1 Catalytic performance of selected bimetallic catalysts in CO_2 hydrogenation to methanol

Synthesis method	Catalyst Active species/ (support)	Reaction conditions			Catalytic performance					Ref.
		P (MPa), T (°C)	Space velocity	H_2/CO_2	CO_2 conversion (%)	Methanol selectivity (%)	STY_{MeOH}[e]	WTY_{MeOH}[f]	TOF (s^{-1})	
Imp.[a]	PdGa/(β-Ga_2O_3)	3, 250	(G)[d] 80000 h^{-1}	3	<1	52	N.A.	N.A.	0.075	84
	Pd/(SiO_2)					12			0.002	
	PdGa/(rod Ga_2O_3)	5, 250	(W) 6000 mL g^{-1} h^{-1}	3	11.04	41.27	N.A.	N.A.	N.A.	85
	PdGa/(plate Ga_2O_3)				17.33	51.62				
	PdZn/(*h*-CNTs)	3, 250	(W) 1800 mL g^{-1} h^{-1}	3	N.A.	99.6	0.371	N.A.	0.0115	86
	PdZn /(activated carbon)					96.5	0.281		0.0098	
	PdZn/(γ-Al_2O_3)					92.1	0.242		0.0097	
	PdCu/(SiO_2)	4.1, 250	(W) 3600 mL g^{-1} h^{-1}	3	6.7	30	0.032	N.A.	N.A.	87
	Pd/(SiO_2)				3.0	23	0.010			
	Cu/(SiO_2)				2.8	15	0.006			
	Ni_5Ga_3/(SiO_2)	0.1, 210	(G) 6000 h^{-1}	3	N.A.	N.A.	~0.02	~0.12	N.A.	53
Co-precip.[b]	Cu/ZnO/Al_2O_3	5, 250	(W) 18000 mL g^{-1} h^{-1}	3	19.7	48.1	0.637	N.A.	N.A.	88
	Zincian georgeite-derived catalyst	2.5, 190	(W) 7000 mL g^{-1} h^{-1}	$CO:CO_2$: $H_2:N_2$ =6:9.2:67:17.8	N.A.	N.A.	0.102	0.167	N.A.	89
	Zincian malachite-derived catalyst						0.083	0.136		
	Commercial Cu/ZnO/Al_2O_3						0.116	0.243		
	PdGa/(Ga_2O_3)	5, 250	(W) 18000 mL g^{-1} h^{-1}	3	19.6	51.5	N.A.	N.A.	0.1139	90
	CuZn/(ZnO)				11.7	36.1	N.A.	N.A.	0.0048	
	Catalyst derived from Cu,Zn,Al-LDH	6, 250	(W) 20000 mL g^{-1} h^{-1}	$H_2:CO:CO_2:He$ =72:10:4:14	N.A.	N.A.	N.A.	N.A.	0.0268	91
	Conventional Cu/ZnO/Al_2O_3								0.018	
	Catalyst derived from Cu,Zn,Al,Y-LDH	5, 250	(W) 10000 mL g^{-1} h^{-1}	3	20.2	69.3	0.39	N.A.	0.00666	92
	Cu/(Zn,Al,Zr-LDH)	5, 250	(W) 7500 mL g^{-1} h^{-1}	3	22.2	45.8	0.30	N.A.	N.A.	93
	Catalyst derived from Cu,Zn,Al,Y-LDH	5, 250	(W) 12000 mL g^{-1} h^{-1}	3	26.9	47.1	0.52	N.A.	N.A.	94
	CuZn from CuZnGa-CO_3 AMO-LDH	4.5, 270	(W) 18000 mL g^{-1} h^{-1}	3	18.8	47.8	0.6	N.A.	N.A.	95
	PdZn derived from PdZnAl LDH	3, 250	(W) 15000 mL g^{-1} h^{-1}	3, with 4 vol% Ar	0.6	60	0.017	N.A.	0.002	96
	Pd_2Ga derived from PdMgGa LDH				1.0	47	0.020	N.A.	0.0085	
	Pd derived from PdMgAl LDH				3	4	0.0006	N.A.	0.00005	

Table 1-1 (cont.) Catalytic performance of selected bimetallic catalysts in CO_2 hydrogenation to methanol

Synthesis method	Catalyst Active species/ (support)	Reaction conditions			Catalytic performance					Ref.
		P (MPa), T (°C)	Space velocity	H_2/CO_2	CO_2 conversion (%)	Methanol selectivity (%)	STY_{MeOH}[e]	WTY_{MeOH}[f]	TOF (s^{-1})	
bimetal carbonyl hydride	$PtCr/(SiO_2)$	3, 200	W/F = 10 g_{cat} h/mol.	3	2.2	51.1	N.A.	N.A.	N.A.	97
	$PtW/(SiO_2)$				2.6	92.2				
Imp.	$Pt/(SiO_2)$				0.4	1.9				
Sol-immob.[c]	PdZn/(ZnO)	2, 250	(W) 3600 mL g^{-1} h^{-1}	3	10.7	60	0.07744	N.A.	N.A.	98
Imp.	PdZn/(ZnO)				8.7	1	0.00176			
Hetero-junction	Pd@Zn/(ZnO+CdSe)	4.5, 270	(W) 18000 mL g^{-1} h^{-1}	3	14.4	64.9	0.60	12.0	0.33	99
		2, 270			7	67.3	0.30	6.1	0.19	54

[a] Impregnation method
[b] Co-precipitation method
[c] Sol-immobilisation
[d] (G) = GHSV = volume flow rate/bed volume, (W) = WHSV = mass flow rate/catalyst mass.
[e] Space time yield of methanol ($g_{MeOH} \cdot g_{cat}^{-1} \cdot h^{-1}$)
[f] Weight time yield of methanol ($g_{MeOH} \cdot . g_{active\ metal}^{-1} \cdot h^{-1}$)

1.3.2.1 Impregnation method

Impregnation is the simplest method for mounting of dissolved aqueous metal precursors on oxide supports to prepare supported catalysts. A known advantage of impregnation method is that the materials dissolved in the solution will not get lost, which makes this method attractive when preparing precious metal-containing catalysts. Pd-containing bimetallic catalysts made via impregnation method were first discovered in the 1900s by Iwasa *et al*.[100] The authors observed that the original catalytic functions of monometallic Pd for steam reforming of methanol, the reverse reaction of CO_2 hydrogenation to methanol, was greatly modified by the formation of bimetallic alloys, i.e., Pd-Zn, Pd-Ga and Pd-In, upon the reduction of the Pd-metal oxides. It was found that the reactions proceeded selectively when using the catalysts having the alloy phase, whereas poor selectivities were exhibited on the catalysts having monometallic phase.[101] A few years later the Pd-Ga system was further investigated by other researchers[84], and the Pd-Ga bimetallic particles were found to be the sites responsible for the increased selectivity to methanol in CO_2 hydrogenation as well as the inhibition of the methanol decomposition and/or reverse water-gas shift (RWGS) reaction to produce CO. As a result, the Ga-modified Pd catalyst showed much better selectivity and TOF toward methanol production[84]. Qu *et al*. [85] further proposed that using the plate-form Ga_2O_3, which has a higher degree of defects and electron-richer polar (002) surface, could exert a stronger electronic interaction with Pd than the rod-form surface Ga_2O_3. This would lead to a deep reduction of Ga^{3+} to generate bimetallic $PdGa_x$ nanoparticles with superior catalytic properties for methanol synthesis by CO_2 hydrogenation. As the importance of bimetallic nanoparticles has been increasingly recognised, the characterisation techniques for revealing the structure of a bimetallic catalyst become more and more proficient. By using a combination of advanced electron microscopy techniques and structure characterisation tools, highly dispersed $GaPd_2$ nanoparticles on a

high surface area SiO_2 support synthesised by impregnation of the high surface area SiO_2 with Pd and Ga nitrates were identified. Besides, this nanodispersed intermetallic $GaPd_2$ catalyst showed a much better methanol selectivity than the traditional $Cu/ZnO/Al_2O_3$ catalyst under ambient pressure[102].

Apart from the Pd-Ga system, several supported Pd catalysts have also been found to exhibit considerable activity and selectivity for hydrogenation of CO_2 to methanol. Liang *et al.*[86] incorporated multi-walled carbon nanotubes (MWNTs) into Pd/ZnO catalysts prepared via a stepwise incipient wetness method. They found that the unique features of MWNTs were leading to the increase of the surface concentration of the Pd^0 species in the form of PdZn alloys as well as helping with H_2 activation, thus increasing the rate of surface hydrogenation reactions. On the other hand, amorphous silica supported Pd-Cu bimetallic catalysts prepared by co-impregnation method also found to have a strong synergistic promotion compared to the monometallic Pd and Cu catalysts[87]: The production rate of methanol on the Pd-Cu bimetallic catalyst is 2 times as much as the sum of those on the monometallic catalysts, indicating a considerable bimetallic promotion on methanol synthesis from hydrogenation of CO_2. Another example of the precious bimetallic metal surface for enhancing methanol production can be found in the Rh-Co catalyst[83]. Although the methanol selectivity was very low (< 20%), it was suggested that the changed electronic states of rhodium in the Rh-Co alloy resulting in the promotion of methanol formation. On the other hand, non-precious Ni-Ga catalysts synthesised via impregnation method was recently discovered to be superior to the traditional $Cu/ZnO/Al_2O_3$ catalyst with respect to their ability to inhibit the RWGS activity[53]. The Ni-Ga intermetallic compounds were found to possess mixed sites: the gallium-rich sites facilitate methanol synthesis, whereas the nickel-rich sites perform RWGS and methanation until they get poisoned by CO and carbon, which

makes the Ni-Ga catalysts to display good methanol synthesis activity with considerably lower production of CO as compared to the conventional $Cu/ZnO/Al_2O_3$ catalysts under atmospheric pressure[53].

1.3.2.2 Co-precipitation method

The catalysts based on more than one component can be prepared by the simultaneous precipitation from a solution containing desired soluble species to generate a homogeneous distribution of catalyst components or catalyst precursors with a definite stoichiometry. Co-precipitation method provides the advantage of obtaining high dispersions of catalyst components, which is difficult to achieve by other synthesis approaches. Therefore, it is very suitable to use in preparing multi-component catalysts and catalyst precursors.

1.3.2.2.1 Cu/ZnO based catalysts

The industrial $Cu/ZnO/Al_2O_3$ catalyst for methanol synthesis is made via coprecipitation method. Since the prevailing of $Cu/ZnO/Al_2O_3$ catalyst, the Cu/ZnO based catalysts have attracted increasing attention and many systematic studies have focused on elucidating the structure of active sites[56,79,103]. Although the active sites of methanol synthesis over commercial $Cu/ZnO/Al_2O_3$ catalysts have recently been the subject of intense debate, many studies over the past 20 years have shown that the good performance of Cu/ZnO based catalysts for methanol synthesis could be attributed to the active Zn-Cu bimetallic sites. Early researches done by Fujitani *et al*.[88,104,105] focused on the promotion mechanism of ZnO to Cu catalysts for methanol synthesis. Their result revealed that the partially reduced ZnO_x could migrate to the surface of Cu particles to form Cu-Zn alloy when reducing a Cu/ZnO catalyst with H_2 at above 600 K. The Cu-Zn alloy phase was then believed to be a catalytically active species for the methanol synthesis from CO_2 and H_2 [106,107]. Topsøe and

co-workers observed that Cu/ZnO changed the CO adsorption properties under severe reducing conditions from in-situ IR during methanol synthesis, suggesting that Cu-Zn alloy structures could be formed due to the migration of reduced ZnO species[108]. After conducting careful investigations using other in-situ techniques, which includes electron energy loss spectroscopy (EELS), high-resolution transmission electron microscopy (HR-TEM) and extended X-ray absorption fine structure (EXAFS), the presence of Cu-Zn alloy in the reduced Cu/ZnO catalysts was further confirmed[109,110]. Recently, with rapid development of advanced characterisation techniques, it has been shown that Cu steps stabilised by bulk defects and decorated with Zn atoms upon reduction can lead to a subtle change in the geometric and electronic structure of Cu due to the desirable bimetallic properties[79]. Consequently, the high activity of $Cu/ZnO/Al_2O_3$ methanol synthesis catalyst is attributed to the surface alloy of Zn and Cu[78,103].

It is noted that Cu/ZnO based catalysts prepared by coprecipitation are much more active than those prepared by impregnation methods. Moreover, the structure of catalyst precursor obtained in the coprecipitation synthesis, such as malachite $Cu_2CO_3(OH)_2$, zincian malachite (sometimes called rosasite) $(Cu,Zn)_2CO_3(OH)_2$, aurichalcite $(Cu,Zn)_5(CO_3)_2(OH)_6$, or hydrozincite $Zn_5(CO_3)_2(OH)_6$, can significantly affect the catalytic activity for methanol production[107,111,112]. Baltes *et al.*[113] discovered that the synthesis history would influence strongly to the catalytic activity of methanol production. In their study, ternary $Cu/ZnO/Al_2O_3$ catalysts were systematically prepared via the coprecipitation method under various synthetic parameters, and the best methanol productivity was found in the catalysts with the following preparation conditions: Precipitation temperature of 70 ^oC, pH of 6-8, time of aging in the mother liquor of 20-60 min, and calcination at 300 ^oC, which resulted in the catalysts with relatively high BET and Cu^0 surface areas[113]. Other studies on this

system by Behrens *et al*.[114–116] further concluded that zincian malachite was the optimum precursor for the methanol synthesis catalyst due to its interwoven, nano-scale needle morphology that facilitates the formation of a highly porous mesostructure catalyst. On the other hand, it was recently reported that a disordered zincian georgeite catalyst precursor could be prepared using supercritical antisolvent (SAS) precipitation method[117], which enabled the preparation of an active Cu/ZnO catalysts that could compete with those catalysts prepared from other hydroxycarbonates precursors. Soon after it was found that zincian georgeite could be readily prepared by co-precipitation method[89]. Although the zincian georgeite made by co-precipitation led to a catalyst with a slightly poorer performance than those derived from SAS precipitation due to the impurity contamination and less-disordered structure in the co-precipitated phases, it still displayed superior performance for methanol synthesis compared to a conventional preferred zincian malachite derived catalyst[89].

1.3.2.2.2 Precious metal based bimetallic catalysts

Apart from the Cu/ZnO based catalysts, co-precipitation method was also widely employed in the preparation of precious metal based bimetallic catalysts. Fujitani *et al*.[90] synthesised a series of palladium catalysts by co-precipitation method. The authors found that the Pd/Ga_2O_3 catalyst was more active than Cu/ZnO by a factor of 2 in the methanol yield and 20 in the turnover frequency (TOF) for the synthesis of methanol from CO_2 and hydrogen, due to the optimal amount of Pd^{n+} ($0 < n < 2$) stabilised by Ga_xO_y on the surface of palladium. Remember that many studies have identified the formation of Pd-Ga bimetallic alloys in such catalyst composition, as discussed previously in section 1.3.2.1 of this chapter, which are experimentally proven to be active for methanol production from CO_2 and hydrogen. On the other hand, carbon nanotubes (CNTs) was found to play a dual role (acting as a catalyst

supporter as well as a promoter) for Pd-based catalysts[86]. CNTs-promoted Pd-Zn and Pd-Ga catalysts were synthesised via co-precipitation method and studied for methanol production from CO_2 hydrogenation by Zhang and co-workers[86,118]. The authors found that Pd-Zn and Pd-Ga catalyst with an appropriate incorporation of CNTs displayed enhanced activity for CO_2 hydrogenation to methanol compared to those non-promoted Pd-based bimetallic catalysts.

1.3.2.2.3 Layered double hydroxide (LDH)-derived catalysts

Recently, hydrotalcite-like compounds (or layered double hydroxide, LDH) with the general formula $[M^{2+}_{1-x}M^{3+}_{x}(OH)_2]^{x+}(An^{-})_{x/n}\cdot mH_2O$ where M^{2+} and M^{3+} are divalent and trivalent cations, respectively, have attracted numerous attention. LDH structure provides a homogeneous distribution of all metal cations inside the layers, which is believed to offer a suitable matrix for generating small, stable, and well-dispersed metal nanoparticles after calcination and reduction. It was reported that monophasic catalyst precursor containing M^{2+} and M^{3+} could be obtained by controlled thermal treatment of an LDH structure[119], since that, the application of LDH as a catalyst precursor for CO_2 hydrogenation reaction has been developed immediately. Many studies have discussed the advantages of LDH precursors for Cu/ZnO-based catalysts[120,121], such as good dispersion of M^{2+} (Cu^{2+}, Zn^{2+}) and M^{3+} (Al^{3+}, Y^{3+} or Ga^{3+}) at an atomic level, homogeneous microstructure, good thermal stability against sintering/reduction, high dispersion for small Cu clusters, and high specific surface area. An active catalyst derived from a phase pure Cu, Zn, Al hydrotalcite-like precursor was prepared and studied by Kühl *et al*[91]. This sample showed intrinsically more active than a conventionally prepared reference catalyst. Furthermore, Gao *et al.*[92–94] synthesised a series of $Cu/ZnO/Al_2O_3$ catalysts derived from hydrotalcite-like precursors with modifier (Mn, La, Ce, Zr and Y) or promoter (Y_2O_3) and tested for the CO_2 hydrogenation to methanol. They

have concluded that the introduction of additives to $Cu/ZnO/Al_2O_3$ catalysts derived from hydrotalcite-like compounds could give higher BET specific surface area, Cu surface area and Cu dispersion, thus leading to an enhanced catalytic performance with high stability[92–94]. Tsang and co-workers[95] have just reported a CuZnGa catalyst derived from ultra-thin (1-3 cationic-layers) $(CuZn)_{1-x}Ga_x$-CO_3 layered double hydroxides (AMO-LDH) nanosheets synthesized following the aqueous miscible organic solvent method (AMOST)[122]. It has been found that upon reduction, the AMO-LDH-derived catalysts give consistently and significantly higher Cu surface areas and dispersions than the catalysts prepared from conventional co-precipitation methods. It is also evident that Zn metal atoms decorating on Cu nanoparticles can be formed in the catalyst derived from ultrathin LDH precursor, thus exerting a great promoting effect to the CO_2 hydrogenation reaction to methanol and leading to a high methanol production rate. On the other hand, Ota *et al*.[96] synthesised Pd-based catalysts derived from ternary hydrotalcite-like compounds obtained by co-precipitation from aqueous solutions. They found that the intermetallic Pd_2Ga and PdZn nanoparticles with a homogeneous distribution of Pd and intimate interaction with the other reducible metal species were formed upon reduction in hydrogen, which were more active for methanol synthesis from CO_2 hydrogenation than the monometallic Pd catalyst.

1.3.2.3 Other synthesis method

Shao *et al*.[97] reported the supported PtW and PtCr bimetallic catalysts made by the bimetal carbonyl hydride complexes precursors. The PtW and PtCr bimetallic catalysts exhibited higher activity and methanol selectivity in CO_2 hydrogenation reaction than the monometallic or bimetallic catalysts prepared via impregnation method. Nerlov *et al*.[123] applied CO as a promoter in the catalyst system and observed a CO gas phase induced surface segregation of Ni on Cu(100). The authors also found that the Ni/Cu(100) bimetallic

sites were 60 times more active for CO_2 activation compared with pure Cu ones[124]. Hartadi *et al.*[66] found that a commercially available Au/ZnO catalyst prepared by deposition-precipitation could benefit from the same effect as the Cu/ZnO catalyst, that is, containing the partially reduced ZnO in the highly reductive atmosphere that could induce the formation of AuZn (surface) alloys or the formation of a partially reduced ZnO_x shell, implying the potential of Au/ZnO catalysts for the application in hydrogenation of CO_2 to methanol. Bahruji *et al.*[98] identified the PdZn alloy nanoparticles with a controlled particle size from the Pd/ZnO catalysts prepared by sol-immobilisation. The authors suggested that the catalysts prepared by sol-immobilisation were relatively stable to thermal treatment and showed a higher conversion of CO_2 towards methanol than the classic impregnated catalysts.

Tsang and co-workers[54,99] reported a novel heterojunction approach to synthesize supported Pd@Zn nano-structures with tuneable Zn shell thickness by a simple reduction of Pd/CdSe-ZnO solid precursors in hydrogen. The precursors contained CdSe-ZnO type-II heterojunction interfaces that could promote the reduction process of ZnO to metallic Zn^0 atom and form Zn decorate Pd nanoparticles, which would exert enhanced catalytic performance in methanol production from CO_2 hydrogenation. The similar heterojunction approach was then applied to the Cu/ZnO based catalyst. It was found that the presence of a small amount of Ga^{3+} in the Cu/ZnO system could lead to the formation of Ga-containing spinel structure, which would create electronic heterojunction with excess ZnO phase to facilitate the reduction of Zn^{2+} to Zn^0 in contact with Cu to form highly active CuZn bimetallic nanoparticles and offer catalytic sites. The authors also discovered a correlation between Zn^0 concentration in the CuZn alloy nanoparticle to the catalytic performance, showing that CO_2 conversion and methanol selectivity were significantly improved by increasing the Zn^0 content in these CuZn bimetallic catalysts[80].

References

1. Watson, C. S., White, N. J., Church, J. A., King, M. A., Burgette, R. J. & Legresy, B. . Unabated global mean sea-level rise over the satellite altimeter era. *Nat. Clim. Chang.* **5,** 565–568 (2015).
2. Fischer, E. M. & Knutti, R. Anthropogenic contribution to global occurrence of heavy-precipitation and high-temperature extremes. *Nat. Clim. Chang.* **5,** 560–564 (2015).
3. International energy agency. Key World Energy Statistics 2017. *IEA Statistics* (2017). Available at: https://www.iea.org/publications/freepublications/publication/KeyWorld2017.pdf.
4. McGrath, M. Record surge in atmospheric CO_2 seen in 2016. *BBC* (2017). Available at: http://www.bbc.co.uk/news/science-environment-41778089.
5. International Energy Agency. CO_2 Emissions from Fuel Combustion: Overview. *IEA Statistics* (2017). Available at: http://www.iea.org/publications/freepublications/publication/CO2EmissionsFromFuelCombustion2017Overview.pdf.
6. Cuéllar-Franca, R. M. & Azapagic, A. Carbon capture, storage and utilisation technologies: A critical analysis and comparison of their life cycle environmental impacts. *J. CO_2 Util.* **9,** 82–102 (2015).
7. Herzog, H., Drake, E. & Adams, E. *CO_2 Capture, Reuse, and Storage Technologies for Mitigating Global Climate Change: A White Paper, Final Report*. (Energy Laboratory, Massachusetts Institute of Technology, 1997).
8. Olah, G. A., Goeppert, A. & Prakash, G. K. S. Beyond oil and gas: the methanol economy. *Angew. Chemie - Int. Ed.* **44,** 2636–2639 (2005).
9. Wang, W., Wang, S., Ma, X. & Gong, J. Recent advances in catalytic hydrogenation of carbon dioxide. *Chem. Soc. Rev.* **40,** 3703–3727 (2011).
10. Liu, X.-M., Lu, G. Q., Yan, Z.-F. & Beltramini, J. Recent advances in catalysts for methanol synthesis via hydrogenation of CO and CO_2. *Ind. Eng. Chem. Res.* **42,** 6518–6530 (2003).
11. Jadhav, S. G., Vaidya, P. D., Bhanage, B. M. & Joshi, J. B. Catalytic carbon dioxide hydrogenation to methanol: A review of recent studies. *Chem. Eng. Res. Des.* **92,** 2557–2567 (2014).
12. Álvarez, A., Bansode, A., Urakawa, A., Bavykina, A. V., Wezendonk, T. A., Makkee, M., Gascon, J. & Kapteijn, F. Challenges in the greener production of formates/formic acid, methanol, and DME by heterogeneously catalyzed CO_2 hydrogenation processes. *Chem. Rev.* **117,** 9804–9838 (2017).
13. Yu, K. M. K., Curcic, I., Gabriel, J. & Tsang, S. C. E. Recent advances in CO_2 capture and utilization. *ChemSusChem* **1,** 893–899 (2008).
14. Songolzadeh, M., Soleimani, M., Takht Ravanchi, M. & Songolzadeh, R. Carbon dioxide separation from flue gases: A technological review emphasizing reduction in greenhouse gas emissions. *Sci. World J.* **2014,** 1–34 (2014).
15. D'Alessandro, D. M., Smit, B. & Long, J. R. Carbon dioxide capture: Prospects for new materials. *Angew. Chemie - Int. Ed.* **49,** 6058–6082 (2010).
16. Chu, S. Carbon capture and sequestration. *Science* **325,** 1599 (2009).
17. Idem, R. Wilson, M., Tontiwachwuthikul, P., Chakma, A., Veawab, A., Aroonwilas, A. & Gelowitz, Don. Pilot plant studies of the CO_2 capture performance of aqueous MEA and mixed MEA/MDEA solvents at the University of

Regina CO_2 capture technology development plant and the boundary dam CO_2 capture demonstration plant. *Ind. Eng. Chem. Res.* **45,** 2414–2420 (2006).

18. Figueroa, J. D., Fout, T., Plasynski, S., McIlvried, H. & Srivastava, R. D. Advances in CO_2 capture technology-The U.S. Department of Energy's Carbon Sequestration Program. *Int. J. Greenh. Gas Control* **2,** 9–20 (2008).
19. Bates, E. D., Mayton, R. D., Ntai, I. & Davis, J. H. CO_2 capture by a task-specific ionic liquid. *J. Am. Chem. Soc.* **124,** 926–927 (2002).
20. Merel, J., Clausse, M. & Meunier, F. Experimental investigation on CO_2 post-combustion capture by indirect thermal swing adsorption using 13X and 5A zeolites. *Ind. Eng. Chem. Res.* **47,** 209–215 (2008).
21. Choi, S., Drese, J. H. & Jones, C. W. Adsorbent materials for carbon dioxide capture from large anthropogenic point sources. *ChemSusChem* **2,** 796–854 (2009).
22. Lu, C., Bai, H., Wu, B., Su, F. & Hwang, J. F. Comparative study of CO_2 capture by carbon nanotubes, activated carbons, and zeolites. *Energy & Fuels* **22,** 3050–3056 (2008).
23. Gadipelli, S. & Guo, Z. X. Graphene-based materials: Synthesis and gas sorption, storage and separation. *Prog. Mater. Sci.* **69,** 1–60 (2015).
24. Nugent, P. Belmabkhout, Y., Burd, S. D., Cairns, A. J., Luebke, R., Forrest, K., Pham, T., Ma, S., Space, B., Wojtas, L., Eddaoudi, M., & Zaworotko, M. J. Porous materials with optimal adsorption thermodynamics and kinetics for CO_2 separation. *Nature* **495,** 80–84 (2013).
25. Khalilpour, R., Mumford, K., Zhai, H., Abbas, A., Stevens, G. & Rubin, E. S. Membrane-based carbon capture from flue gas: A review. *J. Clean. Prod.* **103,** 286–300 (2015).
26. Pera-Titus, M. Porous inorganic membranes for CO_2 capture: Present and prospects. *Chem. Rev.* **114,** 1413–1492 (2014).
27. Kalamaras, C. M. & Efstathiou, A. M. Hydrogen Production Technologies: Current State and Future Developments. *Conf. Pap. Energy* **2013,** 1–9 (2013).
28. Holladay, J. D., Hu, J., King, D. L. & Wang, Y. An overview of hydrogen production technologies. *Catal. Today* **139,** 244–260 (2009).
29. Hosseini, S. E. & Wahid, M. A. Hydrogen production from renewable and sustainable energy resources: Promising green energy carrier for clean development. *Renew. Sustain. Energy Rev.* **57,** 850–866 (2016).
30. Zeng, K. & Zhang, D. Recent progress in alkaline water electrolysis for hydrogen production and applications. *Prog. Energy Combust. Sci.* **36,** 307–326 (2010).
31. Chen, X., Shen, S., Guo, L. & Mao, S. S. Semiconductor-based photocatalytic hydrogen generation. *Chem. Rev.* **110,** 6503–6570 (2010).
32. Ni, M., Leung, M. K. H., Leung, D. Y. C. & Sumathy, K. A review and recent developments in photocatalytic water-splitting using TiO_2 for hydrogen production. *Renew. Sustain. Energy Rev.* **11,** 401–425 (2007).
33. Li, M. J., Mills, P., Fairclough, S. M., Robertson, A., Peng, Y. K., Warner, J., Nie, C., Flahautc, E. & Tsang, S. C. E. Importance of the structural integrity of a carbon conjugated mediator for photocatalytic hydrogen generation from water over a CdS–carbon nanotube–MoS_2 composite. *Chem. Commun.* **52,** 13596–13599 (2016).
34. Jia, T., Li, M., Ye, L., Wiseman, S., Liu, G., Qu, J., Nakagawaa, K. & Tsang, S. C. E. The remarkable activity and stability of a dye-sensitized single molecular layer MoS_2 ensemble for photocatalytic hydrogen production. *Chem. Commun.* **51,** 13496–13499 (2015).

35. Reddy, S. N., Nanda, S., Dalai, A. K. & Kozinski, J. A. Supercritical water gasification of biomass for hydrogen production. *Int. J. Hydrogen Energy* **39,** 6912–6926 (2014).
36. Guo, Y., Wang, S. Z., Xu, D. H., Gong, Y. M., Ma, H. H. & Tang, X. Y. Review of catalytic supercritical water gasification for hydrogen production from biomass. *Renew. Sustain. Energy Rev.* **14,** 334–343 (2010).
37. Chen, G., Li, W., Chen, H. & Yan, B. Progress in the aqueous-phase reforming of different biomass-derived alcohols for hydrogen production. *J. Zhejiang Univ.-Sci. A* **16,** 491–506 (2015).
38. Specht, M., Bandi, A., Baumgart, F., Murray, C. N. & Gretz, J. Synthesis of methanol from biomass/CO_2 resources. *Greenh. Gas Control Technol.* **723,** 1–6 (1999).
39. Wambach, J., Baiker, A. & Wokaun, A. CO_2 hydrogenation over metal/zirconia catalysts. *Phys. Chem. Chem. Phys.* **1,** 5071–5080 (1999).
40. Shen, W., Jun, K., Choi, H., Lee, K. & H, O. H. C. Thermodynamic Investigation of Methanol and Dimethyl Ether Synthesis from CO to Hydrogenation. *Korean J. Chem. Eng.* **216,** 210–216 (2000).
41. BASF AG, German Patent, 415,686, 1925.
42. BASF AG, US Patent, 1,201,850, 1916.
43. BASF AG, US Patant, 1,569,775, 1926.
44. ICI Ltd, UK Patent, 1,010,871, 1965.
45. Ipatieff, V. N. & Monroe, G. S. Synthesis of methanol from carbon dioxide and hydrogen over copper-alumina catalysts. Mechanism of reaction. *J. Am. Chem. Soc.* **67,** 2168–2171 (1945).
46. Bansode, A. & Urakawa, A. Towards full one-pass conversion of carbon dioxide to methanol and methanol-derived products. *J. Catal.* **309,** 66–70 (2014).
47. Gaikwad, R., Bansode, A. & Urakawa, A. High-pressure advantages in stoichiometric hydrogenation of carbon dioxide to methanol. *J. Catal.* **343,** 127–132 (2016).
48. Hinkley, J., Hayward, J., McNaughton, R., Gillespie, R., Matsumoto, A., Watt, M. & Lovegrove, K. Cost assessment of hydrogen production from PV and electrolysis. 2016. CSIRO, Australia. *CSIRO, Australia* (2016). Available at: https://arena.gov.au/assets/2016/05/Assessment-of-the-cost-of-hydrogen-from-PV.pdf.
49. Yang, Y., Evans, J., Rodriguez, J. A., White, M. G. & Liu, P. Fundamental studies of methanol synthesis from CO_2 hydrogenation on Cu(111), Cu clusters, and Cu/ZnO(000$\bar{1}$). *Phys. Chem. Chem. Phys.* **12,** 9909–9917 (2010).
50. Toyir, J., Ramírez De La Piscina, P., Fierro, J. L. G. & Homs, N. Highly effective conversion of CO_2 to methanol over supported and promoted copper-based catalysts: Influence of support and promoter. *Appl. Catal. B Environ.* **29,** 207–215 (2001).
51. Martin, O., Martín, A. J., Mondelli, C., Mitchell, S., Segawa, T. F., Hauert, R., Drouilly, C., Curulla-Ferré, D. & Pérez-Ramírez, J. Indium oxide as a superior catalyst for methanol synthesis by CO_2 hydrogenation. *Angew. Chemie - Int. Ed.* **55,** 6261–6265 (2016).
52. Graciani, J., Mudiyanselage, K., Xu, F., Baber, A. E., Evans, J., Senanayake, S. D., Stacchiola, D. J., Liu, P., Hrbek, J., Sanz, J. F. & Rodriguez, J. A. Highly active copper-ceria and copper-ceria-titania catalysts for methanol synthesis from CO_2.

Science **345,** 546–650 (2014).

53. Studt, F., Sharafutdinov, I., Abild-Pedersen, F., Elkjær, C. F., Hummelshøj, J. S., Dahl, S., Chorkendorff, I. & Nørskov, J. K. Discovery of a Ni-Ga catalyst for carbon dioxide reduction to methanol. *Nat. Chem.* **6,** 320–324 (2014).
54. Liao, F., Wu, X., Zheng, J., Li, M., Kroner, A., Zeng, Z., Hong, X., Yuan, Y., Gong, X. & Tsang, S. C. E. A promising low pressure methanol synthesis route from CO_2 hydrogenation over Pd@Zn core–shell catalysts. *Green Chem.* **19,** 270–280 (2017).
55. Grabow, L. C. & Mavrikakis, M. Mechanism of methanol synthesis on Cu through CO_2 and CO hydrogenation. *ACS Catal.* **1,** 365–384 (2011).
56. Kattel, S., Ramírez, P. J., Chen, J. G., Rodriguez, J. A. & Liu, P. Active sites for CO_2 hydrogenation to methanol on Cu/ZnO catalysts. *Science* **355,** 1296–1299 (2017).
57. Fujitani, T., Nakamura, I. & Uchijima, T. The kinetics and mechanism of methanol synthesis by hydrogenation of CO_2 over a Zn-deposited Cu (111) surface. *Surf. Sci.* **383,** 4–8 (1997).
58. Yatsu, T., Nishimura, H., Fujitani, T. & Nakamura, J. Synthesis and decomposition of formate on a Cu/SiO_2 catalyst: comparison to Cu(111). *J. Catal.* **191,** 423–429 (2000).
59. Fujitani, T., Choi, Y., Sano, M., Kushida, Y. & Nakamura, J. Scanning tunneling microscopy study of formate species synthesized from CO_2 hydrogenation and prepared by adsorption of formic acid over Cu(111). *J. Phys. Chem. B* **104,** 1235–1240 (2000).
60. Gao, H., Yan, T., Zhang, C. & He, H. Theoretical and experimental analysis on vibrational spectra of formate species adsorbed on $Cu–Al_2O_3$ catalyst. *J. Mol. Struct. THEOCHEM* **857,** 38–43 (2008).
61. Millar, G. J., Rochester, C. H. & Waugh, K. C. An in situ high pressure FT-IR study of CO_2/H_2 interactions with model ZnO/SiO_2, Cu/SiO_2 and $Cu/ZnO/SiO_2$ methanol synthesis catalysts. *Catal. Letters* **14,** 289–295 (1992).
62. Collins, S., Baltanas, M. & Bonivardi, A. An infrared study of the intermediates of methanol synthesis from carbon dioxide over $Pd/\beta\text{-}Ga_2O_3$. *J. Catal.* **226,** 410–421 (2004).
63. Zhao, Y.-F., Yang, Y., Mims, C. A., Peden, C. H. F., Li, J. & Mei, D. Insight into methanol synthesis from CO_2 hydrogenation on Cu(111): Complex reaction network and the effects of H2O. *J. Catal.* **281,** 199–211 (2011).
64. Yang, Y., Mims, C. A., Mei, D. H., Peden, C. H. F. & Campbell, C. T. Mechanistic studies of methanol synthesis over Cu from $CO/CO_2/H_2/H_2O$ mixtures: The source of C in methanol and the role of water. *J. Catal.* **298,** 10–17 (2013).
65. Rodriguez, J. A., Evans, J., Feria, L., Vidala, A. B., Liu, P., Nakamura, K. & Illas. F. CO_2 hydrogenation on Au/TiC, Cu/TiC, and Ni/TiC catalysts: Production of CO, methanol, and methane. *J. Catal.* **307,** 162–169 (2013).
66. Hartadi, Y., Widmann, D. & Behm, R. J. Methanol synthesis via CO_2 hydrogenation over a Au/ZnO catalyst: an isotope labelling study on the role of CO in the reaction process. *Phys. Chem. Chem. Phys.* **18,** 10781–10791 (2016).
67. Kunkes, E. L., Studt, F., Abild-Pedersen, F., Schlögl, R. & Behrens, M. Hydrogenation of CO_2 to methanol and CO on $Cu/ZnO/Al_2O_3$: Is there a common intermediate or not? This work is dedicated to the memory and achievements of Dr. Haldor Topsøe. *J. Catal.* **328,** 43–48 (2015).

68. Ferrando, R., Jellinek, J. & Johnston, R. L. Nanoalloys: From theory to applications of alloy clusters and nanoparticles. *Chem. Rev.* **108,** 845–910 (2008).
69. Guisbiers, G., Khanal, S., Ruiz-Zepeda, F., Roque de la Puente, J. & José-Yacaman, M. Cu–Ni nano-alloy: mixed, core–shell or Janus nano-particle? *Nanoscale* **6,** 14630–14635 (2014).
70. Hammer, B. & Nørskov, J. K. Electronic factors determining the reactivity of metal surfaces. *Surf. Sci.* **343,** 211–220 (1995).
71. Hammer, B. & Nørskov, J. K. Theoretical surface science and catalysis—calculations and concepts. *Adv. Catal.* **45,** 71–129 (2000).
72. Liu, P. & Nørskov, J. K. Ligand and ensemble effects in adsorption on alloy surfaces. *Phys. Chem. Chem. Phys.* **3,** 3814–3818 (2001).
73. Kitchin, J. R., Nørskov, J. K., Barteau, M. A. & Chen, J. G. Modification of the surface electronic and chemical properties of Pt(111) by subsurface 3d transition metals. *J. Chem. Phys.* **120,** 10240–10246 (2004).
74. Mavrikakis, M., Hammer, B. & Nørskov, J. K. Effect of strain on the reactivity of metal surfaces. *Phys. Rev. Lett.* **81,** 2819–2822 (1998).
75. Herron, J. A., Scaranto, J., Ferrin, P., Li, S. & Mavrikakis, M. Trends in formic acid decomposition on model transition metal surfaces: A density functional theory study. *ACS Catal.* **4,** 4434–4445 (2014).
76. Liu, C., Cundari, T. R. & Wilson, A. K. CO_2 reduction on transition metal (Fe, Co, Ni, and Cu) surfaces: In comparison with homogeneous catalysis. *J. Phys. Chem. C* **116,** 5681–5688 (2012).
77. Dietz, L., Piccinin, S. & Maestri, M. Mechanistic insights into CO_2 activation via reverse water - Gas shift on metal surfaces. *J. Phys. Chem. C* **119,** 4959–4966 (2015).
78. Kuld, S., Thorhauge, M., Falsig, H., Elkjær, C. F., Helveg, S., Chorkendorff, I. & Sehested, J. Quantifying the promotion of Cu catalysts by ZnO for methanol synthesis. *Science* **352,** 969–974 (2016).
79. Behrens, M., Studt, F., Kasatkin, I., Kühl, S., Hävecker, M., Abild-Pedersen, F., Zander, S., Girgsdies, F., Kurr, P., Kniep, B., Tovar, M., Fischer, R. W., Nørskov, J. K.& Schlögl, R. The active site of methanol synthesis over $Cu/ZnO/Al_2O_3$ industrial catalysts. *Science* **336,** 893–898 (2012).
80. Li, M. M.-J., Zeng, Z., Liao, F., Hong, X. & Tsang, S. C. E. Enhanced CO_2 hydrogenation to methanol over CuZn nanoalloy in Ga modified Cu/ZnO catalysts. *J. Catal.* **343,** 157–167 (2016).
81. Van Den Berg, R., Prieto, G., Korpershoek, G., van der Wal, L. I., van Bunningen, A. J., Lægsgaard-Jørgensen, S., de Jongh P. E. & de Jong, K. P. Structure sensitivity of Cu and CuZn catalysts relevant to industrial methanol synthesis. *Nat. Commun.* **7,** 13057 (2016).
82. Kusama, H., Okabe, K., Sayama, K. & Arakawa, H. Ethanol synthesis by catalytic hydrogenation of CO_2 over $Rh\text{-}Fe/SiO_2$ catalysts. *Energy* **22,** 343–348 (1997).
83. Kusama, H., Okabe, K., Sayama, K. & Arakawa, H. Alcohol synthesis by catalytic hydrogenation of CO_2 over $Rh\text{-}Co/SiO_2$. *Appl. Organomet. Chem.* **14,** 836–840 (2000).
84. Collins, S. E. Delgado, J. J., Mira, C., Calvino, J. J., Bernal, S., Chiavassa, D. L., Baltanás, M. A. & Bonivardi, A. L. The role of Pd-Ga bimetallic particles in the bifunctional mechanism of selective methanol synthesis via CO_2 hydrogenation on a Pd/Ga_2O_3 catalyst. *J. Catal.* **292,** 90–98 (2012).

85. Qu, J., Zhou, X., Xu, F., Gong, X. Q. & Tsang, S. C. E. Shape effect of Pd-promoted Ga_2O_3 nanocatalysts for methanol synthesis by CO_2 hydrogenation. *J. Phys. Chem. C* **118,** 24452–24466 (2014).
86. Liang, X. L., Dong, X., Lin, G. D. & Zhang, H. B. Carbon nanotube-supported Pd-ZnO catalyst for hydrogenation of CO_2 to methanol. *Appl. Catal. B Environ.* **88,** 315–322 (2009).
87. Jiang, X., Koizumi, N., Guo, X. & Song, C. Bimetallic Pd-Cu catalysts for selective CO_2 hydrogenation to methanol. *Appl. Catal. B Environ.* **170–171,** 173–185 (2015).
88. Fujitani, T., Saito, M., Kanai, Y., Takeuchi, M., Moriya, K., Watanabe, T., Kawai, M. & Kakumoto, T. Methanol synthesis from CO_2 and H_2 over $Cu/ZnO/Ga_2O_3$ catalyst. *Chem. Lett.* **22,** 1079–1080 (1993).
89. Smith, P. J., Kondrat, S. A., Chater, P. A., Yeo, B. R., Shaw, G. M., Lu, Li., Bartley, J. K., Taylor, S. H., Spencer, M. S., Kiely, C. J., Kelly, G. J., Park, C. W. & Hutchings, G. J. A new class of Cu/ZnO catalysts derived from zincian georgeite precursors prepared by co-precipitation. *Chem. Sci.* **8,** 2436–2447 (2017).
90. Fujitani, T. Saito, M., Kanai, Y., Watanabe, T., Nakamura, J. & Uchijima, T. Development of an active Ga_2O_3 supported palladium catalyst for the synthesis of methanol from carbon dioxide and hydrogen. *Appl. Catal. A Gen.* **125,** 199–202 (1995).
91. Kühl, S., Tarasov, A., Zander, S., Kasatkin, I. & Behrens, M. Cu-based catalyst resulting from a Cu,Zn,Al hydrotalcite-like compound: A microstructural, thermoanalytical, and in situ XAS study. *Chem. - A Eur. J.* **20,** 3782–3792 (2014).
92. Gao, P., Zhong, L., Zhang, L., Wang, H., Zhao, N., Wei, W. & Sun, Y. Yttrium oxide modified $Cu/ZnO/Al_2O_3$ catalysts via hydrotalcite-like precursors for CO_2 hydrogenation to methanol. *Catal. Sci. Technol.* **5,** 4365–4377 (2015).
93. Gao, P., Zhong, L., Zhang, L., Wang, H., Zhao, N., Wei, W. & Sun, Y. Effect of hydrotalcite-containing precursors on the performance of Cu/Zn/Al/Zr catalysts for CO_2 hydrogenation: Introduction of Cu^{2+} at different formation stages of precursors. *Catal. Today* **194,** 9–15 (2012).
94. Gao, P., Zhong, L., Zhang, L., Wang, H., Zhao, N., Wei, W. & Sun, Y. Influence of modifier (Mn, La, Ce, Zr and Y) on the performance of Cu/Zn/Al catalysts via hydrotalcite-like precursors for CO_2 hydrogenation to methanol. *Appl. Catal. A Gen.* **468,** 442–452 (2013).
95. Li, M. M.-J., Chen, C., O'Hare, D. & Tsang, S. C. E. CO_2 hydrogenation to methanol over CuZnGa AMO-LDH based catalysts. (2017).
96. Ota, A. Kunkes, E. L., Kasatkin, I., Groppo, E., Ferri, D., Poceiro, B., Navarro, R. M., Yerga, N. & Behrens, M. Comparative study of hydrotalcite-derived supported Pd_2Ga and PdZn intermetallic nanoparticles as methanol synthesis and methanol steam reforming catalysts. *J. Catal.* **293,** 27–38 (2012).
97. Shao, C., Fan, L., Fujimoto, K. & Iwasawa, Y. Selective methanol synthesis from CO_2/H_2 on new SiO_2-supported PtW and PtCr bimetallic catalysts. *Appl. Catal. A Gen.* **128,** 1–6 (1995).
98. Bahruji, H. Bowker, M., Hutchings, G., Dimitratos, N., Wells, P., Gibson, E., Jones, W., Brookes, C., Morgan ,D. & Lalev, G. Pd/ZnO catalysts for direct CO_2 hydrogenation to methanol. *J. Catal.* **343,** 133–146 (2016).
99. Liao, F., Wu, X., Zheng, J., Li, M., Zeng, Z., Hong, X., Kroner, A., Yuan, Y., Gong, X. & Tsang, S. C. E. Pd@Zn core–shell nanoparticles of controllable shell thickness for catalytic methanol production. *Catal. Sci. Technol.* **6,** 7698–7702

(2016).

100. Iwasa, N., Masuda, S., Ogawa, N. & Takezawa, N. Steam reforming of methanol over Pd/ZnO: Effect of the formation of PdZn alloys upon the reaction. *Appl. Catal. A Gen.* **125,** 145–157 (1995).
101. Iwasa, N., Mayanagi, T., Ogawa, N., Sakata, K. & Takezawa, N. New catalytic functions of Pd-Zn, Pd-Ga, Pd-In, Pt-Zn, Pt-Ga and Pt-In alloys in the conversions of methanol. *Catal. Letters* **54,** 119–123 (1998).
102. Fiordaliso, E. M., Sharafutdinov, I., Carvalho, H. W. P., Grunwaldt, J. D., Hansen, T. W., Chorkendorff, I., Wagner, J. B. & Damsgaard, C. D. Intermetallic $GaPd_2$ nanoparticles on SiO_2 for low-pressure CO_2 hydrogenation to methanol: catalytic performance and in situ characterization. *ACS Catal.* **5,** 5827–5836 (2015).
103. Kuld, S., Conradsen, C., Moses, P. G., Chorkendorff, I. & Sehested, J. Quantification of zinc atoms in a surface alloy on copper in an industrial-type methanol synthesis catalyst. *Angew. Chemie - Int. Ed.* **53,** 5941–5945 (2014).
104. Fujitani, T., Saito, M., Kanai, Y., Watanab, T., Nakamura, K. & Uchijimi, T. Effect of support on methanol synthesis over Cu catalyst. *Chem. Lett.* **23,** 1877–1880 (1994).
105. Fujitani, T., Saito, M., Kanai, Y., Watanab, T., Nakamura, K. & Uchijimi, T. The role of metal oxides in promoting a copper catalyst for methanol synthesis. *Catal. Letters* **25,** 271–276 (1994).
106. Kanai, Y., Watanab, T., Fujitani, T., Saito, M., Nakamura, K. & Uchijimi, T. Evidence for the migration of ZnO_x in a Cu/ZnO methanol synthesis catalyst. *Catal. Letters* **27,** 67–78 (1994).
107. Fujitani, T. & Nakamura, J. The chemical modification seen in the Cu/ZnO methanol synthesis catalysts. *Appl. Catal. A Gen.* **191,** 111–129 (2000).
108. Topsøe, N. & Topsøe, H. On the nature of surface structural changes in Cu/ZnO methanol synthesis catalysts. *Top. Catal.* **8,** 267–270 (1999).
109. Grunwaldt, J.-D., Molenbroek, A. M., Topsøe, N.-Y., Topsøe, H. & Clausen, B. S. In situ investigations of structural changes in Cu/ZnO catalysts. *J. Catal.* **194,** 452–460 (2000).
110. Wagner, J. B., Hansen, P. L., Molenbroek, A. M., Topsøe, H., Clausen, B. S. & Helveg, S. In situ electron energy loss spectroscopy studies of gas-dependent metal-support interactions in Cu/ZnO catalysts. *J. Phys. Chem. B* **107,** 7753–7758 (2003).
111. Behrens, M., Girgsdies, F., Trunschke, A. & Schlögl, R. Minerals as model compounds for Cu/Zno catalyst precursors: structural and thermal properties and IR spectra of mineral and synthetic (zincian) malachite, rosasite and aurichalcite and a catalyst precursor mixture. *Eur. J. Inorg. Chem.* **2009,** 1347–1357 (2009).
112. Höppener, R. H., Doesburg, E. B. M. & Scholten, J. J. F. Preparation and characterization of stable copper/zinc oxide/alumina catalysts for methanol systhesis. *Appl. Catal.* **25,** 109–119 (1986).
113. Baltes, C., Vukojević, S. & Schüth, F. Correlations between synthesis, precursor, and catalyst structure and activity of a large set of $CuO/ZnO/Al_2O_3$ catalysts for methanol synthesis. *J. Catal.* **258,** 334–344 (2008).
114. Behrens, M. Meso- and nano-structuring of industrial $Cu/ZnO/(Al_2O_3)$ catalysts. *J. Catal.* **267,** 24–29 (2009).
115. Zander, S., Seidlhofer, B. & Behrens, M. In situ EDXRD study of the chemistry of aging of co-precipitated mixed Cu,Zn hydroxycarbonates – consequences for the preparation of Cu/ZnO catalysts. *Dalt. Trans.* **41,** 13413–13422 (2012).

116. Behrens, M., Kißner, S., Girsgdies, F., Kasatkin, I., Hermerschmidt, F., Mette, K., Ruland, H., Muhler, M. & Schlögl, R. Knowledge-based development of a nitrate-free synthesis route for Cu/ZnO methanol synthesis catalysts via formate precursors. *Chem. Commun.* **47,** 1701–1703 (2011).
117. Kondrat, S. A., Smith, P. J., Wells, P. P., Chater, P. A., Carter, J. H., Morgan, D. J., Fiordaliso, E. M., Wagner, J. B., Davies, T. E., Lu, L., Bartley, J. K., Taylor, S. H., Spencer, M. S., Kiely, C. J., Kelly, G. J., Park, C. W., Rosseinsky, M. J. & Hutchings, G. J. Stable amorphous georgeite as a precursor to a high-activity catalyst. *Nature* **531,** 83–87 (2016).
118. Kong, H., Li, H. Y., Lin, G. D. & Zhang, H. Bin. Pd-decorated CNT-promoted Pd-Ga_2O_3 catalyst for hydrogenation of CO_2 to methanol. *Catal. Letters* **141,** 886–894 (2011).
119. Zhang, L., Li, F., Evans, D. G. & Duan, X. Structure and surface characteristics of Cu-based composite metal oxides derived from layered double hydroxides. *Mater. Chem. Phys.* **87,** 402–410 (2004).
120. Zhang, L. H., Zheng, C., Li, F., Evans, D. G. & Duan, X. Copper-containing mixed metal oxides derived from layered precursors: Control of their compositions and catalytic properties. *J. Mater. Sci.* **43,** 237–243 (2008).
121. Behrens, M., Kasatkin, I., Kühl, S. & Weinberg, G. Phase-pure Cu,Zn,Al hydrotalcite-like materials as precursors for copper rich $Cu/ZnO/Al_2O_3$ catalysts. *Chem. Mater.* **22,** 386–397 (2010).
122. Chen, C., Yang, M., Wang, Q., Buffet, J.-C. & O'Hare, D. Synthesis and characterisation of aqueous miscible organic-layered double hydroxides. *J. Mater. Chem. A* **2,** 15102–15110 (2014).
123. Nerlov, J. & Chorkendorff, I. Promotion through gas phase induced surface segregation : methanol synthesis from CO , CO_2 and H_2 over Ni / Cu (100). *Catal. Letters* **54,** 171–176 (1998).
124. Nerlov, J. & Chorkendorff, I. Methanol Synthesis from CO_2, CO, and H_2 over Cu(100) and Ni/Cu(100). *J. Catal.* **181,** 271–279 (1999).

Chapter 2: Analytical techniques

2.1 Chapter overview

The characterisation is a very crucial part in catalysis as the specific physical and chemical properties of the material have direct impacts on the catalytic activity and stability[1,2]. Today, with the advancement of scientific technologies, a wide variety of powerful instruments are invented to provide information about chemical compositions, electronic states, crystalline structures, surface environments, and local structures of the materials. To resolve the catalytic sites, the investigation with a combination of several advanced techniques is usually required. This chapter briefly introduces the important analytical tools used throughout this thesis by presenting their theoretical principles and applications.

2.2 X-ray diffraction (XRD)

XRD is one of the most commonly used techniques to characterise nanoparticle catalysts[3]. It is a nondestructive technique and can be used to identify crystalline phases and orientation as well as to determine structural properties such as lattice unit cell parameters, lattice strain, and crystallite size. This technique is based on the constructive interference of the scattered monochromatic X-rays emitted by interactions between X-rays and the atoms with the periodical arrangement in the lattice when conditions satisfy Bragg's Law (Equation 2-1).

$$\boldsymbol{n\lambda = 2d\,sin\theta};\ \ \boldsymbol{n = 1, 2}, \ldots \ldots \quad \text{(Equation 2-1)}$$

where n is the integer corresponds to the order of reflection; conventional lab XRD use Cu-Kα radiation with λ= 0.154 nm; d is the spacing distance of reflecting lattice planes; θ is Bragg angle: The angle between an incident X-ray beam and a set of crystal planes, see Figure 2-1.

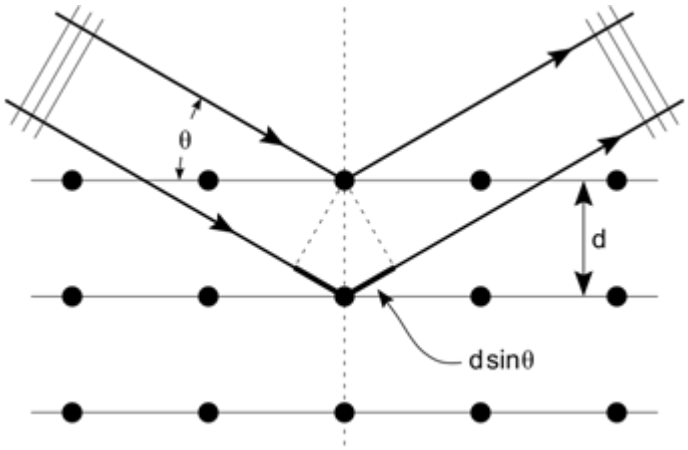

Figure 2-1. Diffraction of X-rays from crystal lattice planes illustrating Bragg's law[4].

The spacing distance of lattice planes and the lattice parameters can be calculated using the characteristic peak position of the obtained diffraction pattern. Taking the cubic system as an example, the correlation can be described by the following equation:

$$\frac{1}{d^2} = \frac{h^2+k^2+l^2}{a^2} \quad \text{(Equation 2-2)}$$

where h, k and l are the Miller indices; a is the lattice parameters (for cubic system a=b=c); d is the spacing distance between lattice planes.

Another important characteristic of XRD pattern is peak broadening along with the reduction of material crystallite size, due to the incomplete destructive where the X-rays are out of phase. The crystallite size can be calculated based on the peak positions and the corresponding full width half maximum (FWHM) according to the Scherrer equation:

$$L = K\lambda/\beta \cos\theta \quad \text{(Equation 2-3)}$$

where L is the averaged diameter of the crystallites; λ is the wavelength of the incident X-ray; β is the width of a diffraction peak at half the maximum intensity (FWHM) in radians; θ is Bragg angle; K is a value which is in the range 0.87-1.00 (it is commonly assumed to be 1).

2.3 X-ray photoelectron spectroscopy (XPS)

XPS, also known as electron spectroscopy for chemical analysis (ESCA), is a surface-sensitive quantitative spectroscopic technique that provides information of surface chemical composition and oxidation state of individual elements. XPS spectra are obtained by irradiating the sample surface with a beam of soft (low energy) X-rays under ultra-high vacuum conditions while simultaneously measuring the kinetic energy of the ejected electron from the materials with binding energy lower than the X-ray energy. Because the energy of the X-ray with a particular wavelength is known, the electron binding energy of each of the emitted electrons can be determined by using the following equation:

$$\boldsymbol{Ek = h\upsilon - EB - \varphi} \quad \text{(Equation 2-4)}$$

where Ek is the kinetic energy of the ejected electron; h is Planck's constant; υ is the frequency of the incident X-ray; EB is the binding energy of the ejected electron with respect to the Fermi level of the sample; φ is the work function of the spectrometer. The relationship of the parameters is illustrated in Figure 2-2.

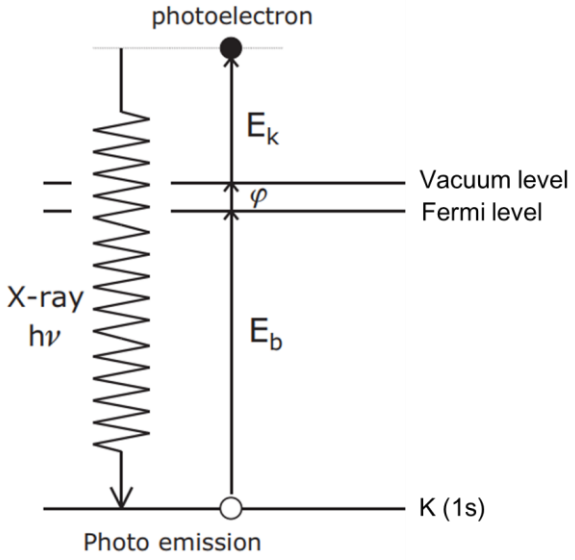

Figure 2-2. Illustration of photoelectron emission stimulated by X-ray absorption[5].

The kinetic energy (Ek) of the ejected electron is an experimental value measured by the spectrometer, which depends on the wavelength of the employed X-rays so that is not an intrinsic property of the material. On the contrary, the binding energy of the electron (EB) is characteristic of the electronic structure of the parent atom and also reflects the oxidation state[6]. The total number of detected electrons at certain binding energy region is proportional to the amount of the parent element, therefore, XPS is usually used to quantitatively analyse surface chemical composition by the integration of the signal peaks area of elements normalised by their relevant sensitivity factors. Although X-ray penetrates deeply into the material, most of the ejected electrons are captured by the parent atom and only a small fraction of surface (10-100 Å) photoelectrons can escape from the material and be detected by the spectrometer. The elemental composition provided by XPS is assigned to the surface or near the surface of the analysed material, thus, it can present the information of the surface catalytic site more precisely than other bulk analysis techniques.

2.4 X-ray absorption fine structure (XAFS)

XAFS refers to the details of how X-rays are absorbed by an atom at energies near and above its core-level binding energies in various chemical and physical state. The X-ray absorption spectrum is derived from the measurement of the X-ray absorption coefficient μ of a material as a function of X-ray energy, and μ is defined as:

$$\boldsymbol{\mu} = -\mathbf{ln}(\frac{\boldsymbol{I_t}}{\boldsymbol{I_0}}) \,/\, \boldsymbol{X} \quad \text{(Equation 2-5)}$$

where I_0 is the intensity of X-ray light irradiated on the sample; I_t is the intensity of X-ray light transmitted through the sample; X is the thickness of the sample.

The result consists of two regimes: X-ray absorption near-edge structure (XANES) and extended X-ray absorption fine structure (EXAFS), see Figure 2-3. XANES is especially sensitive to formal oxidation state and coordination chemistry, i.e., octahedral or tetrahedral coordination of the absorbing atom, while the EXAFS is used to determine the local environment such as bond distances, coordination number, and species of the neighbours of the absorbing atom. When the incident X-ray energy closes the energies near and above the core-level binding energies of an element within the sample, the absorption coefficient μ increases dramatically, causing an absorption edge in XAFS spectrum. The position of absorption edge usually reflects the oxidation state and the electronic configuration of the absorbing atom. After the absorption edge, the excited electrons escape from the nucleus of the absorbing atom with kinetic energy, and the ejected electrons are likely to be backscattered by the neighbour atoms then interfere with the forward ejected electrons. This interference then develops oscillation in XAFS spectrum and is called EXAFS, which is related to the type of scattering atoms around the absorbing atom and the distance between them. EXAFS is best understood in terms of the wave behaviour of the photo-electron

created in the absorption process. Because of this, it is common to convert the X-ray energy to k, the wave number of the ejected electron, which is defined as:

$$\boldsymbol{k = \frac{2\pi}{h}\sqrt{2m_e E_{kin}} = \frac{2\pi}{h}\sqrt{2m_e(h\nu - EB)}} \quad \text{(Equation 2-6)}$$

where k is the wavenumber of the photoelectron; h is Planck's constant; m_e is the mass of an electron; E_{kin} is the kinetic energy of the photoelectron; ν is the X-ray frequency; EB is the binding energy of the ejected electron.

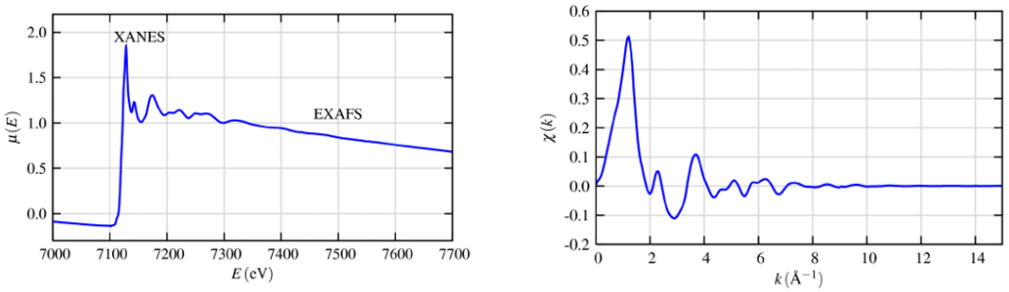

Figure 2-3. Left: XAFS spectrum is shown with the XANES and EXAFS regions identified; Right: Isolated EXAFS (k) spectrum[7].

χ(k) is the oscillations as a function of photo-electron wave number (Figure 2-3). The different frequencies revealed in the oscillations in χ(k) correspond to diverse near-neighbour coordination environments which can be described and modelled according to the EXAFS Equation:

$$\boldsymbol{\chi(k) = \sum_j \frac{N_j f_j(k) e^{-2k^2\sigma_j^2}}{kR_j^2} \sin[2kR_j + \delta_j(k)]} \quad \text{(Equation 2-7)}$$

where f(k) and δ(k) are scattering properties of the atoms near the excited atom; N is the number of neighbouring atoms; R is the distance from the absorbing atom to the neighbouring atom, and σ^2 is the disorder in the neighbour distance. The model of EXAFS function χ(k) is quite complicated, but it allows us to obtain the chemical environment of the absorbing atom at the atomic scale. Moreover, since these scattering factors depend on the atomic number Z of the neighbouring atom, EXAFS is also sensitive to the atomic species of the neighbouring atom[7].

2.5 Transmission electron microscopy (TEM)

TEM is a powerful technique for examining nanomaterial-based catalyst, as it can allow a direct observation of particle aggregation, particle size and provide morphological and structural information. The principle of TEM is similar to that of an optical microscope but using electrons instead of visible photons as a light source. In addition, electromagnetic lenses are used in TEM to focus electron beam rather than using optical lenses as that of in an optical microscope. Figure 2-4 shows the structure and cross-section of a typical TEM. To describe it, in brief, an electron beam with high intensity is generated either by a tungsten filament, a LaB_6 crystal, or a field emission gun, and then it is accelerated to high energy and produce electrons with a wavelength (de Broglie wavelength) much smaller than typical interatomic spacing. The high-speed electron beam passes through a condenser to produce parallel rays and then impinge on the specimen. The transmitted electron beam through the specimen is refocused and expanded through sets of projector lenses onto the phosphor screen or a charge coupled device (CCD) camera or film[8].

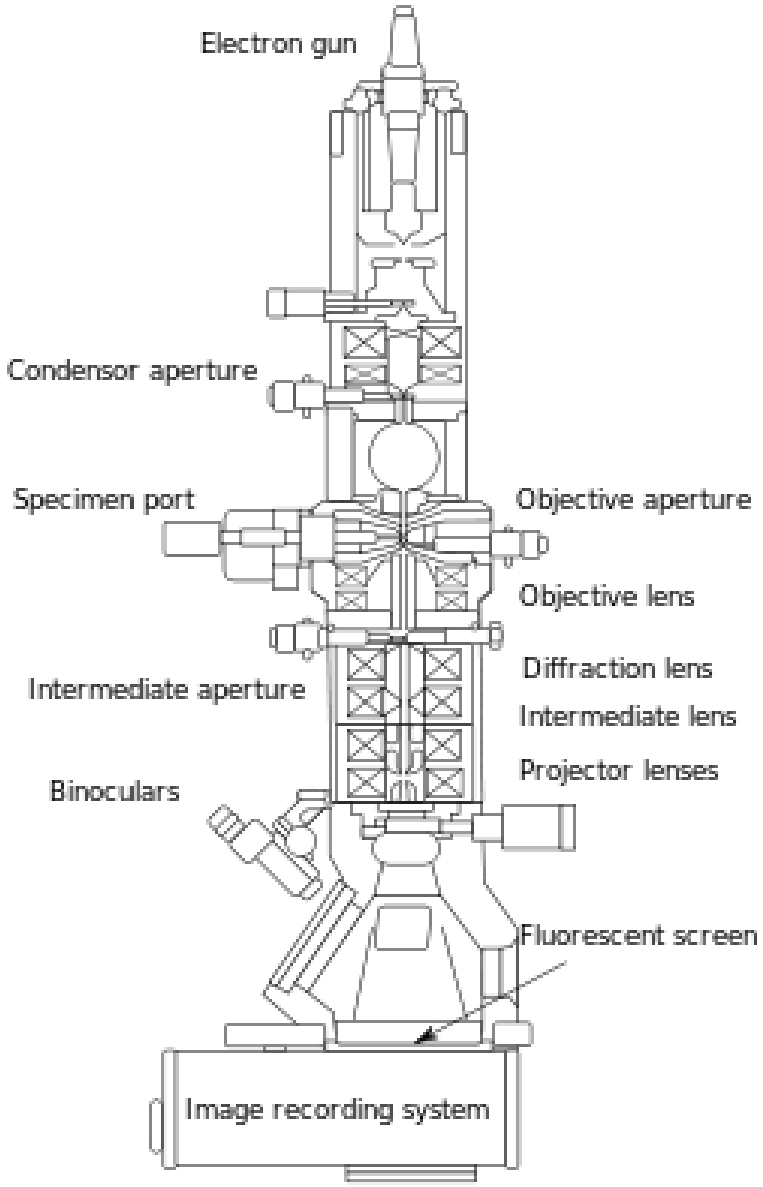

Figure 2-4. The layout of optical components of a typical TEM machine[8].

According to Rayleigh criterion (defined as Equation 2-8), the resolution of TEM depends on the wavelength of the electron. Typically, to achieve a resolution of 0.3 nm, which is thousands of times smaller than the smallest resolvable object in an optical microscope, the operating voltage of a TEM instrument is 100 ~200 keV (λ = 2.5 to 3.7 pm) under 10^{-6} mbar vacuum.

$$\boldsymbol{\delta_d = \frac{0.61\lambda}{n\,sin\beta}} \quad \text{(Equation 2-8)}$$

where λ is the wavelength of the radiation; n is the refractive index of the view medium; β is the semi-angle of collection of the magnifying lens[8].

On the other hand, a scanning transmission electron microscope (STEM) is a type of TEM. STEM is a powerful and versatile instrument, which can provide better atomic resolution imaging and nanoscale analysis, and is more efficient than conventional TEM. In principle, the STEM differs from conventional TEM in that the electron beam is focused into a narrow spot, which is scanned through the specimen in a raster pattern. Scattered electrons are detected and their intensity is plotted as a function of probe position to create an image[9].

2.6 Atomic force microscopy (AFM)

AFM was invented in 1986[10], which has the advantage that it can provide the topography and structure of both conducting and non-conducting samples in a variety of types including inorganic materials, polymers, composites, and many more. AFM is a high-resolution type of scanning probe microscope. It scans a probe over the surface of the sample and measures the forces between probe tip and surface. The typical AFM configuration is shown in Figure 2-5. The distance between probe and sample varies with the mode in which the AFM is operated.

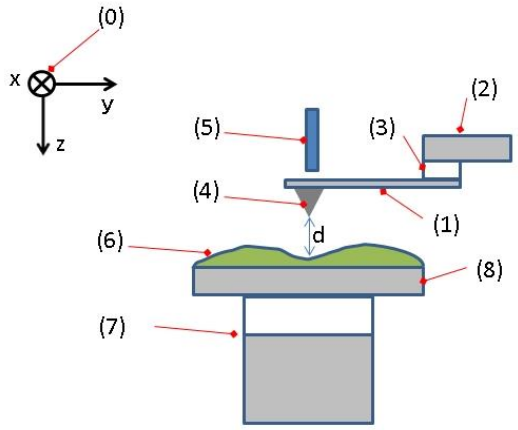

Figure 2-5. Typical configuration of an AFM[11]: (0) coordinate system; (1) Cantilever; (2) Support for cantilever; (3) Piezoelectric element (to oscillate cantilever at its eigen frequency.); (4) Tip (Fixed to open end of a cantilever, acts as the probe); (5) Detector of deflection and motion of the cantilever; (6) Sample to be measured by AFM; (7) xyz drive, (moves sample (6) and stage (8) in x, y, and z directions with respect to a tip apex (4)); (8) Stage.

Three commonly used AFM scanning modes are contact mode, non-contact mode, and tapping mode[11]. The contact mode of AFM measures topography by sliding a probe tip across the surface as well as in contact with the sample. On the contrary, in the non-contact mode, the tip is suspended 50-150 Å above the sample surface. Attractive Van der Waals forces acting between the tip and the sample are measured, and topographic images are constructed by scanning the tip above the surface. On the other hand, the tapping mode of AFM measures topography by tapping the surface with an oscillating tip. Tapping mode can eliminate the shear forces so that can protect soft samples and allow high-resolution topographic imaging of the sample surfaces. Therefore, this is the technique of choice for most AFM work.

2.7 Fourier transform infrared (FTIR) spectroscopy

FTIR is a technique used to obtain an infrared absorption spectrum of materials. For the catalysts, this technique is usually employed for determining reaction intermediates and organic functional groups on the surface of catalyst through detection of the characteristic stretching and bending frequencies of specific functional groups. Molecules possess discrete rotational and vibrational energy levels. A vibrational transition can occur by absorbing infrared light, in particular with a wavenumber of (200-4000 cm^{-1}). According to the simple harmonic oscillator model, vibrational frequencies increase with the increasing of bond strength between the atoms and decrease as the decreasing of the masses of atoms in the chemical bond:

$$\boldsymbol{\nu_0 = \frac{1}{2\pi}\sqrt{\frac{k}{\mu}}} \quad \boldsymbol{\mu = \frac{m_1 \times m_2}{m_1 + m_2}} \quad \text{(Equation 2-9)}$$

where ν_0 is the Harmonic Oscillator frequency of the two-atom chemical bond; m_1 and m_2 are the masses of atoms in the chemical bond; k is the force constant which is proportional to the bond strength between the atoms. A general selection rule for the absorption of infrared light is a change in dipole moment in the molecule during the vibration process, hence not all vibration modes cause absorption. Furthermore, various vibrations can be observed, including stretch, bend in/out of the plane, torsion, symmetric and asymmetric.

Attenuated total reflection (ATR-IR), the most widely used FTIR sampling tool and is employed in the work of this thesis. ATR generally allows qualitative or quantitative analysis of samples with a convenient sample preparation. The main advantage of ATR sample preparation comes from its very thin sampling path length and depth of penetration of the IR beam into the sample. This contrasts with traditional FTIR sampling by transmission where the sample must be diluted with IR transparent salt, pressed into a pellet

or to a thin film to prevent totally absorbing bands in the infrared spectrum. In ATR sampling the IR beam is directed into a crystal with relatively higher refractive index. The IR beam reflects from the internal surface of the crystal and creates an evanescent wave, which projects orthogonally into the sample in intimate contact with the ATR crystal. The sample absorbs some of the energy while the reflected radiation is returned to the detector. Figure 2-6 illustrates the principle of a single internal reflection ATR spectroscopic technique, where infrared radiation is passed through a material with a high optical density at an angle such that total internal reflection occurs. Once the total internal reflection occurs, an evanescent field is formed that extends beyond the crystal surface. By increasing the number of reflections in the crystal the amount of interaction with the sample is enhanced, which can result in a highly sensitive technique to monitor catalyst surface.

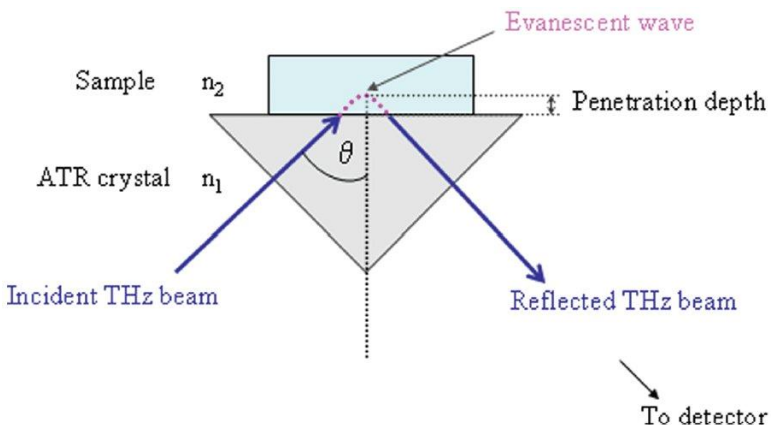

Figure 2-6. Illustration of the principle of the ATR spectroscopic technique: n_1 and n_2 are refractive indices of the ATR crystal and the sample material ($n_1 > n_2$)[12].

2.8 Temperature programmed reduction (TPR)

Most of the metal oxide catalysts need a pre-reduction treatment to generate the active metal sites before they are used to catalyse the reaction. TPR is a technique employed for the investigation of the reduction behaviour of materials. The diluted reductive gas, used as the probe molecules and are usually H_2 or CO, is used to interact with the specimen loaded in a quartz tube by passing a continuous gas stream under a defined temperature programme. The changes of the probe molecule concentration in the gas flow are monitored in situ by a thermal conductivity detector (TCD) at elevated temperatures. The illustration of a TPR instrument configuration is shown in Figure 2-7. Two reductive gas streams with the same composition are supplied at the same time. One of them is taken as the reference flowing into the TCD detector directly (in the reference channel of Figure 2-7). The other passes through and interacts with the specimen before it reaches the detector (in the sample channel of Figure 2-16). The intensity of TCD signal is proportional to the composition difference of the two gas streams. Thereby, the variation of probe molecule concentration in the sample channel is recorded during the defined temperature programme with reference to the unreacted gas stream, which reflects the reduction process of the sample.

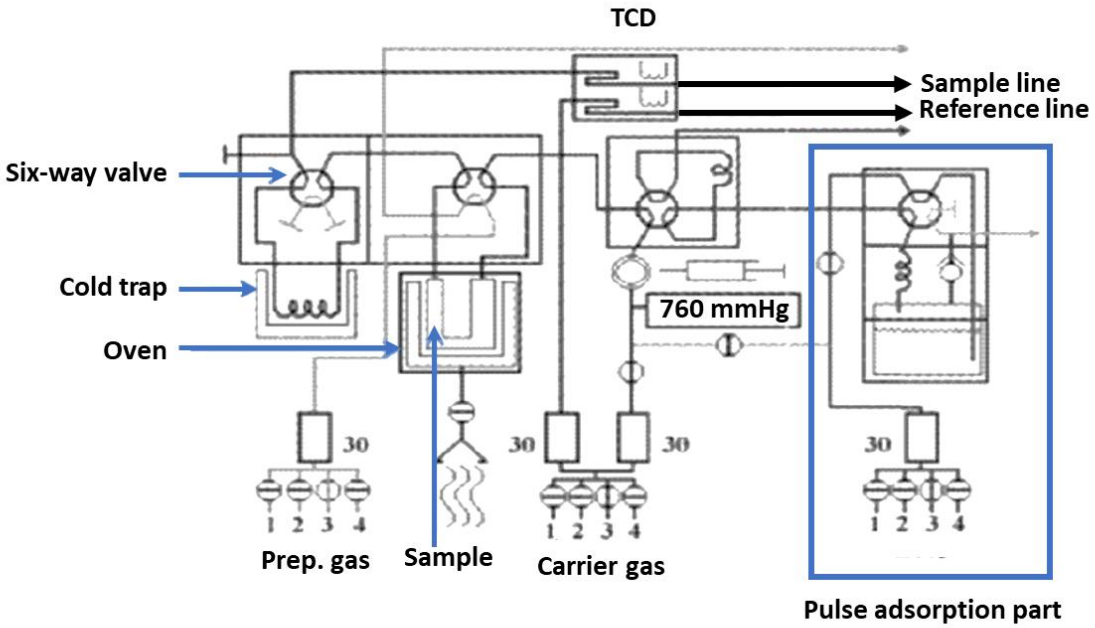

Figure 2-7. Schematic representation of a typical TPR instrument[13].

In a typical measurement, a sample is sandwiched between two layers of quartz wool that is loaded in a quartz tube. The tube with the sample is then placed into a larger quartz tube where it is attached to a stainless-steel holder and sealed with a rubber o-ring (Figure 2-8). Once obtained the TPR analysis result, the integration of TCD signal versus temperature gives the total uptake of the probe molecules (an accurate calibration prior to the measurement is needed) which can provide the information of the number of reductive sites as well as the corresponding reduction temperature.

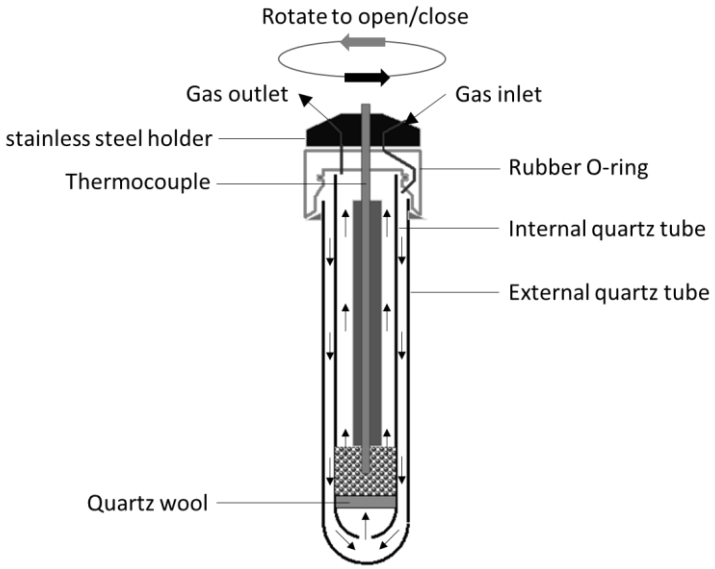

Figure 2-8. Diagram of the TPR reactor assembly[13].

2.9 Photoluminescence (PL) emission spectroscopy

Photoluminescence (PL) is light emission from a semiconductor material after it is excited by an external source and absorbs photons[14]. It is a useful analytical technique for probing exciton behaviour of materials and also provides information of band structure and the surface state of solid materials. In the excitation process, the electrons in the valence band (VB) jump across the band gap and temporarily occupy conduction band (CB) and leave the holes in VB. The excited electrons usually drop back to VB rapidly and recombine with the holes, leading to an emission of energy that is equal to the value of the band gap, namely, band to band luminescence. On the other hand, the excitons can be stabilised by some surface defects or impurities with energy levels close to the band edge. Once got trapped in those defects, the recombination rate of electrons and holes will decrease accompanied by a lifetime extension of the excitons. This delayed recombination usually gives an emitted

radiation at a longer wavelength, which is called deep level luminescence, as illustrated in Figure 2-9.

(a)

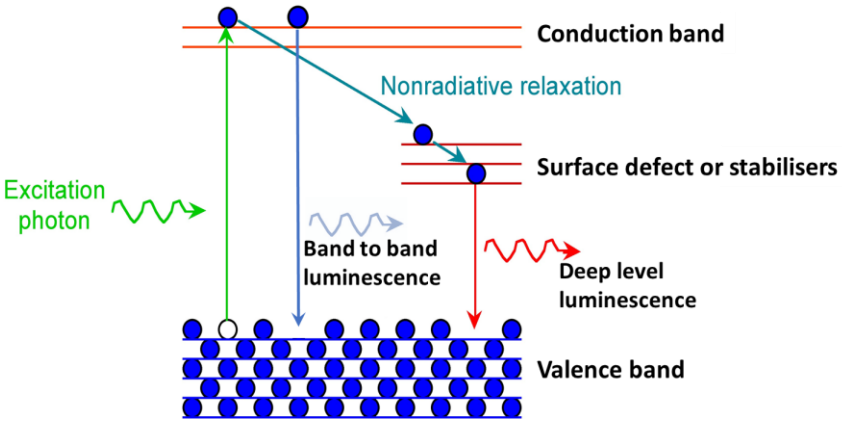

(b)

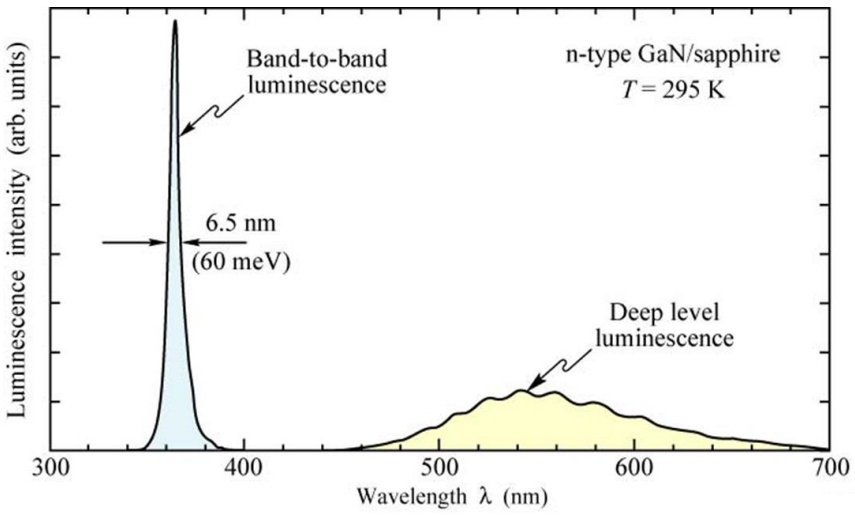

Figure 2-9. (a) Illustration of the excitation and recombination processes of excitons of semiconductor with emitted irradiation[15]; (b) An example of PL spectra of GaN semiconductor which shows both band to band luminescence and deep level luminescence[16].

PL spectroscopy measurement mode can be steady-state or time-resolved. Steady-state PL measures the emission across a range of energies under a constant wavelength of excitation light source, yielding a fluorescence spectrum. This spectrum provides the information of band structure, defects, impurity, etc., of a material. Time-resolved photoluminescence (TRPL) is measured by exciting luminescence from a sample with a pulsed light source and then recording the subsequent decay in PL as a function of time. The time resolution can be obtained in a number of ways. Taking the time-correlated single photon counting (TCSPC) technique as an example, TCSPC requires a defined "start", provided by the electronics steering the laser pulse or a photodiode, and a defined "stop" signal, realised by detection of single-photon with sensitive detectors[17]. The measurement of the time delay through TCSPC is repeated many times to account for the statistical nature of the fluorophores emission. The arrival times of emitted photons are collected and sorted into a histogram that plots the occurrence of emission over time after the excitation light pulse[17].

The decay of the emitted photon intensity with time after the excitation can be expressed as:

$$\boldsymbol{I_t = I_o \sum A_i e^{(-t/\tau_i)}} \quad \text{(Equation 2-10)}$$

where I_0 is the intensity at the time upon excitation; I_t is the fluorescence intensity measured at time t; A is the amplitude of the i^{th} component; τ is the lifetime which is usually used to indicate the life length of excitons reflecting the recombination rate of excited electrons and holes. Formally, the excitons lifetime is defined as the time in which the initial fluorescence intensity of a fluorophore decays to 1/e (approximately 37%) of the initial intensity, see Figure 2-10. This quantity is the reciprocal of the rate constant for fluorescence decay from the excited state to the ground state. In an ideal case, fluorescence decay is usually a mono-exponential function (linear when plotted on the log-linear scale). However, in the case of nano-material with the imperfect interface, defective surface, or adsorbed impurity that lead

to various recombination mechanisms, the approximation of multi-exponential is needed. In that case, a series of τ can be obtained, implying the existence of the variable recombination mechanism of excitons.

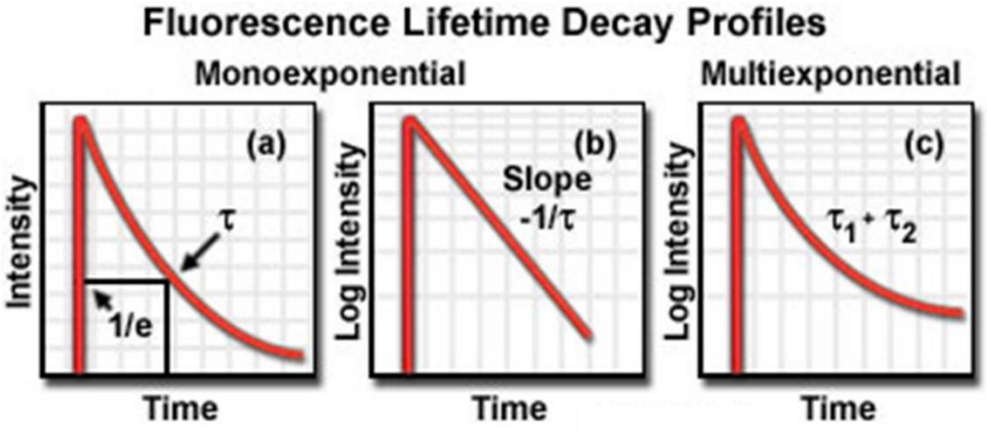

Figure 2-10. Illustration of time-resolved decay profile. (a) and (b) Fluorescence decay is a mono-exponential function in a uniform system, e.g. a solvent; (c) fluorescence decay shows a multiexponential function in a more complex system[17].

2.10 BET surface area analysis

The determination of surface area of materials relies on the measurement of adsorption. Brunauer-Emmett-Teller (BET) theory was developed in 1938. It aims to explain the physical adsorption of gas molecules on a solid surface and serves as the basis for an important analysis technique for the measurement of the specific surface area of materials. From BET analysis, it provides information on adsorption phenomenon to be correlated to physically relevant properties of a material such as specific surface area, pore-size distribution, micro-pore analysis, and porosity.

The process of adsorption is usually studied through graphs know as adsorption isotherm. It is the graph between the amounts of adsorbate adsorbed on the surface of adsorbent and the relative pressure (the equilibrium pressure divided by the saturation pressure, p/p^0) at a fixed temperature. Most of the adsorption isotherm can be categorised into six types according to IUPAC[18], as shown in Figure 2-11. The six types of isotherm are determined by the pore size and surface character of the material, which are: Type I- microporous materials (pore widths below 2 nm); type II- nonporous materials; Type III- nonporous materials and materials having weak interactions between the adsorbate and adsorbent; Type IV- mesoporous materials (pore widths from 2 nm to 50 nm); Type V- mesoporous materials and materials having weak interaction between the adsorbate and adsorbent; type VI- a layer-by-layer adsorption on homogeneous surface, which usually happens when the temperature is near the melting point of the adsorbed gas[19].

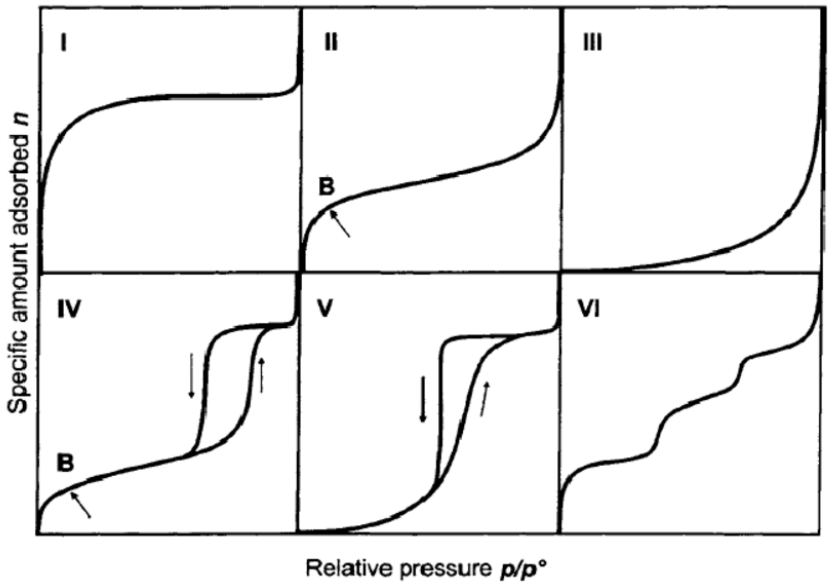

Figure 2-11. The six main types of isotherm from IUPAC classification[18].

In general, the surface area analysis is performed by N_2 adsorption/desorption. The volume of gas adsorbed to the surface of the particles is measured at the boiling point of liquid nitrogen (-196°C). The calculation is based on the BET theory, and the amount of adsorbed gas is correlated to the total surface area of the particles including pores in the surface. From the collected data it is not only possible to calculate the specific surface area (BET surface area) but also the materials pore sizes distribution and shapes. Moreover, the shapes of the adsorption/desorption isotherms can provide information on the nature of the material studied, as mentioned above.

2.11 Raman spectroscopy

Raman spectroscopy is a fast and non-destructive technique to provide information on the electronic and lattice structures of a material[20]. Raman spectroscopy is used to observe vibrational, rotational, and other low-frequency transitions in molecules. It relies on inelastic scattering, or Raman scattering, of monochromatic light, usually from a laser in the visible, near infrared, or near ultraviolet region[21]. The laser interacts with molecular vibrations, phonons or other excitations in the system, resulting in the energy of the laser photons being shifted up or down, and the shift in energy gives information about the vibrational modes in the system[20], see Figure 2-12.

Raman and IR spectroscopy are complementary methods used for studying of molecular vibrations. It has been revolutionised by advancements in laser technology, with sources readily available for the whole visible and near-IR spectral range[20]. In general, Raman has higher spatial resolution than IR and can readily access the low wavenumber spectral range where most phases of catalyst materials have their characteristic absorption bands. Therefore, Raman has been employed for the characterisation of bulk and supported

catalysts. Moreover, Raman spectroscopy is an ideal characterisation technique for carbon materials owing to its high resolution offering the structure and electronic information. Recently, Raman spectroscopy has become one of the most popular techniques for the characterisation of disordered and amorphous carbons, fullerenes, carbon nanotubes, diamonds, carbon chains, and poly-conjugated molecules[22,23]. In addition, Raman scattering on phonons is to a considerable extent determined by electrons, depending on how they move, interfere and scatter. Thus, any vibration of electronic properties induced by defects, edges, doping, or magnetic fields can affect the positions, widths, and intensities of the Raman spectra, enabling one to probe electrons via phonons[23].

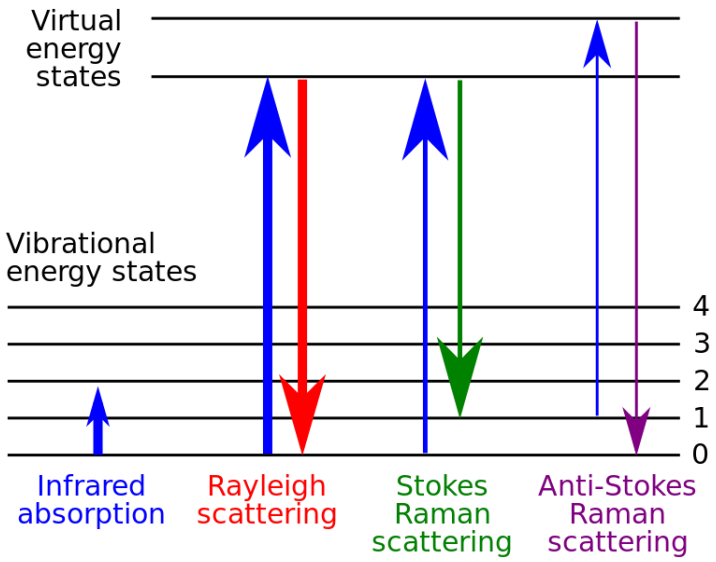

Figure 2-12. Energy-level diagram showing the states involved in Raman signal[20].

2.12 High sensitivity-low energy ion scattering (HS-LEIS)

HS-LEIS is a sensitive analytical technique for analysing the composition of the outermost atomic layer of a sample. For a heterogeneous catalyst, the outermost atomic layer is the location where the catalytic reaction takes place. In comparison to XPS, HS-LEIS gives the information for the outermost atomic layer, while the information depth for XPS is several nanometers (about 20 layers). HS-LEIS determines the mass of surface atoms by measuring the energy from ions that are scattered from the surface. The principle behind this technique is that: A noble gas ion ($^{4}He^{+}$, $^{20}Ne^{+}$, or $^{40}Ar^{+}$) beam with a known primary energy E_i is aimed perpendicularly at the sample surface where this ion collides with a surface atom in a binary collision[24], see Figure 2-13. The energy of the backscattered ion (E_f) is determined by the classic laws of mechanics (conservation of momentum and conservation of energy) and is described as:

$$\boldsymbol{E_f = k^2(\frac{m_2}{m_1}, \theta)E_i} \quad \text{(Equation 2-11)}$$

where m_1 and m_2 are the masses of the gas ion and the scattering surface atom, respectively; θ is the back-scattering angle (determined via the geometry of the instrument). In the HS-LEIS experiment, θ, m_1 and E_i are known and E_f can be measured with a dedicated energy analyser. The factor k^2 is a known function of m_2/m_1 and θ. Therefore, the mass of the scattering surface atom can be calculated[24].

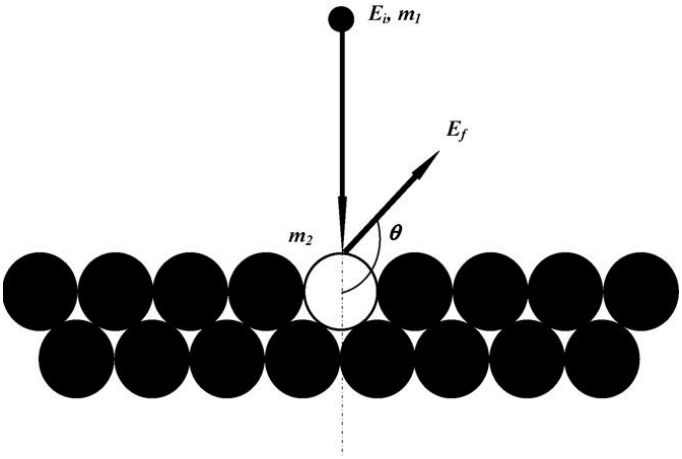

Figure 2-13. Schematic representation of the HS-LEIS process[24].

References

1. Thomas, J. M. & Thomas, W. J. *Principles and practice of heterogeneous catalysis*. (Wiley-VCH, Weinheim, 1997).
2. Deutschmann, O., Knözinger, H., Kochloefl, K. & Turek, T. *Heterogeneous catalysis and solid catalysts*. (Wiley-VCH, Weinheim, 2009).
3. Brundle, C. R., Evans, C. A. & Wilson, S. *Encyclopedia of materials characterization : surfaces, interfaces, thin films*. (Butterworth-Heinemann ; Manning, 1992).
4. Blake, A. J. *Crystal structure analysis*. (Oxford University Press, 2009).
5. Niemantsverdriet, J. W. *Spectroscopy in catalysis: An introduction*. (Wiley-VCH, Weinheim, 2007).
6. Watts, J. F. & Wolstenholme, J. *An introduction to surface analysis by XPS and AES*. (Wiley, New York, Chichester, 2003).
7. Newville, M. Fundamentals of XAFS. *Rev. Mineral. Geochemistry* **78,** 33–74 (2004).
8. F. Liao, The Development of Pd-based Bimetallic Nano-catalysts in Green Chemistry, D.Phil thesis, University of Oxford, 2015.
9. Jensen, E. Types of imaging, part 1: Electron microscopy. *Anat. Rec.* **295,** 716–721 (2012).
10. Giessibl, F. J. Advances in atomic force microscopy. *Rev. Mod. Phys.* **75,** 949–983 (2003).
11. Binnig, G., Quate, C. F. & Gerber, C. Atomic Force Microscopy, Phys. Rev. Lett. **56**, 930–933 (1986)
12. Obradovic, J., Newnham, D. A. & Taday, P. F. Attenuated total reflection explores the terahertz region. *American Laboratory* (2007). Available at: https://www.americanlaboratory.com/913-Technical-Articles/1457-Attenuated-Total-Reflection-Explores-the-Terahertz-Region/.

13. Chan, C. W. A. *Ultraselective nanocatalysts in fine chemical and pharmaceutical synthesis, D.Phil thesis*. (University of Oxford, 2012).
14. Che, M. & Védrine, J. C. *Characterization of solid materials and heterogeneous catalysts. From structure to surface reactivity*. (Wiley-VCH, Weinheim, 2012).
15. Barron, A. R. Optical characterization of group 12-16 (II-VI) semiconductor nanoparticles by fluorescence spectroscopy. Available at: https://qa.cnx.org/contents/gRPw0_eN@1/Optical-Characterization-of-Gr.
16. Schubert, E. F. *Light-emitting diodes*. (Cambridge University Press, 2006).
17. PicoQuant. Time-resolved photoluminescence (TRPL). Available at: https://www.picoquant.com/applications/category/materials-science/time-resolved-photoluminescence.
18. Rouquerol, F., Rouquerol, J., Sing, K. S. W., Llewellyn, P. & Maurin, G. *Adsorption by powders and porous solids: Principles, methodology and applications*. (Elsevier Ltd., 2014).
19. Alothman, Z. A. A review: Fundamental aspects of silicate mesoporous materials. *Materials* **5,** 2874–2902 (2012).
20. Gardiner, D. J. & Graves, P. R. *Practical Raman spectroscopy*. (Springer-Verlag Berlin Heidelberg, 1989).
21. Losurdo, M. & Hingerl, K. *Ellipsometry at the nanoscale*. (Springer Science & Business Media, 2013).
22. Bortolamiol, T., Lukanov, P., Galibert, A., Soula, B., Lonchambon, P., Datas, L. & Flahauta, E. Double-walled carbon nanotubes: Quantitative purification assessment, balance between purification and degradation and solution filling as an evidence of opening. *Carbon* **78,** 79–90 (2014).
23. Ferrari, A. C. & Basko, D. M. Raman spectroscopy as a versatile tool for studying the properties of graphene. *Nat. Nanotechnol.* **8,** 235–246 (2013).
24. ter Veen, H. R. J., Kim, T., Wachs, I. E. & Brongersma, H. H. Applications of high sensitivity-low energy ion scattering (HS-LEIS) in heterogeneous catalysis. *Catal. Today* **140,** 197–201 (2009).

Chapter 3: Experimental methods

3.1 Synthesis procedure

3.1.1 Synthesis of CuZnGa-based catalyst

3.1.1.1 Synthesis of catalyst precursors by the conventional co-precipitation method (CZG precursor)

Ga^{3+} modified Cu/ZnO catalyst precursors were synthesised using a pH-controlled conventional co-precipitation method[1]. The metal precursors were hydrated metal nitrate salts: $Cu(NO_3)_2 \cdot 3H_2O$ (Aldrich), $Zn(NO_3)_2 \cdot 6H_2O$ (Aldrich), and $Ga(NO_3)_3 \cdot 9H_2O$ (Aldrich). For a typical preparation, the metal nitrates [3.77g $Cu(NO_3)_2 \cdot 3H_2O$; 5.53g $Zn(NO_3)_2 \cdot 6H_2O$; 0.75g $Ga(NO_3)_3 \cdot 9H_2O$] were dissolved completely in 100 mL deionised water. A Na_2CO_3 aqueous solution was prepared by dissolving 3.50 g of Na_2CO_3 in 100 mL of DI water. The solutions were added simultaneously into a plastic reactor containing 250 mL of preheated DI water. A delivery pump with two 50 mL syringes was used to inject the precursor metal nitrate solution at a constant rate of 0.42 $mL \cdot min^{-1}$ in an automatic and reproducible manner. An HPLC pump was used to deliver the Na_2CO_3 solution at a rate of 0.35–0.70 $mL \cdot min^{-1}$. The mixture was stirred at 1000 rpm while pH of the precipitating solution was carefully maintained at 6.5. The precipitation process took place at around 80 ^oC. The pH of the liquid was measured using a temperature-dependent pH meter and was controlled at pH 6.5, with an error range of ±0.1. After ageing for 16h, the precipitate was extracted by centrifugation at 5000 rpm. The centrifuged precipitate was washed with DI water five times to remove residual Na^+ ions. The resulting wet solid was dried in air at 80 ^oC for 18 h. The catalysts were labelled as CZ (referring to Cu/ZnO catalysts in the absence of Ga) and CZG*x*Ga (referring to Ga modified Cu/ZnO catalysts where *x* indicates the mole % of Ga), see Table

3-1. A typically measured surface area of CZG5Ga was 85 m^2g^{-1}. We also rinsed two equal portions of powders in acetone for 1h (CZG5Ga-A1) and 18h (CZG5Ga-A2) before they were dried. The measured surface areas were 82 m^2g^{-1} and 93 m^2g^{-1}, respectively. The procedure for the synthesis is graphically summarised in Figure 3-1.

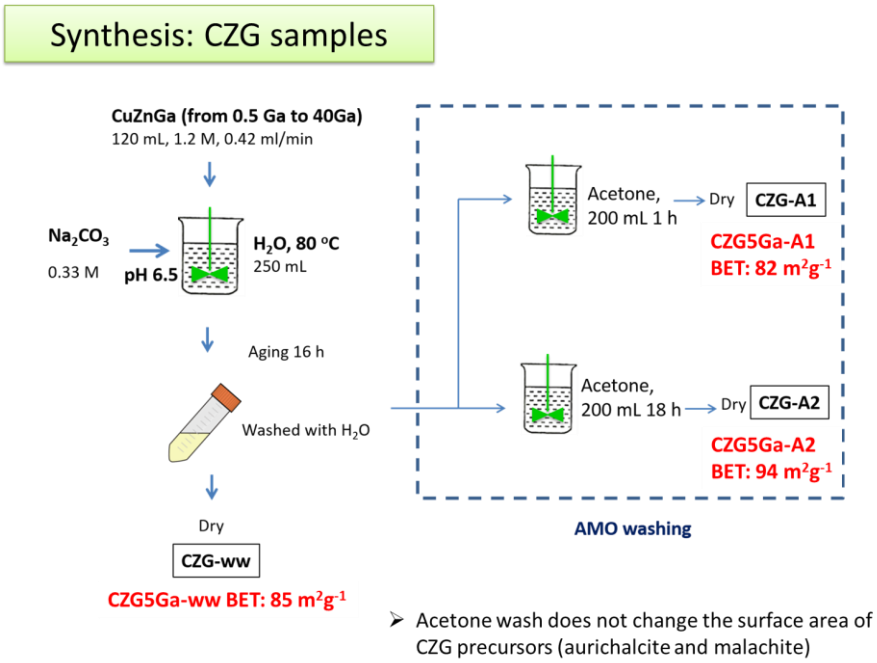

Figure 3-1. Procedure for the synthesis of CuZnGa precursors by the conventional co-precipitation (CZG precursor).

3.1.1.2 Synthesis of catalyst precursors via aqueous miscible organic solvent method (AMO-LDH precursor)

The metal precursor solution (50 mL) including desired amounts of $Cu(NO_3)_2{\cdot}3H_2O$ (Aldrich), $Zn(NO_3)_2{\cdot}6H_2O$ (Aldrich) and $Ga(NO_3)_3{\cdot}9H_2O$ (Aldrich) was added drop-wise into the 50 mL of 0.5 M Na_2CO_3 base solution under rapid stirring. During the nucleation

step, the pH value was kept at *ca.* 10.0 by dropwise addition of a 4.0 M NaOH solution. After ageing for 16 h with stirring at room temperature, the mixture was filtered and washed with DI water until the pH was close to 7. The obtained wet cake solid layered double hydroxides (LDHs) was re-dispersed in 200 mL acetone and stirred at room temperature for 1-2 h. Then, the resultant solid was filtered, washed thoroughly with acetone and dried overnight (18 h) in a vacuum oven at room temperature which led to aqueous miscible organic solvent treated LDHs (AMO-LDHs) with a formula of $[(Cu_a, Zn_b)^{2+}_{1-x}M^{3+}_x(OH)_2](CO_3^{2-})_{x/2}\cdot mH_2O\cdot nC_3H_6O$.[2] The samples were labelled as LDH*x*Ga where *x* indicates the mole % of Ga in the synthesis recipe (see Table 3-1). These washed samples were characterised by XRD or SXRD. The super-fine portions of the washed samples were kept for catalysis use and TEM/AFM characterisation. As similar to the literature, the powder sample with and without acetone treatment showed a large difference in their surface area per gram basis. Typically, the surface areas of LDH30Ga-ww (ww: water washed, no acetone treatment) and LDH30Ga-Aw (Aw: acetone washed) were determined as 37 m^2g^{-1} and 159 m^2g^{-1}, respectively. The synthesis recipes can be found in Table 3-1 and the procedure for the synthesis is graphically summarised in Figure 3-2.

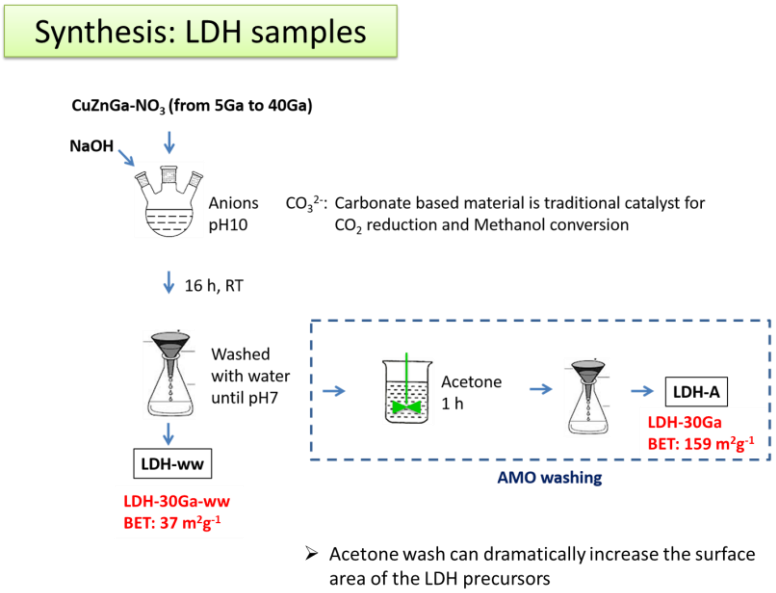

Figure 3-2. Procedure for the synthesis of CuZnGa catalyst precursors by AMOST method (AMO-LDH precursor).

Table 3-1. Synthesis recipes and determined compositions for CZG and LDH-derived samples.

Catalysts	**Synthesis recipe Cu:Zn:Ga (mol%)**	**Cu:Zn:Ga from ICP**	
		Cu:Zn:Ga (wt%)	Cu:Zn:Ga (mol%)
CZ	40:60: 0	45:55: 0	44:55: 0
CZG5Ga	40:55: 5	43:51: 6	44:51: 5
CZG10Ga	40:50:10	44:46:10	45:45:10
CZG30Ga	40:30:30	44:26:30	45:26:29
CZG40Ga	40:20:40	42:17:41	43:18:39
LDH5Ga	40:55: 5	42:54: 4	43:53: 4
LDH10Ga	40:50:10	43:50: 7	44:49: 7
LDH20Ga	40:40:20	44:41:15	45:41:14
LDH30Ga	40:30:30	45:32:23	47:32:21
LDH40Ga	40:20:40	47:22:31	49:22:29
LDH30Ga-ww	40:30:30	45:31:24	46:31:23

3.1.1.3 Calcination of CuZnGa-based catalyst precursors

All precursor materials were calcined under constant air flow (50 mln·min^{-1}) at 330 ^{o}C for 3 h (heating rate of 10 ^{o}C·min^{-1} followed by 1 hour of dwell at 80 ^{o}C and 150 ^{o}C) prior to being used.

3.1.2 Synthesis of Rh-based catalyst

3.1.2.1 Synthesis of the binary metal oxide supports

The binary metal oxide supports were synthesised using a co-precipitation method. The metal precursors were hydrated metal nitrate salts: $Al(NO_3)_2{\cdot}3H_2O$ (Aldrich), $Zn(NO_3)_2{\cdot}6H_2O$ (Aldrich), $In(NO_3)_3{\cdot}xH_2O$ (Aldrich). and $Ga(NO_3)_3{\cdot}9H_2O$ (Aldrich). Two of the selected metal nitrates were dissolved completely in 150 mL deionised water to make a solution with a concentration of 0.05M. A Na_2CO_3 aqueous solution was prepared by dissolving 7.5 g of Na_2CO_3 in 300 mL of deionised water. The solutions were added simultaneously into a plastic reactor containing 50 mL of preheated deionised water at 80 ^{o}C. A delivery pump was used to inject the metal nitrate solution at a constant rate of 0.4 mL min^{-1} in an automatic and reproducible manner. An HPLC pump was used to deliver the Na_2CO_3 solution at a rate of 0.4-0.8 mL min^{-1}. The mixture was stirred at 1,000 rpm, with pH of the precipitating solution carefully maintained at 9 ± 0.1. Once the addition of the precursor metal nitrate solution was completed, the resulting precipitate was aged in solution for 18 h. After the ageing process, the precipitate was extracted by centrifugation at 5,000 rpm. The centrifuged precipitate was washed with deionised water several times at 5,000 rpm to remove residual Na^+ ions and then washed with acetone before drying in vacuum. The dried powder was then calcined in N_2 at a ramp of 5 ^{o}C min^{-1}up to desired temperature (450 ^{o}C, if not indicated) for 4 h to get the final binary metal oxide supports.

3.1.2.2 Synthesis of the binary metal oxides supported Rh catalysts

The loading of Rh onto above synthesised binary metal oxide support was achieved by the wet-impregnation method: the selected binary metal oxide support was immersed into a $Rh(NO_3)_3$ (Aldrich) aqueous solution and the mixture was kept stirring until the solid and liquid were mixed evenly. The slurry was set aside in air for one night (18 h) before drying in an oven at 80 ^oC. The dried powder was then calcined in N_2 at a ramp of 5 ^oC min^{-1} up to 450 ^oC for 4 h to get the final binary metal oxides supported Rh samples. The detailed information of the samples is listed in Table 3-2.

Table 3-2. The details of the binary metal oxides supported Rh samples.

Sample	**Binary metal oxide $Metal_1$: $Metal_2$ = 1 : 1**		**Binary metal oxide preparation**	**N_2 heat treatment temperature for the metal oxide**	**Rh loading and method**
	$Metal_1$	$Metal_2$			
Rh/ZnAlO	Zn	Al	Co-precipitation method	450 ^oC	0.6%, wet-impregnation method
Rh/GaAlO	Ga	Al			
Rh/GaZnO	Ga	Zn			
Rh/InZnO	In	Zn			
Rh/InAlO	In	Al			
Rh/InGaO	In	Ga			

3.1.2.3 Synthesis of the Rh-containing, Ru-containing samples and the indium-aluminium oxides support with different In/Al ratios.

The detailed information of the samples is listed in Table 3-3. In this part, the samples are classified into two categories: those loaded Rh or Ru by the wet-impregnation method and those by co-precipitation method. For the wet-impregnation samples, the synthesis followed the same process as the binary metal oxides supported Rh samples described above: The rhodium-indium supports with different recipe Rh:In ratios were synthesised using co-precipitation method. Then the derived supports were loaded with Rh or Ru using wet-impregnation method and dried, calcined in N_2 to get the final catalyst. The co-precipitation samples were prepared by the following process: Metal nitrates ($Rh(NO_3)_3$ aqueous solution, $Al(NO_3)_2 \cdot 3H_2O$ and/or $In(NO_3)_3 \cdot xH_2O$) were dissolved completely in 150 mL deionised water to make a solution with a concentration of 0.05M. A Na_2CO_3 aqueous solution was prepared by dissolving 7.5 g of Na_2CO_3 in 300 mL of deionised water. The solutions were added simultaneously into a plastic reactor containing 50 mL of preheated deionised water at 80 ^oC. A delivery pump was used to inject the metal nitrate solution at a constant rate of 0.4 $mL \cdot min^{-1}$ in an automatic and reproducible manner. An HPLC pump was used to deliver the Na_2CO_3 solution at a rate of 0.4-0.8 mL min^{-1}. The mixture was stirred at 1,000 rpm, with pH of the precipitating solution carefully maintained at 9 ± 0.1. Once the addition of the precursor metal nitrate solution was completed, the resulting precipitate was aged in solution for 18 h. After the ageing process, the precipitate was extracted by centrifugation at 5,000 rpm. The centrifuged precipitate was washed with deionised water several times at 5,000 rpm to remove residual Na^+ ions and then washed with acetone before drying in vacuum. The dried powder was then calcined in N_2 at a ramp of 5 ^oC min^{-1}up to desired temperature (450 ^oC, if not indicated) for 4 h to get the final catalysts.

Table 3-3. The details of the Rh-containing, Ru-containing samples and the indium-aluminium oxides support with different In/Al ratio.

Sample	Rh or Ru loading & method	Recipe composition of the support In : Al
Rh/(10Al)O	5%, wet-impregnation	0 : 10
Rh/(1In9Al)O	5%, wet-impregnation	1 : 9
Rh/(3In7Al)O	5%, wet-impregnation	3 : 7
Rh/(5In5Al)O	5%, wet-impregnation	5 : 5
Rh/(10In)O	5%, wet-impregnation	10 : 0
(5In5Al)O support	-	5 : 5
Copre-Rh/(5In5Al)O	2.5%, co-precipitation	5 : 5
Copre-Rh/(10Al)O	2.5%, co-precipitation	0:10
Ru/(5In5Al)O	5%, wet-impregnation	5 : 5

3.1.3 Synthesis of CdS/CNT/*s*-MoS_2 photocatalyst

3.1.3.1 Materials for preparing CdS/CNT/s-MoS_2 photocatalyst

Reagents used throughout this section were purchased from Sigma Alrdrich and were used without modification or purification unless stated: Cadmium chloride-$CdCl_2$ (99.99% trace metals basis), oleylamine (technical grade,70%), sulfur (99.998% trace metals basis), molybdenum disulfide- MoS_2 (99% 2H-MoS_2), n-butyllithium (1.6 M solution in hexane), hexane (97 ≥ chromasolv for HPLC), nitric acid- HNO_3 (ACS reagent), lactic acid (85%), SWNT (carbon > 90%, ≥ 80.0% carbon as SWNT (BET≈ 560 m^2g^{-1}), 0.7-1.4 nm diameter).The DWNTs (345 m^2g^{-1}) were produced by catalytic chemical vapour deposition (CCVD) of an H_2-CH_4 mixture at 1000 ºC with CoMo-MgO catalyst[3,4]. MWNTs (369 m^2g^{-1}) were synthesised by CCVD using a Co:Mo-MgO catalyst with an elemental composition of $Mg_{0.9}Co_{0.033}Mo_{0.067}O$. The catalyst was heated in an atmosphere containing 36% of CH_4

and 64% of H_2, at a total flow-rate of 15L h^{-1}, starting from room temperature to 1000 ^oC at 5 ^oC min^{-1}. No dwell was applied and the gaseous atmosphere was maintained constant during all the procedure[5]. CNTs are free from amorphous carbon coating. During the extraction process, oxides (unreacted CoMo-MgO) and unprotected metal nanoparticles (Co, Mo) were dissolved by addition of aqueous HCl solution. The acidic suspension was then filtered on 0.45 μm pore-size polypropylene membranes and washed with deionised water until neutrality. The sample was freeze-dried.

3.1.3.2 Synthesis of cadmium sulphide

The synthesis of CdS spherical NPs followed the method described by Joo *et al*.[6] Firstly, 604 mg of cadmium chloride (3 mmol) was dissolved in 30 mL of oleylamine with the assistance of sonication and stirring using a magnetic stirrer bar. This solution was then heated to 90 ^oC with constant stirring in a three-necked flask for 1 h in air. 48 mg of sulfur dissolved in 5 mL oleylamine was then injected into the mixture dropwise. The solution was then heated to 160 ^oC under an N_2 atmosphere and left for 6 h under vigorous stirring. After leaving to cool overnight (18 h), the nanoparticles were then collected using centrifugation (5000 rpm for 10 min) and were thoroughly washed with acetone five times to ensure all solvent and excess ligand had been removed.

3.1.3.3 Synthesis of single-layer molybdenum disulphide (s-MoS_2)

Single-layer MoS_2 (s-MoS_2) was synthesised by the Tsang group following a well-documented route of exfoliation of bulk MoS_2 with lithium intercalation[7,8]. Initially, the black MoS_2 powder was soaked for 48 h in 1.6 M solution of n-butyllithium in hexane under N_2 atmosphere. After this initial intercalation step of MoS_2 with lithium, the Li_xMoS_2 was then repeatedly washed with hexane to remove excess butyl lithium and dried under N_2

atmosphere. The powder was then sonicated in de-ionised water for 48 h to assist exfoliation. The reaction between water and intercalated lithium forms H_2 between the layers and the gas expansion tends to separate the MoS_2 layers until the layers become completely separated and suspended in the aqueous solution. The product was filtered, washed extensively with water and ethanol and then dried under vacuum. Atomic force microscopy (AFM) image of the synthesised s-MoS_2 can be found in Figure 3-3.

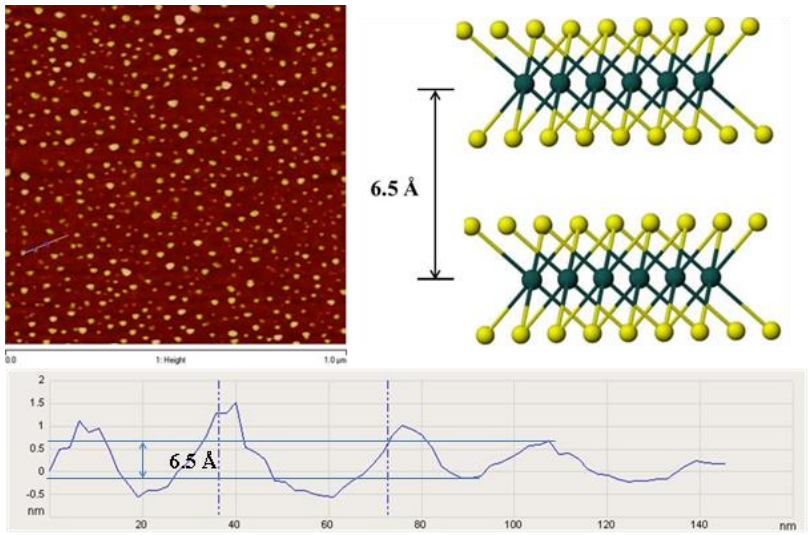

Figure 3-3. Atomic Force Microscopy images of s-MoS_2 and drawing of MoS_2 structure perpendicular to the c axis[9].

3.1.3.4 Acid treatment of CNTs

Following a method reported by E. Flahaut *et al.*[8], initially, 200 mg of raw CNTs were placed into 200 mL 3M HNO_3 solution in a 500 mL Pyrex flask and sonicated for 30 min then refluxed under vigorous stirring for 24 h at 130 ^oC. The black suspension was then washed three times with 100 mL DI water before drying the product at 80 ^oC in air overnight (18 h).

3.1.3.5 Preparation of CdS/CNT/s-MoS_2 nanocomposites

CdS/CNT/*s*-MoS_2 composites were synthesised using a method similar to the previously reported CdS-graphene oxide-MoS_2 synthesis method[10]. Initially, 100 mg CdS, 2 mg *s*-MoS_2 and acid treated CNTs (0.4, 2, 5 and 7mg) in 50 mL ethanol were sonicated for 4 h and then stirred at room temperature for a further 24 h. The suspensions were filtered using a 0.2 μm membrane and washed with 250 mL ethanol. The sample was then vacuum dried at 80 ^oC in air overnight (18 h).

3.2. Catalytic testing

3.2.1 Catalytic testing of CO_2 hydrogenation reaction

Catalytic tests in the hydrogenation of CO_2 to produce methanol were carried out in a tubular fixed bed reactor (stainless outer tube with 12.7 mm diameter; quartz inner tube with 8mm diameter) using a 0.1 g calcined catalyst precursor without dilution. Before each test, the calcined catalyst precursor was pre-reduced at 290 ^oC for 2 h under atmospheric pressure with the pure H_2 stream (20 stp mL·min^{-1}, stp = standard temperature and pressure; P = 101.3 kPa, T = 298 K). After the reduction, the temperature was cooled to below 50 ^oC and the reactor was pressurised to 4.5 MPa with CO_2/H_2 (molar ratios ranging from CO_2 : H_2 = 1 : 3 to 3 : 1) gas mixture. The activities of the catalysts were determined under a constant flow of the CO_2/H_2 gas mixture through the catalyst bed (30 stp mL·min^{-1}) at desired temperatures (190-310 ^oC). The activity measurements were taken after at least 2 h on the stream at each selected reaction temperature. Heating tape was used to heat (at 200 ^oC) the stainless-steel lines that connected between reactor tube and the GC to prevent condensation of methanol and water. The products were quantitatively analysed by an Agilent 7890B gas chromatograph equipped with calibrated thermal conductivity detector (TCD) and flame

ionisation detector (FID). Figure 3-4 shows the picture of the CO_2 hydrogenation reactor used for this thesis.

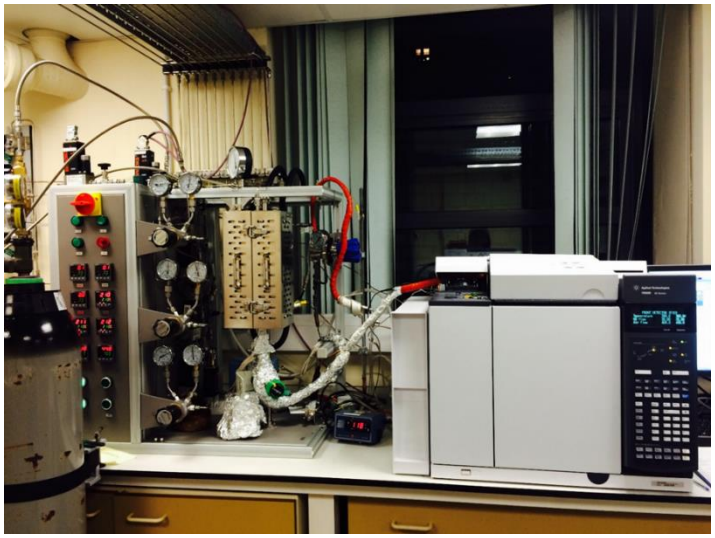

Figure 3-4. The CO_2 hydrogenation reactor used for the works in this thesis

3.2.2 Catalytic testing of photocatalytic splitting of water

Photocatalytic H_2 evolution experiments were performed in a 500 mL sealed Pyrex flask at ambient temperature and atmospheric pressure. The reactor was positioned 10 cm away from the 500 W UV-vis lamp. In a typical photocatalytic experiment, 20 mg catalyst was suspended in 90 mL deionised water and 10 mL lactic acid and sonicated for 30 min. Prior to irradiation, the suspension was bubbled with 5 % CH_4/Ar for 15 min to remove the dissolved oxygen and to ensure the reaction was under anaerobic conditions, the CH_4 acted as an internal reference for gas chromatography calibration. Continuous magnetic stirring was applied in order to keep the photocatalyst particles suspended during the irradiation. 20

mL of sample was collected from the generated gas and analysed by Agilent 7890A gas chromatography with TCD detector.

3.3 Characterisation procedure

3.3.1 X-ray diffraction (XRD)

The powder X-ray diffraction (PXRD) data were collected by a Philips PW-1729 diffractometer with Bragg-Brentano focusing geometry using Cu Kα radiation (λ = 1.5418 Å) from a generator operating at 40 kV and 40 mA.

High-resolution synchrotron X-ray diffraction (SXRD) data were collected on Beamline I11, Diamond Light Source, UK. A detailed description of the beamline can be found elsewhere[11]. The energy of the incident X-ray beam was set at 15 keV. The wavelength and the 2θ-zero point correction were refined using a diffraction pattern obtained from a high-quality silicon powder (SRM640c). At room temperature, the sample powder was loaded in a 0.1 mm borosilicate glass capillary. High-resolution SXRD data were obtained from the samples using the multi-analyser crystal (MAC) detectors. The patterns were collected in the 2θ range 0-150^{o} with 0.001^{o} data binning. Each pattern was collected for an hour for good statistics. In total, there were more than 100 *hkl* reflections measured, of which at least 72 independent *hkl* reflections were observed. The quality of the Pawley refinements of SXRD data has been assured with a low goodness-of-fit (Gof) factor, a low weighted profile factor (R_{wp}) and a well fitted within experimental errors.

3.3.2 X-ray photoelectron spectroscopy (XPS)

XPS was performed on the reduced samples. The samples were calcined and then reduced before they were carefully sealed in a glove bag filled with nitrogen to prevent air exposure. The measurement was conducted using a Quantum 2000 Scanning ESCA Microprobe instrument (Physical Electronics) equipped with an Al Kα X-ray radiation source ($h\upsilon$ = 1486.6 eV). A flood gun with variable electron voltage (from 6 eV to 8 eV) was used for charge compensation. The raw data were corrected for substrate charging with the BE of the C peak (285 eV), as shown in the XPS handbook[12]. The measured spectra were fitted using a least-squares procedure to a product of Gaussian–Lorentzian functions after removing the background noise. The concentration of each element was calculated from the area of the corresponding peak and calibrated with the sensitivity factor of Wagner.

3.3.3 X-ray absorption fine structure (XAFS)

After hydrogen reduction, samples were carefully transferred into capillary tubes (quartz NMR tubes) in a nitrogen glove box. The reduced samples were sandwiched between silica wool to fix the samples in the middle of the capillary tubes, and then the capillary tubes were sealed and stored in a glove box until the XAFS experiments. Local structures surrounding the selected absorbing atoms were probed by using XAFS technique at beamlines BL07A and BL01C (depends on the energy required for the measurements) of Taiwan Light Source at National Synchrotron Radiation Research Center (NSRRC) in Taiwan. A Si(111) Double Crystal Monochromator (DCM) was used to scan the photon energy. The energy resolution ($\Delta E/E$) for the incident X-ray photons was estimated to be 2×10^{-4}. Conventional transmission mode was adopted for Cu K-edge, while fluorescence mode was used for Rh K-edge measurements. The Rh and In L_3-edge X-ray absorption near edge structure (XANES) spectra were recorded with a beamline BL16A1.

To ascertain the reproducibility of the experimental data, at least two scan sets were collected and compared for each sample. The EXAFS data analysis was performed using IFEFFIT 1 with Horae packages 2 (Athena and Artemis). The spectra were calibrated with metal foils as a reference to avoid energy shifts of the samples. And the amplitude parameter was obtained from EXAFS data analysis of the foil, which was used as a fixed input parameter in the data fitting to allow the refinement in the coordination number of the absorption element. In this work, the first shell data analyses under the assumption of single scattering were performed with the errors estimated by R-factor.

3.3.4 Transmission electron microscopy (TEM)

For Chapter 4: Field emission TEM/STEM (FEI Technai F20S-TWIN) was conducted at Johnson Matthey plc., with the help from Dr Winson Kuo using EDAX Si(Li) LN2 EDS detector with SUTW (super ultra-thin window) of active area of 30 mm^2 at the energy resolution of 135eV measured at Mn K alpha.

For Chapter 5: TEM images were taken using a JEOL 2010 TEM at 200 kV. The sample particles were deposited on an Agar Scientific holey carbon supported copper 400 mesh grid. TEM samples were prepared by sonicating a suitable amount of material in 1 mL ethanol for 15 minutes before dropwise addition of the solution onto the copper grid.

For Chapter 6: TEM images were taken using an aberration-corrected TEM JEOL 2200MCO operated at 80kV. Samples were reduced in H_2 at 290 ^oC then dispersed in 1 mL ethanol for 15 minutes (in the N_2 atmosphere) before dropwise addition of the solution onto Agar Scientific Holey carbon supported copper 400 mesh grid. After drying the samples were quickly placed into the vacuum chamber of TEM to prevent or minimise re-oxidation.

For Chapter 7: TEM images were taken using a JEOL 2100 TEM at 200 kV. The sample particles were deposited on an Agar Scientific Holey carbon supported copper 400 mesh grid. TEM samples were prepared by sonicating a suitable amount of material in 1 mL ethanol for 15 minutes before dropwise adding the solution onto the copper grid.

3.3.5 Atomic force microscopy (AFM)

AFM measurements were collected by Agilent 5400 microscope. AFM samples were prepared by deposition of a freshly diluted emulsion of LDH samples onto a clean Si wafer by dip coating. The images were obtained with a Si tip cantilever (MikroMasch NSC35/ALBS) working with frequency and force constant of 150 kHz and 4.52 $N \cdot m^{-1}$, respectively, using non-contact mode in the air at room temperature. Images were recorded with 512 × 512 pixels and 0.5–1 Hz scan rate. Processing and analysis of the images were carried out using the PicoView version 1.20.2 software.

3.3.6 Temperature programmed reduction (TPR)

TPR measurements were obtained using a ThermoQuest TPDRO 1100 instrument. Inside the TPR quartz tube, 0.026 g of the calcined catalyst sample was sandwiched between two layers of glass wool with a thermocouple placed in contact with the sample. The TPR tube was then inserted into the instrument for helium pretreatment. The helium gas pretreatment (helium is running through the TPR tube at 10 $mL \cdot min^{-1}$ at a temperature ramp of 10 $^{o}C \cdot min^{-1}$ from 40 to 150 ^{o}C, then held for 5 min before cooling) cleaned the catalyst surface by removing any absorbed ambient gas molecules. After the pretreatment, the reduction (5% H_2 in Argon flowing through the TPR tube at 20 $mL \cdot min^{-1}$ at a temperature ramp of 10 ^{o}C min^{-1} from 40 to 400 ^{o}C, then held at 400 ^{o}C for 30 min before cooling to room temperature) of catalysts was carried out to reduce the Cu^{2+} within the sample. Cu^{2+} and Cu^{+} were reduced

to Cu^0 by the flow of hydrogen gas in the reduction treatment. The consumption of hydrogen gas changed the conductivity of the gas stream; hence, the change in conductivity was measured and calibrated as a function of both temperature and time to produce the TPR profile.

3.3.7 Thermogravimetric analysis (TGA)

The thermal decomposition of the freshly prepared catalyst precursors was studied by a thermogravimetric method using an SDT Q600 thermal analyser. Measurements were performed in the temperature range of 20–800 ^oC under continuous flow of compressed air (100 $mL \cdot min^{-1}$)

3.3.8 BET surface area analysis

The surface area of the samples was determined by N_2 adsorption-desorption at a liquid nitrogen temperature of -196 ^oC using the Micromeritics ASAP 2020M analyser. Sample degassing was carried out at 200 ^oC for 3 h prior to the acquisition of the adsorption isotherm. Calculations were conducted according to the Brunauer–Emmett–Teller (BET) method.

3.3.9 Inductively coupled plasma mass spectrometry (ICP-MS)

The elemental chemical analysis was performed using inductively coupled plasma mass spectrometry (ICP-MS), NexION 300, PerkinElmer. The calcined samples were digested in nitric acid then diluted with MilliQ water prior to carrying out the experiments.

3.3.10 N_2O chemisorption for the measurement of Cu dispersion

The reduction treatment of Cu^{2+} to Cu^0 in the catalyst sample (1st TPR) was followed by N_2O chemisorption at room temperature to determine the average size of the copper metal particle. Treatment with 5% N_2O/Ar at 20 mL min^{-1} for 40 min was carried out to re-oxidise only the Cu surface via dissociative chemisorption. To remove remaining adsorbed N_2O, another He pre-treatment (He flowing at 10min^{-1} for 10 min at room temperature) was carried out. This was followed by a second reduction treatment (2nd TPR: 5% H_2 in Argon at 20 ml min^{-1} at a temperature ramp of 10 ^oC min^{-1} from 40 ^oC up to 330 ^oC). By analysing data from the first and second TPR, it was possible to determine the Cu surface area of the catalyst sample by pre-calibrating the TPR with a Cu(II)O standard of known Cu content. Standard samples of Cu(II)O: 0.005, 0.0010 and 0.0015 g (Aldrich) were used to perform the TPR and the number of moles of hydrogen consumed was calculated.

3.3.11 Hydrogen/Oxygen titration method for the measurement of Rh dispersion

The dispersion and exposed surface area (S_{Rh}) of Rh were determined by oxygen chemisorption followed by hydrogen pulse reduction. Oxygen chemisorption was carried out on a Micromeritics AutoChem II 2920 instrument. Before the measurement, 100 mg of sample was reduced at 350 ^oC in a 5% H_2/Ar mixture (50 mL.min^{-1}) for 4 h. After cooling to RT, the sample was exposed to dilute 1%O_2/He (20 mL.min^{-1}) for 1 h to ensure complete oxidation of surface metallic Rh to RhO. Finally, calibrated hydrogen pulse reduction at 300 ^oC was conducted to determine the amount of surface RhO species. S_{Rh} was calculated by dividing the amount of surface Rh by the actual Rh loading determined by ICP.

3.3.12 Fourier transform infrared (FTIR) spectroscopy

FTIR spectra were acquired using a Thermo Scientific Nicolet 6700 FTIR spectrometer with a liquid-nitrogen-cooled detector. The solid samples were pressed onto the smart golden gate- ZeSe/diamond crystal. The spectra were obtained by averaging 128 scans with a resolution of 2 cm^{-1} over the wavenumbers ranging from 1000-3500 cm^{-1}.

In-situ FTIR spectra were recorded using a Thermo Scientific Nicolet 6700 FTIR spectrometer equipped with a Specac's high-temperature high-pressure cell. Spectra were obtained by collecting 32 scans with a resolution of 4 cm^{-1} and are presented in absorbance units. The catalysts were pressed into pellets and loaded onto the sample holder. The sample was then flushed with 5% H_2/Ar (20 mL min^{-1}) for 20 min and then reduced for 2 h at 290 ^oC. After the pre-reduction, the backgrounds were recorded at 50 ^oC, 100 ^oC, 150 ^oC, 200 ^oC, 250 ^oC and 290 ^oC in the atmosphere of 5% H_2/Ar. After collecting the backgrounds, a mixture of CO_2/H_2 (CO_2 : H_2 = 1 : 3) was passed through the reduced sample pellet and then the in situ FTIR spectra were collected at 50 ^oC, 100 ^oC, 150 ^oC, 200 ^oC, 250 ^oC and 290 ^oC with each temperatures maintaining for at least 30 min.

3.3.13 Raman spectroscopy

Raman spectra were recorded using a Perkin-Elmer Raman Station 400. This instrument is a bench-top spectrometer with laser excitation wavelength at 785 nm and equipped with CCD detector. Powder samples were prepared by placing the powder on a glass slide.

3.3.14 Ultraviolet-visible (UV-vis) absorption spectroscopy

UV-vis absorption spectra were taken using a Varian 100 Bio UV-Visible Spectrometer in absorbance mode in the range 200-800 nm with a step interval of 1 nm. Samples were

prepared by sonicating 2 mg of sample in 10 mL ethanol for 15 minutes before putting the sonicated solution into an optical glass cuvette. Ethanol was thus used as the reference.

3.3.15 Photoluminescence (PL) spectroscopy

For Chapter 4: Time-resolved photoluminescence (TRPL) experiments were conducted with the assistance of Dr. Wai-Ming Kwok and Dr. Chensheng Ma in Hong Kong Polytechnic University. TRPL measurements were performed with a commercial Ti:sapphire regenerative amplifier laser system (800 nm, 40 fs, 1 kHz, and 3.5 mJ/pulse). The 300 nm excitation pulse was generated from the second harmonic of the sum of the frequency generation between a one-photon absorption (OPA) output and the 800 nm fundamental laser pulse. The samples were prepared by placing drops of nanoparticle ethanol suspension onto a quartz plate and left the solvent to evaporate until a layer of the sample was deposited on the plate. TRPL signals were collected by an intensified CCD (ICCD) detector that was used to detect transient spectra with the controlled pump/probe time delay covering from ~2 ns and afterwards. All the measurements were conducted at room temperature and atmospheric pressure.

For Chapter 7: Steady-state and time-resolved PL measurements were acquired using a time-correlated single photon counting (TCSPC) setup (FluoTime 300, PicoQuant GmbH). Samples were excited using 405 nm laser pulsed at frequencies of 40MHz (for steady state measurements) and 10MHz (for time-resolved measurements). The PL was collected using a high-resolution monochromator and hybrid photomultiplier detector assembly (PMA Hybrid 40, PicoQuant GmbH).

Parameters describing the photoluminescence were obtained by fitting the background-corrected PL with a decay equation of emission intensity I(λ,t) at the time (t) and wavelength (λ) of the form:

$$I(\lambda, t) = I_0(\lambda, t = 0) \sum a_i e^{\frac{t}{\tau_i}}$$

Where τ_i is the characteristic lifetime of the i^{th} decay component, a_i is the subsequent decay amplitude, and $I_0(\lambda)$ is the emission intensity at time t=0. Errors in the fitting parameters were determined by examining the adjusted r-squares obtained by independently varying each fitting parameter.

For ease of comparison of lifetimes between each sample, the intensity weighted average lifetime is given by:

$$\tau_{avg} = \frac{\sum a_i \tau_i^2}{\sum a_i \tau_i} = \sum f_i \tau_i$$

Where f_i is the fractional contribution of each decay components and the denominator is over all amplitudes and decay times which is proportional to the total intensity[13].

3.3.16 High sensitivity-low energy ion scattering (HS-LEIS)

HS-LEIS measurements were carried out on an IonTOF Qtac100 low-energy ion scattering analyser. Ne^+ ions with a kinetic energy of 5 keV were applied at a low ion flux equal to 445 pA cm^{-2}. The surface composition was obtained from the area of the corresponding peak and calibrated with the sensitivity factors.

References

1. Li, M. M., J. Zheng, J., Q, J., Liao, F., Raine, E., Kuo, W. C., Su, S. S., Po, P., Yuan, Y. & Tsang, S. C. The remarkable activity and stability of a highly dispersive beta-brass Cu-Zn catalyst for the production of ethylene glycol. *Sci. Rep.* **6,** 4–11 (2016).
2. Chen, C., Yang, M., Wang, Q., Buffet, J.-C. & O'Hare, D. Synthesis and characterisation of aqueous miscible organic-layered double hydroxides. *J. Mater. Chem. A* **2,** 15102–15110 (2014).
3. Flahaut, E., Peigney, A., Bacsa, W. S., Bacsa, R. R. & Laurent, C. CCVD synthesis of carbon nanotubes from (Mg,Co,Mo)O catalysts: influence of the proportions of cobalt and molybdenum. *J. Mater. Chem.* **14,** 646–653 (2004).
4. Flahaut, E., Bacsa, R., Peigney, A. & Laurent, C. Gram-scale CCVD synthesis of double-walled carbon nanotubes. *Chem. Commun.* 1442 (2003).
5. García-Hevia, L., Valiente, R., Fernández-Luna, J. L., Flahaut, E., Rodríguez-Fernández, L., Villegas, J. C., González, J. & Fanarraga., M. L. Inhibition of Cancer Cell Migration by Multiwalled Carbon Nanotubes. *Adv. Healthc. Mater.* **4,** 1640–1644 (2015).
6. Joo, J., Na, H. B., Yu, T., Yu, J. H., Kim, Y. W., Wu, F., Zhang, J. Z. & Hyeon, T. Generalized and facile synthesis of semiconducting metal sulfide nanocrystals. *J. Am. Chem. Soc.* **125,** 11100–5 (2003).
7. Joensen, P., Frindt, R. F. & Morrison, S. R. Single-layer MoS_2. *Mater. Res. Bull.* **21,** 457–461 (1986).
8. Bortolamiol, T., Lukanov, P., Galibert, A. M., Soula, B., Lonchambon, P., Datas, L. & Flahaut, E. Double-walled carbon nanotubes: Quantitative purification assessment, balance between purification and degradation and solution filling as an evidence of opening. *Carbon N. Y.* **78,** 79–90 (2014).
9. Jia, T., Li, M., Ye, L., Wiseman, S., Liu, G., Qu, J., Nakagawaa, K. & Tsang, S. C. E. The remarkable activity and stability of a dye-sensitized single molecular layer MoS_2 ensemble for photocatalytic hydrogen production. *Chem. Commun.* **51,** 13496–13499 (2015).
10. Jia, T., Kolpin, A., Ma, C., Chan, R. C. T., Kwok, W. M. & Tsang, S. C. E. A graphene dispersed CdS–MoS_2 nanocrystal ensemble for cooperative photocatalytic hydrogen production from water. *Chem. Commun.* **50,** 1185–1188 (2014).
11. Thompson, S. P., Parker, J. E., Potter, J., Hill, T. P., Birt, A., Cobb, T. M., Yuan, F. & Tang, C. C. Beamline I11 at Diamond: A new instrument for high resolution powder diffraction. *Rev. Sci. Instrum.* **80,** 75107 (2009).
12. Moudler, J. F., Stickle, W. F., Sobol, P. E. & Bomben, K. D. *Handbook of X-ray photoelectron spectroscopy: A reference book of standard spectra for identification and interpretation of XPS data*. (Physical Electronics Division, Perkin-Elmer Corporation, Eden Prairie, 1992).
13. Seo, J., Fudala, R., Kim, W. J., Rich, R., Tabibi, B., Cho, H., Gryczynski, Z., Gryczynski, I & Yu, W. Hybrid optical materials of plasmon-coupled CdSe/ZnS coreshells for photonic applications. *Opt. Mater. Express* **2,** 1026–1039 (2012).

Chapter 4: Enhanced CO_2 hydrogenation to methanol over CuZn nanoalloy in Ga modified Cu/ZnO catalysts

4.1 Chapter overview

With the introduction of Ga^{3+} into Cu/ZnO catalyst precursors, a series of catalysts have been prepared using a simple co-precipitation method and tested as catalysts for the synthesis of methanol from CO_2 hydrogenation. It is found that the presence of a small amount of Ga^{3+} can facilitate thermal deep reduction of ZnO support to Zn atoms under hydrogen prior to catalysis hence a highly active CuZn bimetallic nanoparticle offering catalytic sites is generated. The effect of Ga^{3+} incorporation is attributed to the formation of Ga-containing spinel, $ZnGa_2O_4$ structure, which creates electronic heterojunction with excess ZnO phase to account for the facilitated reduction of Zn^{2+} to Zn^0 to form CuZn when in contact with Cu nanoparticle. Furthermore, HR-TEM, nano-diffraction and EXAFS characterisation reveal the presence of a small *beta*-brass CuZn alloy phase (body-centred cubic, *bcc*). In addition, a correlation between Zn^0 concentration in the CuZn alloy nanoparticle to the catalytic performance can thus be clearly demonstrated, which shows CO_2 conversion and methanol selectivity can be significantly improved by increasing the Zn^0 content in these heterojunction catalysts.

4.2 Introduction

Due to the increases in fossil fuels combustion by the increasing population and human activities, the concentration of carbon dioxide, CO_2, in the atmosphere is rising year by year, which causes a significant global warming. The present attempts to reduce the CO_2 emission, and various technologies for CO_2 capture and transformation are being paid intensive investigation. It has been recently demonstrated that by utilising solar energy, wind power, hydropower and biomass, renewable hydrogen gas can be produced at large scale[1,2]. Therefore, the recycling of 'waste' CO_2 through its hydrogenation to high-energy-content fuels such as alcohols or hydrocarbons appears to be a very attractive approach[3]. Particularly, the CO_2 hydrogenation to methanol is becoming a potentially strategic important process due to the positions of methanol as both key chemical platform and clean liquefied fuel. For sustainable development of our society, the feasibility and advantages of the methanol-based economy have recently been advocated by Olah *et al.*[4]

Cu-based catalysts are widely used for many important reactions in the chemical industry, including methanol synthesis[5–7], the water-gas shift reaction[8–10], steam reforming[11–13], and many more. Thanks to the development of the active $Cu/ZnO/Al_2O_3$ catalysts, Cu/ZnO based catalysts are well known for methanol synthesis from syngas (CO/H_2) which has attracted much attention. Recent research has reported that these catalysts also show superior activity in CO_2 hydrogenation. Cu is usually regarded as the active site but the role of ZnO support is still in debate despite the fact that numerous investigations have been carried out over the past few decades[5,14–20]. With the rapid development of advanced characterisation techniques, it is shown that a very small amount of Zn atoms is reduced from ZnO and decorate on Cu nanoparticle at the interface, which results in a subtle change in the Cu electronic structure[21–23]. Consequently, the high activity is assigned to the formation of this CuZn alloy in contact

region[6]. It is, however, the mechanism for the deep reduction of support metal ions to corresponding metal atoms is still obscure. On the other hand, it is reported the incorporation of different additives, such as Al_2O_3, ZrO_2, SiO_2, and Ga_2O_3 can further improve the activity, stability and thermal resistance compared with the unmodified Cu/ZnO[6,7,24–27]. Recently, using atom probe tomography technique, small, active but stable Cu containing crystallites (~0.5–2 nm) were identified in the working catalyst prepared from Ga^{3+} promoted Cu/ZnO[28–30]. The formation of $ZnGa_2O_4$ spinel structure was believed to play a significant role in the generation of the extremely small Cu clusters under methanol synthesis conditions. However, the promotion mechanism of Ga^{3+} and the nature of active site for the CO_2 hydrogenation are still not yet clear due to some complex solid-solid interaction(s).

On the other hand, semiconductor materials such as ZnO and $ZnGa_2O_4$ usually play a critical role in catalysis reactions since many working catalysts involve the use of semiconductor component(s), particularly in the form of a metal oxide(s) as support. The catalytic properties of semiconductor are strongly related to its band structure which can be well-tuned by several methods: Doping, heterojunction, hybridisation, morphology control, etc.[31,32] Introducing another semiconductor modifier to establish a heterojunction with a specific energy level alignment is one of the simplest methods for structure tuning, due to a wide range of choices of modifiers and well-acquired skills for their syntheses. There are at least three types of heterojunctions, especially, type-II, where the band gaps of two semiconductors are similar but not at the same band energy positions (as staggered bands) is found to be important in catalysis[33–36]. As to this type-II heterojunction, the electrons and holes are spatially separated across the interface during excitation and are localised on different sides of the hetero-interface. Thus, the polarisation of two carriers over the two semiconductor materials at the interface is taken place. This allows more involvements of

these carriers in catalysis processes before their recombination. As a result, some novel properties are usually observed in type-II heterojunction compared with other junctions.

$ZnGa_2O_4$ is a well-known photocatalyst component with wide proposed applications in water splitting and pollutant removal[37]. The integration of ZnO and $ZnGa_2O_4$ forming type-II heterojunction was also reported to show enhanced photocatalytic activity compared to the individual components. The enhancement is mainly attributed into the separation of holes and electrons across the interface upon light excitation[37–39], however, the application of this type-II heterojunction in thermal catalysis reaction like the present methanol synthesis reaction from CO_2 hydrogenation has not been reported. In this chapter, the preparation of a Cu/$ZnGa_2O_4$-ZnO mixture by the introduction of Ga^{3+} into Cu/ZnO is demonstrated. It is shown that Ga^{3+} can readily react with ZnO to form $ZnGa_2O_4$ spinel structure, which thus forms $ZnGa_2O_4$-ZnO heterojunction with excess ZnO where Cu nanoparticles are dispersed upon hydrogen reduction. With the presence of Ga^{3+} in form of heterojunction, the thermal reduction of ZnO to Zn^0 atom is significantly facilitated. As a result, small CuZn bimetallic nanoparticles are thus generated on the surface of these mixed support phases during the reaction. Importantly, the concentration of Zn^0 in the bimetallic phase is tunable by controlling the amount of Ga^{3+} used in the synthesis. It is also demonstrated that Cu based catalyst with Zn enrichment through the use of heterojunction shows a pronounced enhancement in methanol synthesis from CO_2 hydrogenation reaction.

4.3 Results and discussion

4.3.1 Formation of CuZn bimetallic alloy facilitated by heterojunction

With the introduction of Ga^{3+} into Cu/ZnO catalyst, a series of catalysts have been prepared using a simple co-precipitation method with carefully control of precursor injection rate, pH

value and precipitation temperature, see Figure 3-1 and Table 3-1 of Chapter 3, for the synthesis details. Figure 4-1 shows the H_2-TPR results of the CZ (without adding Ga) and CZG samples. It can be noticed that the reduction of CuO to Cu occurred at a lower temperature when the sample was doped with Ga^{3+}, which indicates the facilitation of the reduction when Ga was incorporated. In addition, the presence of H_2-TPR shoulder peak for the sample with Ga^{3+} content indicates the reduction of Cu^+ is detected. According to the previous report[28], it has been proposed that Ga incorporation into Cu/ZnO can lead to the formation of a cubic spinel phase containing interstitial Cu^+ ions on a defective $ZnGa_2O_4$ surface, which can produce a high population of extremely small copper clusters upon their further reduction for effective catalysis. The physical characterisations of selected CZ and CZG catalysts show that Ga-containing sample (CZG-5Ga, 85 m^2g^{-1}) gives higher specific surface area per gram of catalyst than the unmodified Cu/ZnO sample (CZ, 58 m^2g^{-1}). The Cu surface area per gram of catalyst (SA_{Cu}) can also be found to follow the order: CZG-5Ga (63 m^2g^{-1}) > CZG-20Ga (53 m^2g^{-1}) > CZ (43 m^2g^{-1}), suggesting the addition of Ga into Cu/ZnO system can improve the dispersion of Cu due to the presence of Ga-containing cubic spinel phase which helps the formation of small Cu clusters. This result is in agreement with the findings by Schumann *et al.*[40], who have found that Ga dopant could act as a structure promoter, which would lead to the high surface area for the Cu catalysts and shows promoted performance in the methanol synthesis condition. In the current study, with the addition of Ga^{3+}, the Cu/ZnO catalysts also show enhanced Cu dispersion, which may lead to a better performance for those Ga-containing samples in CO_2 hydrogenation to produce methanol.

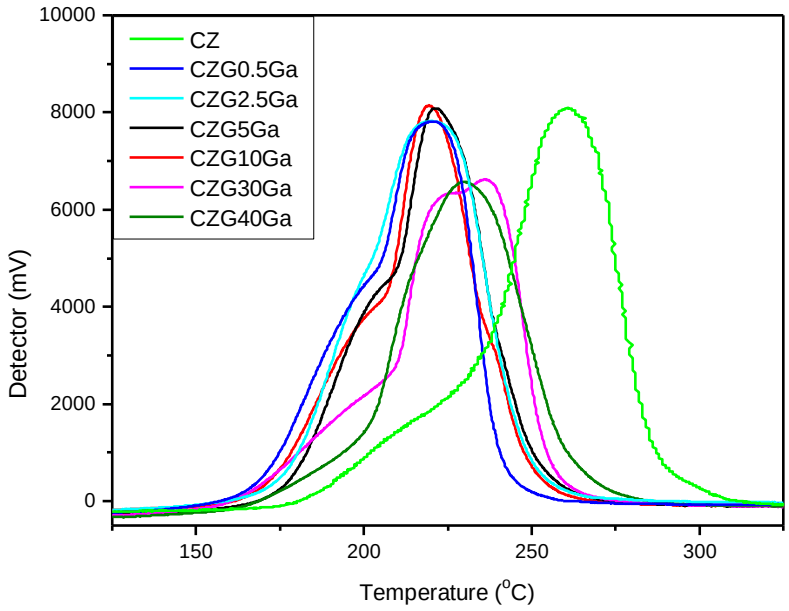

Figure 4-1. TPR profiles of calcined CZ and CZG catalysts with different chemical compositions.

From the XRD patterns of the calcined sample without the addition of Ga (Figure 4-2a, CZ), phases of CuO, ZnO, are clearly identified. With the progressive Ga addition, a spinel phase of MGa_2O_4 (M = Zn, Cu) was emerged in excess ZnO when Ga was over 5% and then dominated the crystallite phases when Ga concentration was higher than 10% (Figure 4-2a). The MGa_2O_4 (M = Zn, Cu) spinel phase observed in our calcined catalysts is a well-known semiconductor phase[37]. The integration of ZnO and MGa_2O_4 spinel forming type-II electronic heterojunction was also reported to improve the charge separation and enhance catalytic activity compared to the individual components[38,39]. Based on such heterojunction approach, it has been reported that the thermally activated reduction of the refractory metal oxide support could be strongly promoted, which facilitates the formation of bimetallic catalysts with enhanced catalytic performance[36]. Therefore, with the great potentialities of

type-II heterojunction effects in our Ga-containing samples, it is logical to anticipate the reduction of ZnO can be facilitated with the help of the MGa_2O_4 and ZnO interfaces, which may promote the production of CuZn bimetallic catalyst and alter the catalytic performance of the Cu/ZnO catalysts. Considering CZG-5Ga sample showed ZnO and MGa_2O_4 as the most prevalent phases than that in other samples, CZG-5Ga was selected to calcine under different temperatures to see the influences of the calcination conditions (XRD is shown in Figure 4-2b). As can be seen in Figure 4-2b that CZG-5Ga is initially in the form of $(Cu, Zn)_5(CO_3)_2(OH)_{16}$, known as aurichalcite phase, with high dispersion of Ga. With the increasing of calcination temperature, MGa_2O_4 could be observed at 330 ^oC, but this phase decomposed into ZnO and CuO phases along with a small amount of Ga_2O_3 (not detected in XRD) as the temperature further raising. From our XRD result, the co-existence of ZnO and the spinel phase can be clearly observed in some CZG samples. Moreover, the relative amounts of these two phases will vary with the synthesis conditions, suggesting that some experimental variables could influence their interfaces and characteristics.

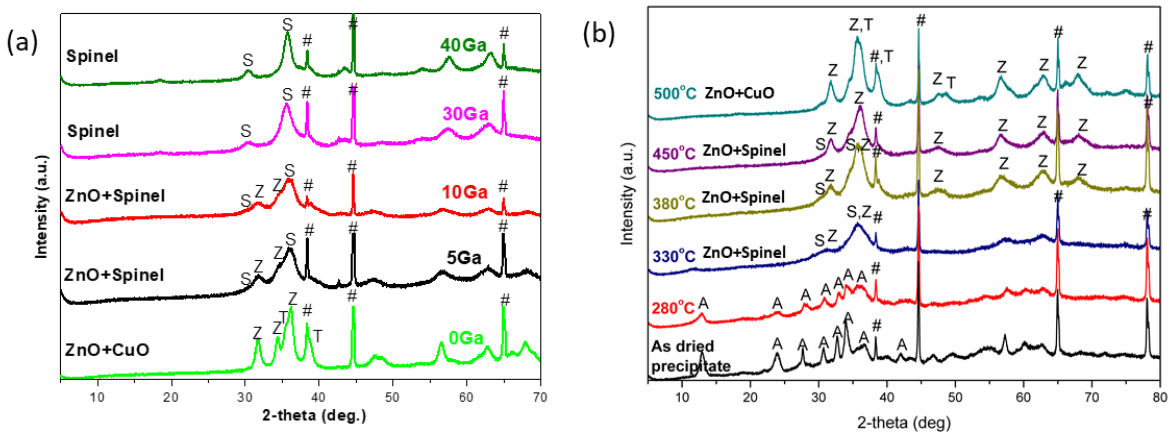

Figure 4-2. XRD profiles of calcined CZG catalyst with various (a) chemical compositions (all calcined 330 ^oC); (b) calcination temperatures (CZG-5Ga sample). (# peaks from Al holder; S: spinel phase; T: tenorite CuO phase; Z: zincite ZnO phase).

It is clear that two semiconductor solid phases, namely, ZnO and spinel structure (MGa_2O_4) can co-exist under our preparation method. In order to reflect the quantity of the ZnO-MGa_2O_4 interfaces, electron energy loss spectroscopy (EELS)-TEM was employed. The EELS elemental mappings for Cu, Zn, Ga and O in the CZG catalysts with varied calcination temperatures are shown in Figure 4-3 (left). The brighter area indicates the relatively higher pixel density of a particular element. In order to characterise the interface of the two phases (ZnO and Ga-containing phases (MGa_2O_4)), differentiation of the EELS digitalised signal ratios of Zn ($Zn_{L2,3}$, 1020 eV) to Ga ($Ga_{L2,3}$, 1115 eV) scanning along a certain region for each sample are displayed in Figure. 4-3 (right). There are stable flat plateau regions with sharp peaks occasionally observed, and the sharp peaks are caused by the drop in Ga concentration from Ga-containing phase to ZnO rich phase. The regions with higher peak frequency within the scan range represent a larger quantity of ZnO-MGa_2O_4 interfaces along the scanned area. From the result, the 330 ^oC sample gives more peaks than all the other samples, indicating the 330 ^oC sample gives the largest amount of interfaces between ZnO and the Ga-containing spinel phase. From the results of XRD and EELS-TEM elements mapping, it is concluded that the amount of ZnO-MGa_2O_4 interface can be optimised at 330 ^oC calcined GZG-5Ga sample from the samples synthesised with the variation of chemical composition and calcination temperature.

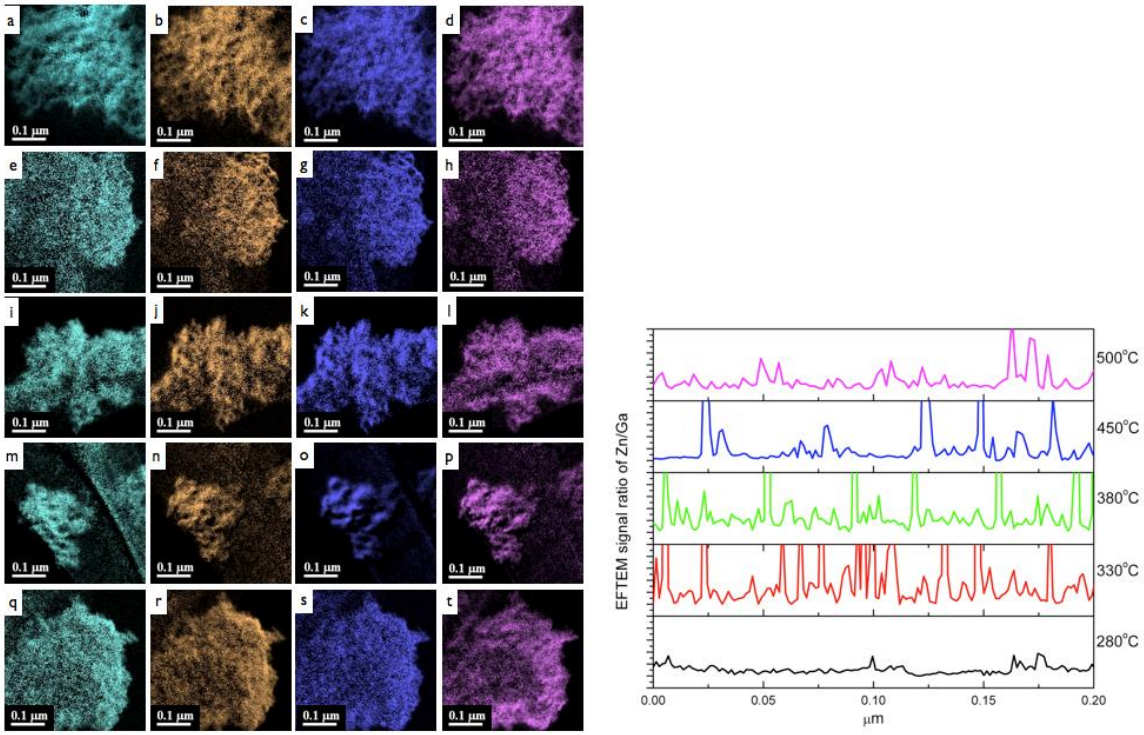

Figure 4-3. Left: EELS-TEM mappings of Cu (a,e,I,m,q), Zn (b,f,j,n,r), Ga (c,g,k,o,s), and O (d,h,i,p,t) for sample 280 ºC (a,b,c,d), 330 ºC (e,f,g,h), 380 ºC (i,j,k,l), 450 ºC (m,n,o,p), and 500 ºC (q,r,s,t); Right: Differential EELS-TEM digital signal ratios of Zn:Ga along a scanning region for 280 ºC, 330 ºC, 380 ºC ,450 ºC, and 500 ºC samples.

From CZ to CZG-5Ga, with the addition of a small quantity of Ga, the energy levels alignment in the catalyst is transformed from type-I (CuO-ZnO) heterojunction to type-II (MGa_2O_4-ZnO), as shown in Figure 4-4 according to their reported bulk energy levels[38,39]. In the CuO-ZnO system, the carriers would thus be confined on the surface of CuO upon thermal excitation. After adding Ga^{3+}, with the formation of the MGa_2O_4 spinel structure, the thermal excited electrons and holes, although in very small quantities, can be separated across the heterojunction interfaces (holes on MGa_2O_4 and electrons on ZnO)[38,39]. Due to

this spatial separation of excitons, the lifetime of the carriers in GZG-5Ga is expected to increase.

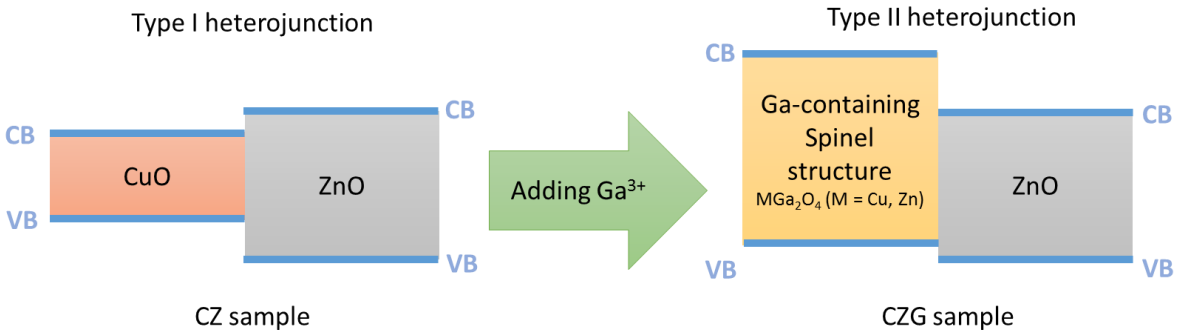

Figure 4-4. A schematic illustration of energy levels alignments of the CZ and CZG samples, where the band edges are positioned according to the reported bulk energy levels[38,39].

To confirm the enhanced lifetime for the charge carriers in this system, time-resolved photoluminescence (TRPL) measurement was conducted with a 300 nm light excitation source for the CZ and CZG-5Ga samples (both were calcined at 330 ^{o}C) to further investigate the influence of the type-II heterojunction. It is noted that light excitation is more efficient than thermal means hence it is easier to follow the TRPL at higher charge carrier concentration. Figure 4-5a gives the temporal changes of emission spectra recorded for the samples. Both samples exhibit broad emissions (with λ_{max} ~580 nm) that decay within hundred nanoseconds after the excitation. Figure 4-5b shows the experimental decay profiles derived from the integration of the TRPL. The curves are fitted using a multi-exponential function to obtain the time constants (τi) and associated fractional contributions (ai%). As seen in Table 4-1, the fractions of the long-lived components (a2, a3) in CZG-5Ga sample

are indeed higher than that in the CZ sample, which implies the increased fraction of non-instant recombination of the carriers in CZG-5Ga by the formation of type-II heterojunction. Moreover, the lifetimes of these long-lived components in CZG-5Ga sample (21, 150 ns) are significantly longer than those of CZ sample (20, 130 ns). Therefore, from the TRPL result, it is clear that the type-II heterojunction of ZnO-MGa_2O_4 in CZG-5Ga sample enhances the spatial separation of excited electrons and holes across the interface which reduces the rapid instant recombination and prolongs their lifetime.

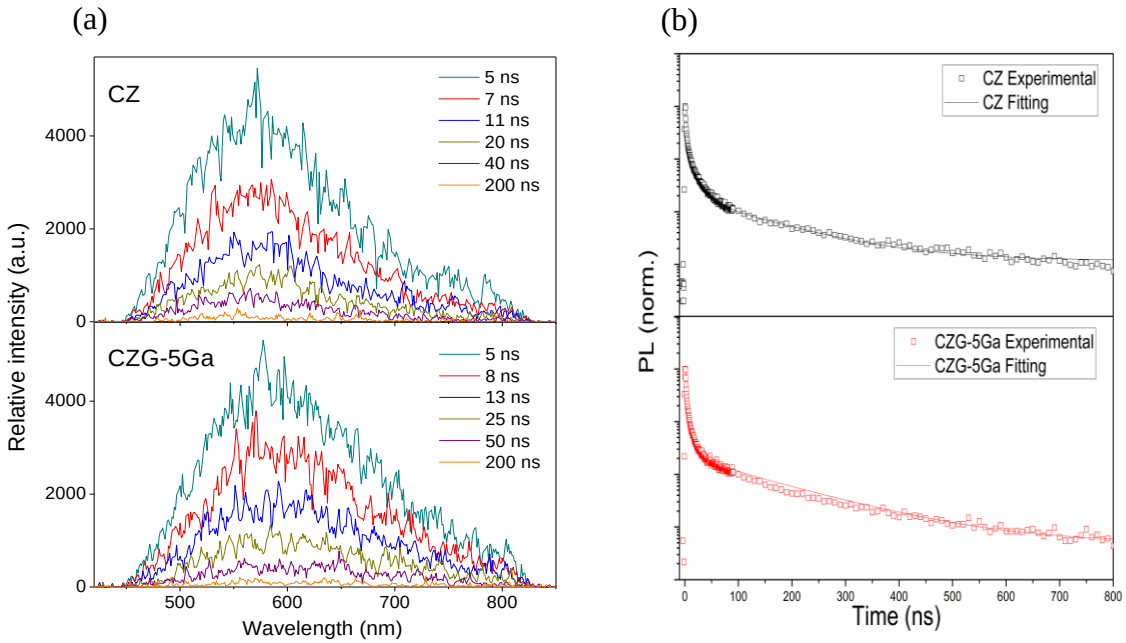

Figure 4-5. (a) the temporal changes of emission spectra with 300 nm excitation recorded for CZ and CZG-5Ga samples; (b) experimental and fitted kinetic decay profiles obtained from integrated intensity of the time-resolved emission spectra of CZ and CZG-5Ga samples.

Table 4-1. Exponential decay components of fractional emission amplitudes of CZ and CZG-5Ga samples

Sample	τ1 (ns)	a1 (%)	τ2 (ns)	a2 (%)	τ3 (ns)	a3 (%)
CZ	5	85.9	20	12.5	130	1.6
CZG-5Ga	3	80.4	21	14.5	150	5.1

As a typical semiconductor oxide, some thermal- or photo-excited electrons could momentarily overcome the forbidden band gap and occupy the higher energy conduction band which is primarily composed of empty bands of cations. The corresponding 'holes' will take residence in the lower energy valence band that is constituted mainly by occupied p-bands of oxygen ions. Thus, the term 'hole' in semiconductor oxide can be appreciated chemically as *activated oxygen species* with lower formal charge (neutral or singularly charged oxygen) than lattice oxygen ions. However, the majority of the excited electrons and holes (excitons) will recombine rapidly in the single-phase semiconductor oxide support with short lifetime as reflected by the TRPL data. On the other hand, with the establishment of type-II heterojunction of ZnO-MGa_2O_4, particularly in CZG-5Ga (calcined at 330 ^oC), more activated oxygen species and electrons are accumulated in MGa_2O_4 and ZnO contact region, respectively, as indicated by the increased fractions of long-lived components in TRPL. In the H_2 pre-treatment process, these activated oxygen species (holes) could then react with spilt H in a proximity to Cu metal nanoparticle to form water as their long lifetime allows the occurrence of this chemical reaction. Thus, corresponding electrons in ZnO region will reduce Zn^{2+} from the support mixture to Zn atoms.

The XPS spectra were collected and analysed. The raw data were corrected for substrate charging with the BE of the C peak (285 eV). We did not see any evidence of the existence of metallic Ga (mainly Ga^{3+} was detected). It is noted that Nørskov and co-workers have recently shown Ni-Ga alloy catalysts are also effective for methanol synthesis from CO_2/H_2[41], in which the Ga-rich sites can activate methanol formation, however, this is not applicable in our case as metallic Ga is not detected in the CZG samples. On the other hand, there appeared to have a reduction of ZnO to metallic Zn atoms. The XPS Zn $2p_{3/2}$ peaks of the reduced samples with various amount of Ga content and calcination temperature are revealed in Figure 4-6a and 4-6b. They clearly show that Zn $2p_{3/2}$ peaks can be deconvoluted into two peaks of Zn^{2+} (1022.5 eV) and Zn^0 (1021.5 eV). According to the peak area of signals, the Zn^0/Cu ratios were calculated and presented in Figure 4-6c and 4-6d. Clearly, the Zn^0/Cu values reach the peaks at GZG-5Ga calcined 330 ^oC sample, indicating the highest concentration of Zn^0 present in this sample, which is resulted from the highest amount of ZnO-MGa_2O_4 type-II heterojunction interfaces as characterised by XRD and EELS-TEM. On the other hand, the lowest ratio of Zn^0/Cu in CZG-40Ga was attributed to the single phase of spinel structure in the support as indicated by the XRD result (Figure 4-2). In order to obtain the accurate composition information of the topmost surface of the catalysts, high sensitivity low-energy ion scattering (HS-LEIS) measurements using Ne^+ as the gas ion beam were also applied. Figure 4-7 with an inserted table shows the HS-LEIS result of CZ sample and CZG-5Ga sample. The XPS result for each sample is presented as a comparison. As seen from Figure 4-7, CZG-5Ga contains a higher concentration of Zn species on the outmost surface compared to the CZ sample, which further confirms the surface enrichment of Zn by the promotion of type-II heterojunction. With the combined results of XPS, HS-LEIS with XRD and TEM mapping, it is clearly established that the addition of an appropriate amount of Ga^{3+} promotes the formation of ZnO-MGa_2O_4

heterojunction interfaces which play a key role in facilitating the reduction of ZnO to Zn^0, as shown in Figure 4-8. Therefore, the optimal Zn^0 reduction point is located in the catalyst mixture with most prominent heterojunction effect (5% Ga^{3+} and 330 ºC calcination temperature).

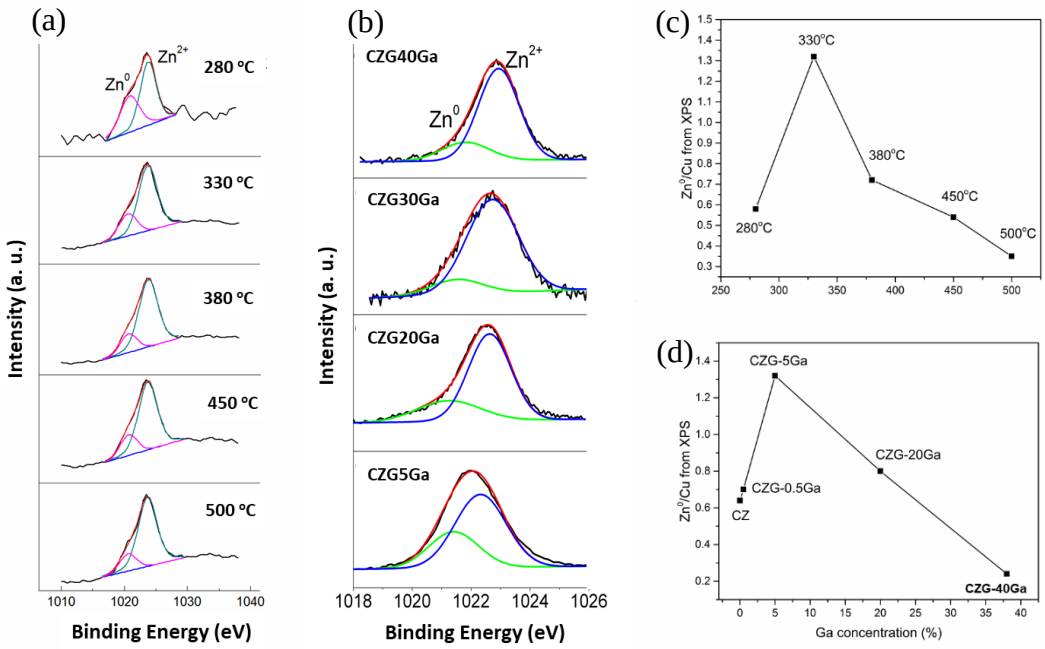

Figure 4-6. XPS Zn $2p_{3/2}$ peaks of (a) the CZG-5Ga with 280 ºC, 330 ºC, 380 ºC, 450 ºC, and 500 ºC calcination temperature and (b) the samples with various Ga concentration; the plots of Zn^0/Cu ratios derived from XPS analysis to various (c) calcination temperature and (d) Ga concentration.

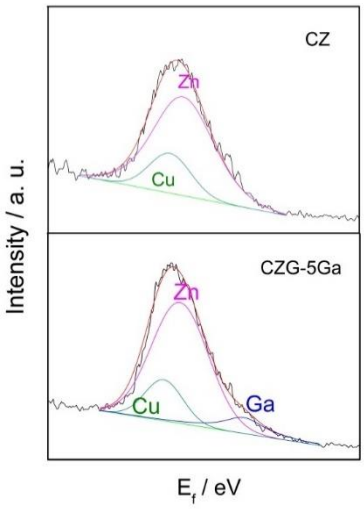

Catalyst	Method	Zn/Cu atomic ratio
CZ	HS-LEIS	3.72
	XPS	3.46
CZG-5Ga	HS-LEIS	4.42
	XPS	4.14

Figure 4-7. HS-LEIS at 5 keV Ne^{+} and the list of Zn/Cu ratios from XPS and HS-LEIS for CZ and CZG-5Ga samples.

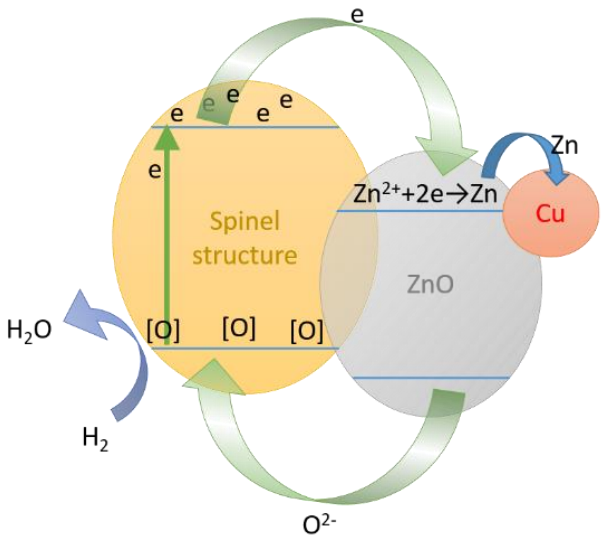

Figure 4-8. The electron flow circle in the reduction process of ZnO to Zn^{0} to form Cu-Zn alloys catalysed by ZnO-$ZnGa_2O_4$ heterojunction.

4.3.2 Structural investigation of CuZn alloy

Given the intimate interface of Zn-containing phase and Cu-containing phase in the materials, the produced Zn^0 will decorate or react with the Cu nanoparticle to form bimetallic nanoparticles. To further confirm the incorporation of Zn^0 into the nano Cu lattice, extended X-ray absorption fine structure (EXAFS) of Cu was studied. This technique explores the local structural information of the Cu atom. The experimental data for the reduced CuZnGa samples were recorded and satisfactory R fittings were achieved, as can be seen in Table 4-2 and Figure 4-9. It was found that the spectra of most of the catalysts in the present work could not be well modelled using only scattering parameters from metallic *fcc* Cu. Therefore, a mixed-structure model is introduced and it is found that the combination of both *fcc* metallic Cu and *bcc* CuZn alloy structures give significantly improved fits to the experimental spectra. The EXAFS were fitted using scattering paths of Cu-Cu (2.56 Å) from metallic *fcc* Cu model, Cu-Zn (2.56 Å) and Cu-Cu (2.99 Å) from *bcc* Cu-Zn alloy model. Note that the longer distance of Cu-Cu (2.99 Å) in the *bcc* Cu-Zn structure is distinctive from the shorter Cu-Cu (2.56 Å) of the *fcc* Cu model and Cu-Zn (2.56 Å) of the *bcc* Cu-Zn model. As shown in Table 4-2, all R-factors are below 0.8% with the coordination number (CN) of the Cu-Zn bond (derived from 2.56 Å scattering path) ranging from 6 to 9. As for the CN(Cu-Cu), derived from 2.99 Å scattering path, it can be seen that the CZG5Ga sample had the highest CN of *bcc* Cu-Cu bond, thus indicates the highest concentration of *bcc* Cu-Zn alloy. We also found that the order of the samples according to the *bcc* CuZn concentration is consistent with that to the concentration of Zn^0/Cu observed from the XPS result (Figure 4-6). In addition, no Cu-Cu bond of 2.99 Å was observed in the 500 ^oC-calcined sample which suggests that no *bcc* CuZn alloy was formed during the reduction procedure if the CuZnGa precursor has been calcined at elevated temperature. The EXAFS

confirmed the existence of *bcc* CuZn alloy in most of our samples, especially those with higher Zn^0 concentration, i.e., CZG5Ga gives the highest quantity of *bcc* CuZn alloy.

Table 4-2. EXAFS of CuZnGa samples of various calcination temperatures and chemical compositions

Sample	**Enot***	**CN (*bcc* Cu-Zn & *fcc* Cu-Cu)**	**DW-factor (Cu-Zn & *fcc* Cu-Cu)**	**Bond length (Å) (Cu-Zn & *fcc* Cu-Cu)**	**CN (*bcc* Cu-Cu)**	**DW-factor (*bcc* Cu-Cu)**	**Bond length (Å) (*bcc* Cu-Zu)**	**R-factor**
CZ	3.4	8.8 (3)	0.009 (1)	2.54 (1)	None	None	None	0.8%
CZG5Ga-280 ºC	4.2	6.9 (4)	0.012 (1)	2.55 (1)	1.1 (4)	0.013 (5)	2.96 (3)	0.8%
CZG5Ga-330 ºC	0.5	7.5 (4)	0.010 (1)	2.54 (1)	1.8 (6)	0.014 (3)	2.94 (1)	0.5%
CZG5Ga-380 ºC	4.7	7.6 (4)	0.011 (1)	2.54 (1)	1.0 (5)	0.014 (5)	2.98 (4)	0.8%
CZG5Ga-450 ºC	4.2	6.4 (3)	0.010 (1)	2.54 (1)	0.6 (3)	0.011 (5)	3.03 (4)	0.7%
CZG5Ga-500 ºC	4.5	9.3 (3)	0.010 (1)	2.54 (1)	None	None	None	0.4%
CZG20Ga	1.5	7.3 (2)	0.008 (1)	2.54 (1)	1.0 (4)	0.013 (4)	3.00 (3)	0.4%
CZG40Ga	3.1	8.2 (2)	0.009 (1)	2.54 (1)	0.6 (1)	0.003 (2)	3.01 (2)	0.4%

*Enot is the energy difference of absorption energy in experimental value and calculated value.

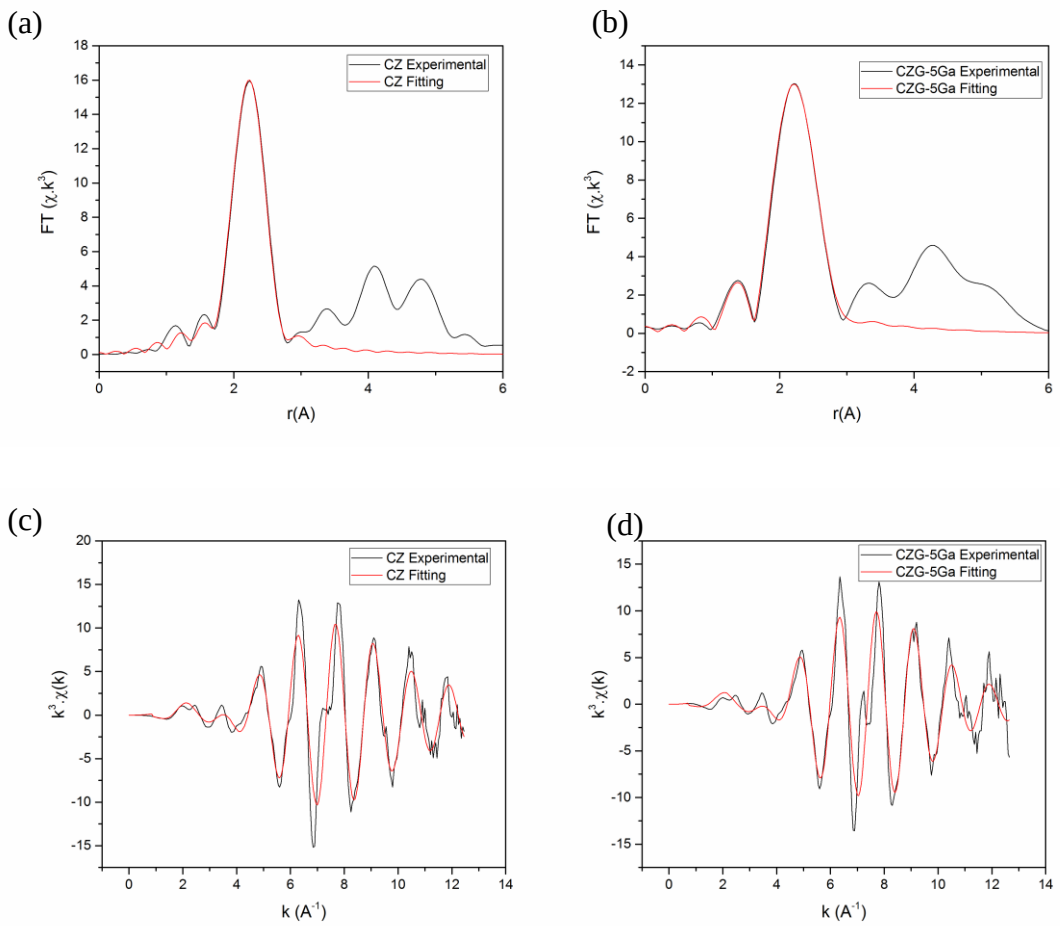

Figure 4-9. EXAFS plots of (a) $k^3.\chi$ Fourier transform of experimental and fitted data for CZ; (b) $k^3.\chi$ Fourier transform of experimental and fitted data for CZG; (c) $k^3.\chi$ experimental and fitted data for CZ; (d) $k^3.\chi$ experimental and fitted data for CZG.

The identification of *bcc* CuZn alloy is rather challenging due to the comparable properties (atomic size, crystalline structure, etc.) in Cu and Zn atoms. By using EXAFS technique, we have determined the presence of body-centred CuZn alloy in the reduced CZG5Ga sample. It is known that in the Cu-Zn system, when the Zn concentration is high enough (>50% in bulk system), the CuZn alloy tends to change the structure from face-centred cubic (*fcc*) to body-centred cubic (*bcc*)[42]. In our EXAFS result, we have identified the presence of high Zn-containing CuZn structure (*bcc* CuZn), suggesting that with the promotion of

heterojunction effect, the reduced Zn^0 is abundant in the vicinity of Cu atoms, which stabilises the *bcc* CuZn alloy. To further confirm the presence of *bcc* CuZn alloy, the HR-TEM and HR-STEM analysis of CZG5Ga, the sample with the highest Zn^0/Cu ratio, was performed, see Figure 4-10 and 4-11. Close examination of the selected area of the diffraction rings, Figure 4-10e and 4-10f clearly indicates a mixture of phases (Cu, ZnO, CuZn phases) in the reduced sample. Through lattice fringes analysis of the HR-TEM images, see Figure 4-10a to 4-10d, there is a straightforward evidence of the formation of the *fcc* Cu (may contain Zn as *fcc* CuZn with same lattice parameter) and *bcc* CuZn. Figure 4-11 shows the HR-STEM images of the reduced CZG5Ga (Figure 4-11a to 4-11c) and CZ (Figure 4-11d to 4-11f) samples, and their corresponding fast-Fourier Transform (FFT) analyses of the selected areas. As shown in Figure 4-11b, the pattern in area 1 is indexed to the *bcc* CuZn alloy whereas that in area 3 (Figure 4-11c) indicates the presence of an *fcc* structure, which could be *fcc* metallic Cu or *fcc* CuZn alloy. On the other hand, only *fcc* CuZn alloy can be found in the reduced CZ sample (see Figure 4-11e and 4-11f), presumably due to the relatively low content of Zn^0 in this sample, which is also depicted by XPS (Figure 4-6) and HS-LEIS (Figure 4-7) mentioned earlier in this chapter.

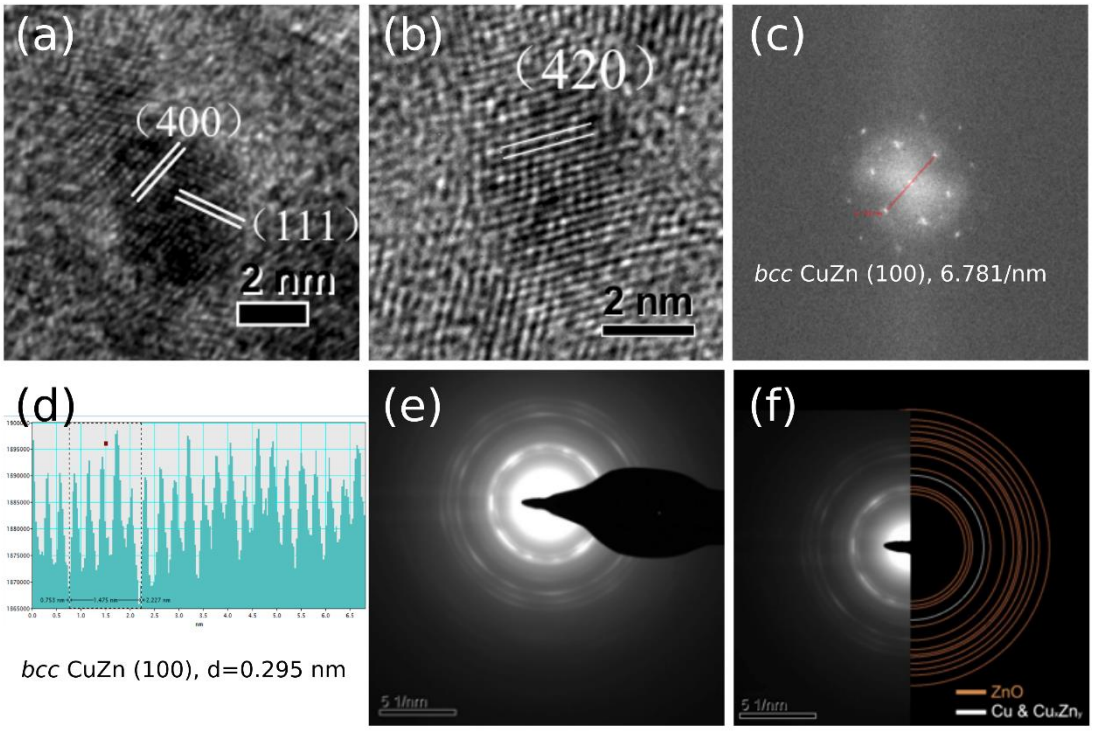

Figure 4-10. Structural analysis of the reduced CZG5Ga sample: (a) and (b) HR-TEM showing (400), (420) *bcc* CuZn and (111) *fcc* Cu(Zn) nanoparticle; (c) nano-diffraction of selected *bcc* CuZn phase and (d) bcc CuZn (100) phase of d=0.295 nm; (e) selected area of diffraction rings; (f) diffraction rings matching well with simulated Braggs' diffractions of mixed phases containing Cu, ZnO and *bcc* CuZn phases.

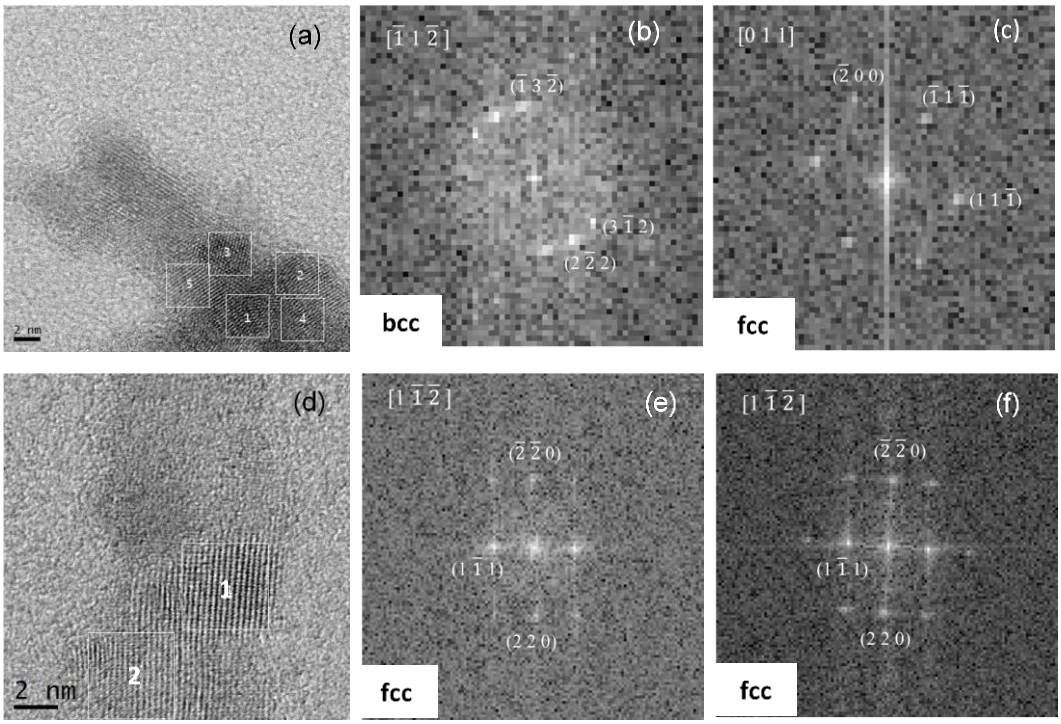

Figure 4-11. High-resolution STEM image of the small regions in the reduced CZG5Ga sample (a), and the fast-Fourier transform (FFT) patterns of area 1 (b) and 3 (c) in (a); the reduced CZ sample (d), and the fast-Fourier transform (FFT) patterns of area 1 (e) and 2 (f) in (d).

4.3.3 CO_2 hydrogenation to methanol over CZG catalysts

To investigate the influence of Zn^0 concentration, the reaction of CO_2 hydrogenation to synthesise methanol was performed. Figure 4-12 shows CO_2 conversion, methanol selectivity and methanol yield of the CZ and CZG samples under different reaction temperatures. In general, CZG5Ga shows better performance than all the other samples. The methanol yield reaches the optimal value at 290 ^oC and drops with further increasing temperature, which suggests the approach of the thermodynamic limit. Therefore, the results obtained at 290 ^oC for the series of CZG samples with various Ga additions were selected

and presented in Figure 4-13 to compare with each other. Interestingly, all the catalysts show a comparable CO_2 conversion but the selectivity follows the order of CZ < CZG-40Ga < CZG30Ga < CZG10Ga < CZG5Ga (Figure 4-13). It is noted that CZG5Ga has the highest Zn^0/Cu ratio determined by the XPS analysis. The generation of the active Zn-rich CuZn alloys is promoted by the addition of Ga^{3+} that can facilitate the deep reduction of ZnO with the help of heterojunction formation. From CZ to CZG5Ga, the methanol yield is raised up by nearly 3%. On the other hand, CZG-40Ga with only pure MGa_2O_4 spinel phase as the support (no heterojunction effect) has the least amount of Zn^0. Therefore, its concentration of the active species is reduced due to the increasing of non-active Ga^{3+} species, which results in the least methanol production rate. By controlling the content of Ga addition, different phase mixture in the catalysts can be obtained. This result suggests that the formulation of the solid phases greatly affects the number of solid interfaces and the nanostructure of the Cu catalysts, which alter the catalytic performance of CO_2 hydrogenation.

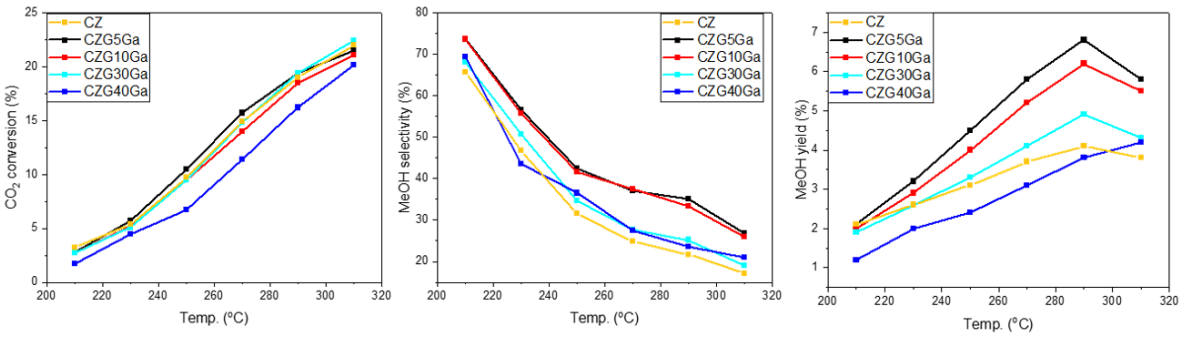

Figure 4-12. Conversion, selectivity and yield for CZ and CZG samples prepared with various chemical compositions (all calcined at 330°C) of CO_2 hydrogenation to methanol.

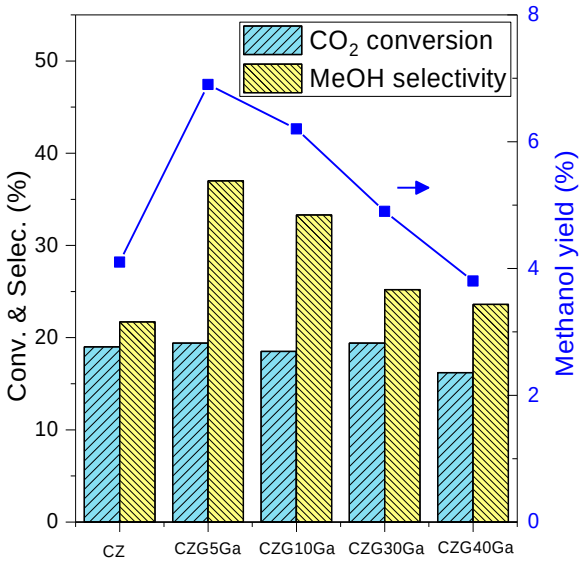

Figure 4-13. Catalytic performances of CZ and CZG samples prepared with various chemical compositions (all calcined at 330 ^{o}C) under CO_2 hydrogenation reaction condition of 290 °C.

4.3.4 Discussion

Although it is widely accepted that the presence of ZnO increases the activity of Cu catalysts towards methanol synthesis from extensive experimental works, the nature of the material interaction(s) and the 'active site' are still under debate. As a result, the enhancement of the activity of Cu by ZnO is crudely assigned to so-called 'strong metal-support interactions' (SMSI)[43–45] with no specificity in the interaction. There have been many proposals to account for this effect, which includes the textural contribution of ZnO to disperse Cu particles[28–30] and the formation of low coordinate Lewis acid Zn sites to assist dihydrogen activation[46]. Similarly, the effect of Ga to promote the catalytic performance of Cu/ZnO for methanol synthesis is not yet known despite the fact that Ga dopant is generally well known to promote hydrogenation reactions. Proposed mechanisms include its improvement of Cu

dispersion[40], facilitation of Ga_2O_3 to stabilise Cu^0/Cu^+ [47], Lewis acid Zn/Ga sites to assist dihydrogen activation[48,49] and the electronic promotion to Cu[50], etc.

Indeed, according to Schumann *et al*.[40], they have found a strong electronic effect of Ga in promoting Cu/ZnO catalysts in reverse water-gas shift (RWGS) reaction. However, for the methanol synthesis, they attributed the main effect of adding Ga dopant as a structure promoter (increase the surface area and the dispersion of Cu). Under reaction conditions of 20 bar, H_2/CO_2 = 3/1, Toyir *et al*.[47] found 99.5% selectivity can be achieved over their Ga promoted Cu/ZnO catalysts. With taking the RWGS equilibrium into account, (finely divided Cu metal particle is an excellent catalyst for RWGS) this selectivity appears to be unexpectedly high. This may relate to the difficulties in the actual gas analysis at their very low conversions (2% to 5%). Nevertheless, they attributed the high performance to the presence of Ga_2O_3 particles at the surface of Cu-ZnO-Ga_2O_3/SiO_2, which stabilised Cu^0/Cu^+ catalysis. However, the precise effect of Ga_2O_3 and the mechanism on activity promotion were not specified. Kazansky and co-workers argued that the low coordinated reduced Ga ion, as similar to Zn ion, may provide active Lewis acid sites to assist the activation of hydrogen[48,49]. Moreover, the recent observation by Martin *et al*.[50] on unusual conductivity ZnO under the reactions conditions is intriguing, which may suggest a strong electronic promotion to the Cu in the catalyst mixture.

In the rich context of the above literature for the Zn/Ga promotion effects on Cu in methanol, we did not discount the structural contribution made by the Ga dopant. In fact, we have shown the enhancement in the dispersion of Cu with Ga promotion. As a result, the textural contribution to Cu/ZnO in the Ga incorporation appears to play a role in the activity promotion. More importantly, Behrens *et al*.[6] have recently used advanced characterisation

techniques to demonstrate a very small amount of reduced Zn atoms from ZnO, which decorated on Cu nanoparticle at the interface resulting in a subtle change in Cu electronic structure. They assigned the active sites as Cu steps decorated with Zn atoms by the DFT calculations. From our present catalytic results, we can see a correlation of catalytic performance to the concentration of Zn^0 on the surface of Cu (higher Zn^0/Cu ratio, better catalytic performance) due to electronic interactions between catalytic components. Thus, we believe it is timely, to re-emphasise the electronic interactions of Ga promoted Cu/ZnO catalysts for this industrial important reaction. The dramatic enhancement in electronic conductivity of ZnO under reactions conditions as observed by Martin *et al*.[50] could support the fact that a high degree of reduction of ZnO to Zn, which subtly changes the concentration of fundamental species (vacancies and interstitials) in ZnO. Thus, such transformation of ZnO to conductive phase in the presence of gallium is consistent with our proposed heterojunction effect as described in this study.

4.4 Chapter conclusion

This study shows the significant influences by the incorporation of Ga^{3+} into Cu/ZnO catalysts. Apart from the structural promotion provided by Ga^{3+} species, our results clearly indicate that the introduction of Ga^{3+} into Cu/ZnO catalyst precursor facilitates the deep reduction of ZnO support to Zn^0 by the establishment of electronic heterojunction of ZnO-MGa_2O_4 (M = Zn or Cu). The reduced Zn^0 when in contact with Cu nanoparticle can form CuZn with high Zn^0 content, which is confirmed by EXAFS and HR-STEM techniques. It is found that the increase of Zn^0 concentration in the catalysts can enhance the catalytic performance of the reaction of methanol synthesis from CO_2 hydrogenation. Both selectivity and yield toward methanol synthesis are dramatically improved after adding an appropriate amount of Ga^{3+} into Cu/ZnO system, which results in a pronounced type-II heterojunction

effect. As stated in the introduction, the recent paper of Behrens *et al*. and their further DFT works clearly suggest that alloying of Zn into the Cu step further increases the adsorption strength of HCO, H_2CO and H_3CO surface intermediates and decrease their barriers to methanol, hence the methanol production rate can be dramatically promoted[6]. Thus, the proposed facilitated reduction of ZnO in the presence of Ga^{3+} gives more CuZn alloys, promoting higher activity for the methanol synthesis. Overall, this type-II heterojunction concept could provide a generic method for tuning thermal reduction behaviour of metal oxide support to metallic atoms which consequently influences the properties of overlying metal nanoparticles through the formation of bimetallic phase at the interface. This allows the rational design of catalyst with optimal performance.

Reference

1. Yu, K. M. K., Curcic, I., Gabriel, J. & Tsang, S. C. E. Recent advances in CO_2 capture and utilization. *ChemSusChem* **1,** 893–899 (2008).
2. Turner, J., Sverdrup, G., K. Mann, M. K., Maness, P. C., Kroposki, B., Ghirardi, M., Evans, R. J., Blake, D. Renewable hydrogen production. *Int. J. Energy Res.* **32,** 379–407 (2008).
3. Song, C. Global challenges and strategies for control, conversion and utilization of CO_2 for sustainable development involving energy, catalysis, adsorption and chemical processing. *Catal. Today* **115,** 2–32 (2006).
4. Olah, G. A., Goeppert, A. & Prakash, G. K. S. Beyond oil and gas: the methanol economy. *Angew. Chem - Int. Ed.* **44,** 2636–2639 (2005).
5. Liao, F., Zeng, Z., Eley, C., Lu, Q., Hung, X. & Tsang, S. C. E. Electronic modulation of a copper/zinc oxide catalyst by a heterojunction for selective hydrogenation of carbon dioxide to methanol. *Angew. Chemie - Int. Ed.* **51,** 5832–5836 (2012).
6. Behrens, M., Studt, F., Kasatkin, I., Kühl, S., Hävecker, M., Abild-Pedersen, F., Zander, S., Girgsdies, F., Kurr, P., Kniep, B., Tovar, M., Fischer, R. W., Nørskov, J. K.& Schlögl, R. The active site of methanol synthesis over $Cu/ZnO/Al_2O_3$ industrial catalysts. *Science* **336,** 893–898 (2012).
7. Kurtz, M., Wilmer, H., Genger, T., Hinrichsen, O. & Muhler, M. Deactivation of supported copper catalysts for methanol synthesis. *Catal. Letters* **86,** 77–80 (2003).
8. Li, Y., Fu, Q. & Flytzani-Stephanopoulos, M. Low-temperature water-gas shift reaction over Cu- and Ni-loaded cerium oxide catalysts. *Appl. Catal. B Environ.* **27,**

179–191 (2000).

9. Yahiro, H., Murawaki, K., Saiki, K., Yamamoto, T. & Yamaura, H. Study on the supported Cu-based catalysts for the low-temperature water-gas shift reaction. *Catal. Today* **126,** 436–440 (2007).
10. Tanaka, Y., Utaka, T., Kikuchi, R., Sasaki, K. & Eguchi, K. Water gas shift reaction over Cu-based mixed oxides for CO removal from the reformed fuels. *Appl. Catal. A Gen.* **242,** 287–295 (2003).
11. Jeong, H., Kim, K. I., Kim, T. H., Ko, C. H., Park, H. C. & Song, I. K. Hydrogen production by steam reforming of methanol in a micro-channel reactor coated with $Cu/ZnO/ZrO_2/Al_2O_3$ catalyst. *J. Power Sources* **159,** 1296–1299 (2006).
12. Li, Y. F., Dong, X. F. & Lin, W. M. Effects of ZrO_2-promoter on catalytic performance of CuZnAlO catalysts for production of hydrogen by steam reforming of methanol. *Int. J. Hydrogen Energy* **29,** 1617–1621 (2004).
13. Ma, L., Gong, B., Tran, T. & Wainwright, M. S. Cr_2O_3promoted skeletal Cu catalysts for the reactions of methanol steam reforming and water gas shift. *Catal. Today* **63,** 499–505 (2000).
14. Fujitani, T. & Nakamura, J. The chemical modification seen in the Cu/ZnO methanol synthesis catalysts. *Appl. Catal. A Gen.* **191,** 111–129 (2000).
15. Zander, S., Kunkes, E. L., Schuster, M. E., Schumann, J., Weinberg, G., Teschner, D., Jacobsen, N., Schlögl, R. & Behrens, M. The role of the oxide component in the development of copper composite catalysts for methanol synthesis. *Angew. Chemie - Int. Ed.* **52,** 6536–6540 (2013).
16. Spencer, M. S. The role of zinc oxide in Cu/ZnO catalysts for methanol synthesis and the water-gas shift reaction. *Top. Catal.* **8,** 259–266 (1999).
17. Fujitani, T. & Nakamura, J. The effect of ZnO in methanol synthesis catalysts on Cu dispersion and the specific activity. *Catal. Letters* **56,** 119–124 (1998).
18. Kanai, Y., Watanab, T., Fujitani, T., Saito, M., Nakamura, K. & Uchijimi, T. Evidence for the migration of ZnO_x in a Cu/ZnO methanol synthesis catalyst. *Catal. Letters* **27,** 67–78 (1994).
19. Fujita, S., Usui, M., Ito, H., Takezawa, N. Mechanisms of Methanol Synthesis from Carbon Dioxide and from Carbon Monoxide at Atmospheric Pressure over Cu/ZnO. *Journal of Catalysis* **157,** 403–413 (1995).
20. Choi, Y., Futagami, K., Fujitani, T. & Nakamura, J. Role of ZnO in Cu/ZnO methanol synthesis catalysts - morphology effect or active site model? *Appl. Catal. A Gen.* **208,** 163–167 (2001).
21. Hambrock, J., Schröter, M. K., Birkner, A., Wöll, C. & Fischer, R. A. Nano-Brass: Bimetallic Copper/Zinc Colloids by a Nonaqueous Organometallic Route Using $[Cu(OCH(Me)CH_2NMe_2)_2]$ and Et_2Zn as Precursors. *Chem. Mater.* **15,** 4217–4222 (2003).
22. Sanches, S. G., Flores, J. H., De Avillez, R. R. & Pais Da Silva, M. I. Influence of preparation methods and Zr and y promoters on Cu/ZnO catalysts used for methanol steam reforming. *Int. J. Hydrogen Energy* **37,** 6572–6579 (2012).
23. Derrouiche, S., Lauron-Pernot, H. & Louis, C. Synthesis and treatment parameters for controlling metal particle size and composition in Cu/ZnO materials-first evidence of Cu_3Zn alloy formation. *Chem. Mater.* **24,** 2282–2291 (2012).
24. Arena, F., Barbera, K., Italiano, G., Bonura, G., Spadaro, L. & Frusteri, F. Synthesis, characterization and activity pattern of $Cu\text{-}ZnO/ZrO_2$ catalysts in the hydrogenation of carbon dioxide to methanol. *J. Catal.* **249,** 185–194 (2007).

25. Saito, M., Fujitani, T., Takeuchi, M. & Watanabe, T. Development of copper/zinc oxide-based multicomponent catalysts for methanol synthesis from carbon dioxide and hydrogen. *Appl. Catal. A Gen.* **138,** 311–318 (1996).
26. An, X., Li, J., Zuo, Y., Zhang, Q., Wang, D. & Wang, J. A Cu/Zn/Al/Zr fibrous catalyst that is an improved CO_2 hydrogenation to methanol catalyst. *Catal. Letters* **118,** 264–269 (2007).
27. Weigel, J., Koeppel, R. A., Baiker, A. & Wokaun, A. Surface species in CO and CO_2 hydrogenation over copper/zirconia: On the methanol synthesis mechanism. *Langmuir* **12,** 5319–5329 (1996).
28. Yu, K. M. K., Tong, W., West, A., Cheung, K., Li, T., Smith, G., Guo, Y. & Tsang, S. C. E. Non-syngas direct steam reforming of methanol to hydrogen and carbon dioxide at low temperature. *Nat. Commun.* **3,** 1230 (2012).
29. Tong, W., Cheung, K., West, A., Yu, K.-M. & Tsang, S. C. E. Direct methanol steam reforming to hydrogen over $CuZnGaO_x$ catalysts without CO post-treatment: mechanistic considerations. *Phys. Chem. Chem. Phys.* **15,** 7240–7248 (2013).
30. Tong, W., West, A., Cheung, K., Yu, K. M. & Tsang, S. C. E. Dramatic effects of gallium promotion on methanol steam reforming Cu-ZnO catalyst for hydrogen production: Formation of 5Å copper clusters from Cu-$ZnGaO_x$. *ACS Catal.* **3,** 1231–1244 (2013).
31. Smith, A. M. & Nie, S. Semiconductor nanocrystals: Structure, properties, and band gap engineering. *Acc. Chem. Res.* **43,** 190–200 (2010).
32. Yin, L. & Bando, Y. Optimizing properties by tuning morphology. *Nature Materials* **4,** 883–884 (2005).
33. Chen, C. Y., Cheng, C. T., Yu, J. K., Pu, S. C., Cheng, Y. M. & Chou, P. T. Spectroscopy and femtosecond dynamics of type-II CdSe/ZnTe core-shell semiconductor synthesized via the CdO precursor. *J. Phys. Chem. B* **108,** 10687–10691 (2004).
34. Chou, P. T., Chen, C. Y., Cheng, C. T., Pu, S. C., Wu, K. C., Cheng, Y. M., Lai, C. W., Chou, Y. H. & Chiu, H. T. Spectroscopy and femtosecond dynamics of type-II CdTe/CdSe core-shell quantum dots. *ChemPhysChem* **7,** 222–228 (2006).
35. Kaniyankandy, S., Rawalekar, S., Verma, S. & Ghosh, H. N. Ultrafast hole transfer in CdSe/ZnTe type II core-shell nanostructure. *J. Phys. Chem. C* **115,** 1428–1435 (2011).
36. Liao, F., Lo, B. T., Sexton, D., Qu, J., Ma, C., Chan, R. C. T., Lu, Q., Che, R., Kwok, W. M., He, H., Fairclough, S. & Tsang, S. C. E. A new class of tunable heterojunction by using two support materials for the synthesis of supported bimetallic catalysts. *ChemCatChem* **7,** 230–235 (2015).
37. Li, Z. S., Li, B., Liu, Z., Li, D., Ge, C. & Fang, Y. Controlled synthesis of $ZnGa_2O_4$ nanorod arrays from hexagonal ZnO microdishes and their photocatalytic activity on the degradation of RhB. *RSC Adv.* **4,** 48590–48595 (2014).
38. Baojun, M., Keying, L., Weiguang, S. & Wanyi, L. One-pot synthesis of $ZnO/ZnGa_2O_4$ heterojunction with X/XY structure for improved photocatalytic activity. *Appl. Surf. Sci.* **317,** 682–687 (2014).
39. Babu, V. J., Vempati, S., Uyar, T. & Ramakrishna, S. Review of one-dimensional and two-dimensional nanostructured materials for hydrogen generation. *Phys. Chem. Chem. Phys.* **17,** 2960–2986 (2015).
40. Schumann, J., Eichelbaum, M., Lunkenbein, T., Thomas, N., Galván, M. C. A., Schlögl, R. & Behrens, M. Promoting strong metal support interaction: Doping ZnO

for enhanced activity of Cu/ZnO:M (M = Al, Ga, Mg) catalysts. *ACS Catal.* **5,** 3260–3270 (2015).

41. Studt, F., Sharafutdinov, I., Abild-Pedersen, F., Elkjær, C. F., Hummelshøj, J. S., Dahl, S., Chorkendorff, I. & Nørskov, J. K. Discovery of a Ni-Ga catalyst for carbon dioxide reduction to methanol. *Nat. Chem.* **6,** 320–324 (2014).
42. Ahlers, M. Martensite and equilibrium phases in CuZn and CuZnAl alloys. *Prog. Mater. Sci.* **30,** 135–186 (1986).
43. Grunwaldt, J.-D., Molenbroek, A. M., Topsøe, N.-Y., Topsøe, H. & Clausen, B. S. In Situ Investigations of Structural Changes in Cu/ZnO Catalysts. *J. Catal.* **194,** 452–460 (2000).
44. Naumann d'Alnoncourt, R., Xia, X., Strunk, J., Löffler, E., Hinrichsen, O. & Muhler, M. The influence of strongly reducing conditions on strong metal–support interactions in Cu/ZnO catalysts used for methanol synthesis. *Phys. Chem. Chem. Phys.* **8,** 1525–1538 (2006).
45. Kuld, S., Conradsen, C., Moses, P. G., Chorkendorff, I. & Sehested, J. Quantification of zinc atoms in a surface alloy on copper in an industrial-type methanol synthesis catalyst. *Angew. Chemie - Int. Ed.* **53,** 5941–5945 (2014).
46. Fichtl, M. B., Schumann, J., Kasatkin, I., Jacobsen, N., Behrens, M., Schlögl, R., Muhler, M. & Hinrichsen, O. Counting of oxygen defects versus metal surface sites in methanol synthesis catalysts by different probe molecules. *Angew. Chemie - Int. Ed.* **53,** 7043–7047 (2014).
47. Toyir, J., Ramírez De La Piscina, P., Fierro, J. L. G. & Homs, N. Highly effective conversion of CO_2 to methanol over supported and promoted copper-based catalysts: Influence of support and promoter. *Appl. Catal. B Environ.* **29,** 207–215 (2001).
48. Kazansky, V. B., Subbotina, I. R., Pronin, A. A., Schlögl, R. & Jentoft, F. C. Unusual infrared spectrum of ethane adsorbed by gallium oxide. *J. Phys. Chem. B* **110,** 7975–7978 (2006).
49. Kazansky, V. B. & Pid'ko, E. A. Diffuse reflectance IR spectra of molecular hydrogen and deuterium adsorbed on zinc oxide. *Kinet. Catal.* **43,** 567–572 (2002).
50. Martin, O., Mondelli, C., Curulla-Ferré, D., Drouilly, C., Hauert, R. & Pérez-Ramírez, J. Zinc-Rich Copper Catalysts Promoted by Gold for Methanol Synthesis. *ACS Catal.* **5,** 5607–5616 (2015).

Chapter 5: CO_2 hydrogenation to methanol over nanosheets derived from single cationic layer CuZnGa LDH precursors

The work in this chapter has been adapted and reproduced in part with permission from: Molly Meng-Jung Li, Chunping Chen, Tuğçe Ayvalı, Hongri Suo, Jianwei Zheng, Ivo F. Teixeira, Lin Ye, Hanbo Zou, Dermot O'Hare, Shik Chi Edman Tsang. The article is accepted by ACS Catalysis with revisions.

5.1 Chapter overview

Ultra-thin (1-3 cationic-layers) $(CuZn)_{1-x}Ga_x$-CO_3 layered double hydroxides (AMO-LDH) nanosheets were synthesised following the aqueous miscible organic solvent method (AMOST) and applied as catalyst precursors for methanol production from CO_2 hydrogenation. It was found that upon reduction, the AMO-LDH samples above a critical Ga^{3+} composition give consistently and significantly higher Cu surface areas and dispersions than the catalysts prepared from conventional hydroxyl-carbonate phases (the CZG catalysts introduced in Chapter 4). Owing to the distinctive local steric and electrostatic stabilisation of the ultra-thin LDH structure, the newly formed Cu metal atoms are stabilised by the cationic layers. It is also evident that Zn metal atoms decorating on Cu nanoparticles can be formed in the AMO-LDH samples, which provides active CuZn sites that may also exert a great enhancement to the catalytic reaction. The best catalyst in this study displayed methanol productivity with a space-time yield of 0.6 $g_{MeOH}{\cdot}g_{cat}^{-1}{\cdot}h^{-1}$ under typical reaction conditions, which as far as we are aware, is higher than most reported Cu-based catalysts in the literature.

5.2 Introduction

Cu/ZnO based catalysts are well known to be active for methanol synthesis from hydrogenation of either CO or CO_2. Due to the increasing emissions by the increasing population and human activities, the concentration of CO_2 in the atmosphere is rising year by year which causes significant climate change. The attempts to reduce the CO_2 emission and develop various technologies for CO_2 capture and transformation are elevated. It has been recently demonstrated that by utilising solar energy, wind power, hydropower and biomass, renewable hydrogen gas can be produced at large scale[1,2]. Therefore, the recycling of CO_2 through its hydrogenation to high-energy-content fuels such as alcohols or hydrocarbons appears to be very attractive[3]. Particularly, the CO_2 hydrogenation to methanol is becoming a strategically important process due to the positions of methanol as both chemical platform and clean fuel.

A Cu surface is generally accepted to provide active sites for the catalytic CO_2 hydrogenation to methanol. Its catalytic activity is a function of surface area to volume ratio (inversely proportional to the particle size) due to the fact that catalysis is a surface phenomenon[4,5]. Thus, the generation of small Cu particles and particularly their stabilisation against Cu sintering under reaction conditions are the important aspects of the catalyst development. Despite the fact that many efforts have been made aiming to investigate how a solid precursor can control the formation of metal atoms, the fine control to the size of metal atoms and their subsequent aggregation in its matrix remain challenging. Additionally, the role(s) of supports such as ZnO on the stabilisation and activity of Cu nanoparticles are still in debate[6–13]. Due to the rapid development of advanced characterisation techniques, many reports have indicated that a very small quantity of Zn atoms is reduced on small Cu nanoparticles which results in a subtle change in the geometric and electronic structure of

Cu due to the desirable bimetallic properties[14–17]. Consequently, it has been proposed that highly active Zn-Cu alloy is the key catalytic site[17]. In the previous chapter of this thesis (Chapter 4) the active CuZn alloy for the enhanced methanol production from CO_2 hydrogenation was identified, which support the idea that CuZn alloy act as the active site. In contrast, other people believe that the reaction happens at the atomic interface between ZnO and Cu, hence the presence of ZnO-Cu interfacial sites and the synergy of Cu and ZnO are important for methanol production[18]. On the other hand, it is reported that the incorporation of different additives, such as Al_2O_3, ZrO_2, SiO_2, and Ga_2O_3 can further improve the activity, stability, and thermal resistance compared with the unmodified Cu/ZnO[19–24]. Particularly, the incorporation of Ga has attracted a considerable attention due to the exhibition of its higher catalytic performance. The mechanism of Ga promotion has been extensively studied, which includes the improvement of the Cu dispersion[24–26], the enhancement of electronic effect[27], the stabilisation of the intermediate state of Cu[28], and the facilitation of the formation of active CuZn alloy[29], which make CuZnGa-containing catalyst a suitable candidate material for CO_2 hydrogenation to methanol.

It has been shown that monophasic catalyst precursor containing M^{2+} and M^{3+} could be obtained by controlled thermal treatment of a layered double hydroxide phase (LDH), which is a class of ionic lamellar solid often represented by the formula $[M^{2+}_{1-x}M^{3+}_{x}(OH)_2](A^{n-})_{x/n}\cdot mH_2O$ with the positive divalent and trivalent metal cations located within the same layer where A^{n-} is the intercalated anion (or anions)[30,31]. Thus, it is believed that Cu^{2+}, Zn^{2+} and Ga^{3+} can also be incorporated into a stable solid LDH phase as a catalyst precursor for CO_2 hydrogenation reaction. In the literature, some studies have discussed the advantages of LDH phases as catalyst precursors[32–34], such as good dispersion of M^{2+} (Cu^{2+}, Zn^{2+}) and M^{3+} (Al^{3+}, Y^{3+} or Ga^{3+}) at an atomic level, homogeneous microstructure, good thermal

stability against sintering/reduction, high dispersion for small Cu clusters and high specific surface area. Those benefits roused our interests in using this inorganic lamellar phase to generate Cu metal atoms and Zn dopant species within the cationic layer such that the active metal particles can be stabilised within the positively-charged sheet, hence reduce sintering. In addition, the recent synthesis of the ultra-high surface area and high pore volume AMO-LDH phases with a reduced number of cationic layers (approaching towards single-layer nanosheets) using aqueous miscible organic solvent treatment (AMOST) method[35] may further inhibit extensive Cu atom aggregation from an otherwise extended lattice. Thus, the controlled reduction of discrete, flexible but sterically separated inorganic ionic layers to produce and stabilise metal atoms is therefore envisaged.

In this chapter, a series of Ga^{3+}-modified Cu/ZnO based catalysts ((Cu^{2+}, Zn^{2+}): Ga^{3+} = 1 to 0.6) derived from AMO CuZnGa-CO_3 LDH precursors were synthesised by following the AMOST method[35]. The prepared catalysts were then evaluated for methanol synthesis from CO_2 hydrogenation and the results were compared with CuZnGa catalysts derived from conventional hydroxyl-carbonate phases[36] (CZG samples, which were introduced in Chapter 4 of this thesis) consisting of comparable metal contents. In order to better understand and design the highly active catalysts for CO_2 hydrogenation to methanol, the precursor structures and physicochemical properties of the catalysts were investigated in detail and correlated with corresponding catalytic activities. In addition, the surface state and compositions of the catalysts were studied by XPS after the reduction process to get the insight into active copper and zinc species.

5.3 Results and discussion

5.3.1 Structural characterisation

With the introduction of Ga^{3+} into Cu/ZnO catalyst, a series of Cu, Zn, and Ga-containing hydroxyl-carbonate precursor phases, denoted by CZG, have been prepared using a simple and conventional co-precipitation method (see Figure 3-1 for the synthesis details). From the XRD patterns, a dominant, aurichalcite phase of $(Cu, Zn)_5(CO_3)_2(OH)_{16}$ with a high dispersion of Ga species from 0, 5, 10 mole% Ga concentration are seen in Figure 5-1a for the freshly prepared samples. At the Ga concentrations of 30 or 40 mole%, the zinc-containing malachite phase of $(Cu, Zn)_2(CO_3)(OH)_2$ is preferably formed. The formation of these two hydroxyl-carbonate phases has been widely reported in the literature using similar co-precipitation preparation method[36]. The peak broadening in the XRD patterns with the increase in Ga concentration provides evidence of the use of Ga to reduce the crystal size of aurichalcite phase. Particularly, at 30-40% Ga, the switch of the dominant aurichalcite phase to malachite phase is interesting. It was found that the type of precursor will sequentially vary as malachite to aurichalcite with increasing ZnO content[6]. Therefore, the switch of the dominant phase observed here is because of the decrease in Zn concentration when increasing Ga in the synthesis process (see Table 3-1 for the compositions of CuZnGa samples). Upon calcination at 330 ^oC (Figure 5-1b), with the sample in the absence of Ga, bulk phases of CuO, ZnO, are clearly identified. As long as Ga is included, a spinel phase of MGa_2O_4 (M = Zn, Cu) readily emerges together with minority phases of ZnO and CuO, which are stabilised over the whole Ga range of 5-40%.

On the other hand, as can be seen in Figure 5-1c that samples prepared by AMOST method (see Figure 3-2 for the synthesis details) via basic solution produced phase pure $((Cu,Zn)_{1-x}Ga_x)(OH)_2(CO_3)_{x/2}.mH_2O.n(C_3H_6O)$ {AMO CuZnGa-CO_3 LDHs} with increasing

crystallinity at or above 20% Ga. The Bragg reflections at 2θ *ca*. 12°, 24°, and 35° were attributed to (0 0 3), (0 0 6), and (0 0 9) crystal planes in the layered structure with a rhombohedral symmetry (R3)[37]. The rhombohedral symmetry of LDH30Ga was further confirmed by synchrotron XRD analysis, shown in Figure 5-2a, revealing the lattice parameters of *a*, *b* = 3.11 Å, *c* = 22.64 Å. In addition to intense Bragg reflections at 2θ = 12°, 24°, and 35°, the broad and asymmetric reflections were also observed at 2θ = 36°, 39°, and 47°, ascribed to (0 1 2), (0 1 5), and (0 1 8) crystal planes, respectively, for the sample with the highest 40% Ga loading (Figure 5-2b). This indicates a homogeneous dispersion of various cations into the same hydroxide layer[38]. No other crystalline phases are observed from the AMO-LDH samples of 20, 30 and 40% mole Ga which correspond to LDH structure of $[(Cu_{0.45}Zn_{0.41}Ga_{0.14})(OH)_2](CO_3)_{0.07}$, $[(Cu_{0.47}Zn_{0.32}Ga_{0.21})(OH)_2](CO_3)_{0.105}$ and $(Cu_{0.49}Zn_{0.22}Ga_{0.29})(OH)_2(CO_3)_{0.145}$, respectively, according to the ICP analyses (see Table 3-1 for the compositions of CuZnGa samples). The discrepancy between nominal and ICP-measured Ga content in the samples comes from the loss of metal ions dissolved in the solution during the filtration process. It is noted that using 30% mole Ga in the synthesis recipe is appropriate to form ultrathin AMO-LDH sheets (by the AMOST method) than the other two AMO-LDH samples as the stability of LDH structure depends critically on the overall charge of the cationic layer with specific M^{3+}: M^{2+} ratio balanced with intercalated anions[39]. For example, the cationic charge for the layer holding the higher ratio of M^{2+}/M^{3+} = 4 (20% mole Ga^{3+}) is anticipated to be at lower end of the stability range. Therefore, it may be relatively unstable and form amorphous precipitates such as hydroxides and hydroxyl-carbonates in the presence of AMO solvent[37]. Below the critical 20% Ga concentration, an amorphous phase is clearly recorded from XRD. Similarly, adding 40 mole % Ga in the synthesis ($M^{3+}/M^{2+} > 0.5$) leads to stronger electrostatic interaction between the layers due to the presence of higher amount of stoichiometric intercalated carbonate anions.

This creates thicker LDH layers (see Figure 5-2b), which is difficult to disrupt (exfoliate) by the AMO solvent treatment. Notably, calcination of the AMO-LDHs at 330 ^{o}C did not reveal any formation of spinel structures or metal oxides from XRD investigation (Figure 5-1d). This clearly indicates that LDHs have a kinetically more stable phase than the conventional hydroxyl-carbonate phases (CZG samples). LDHs normally have two typical distinct thermal events around < 200 ^{o}C (noted as T1) and 500-600 ^{o}C (noted as T2) evaluated by thermogravimetric analysis (see Figure 5-3). The weight loss below T1 is due to the desorption of physisorbed and intercalated solvents and water. After T1, the hydroxyl groups start to decompose and gradually transform the LDH structure to a reversible amorphous phase. This reaches a maximum at 550 ^{o}C (T2), and is ascribed to the partial decomposition of carbonate anions and complete dehydroxylation of the metal hydroxide layers[35]. Thus, the applied calcination temperature of 330 ^{o}C gives mainly the amorphous phase with probably a trace amount of layered double oxides (LDO, although not detected in this work) without reaching the second stage of the layer structure collapse.

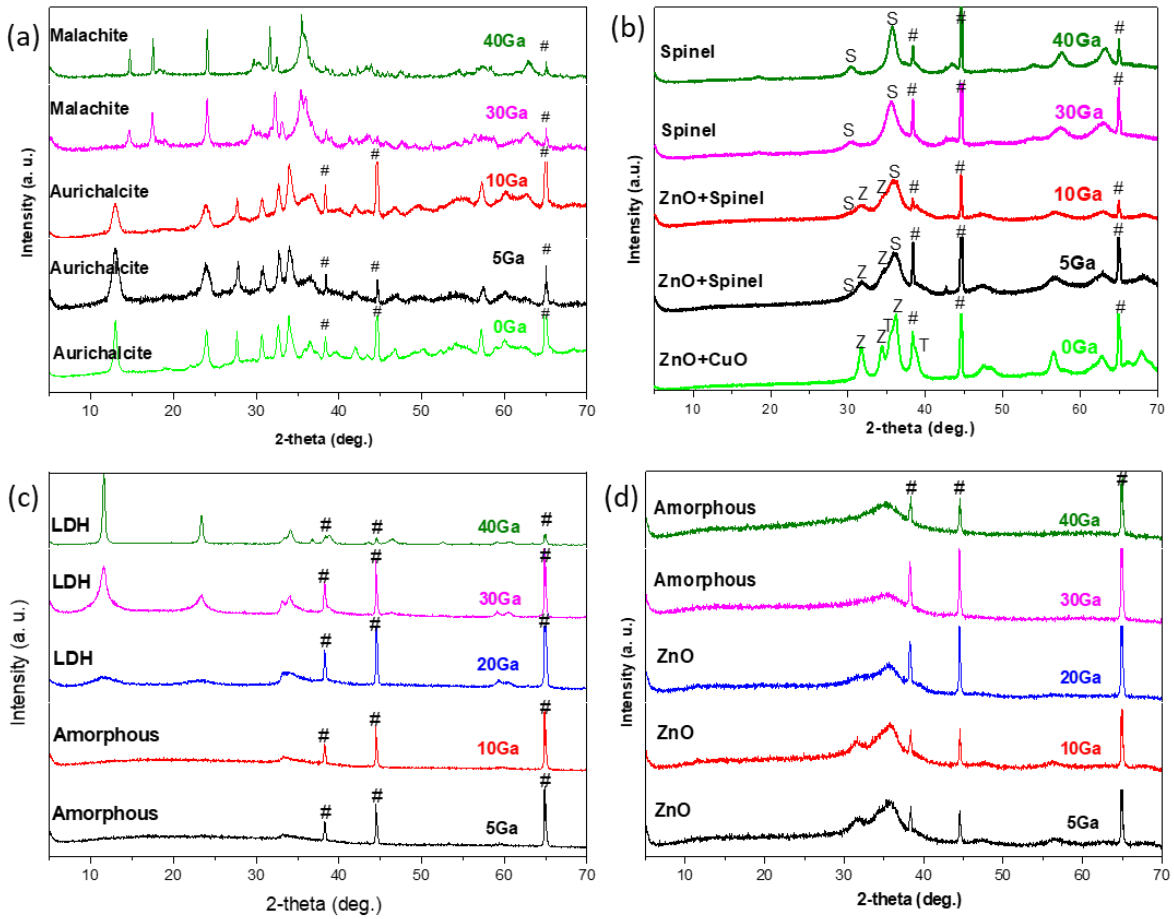

Figure 5-1. XRD profiles of (a) freshly prepared CZG catalysts; (b) calcined CZG catalysts at 330 ^{o}C; (c) freshly prepared AMO-LDH samples; (d) calcined AMO-LDH samples at 330 ^{o}C (# peaks from Al holder; S: spinel phase; T: tenorite phase; Z: zincite phase).

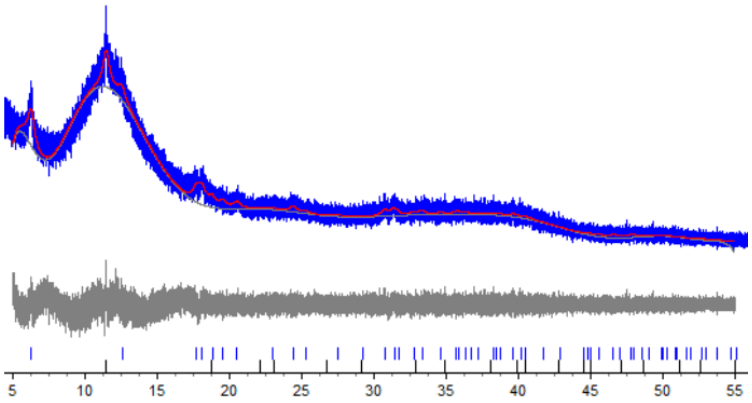

a	**3.1134±0.0011 Å**
b	**3.1134±0.0011 Å**
c	**22.6434±0.0011 Å**
α	**90º**
β	**90º**
γ	**120º**

Figure 5-2a. SXRD of freshly prepared LDH30Ga by synchrotron XRD (Diamond I11). Pawley refinement with the best fitting parameters of R_{wP} 8.1142; R_{exp} 6.2624; R_P 6.3235; *gof* 1.2957. I = 7.1152. Monodispersed spheres diameter = 4×I÷3 = 9.48 nm (~ 10 layers).

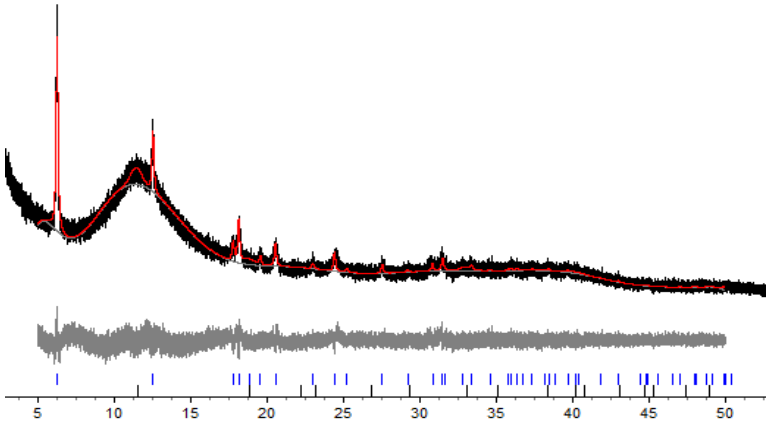

a	**3.1061±0.0010 Å**
b	**3.1061±0.0010 Å**
c	**22.6904±0.0010 Å**
α	**90º**
β	**90º**
γ	**120º**

Figure 5-2b. SXRD of freshly prepared LDH40Ga by synchrotron XRD (Diamond I11). Pawley refinement with the best fitting parameters of R_{wP} 7.9297; R_{exp} 5.7502; R_P 6.1762; *gof* 1.3790. I = 27.8994. Monodispersed spheres diameter = 4×I÷3 = 37.16 nm (~ 46 layers).

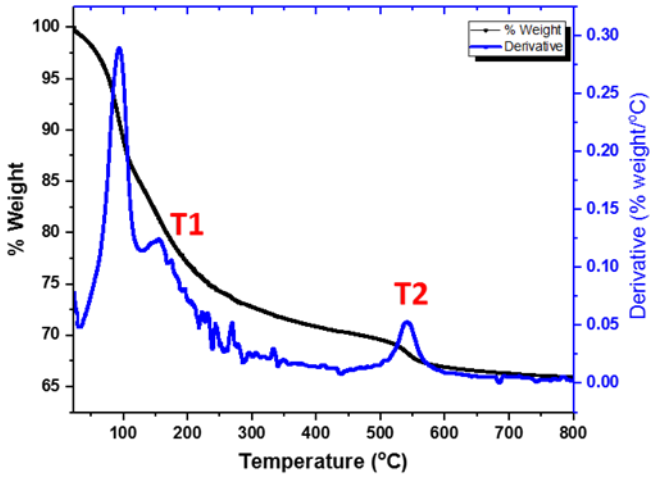

Figure 5-3. Thermogravimetric analysis result of the LDH30Ga sample. T1 and T2: Temperature regions at which decomposition of –OH and CO_3^{2-} groups takes place respectively.

5.3.2 Morphology analysis of the precursors

In order to determine the textural properties of these samples, TEM and AFM were employed. Figure 5-4 shows the typical images of the hydroxyl-carbonate phase of CZ, CZG5Ga, and CZG40Ga prepared by co-precipitation method. It appears that the unmodified CZ sample gives bulk-like structure, while CZG5Ga shows the extended fibrous/sheet-like particles but those are fragmented in the presence of a high Ga concentration, giving many smaller particles in CZG40Ga sample. On the other hand, the LDH5Ga is similar in textual appearance as CZG5Ga although small sheet-like features are occasionally observed. It is noted that the XRD of the AMO-LDH samples with low Ga concentration (LDH5Ga and LDH10Ga) in Figure 5-1c show no indication of LDH phase formation, which is not surprising. Their M^{2+}: M^{3+} is outside the stability range for LDHs, but probably some mixed phases of hydroxyl-carbonate structures of below the detection

limit by the XRD are made, hence giving mixed shapes (particles/fibrous/sheets) in the appearance. At 20% Ga (M^{2+}: M^{3+} = 4) or above, sheet-like structures are observed (see Figure 5-4), which agrees with the expected layered LDH structure identified by the XRD (Figure 5-1c).

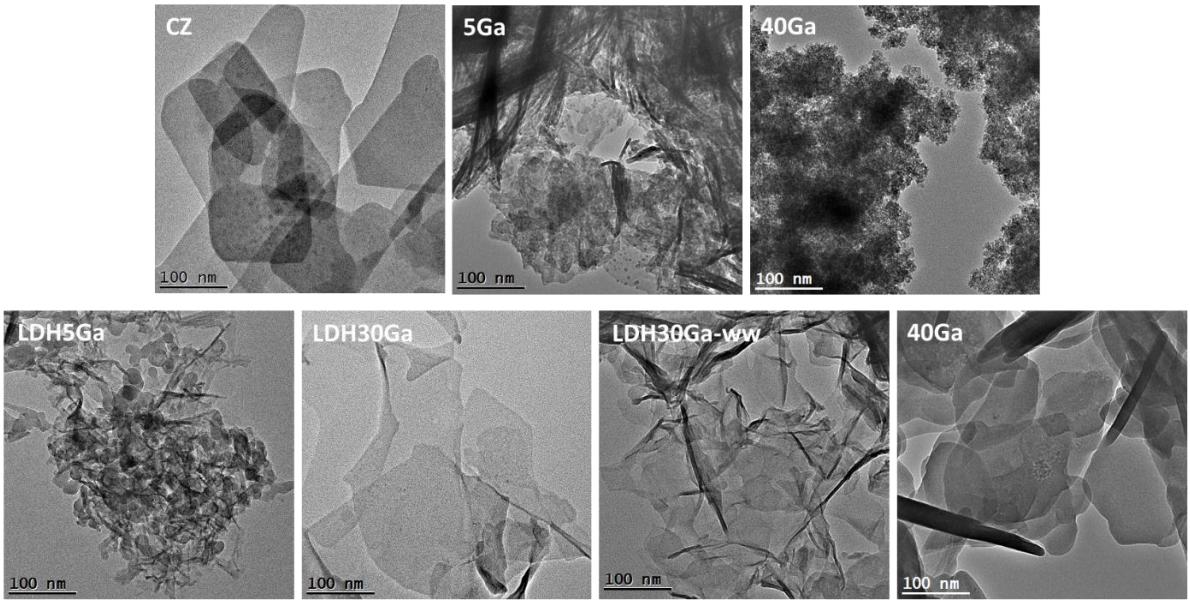

Figure 5-4. TEM images of freshly prepared CZG and AMO-LDH samples.

The striking reduction in the number of cationic layers via acetone (AMO-solvent) inter-layer disruption produced by the AMOST method (fine particle portion) can be identified by AFM on the 30% Ga (M^{2+}: M^{3+} = 2.33) sample (Figure 5-5). As can be seen that the typical height profile of LDH30Ga sample clearly shows a thickness of 0.8–2.3 nm for selected regions, which corresponds to 1–3 layer LDH platelet according to our 3-layer LDH30Ga structural model intercalated with carbonate anions as depicted in Figure 5-6 (for the single cationic layer, the structure stabilised by adsorbed carbonate anions is anticipated).

The formation of such ultra-thin nanosheets which separated by discrete cationic layers and balanced by intercalated carbonate anions suggests that acetone dispersion can override the weaker interlayer electrostatic interaction, thus accounting for the dramatic increase in surface area of this sample.

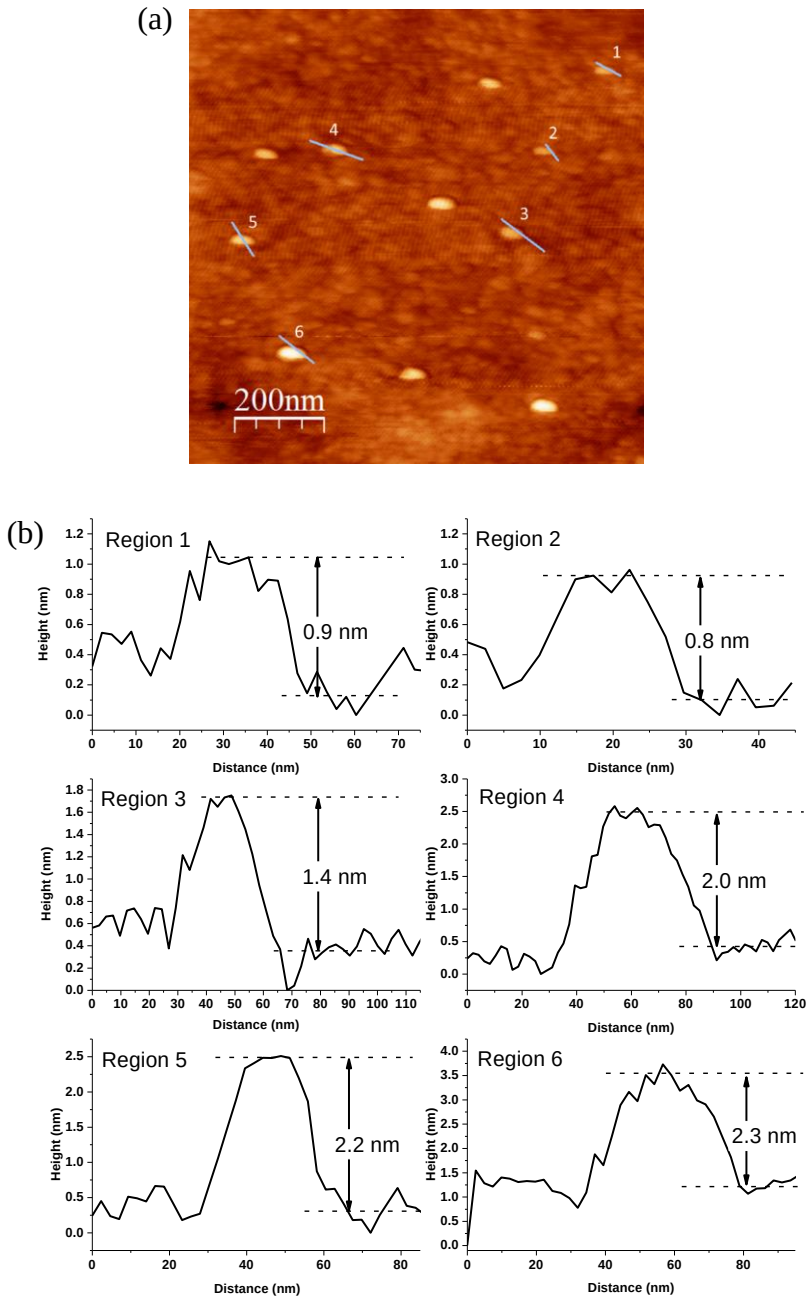

Figure 5-5. (a) AFM image of single layer and few layers freshly prepared LDH30Ga sample on Si substrate; (b) the height profile of the selected lines of (a).

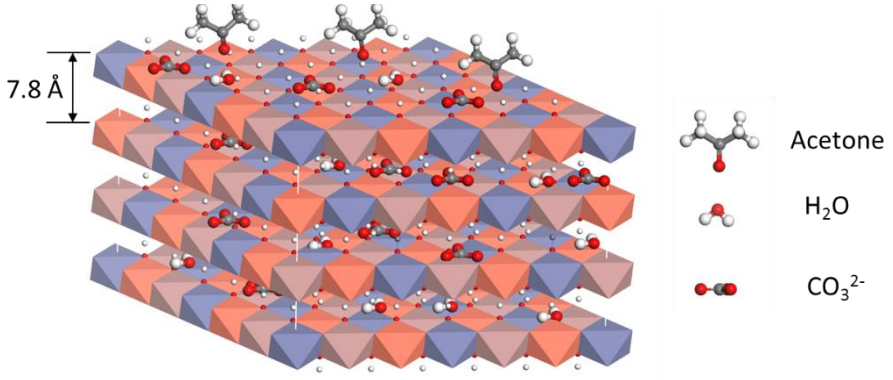

Figure 5-6. The LDH30Ga structural model showing 3 cationic layers with intercalated carbonate anions and water molecules in between; each cationic layer contains Cu^{2+} (blue), Zn^{2+} (grey) and Ga^{3+} (orange) with OH^- vertexes in face-sharing octahedra with an inter-layer separation of 7.8 Å in a rhombohedral (3R symmetry) $[(CuZn)_{1-x}Ga_x(OH)_2](CO_3)_{x/2}$ LDH structure derived from synchrotron XRD data (Figure 5-2). For simplicity, the equal population of Cu, Zn and Ga ions are presented in this model and Jahn-Teller distortion of Cu^{2+} in octahedral sites is also not shown.

5.3.3 Investigation of reduction behaviour and active Cu surface area

The reduction behaviour of calcined CZG and AMO-LDH samples was investigated by H_2-TPR, and the corresponding reduction profiles are given in Figure 5-7. It is known that Cu^{2+} has the more favourable reduction potential than the other two metal cations, i.e., Zn^{2+} and Ga^{3+}. The TPR analysis shows that all samples give virtually the same integral reduction peak area of 5.0 ± 0.5 mmol. $H_2 \cdot g_{cat}^{-1}$ corresponding to the complete reduction of Cu^{2+} to Cu^0. It is, however, interesting to note from Figure 5-7a that CZG samples display a complex and broadened reduction peak accompanied by shoulders in the temperature range of 150–270 ^oC. This indicates that some reduced Cu species exist in heterogeneous chemical environments (variation in size and structure), thus leading to different peak maxima at

different reduction temperatures. The reduction range of 150–200 ^{o}C (low-temperature shoulder) matches with that of Cu_2O but its content in CZG samples diminishes at higher Ga loading[24,36]. The higher temperature main peak is attributed to the broad reduction of $CuGa_2O_4$ and CuO phases of different sizes. Such a large variation in reduction behaviour of Cu^+ and Cu^{2+} in a heterogeneous mixture of extended lattices would expect to induce large Cu particle size variation in the CZG precursor-derived catalysts. Without Ga, the even higher temperature is required for the complete Cu^{2+} reduction, which gives inefficient utilisation of Cu active sites from the CZG precursor samples under dynamic reaction conditions. On the other hand, the reduction profile of LDH samples shown in Figure 5-7b displays more uniform and sharper peak profiles but at a higher temperature range of 200–290 ^{o}C. Comparing to the CZG samples, the LDH samples do not show low-temperature shoulder peak (absence of Cu_2O), therefore, more homogeneous Cu particles are expected to generate from the reduction of ultra-thin LDH phase prepared by the AMOST method. However, the bulk LDH40Ga sample (see TEM image in Figure 5-4) with stronger interlayer charge density requires much higher reduction temperature to reduce the Cu atoms.

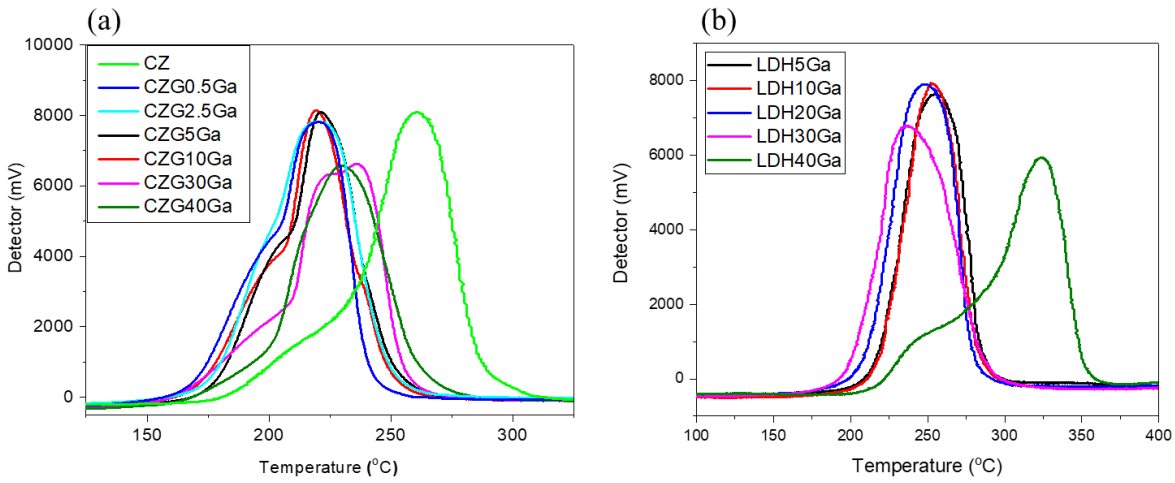

Figure 5-7. Temperature Programmed Reduction (TPR) profile of calcined (a) CZG samples (b) LDH samples.

The Cu loading (determined by ICP), Cu dispersion, Cu surface area (determined by N_2O chemisorption) and BET specific surface areas (selected samples) for the Cu-containing CZG and LDH catalysts were determined accordingly and are shown in Table 5-1. It is noted that the absolute values for Cu dispersion and Cu surface area determined by N_2O should not be taken too literally. This is because recent studies have clearly shown that N_2O is not just oxidising the copper surface but also oxidising other reduced species, i.e., Zn or oxygen vacancies on support[40–42]. However, it is clear from the compiled Cu surface areas and Cu dispersions that CZG samples give consistently lower values than LDH samples, which agree with a similar behaviour as observed from the BET surface area analysis that CZG precursors have much lower specific surface areas than the AMO-LDH precursors. As for the LDH precursor without AMO solvent treatment, LDH30Ga-ww, that shows the lowest BET surface area than other selected samples. Conventional hydroxyl-carbonate precursor phases of Cu-ZnO (zincian malachite and aurichalcite) was discovered to possess higher

S_{BET} compared to LDH precursors, which could be ascribed to the formation of phase-pure hydrotalcite platelets with lower dispersion[37], indicating that the solvent exfoliation process is a very crucial step to generate ultra-thin LDH structure.

Table 5-1. Comparison of Cu loading, Cu dispersion, Cu surface area and BET specific surface areas (selected samples) for the Cu containing CZG and LDH derived catalysts.

Catalysts	Cu loading[a] (wt%)	Cu dispersion[b]	S_{Cu}[b] ($m^2g^{-1}_{cat}$)	S_{BET}[c] ($m^2g^{-1}_{cat}$)
CZ	33.4	21.8	43	Freshly-prepared: 58
CZG5Ga	31.9	22.0	45	Freshly-prepared: 85 Calcined: 56
CZG10Ga	33.9	19.5	43	-
CZG30Ga	32.7	19.6	41	-
CZG40Ga	33.5	21.1	46	-
LDH10Ga	34.3	24.4	54	-
LDH20Ga	33.4	33.8	73	-
LDH30Ga	33.5	46.0	99	Freshly-prepared: 159 Calcined: 79
LDH40Ga	37.9	22.6	55	-
LDH30Ga-ww (water wash)	34.3	28.1	62	Freshly-prepared: 37

[a] Determined by ICP; [b] Dispersion and specific surface area of metallic Cu determined by N_2O chemisorption; [c] BET specific surface areas.

5.3.4 Catalyst screening and correlation between activity and structural parameters

The catalytic performances of Cu-containing CZG and AMO-LDH precursor samples for methanol production via CO_2 hydrogenation were evaluated and are presented in Figure 5-8 as well as Figure 5-9. The major product for all catalysts is methanol and the main by-product is CO under operating conditions of H_2: CO_2 (molar) = 3: 1, T = 190–310 ^oC, P = 4.5 MPa and WHSV = 18,000 $mL \cdot g_{cat} \cdot h^{-1}$. The activity measurements were taken after at

least 2 h on the stream at each selected temperature. Similar catalytic performances of CZ and CZG samples were observed in terms of CO_2 conversion, probably, due to their similar Cu content, surface areas and Cu dispersions, see Table 5-1. However, differences were identified in their selectivities towards methanol. In general, the methanol yields of CZ and CZG catalysts (Figure 5-8) increase with the increasing in temperature and reach the optimal value of about 290 ^oC before they are rapidly attenuated due to the thermodynamic constraints. It can be seen in Figure 5-9a that among all CZG samples, CZG5Ga reveals the best performance. The addition of 5 mole% Ga into CZ leads to an increase in CH_3OH yield, but further increase of Ga content starts to decrease the activity where the performance of CZG40Ga is even lower than the CZ catalyst. The interpretation of these data is not straightforward because there is no general trend for CZG samples that correlates to the small variations in Cu dispersion (Figure 5-10). This observation suggests that the catalytic conversion of CO_2 to methanol of the CZG sample may not only be dependent on copper dispersion but also on other factors, presumably on structural and compositional differences of nanoparticles (structural sensitive), as previously discussed that there is a large morphological and structural variation between the CZG precursors.

Similar to CZG samples, CO_2 conversion of AMO-LDH precursor catalysts increases with the increasing in temperature while selectivity of methanol declines (Figure 5-8). In addition, methanol yield of the homogeneous LDH-based catalysts also presents a volcano trend with increasing temperature: Most of the LDH catalysts reach the optimal methanol yield at 290 ^oC, but the LDH30Ga and LDH20Ga catalysts exhibit methanol yield maxima at a lower temperature (270 ^oC). Interestingly, according to Figure 5-9b and Figure 5-10, the LDH samples which show higher Cu surface areas and Cu dispersions, particularly the LDH20Ga and LDH30Ga (see Table 5-1) also give higher methanol selectivities and yields than

CZG5Ga at 270 ºC. The best performance is obtained by LDH30Ga which gives nearly 9% methanol yield. This matches with the general consent from the literature that Cu surface primarily provides active sites for this hydrogenation reaction[4–7].

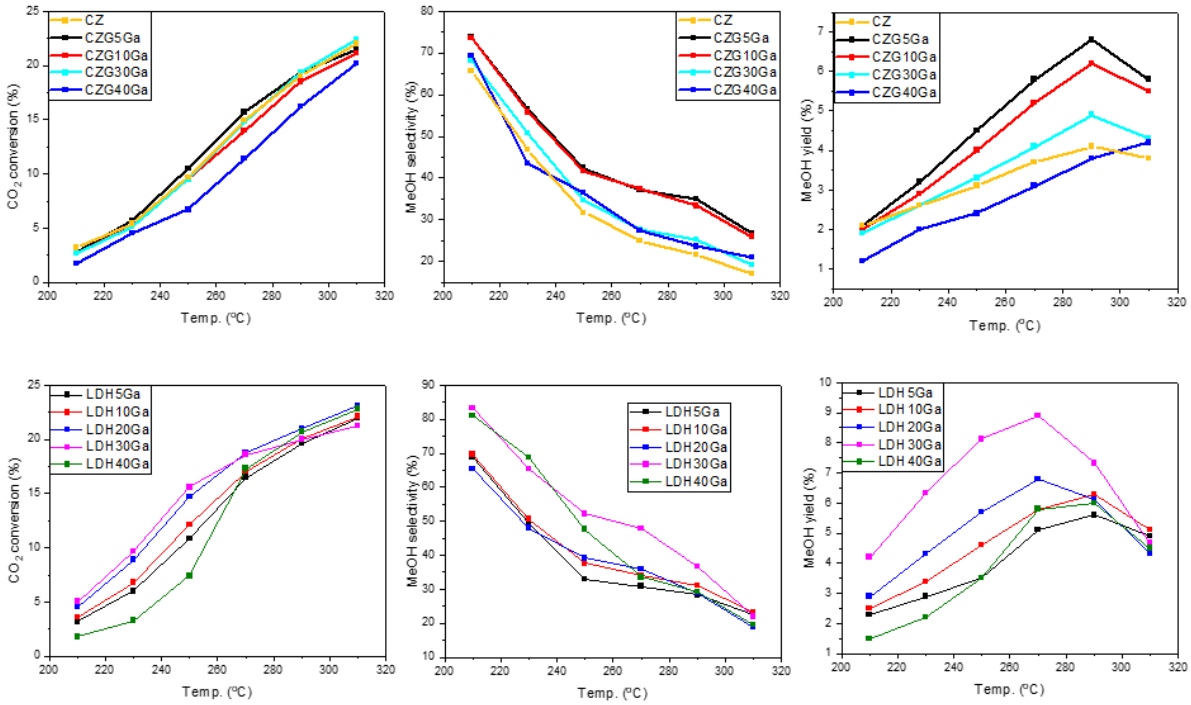

Figure 5-8. Conversion, selectivity and yield for Upper row: CZG precursor catalysts; lower row: AMO-LDH precursor catalysts in CO_2 hydrogenation to methanol.

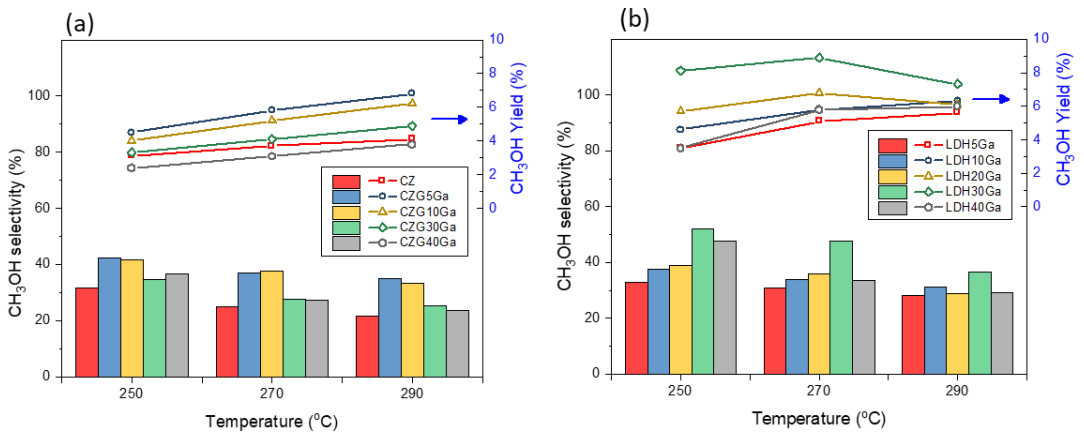

Figure 5-9. Catalytic performance of CZG (a) and AMO-LDH (b) precursor catalysts for CO_2 hydrogenation to methanol. Reaction conditions: T = 190–310 °C, P = 4.5 MPa, WHSV = 18,000 $mL \cdot g_{cat}^{-1} \cdot h^{-1}$, and H_2: CO_2 (molar) = 3: 1. For simplicity and clarity, only 250–290 °C temperature range, at which the catalysts exhibited higher activity, is presented.

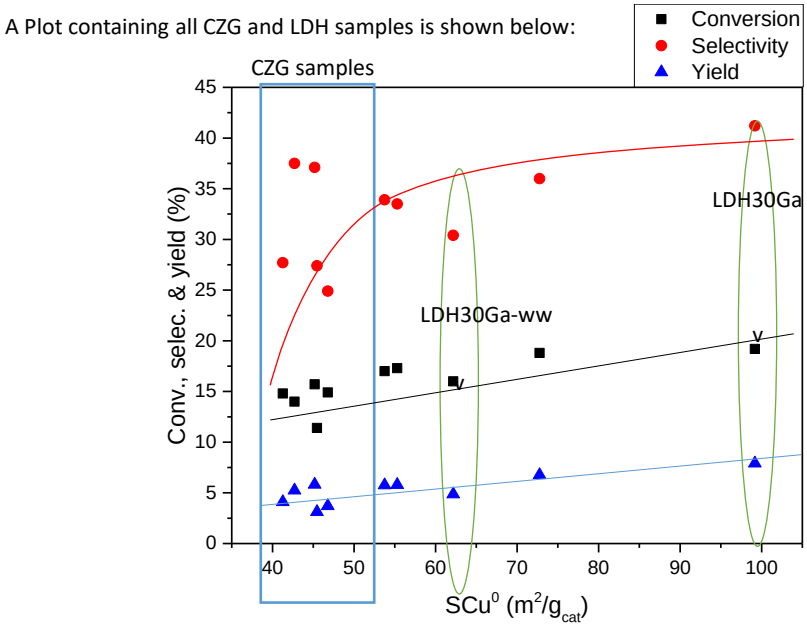

Figure 5-10. Correlation of catalytic performance with Cu surface area for CZG and AMO-LDH precursor catalysts

The enhanced Cu surface areas and dispersions of the LDH-derived samples (Table 5-1) can explain why the AMO-LDH samples are superior to the CZG samples. The surface areas and dispersions are inversely proportional to the particle size, moreover, the effect of the Cu particle size has recently been found to be strong to the catalytic reaction[43], therefore the particle size of the active species also needs to be investigated. Figure 5-11a shows that after calcination in an air atmosphere, the formation of mixed metal oxides (appeared as sphere-like particles) in the calcined CZG5Ga sample can be observed. Figure 5-11(b–d) shows the images of the reduced CZG5Ga sample prepared with an H_2 treatment at 290 ^oC (2 h), which give 5–10 nm Cu-rich particles with occasionally much larger particles (> 10nm) observed. In contrast, the image of calcined LDH30Ga (Figure 5-11e) reveals multiple curved sheets assembled mostly of single discrete layers with some edge regions of 2–3 staggered layers, indicating the AMO-LDH precursor can maintain its ultra-thin layered morphology in spite of exhibiting an amorphous phase (Figure 5-1d) after calcination. Under identical hydrogen treatment shown in Figure 5-11(f–h), many small and rather homogeneous size Cu-rich particles of less than 5 nm (mean size = 4.0 ± 0.1 nm) are formed on this positive charged sheet-like structure. In line with the morphology observation of the reduced catalysts, the reduction behaviour of the AMO-LDH samples, see Figure 5-7, displays more uniform peak profiles compared to the CZG samples. The controlled reduction with the formation of smaller Cu seeds in the AMO-LDH sample clearly reflects that Cu species must be engaged in a stable LDH structure, which offers the finely controlled nucleation and restricted mobility of metal atoms by the high surface, discrete inorganic sheets, thus can lead to small, stable, and homogeneous Cu particles. Recently, Van Den Berg *et al.*[43] have extensively tested a range of supported Cu particles from 2–15 nm and found that smaller Cu particles are more active for CO/CO_2 hydrogenation to methanol but too small Cu particles such as 2 nm show poorer activity, which is attributed to the lack of active step-edge sites and the

subtle change in local electronic structure for such small metal particles. On the other hand, Van Helden *et al.*[44] have computed for cobalt face-centred cubic particles that similar to Cu, the active site fraction of step sites (so-called B5) increases with increasing particle size until 4 nm. We believe the formation of Cu nanoparticles in the catalytically active size domain with narrow size distribution is related to a delicate control of nucleation and growth. For the AMO-LDH derived catalysts, the discrete cationic layer with high charge density appears to offer the required steric and electrostatic stabilisation, which is advantageous to make larger Cu surface area with higher metal dispersion (4 nm particle size) upon reduction. In this respect, Cu containing AMO-LDH samples are superior to those prepared by the conventional co-precipitation method.

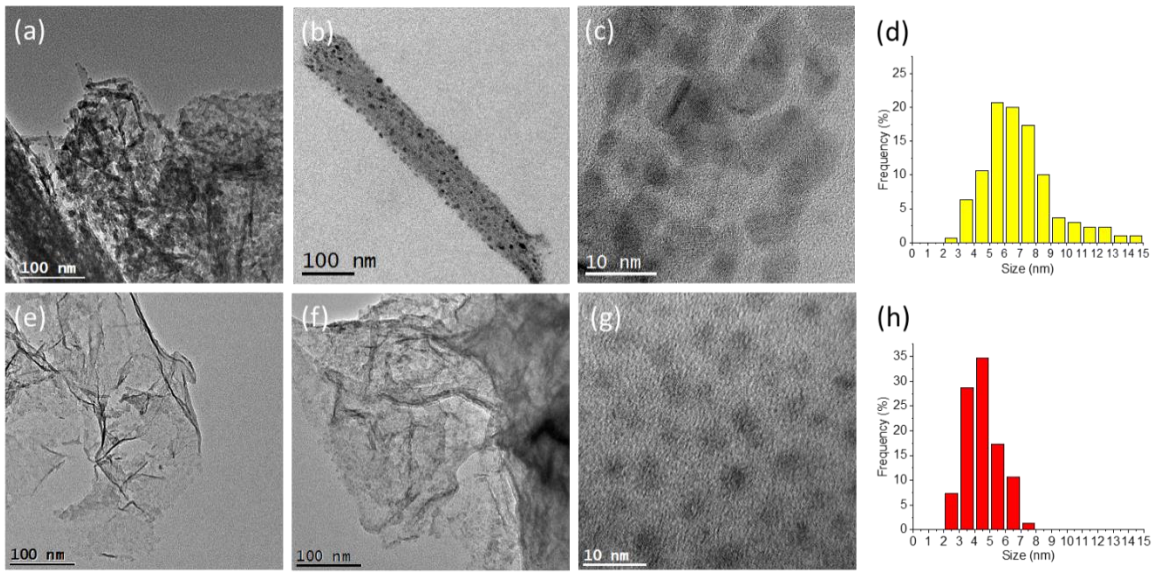

Figure 5-11. TEM images of the calcined (a, e) and reduced (b, c, f, g) samples, and size distribution diagrams (d, h) of the nanoparticles in the reduced samples. Upper row: (a) calcined CZG5Ga; (b-d) reduced CZG5Ga containing 5–10 nm Cu-rich particles (mean size = 6.3 ± 0.2 nm) with some of the much larger sizes. Lower row: (e) calcined sheet-like LDH30Ga sample; (f-h) reduced LDH30Ga containing many homogeneous small Cu-rich particles of < 5nm (mean size = 4.0 ± 0.1 nm).

The XPS results of the reduced AMO-LDH samples with various Ga contents are revealed in Figure 5-12. Figure 5-12a clearly shows the progressive increase in Ga peak area at increasing Ga content. In comparison with the peak position with reference to the C 1s transition at 285 eV, Ga is still maintained as Ga^{3+} with no sign of reduction[45]. However, the positions of $2p_{1/2}$ and $2p_{3/2}$ signals of Cu (Figure 5-12b) match well with those of Cu^0 and their peak sizes remain the same at increasing Ga concentrations. This again suggests that Cu^{2+} is totally reduced from the AMO-LDH samples upon the pre-reduction treatment under H_2 at 290 ^oC. The peak position of Zn $2p_{3/2}$ shown in Figure 5-12c of AMO-LDH samples matches with Zn^{2+} indicating that most of these cations remain unreduced in the solid

structure. However, there is a small degree of Zn^{2+} reduction to Zn^0 at Ga concentrations of 20 and 30 mole% which correspond to the precursors with pure-LDH phases as well as high surface areas. Through careful deconvolution, the broader peak can be separated into two sub-peaks of Zn^{2+} (1022.5 eV) and Zn^0 (1021.5 eV). In the literature, it has been suggested that Cu/Zn interface plays a significant role in CO_2 hydrogenation to methanol as these two species (Cu and Zn) work synergistically. Thus, placing Zn in a proximity to Cu can enhance methanol synthesis[17,29,42]. Catalysts containing Cu/ZnO were recently found to show 10 times higher activity than Cu catalysts of the same sizes but without in contact with ZnO[43]. This agrees with our observations that this composition modification is a very important one. However, many models have been put forward in the literature to explain the role of zinc, including zinc-induced defects in the copper structure[46], hydrogen spillover from zinc oxide to copper[47], the electronic stabilisation[48,49], and the morphological control on Cu nanoparticle[50]. Behrens *et al.*[17] reported that the increase in turnover frequency (TOF) for zinc-containing catalysts is mainly due to the formation of reduced zinc species from zinc oxide and subsequent migration to the copper surface. By using density functional theory (DFT) calculations, their work has indicated that a higher Miller-index copper surface, Cu(211) contains active step sites, can be favourably decorated with Zn metallic atoms rather than on the Cu(111) terrace surface. This exerts a strong electronic effect on Cu phase in this reaction. The formation of a trace amount of Zn^0 atoms upon co-reduction for the decoration on 4 nm step-edge rich Cu nanoparticles made by LDH30Ga sample in our result seems to support their conclusion.

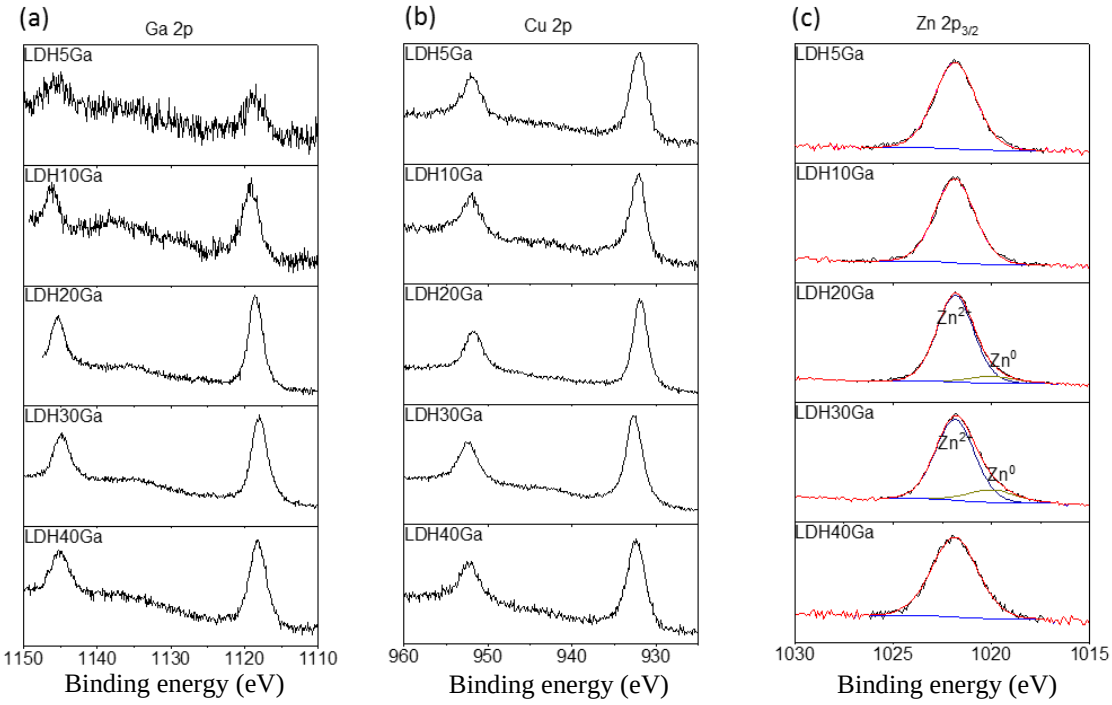

Figure 5-12. XPS spectra of the reduced AMO-LDH derived samples of (a) Ga 2p peaks; (b) Cu 2p peaks; (c) Zn 2 $p_{3/2}$ peaks at various Ga concentrations.

5.3.5 Comparison of catalytic activity

The catalytic performances of CZG5Ga, commercial HiFUEL^{TM} catalyst (Johnson Matthey, plc) and LDH30Ga with and without acetone treatment which contain comparable Cu loadings have been compared in Figure 5-13. It is apparent that the LDH30Ga sample (dispersed with acetone) reveals the best performance among the four samples. As stated[35], when the final wet slurry of LDH was dispersed with an AMO solvent (acetone), it dramatically enhanced the surface area of the final material ($S_{LDH30Ga}$ =159 m^2g^{-1} vs $S_{LDH30Ga\text{-}Ww}$ = 37 m^2g^{-1}) by exfoliating the cationic multilayers (intercalated with carbonate anions) approaching to 1–3 layers. This discrete cationic layer can facilitate the formation of small (~4 nm) and homogeneous Cu particles decorated with trace Zn atoms with narrow

size distribution, which lead to higher CO_2 conversion and methanol production. In comparison with other reported catalysts using Cu-containing LDH as the precursors without solvent exfoliation[37,51–53], our simple AMO-LDH (LDH30Ga) precursor catalyst also shows greater methanol production rate (see Table 5-2). As far as we are aware, the impressive space-time yield of methanol of 0.6 $g_{MeOH}{\cdot}g_{cat}^{-1}{\cdot}h^{-1}$ at typical reaction conditions represents one of the best reported catalytic activities for methanol synthesis using Cu-based catalysts[54]. On the other hand, it was recently reported that In_2O_3/ZrO_2 catalysts exhibited a very high selectivity for the conversion of CO_2 to methanol[55], however, the methanol space-time yield of this catalyst was only 0.3 $g_{MeOH}{\cdot}g_{cat}^{-1}{\cdot}h^{-1}$ even under 5 MPa and a high ratio of H_2: CO_2 (4–8). Moreover, it is surprising to see that our best AMO-LDH (LDH30Ga) catalyst gives a comparable methanol yield to the highly active Pd@Zn core-shell catalysts[56] that was demonstrated recently under the same reaction conditions, though Pd is commonly regarded to be more active than Cu upon modification. The methanol space-time yields of selected materials described above are compared in Table 5-2.

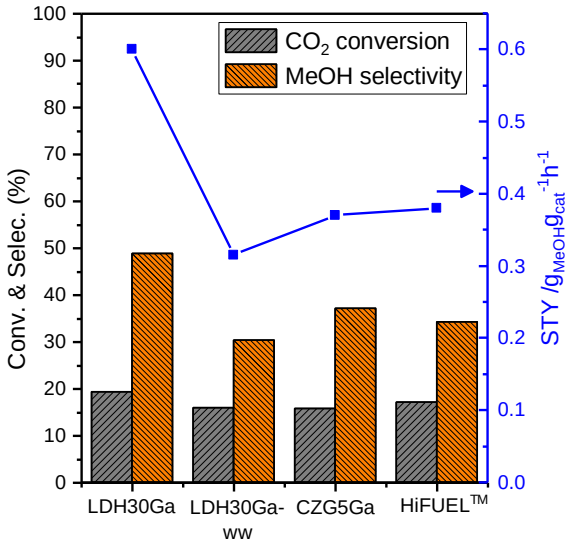

Figure 5-13. Comparison of conversion, selectivity and yield of CZG5Ga, LDH30Ga, LDH30Ga-ww, and an industrial sample, HiFUEL™ with comparable Cu loadings for the CO_2 hydrogenation to methanol at 270 °C

Table 5-2 Comparison of methanol space-time yields of selected catalysts with this work.

Catalyst	Reaction conditions			Catalytic performance	Ref.
	P (bar), T (°C)	Space velocity	H_2/CO_2	STY[b]	
LDH30Ga	45, 270	(W) 18000 mL g^{-1} h^{-1}	3	0.6	This work
LDH30Ga-ww	45, 270	(W) 18000 mL g^{-1} h^{-1}	3	0.3	
CZG5Ga	45, 270	(W) 18000 mL g^{-1} h^{-1}	3	0.4	
JM-HiFUEL™	45, 270	(W) 18000 mL g^{-1} h^{-1}	3	0.4	
LDH (Cu, Zn, Al, Y)	50, 250	(W) 10000 mL g^{-1} h^{-1}	3	0.4	37
Cu on LDH (Zn, Al, Zr) supports	50, 250	(W) 7500 mL g^{-1} h^{-1}	3	0.3	51
LDH (Cu, Zn, Al, Y)	50, 250	(W) 12000 mL g^{-1} h^{-1}	3	0.5	52
LDH (Cu, Zn, Al, Ga)	60, 250	(W) 10000 mL g^{-1} h^{-1}	Syngas H_2:CO:CO_2:He =72:10:4:14	~0.4	53
In_2O_3/ZrO_2	50, 300	(G) 16000 h^{-1}	4	0.3	55
Pd@Zn	45, 270	(W) 18000 mL g^{-1} h^{-1}	3	~0.6	56

[a] (G) = GHSV = volume flow rate/bed volume, (W) = WHSV = mass flow rate/catalyst mass.
[b] Space time yield of methanol ($g_{MeOH} \cdot g_{cat}^{-1} \cdot h^{-1}$)

5.4 Chapter conclusion

At comparable Cu loadings, a catalyst derived from the ultra-thin AMO-LDH precursor $[(Cu_{0.47}Zn_{0.32}Ga_{0.21})(OH)_2](CO_3)_{0.105}\cdot m(H_2O)\cdot n(C_3H_6O)$ (LDH30Ga) was found to give higher Cu surface areas and better catalytic performance in terms of conversion, methanol selectivity and yield. It appears to be superior to the catalyst derived from LDH precursors with normal post-treatment (water wash) as well as the samples from conventional hydroxyl-carbonate precursors (CZG samples). Interestingly, this AMO-LDH precursor can maintain its ultra-thin layered morphology in spite of exhibiting an amorphous phase after calcination and can lead to accessible, well dispersed, small, and high surface area Cu crystallites decorated with Zn atoms. Moreover, this simple catalyst precursor not only displays a better space-time yield of methanol than the commercial HiFUEL^{TM} catalyst but also outperforms those multi-doped LDHs as well as those recently-reported highly active catalysts in the literature. We believe, further optimisation of AMO-LDH catalyst precursors can open new opportunities for the preparation of size-controlled small bimetallic nanocrystallites for many catalytic processes.

Reference

1. Yu, K. M. K., Curcic, I., Gabriel, J. & Tsang, S. C. E. Recent advances in CO_2 capture and utilization. *ChemSusChem* **1,** 893–899 (2008).
2. Turner, J., Sverdrup, G., K. Mann, M. K., Maness, P. C., Kroposki, B., Ghirardi, M., Evans, R. J., Blake, D. Renewable hydrogen production. *Int. J. Energy Res.* **32,** 379–407 (2008).
3. Song, C. Global challenges and strategies for control, conversion and utilization of CO_2 for sustainable development involving energy, catalysis, adsorption and chemical processing. *Catal. Today* **115,** 2–32 (2006).
4. Chinchen, G. C., Waugh, K. C. & Whan, D. A. The activity and state of the copper surface in methanol synthesis catalysts. *Appl. Catal.* **25,** 101–107 (1986).
5. Burch, R. & Chappell, R. J. Support and additive effects in the synthesis of methanol over copper catalysts. *Appl. Catal.* **45,** 131–150 (1988).

6. Fujitani, T. & Nakamura, J. The chemical modification seen in the Cu/ZnO methanol synthesis catalysts. *Appl. Catal. A Gen.* **191,** 111–129 (2000).
7. Liao, F., Zeng, Z., Eley, C., Lu, Q., Hung, X. & Tsang, S. C. E. Electronic modulation of a copper/zinc oxide catalyst by a heterojunction for selective hydrogenation of carbon dioxide to methanol. *Angew. Chemie - Int. Ed.* **51,** 5832–5836 (2012).
8. Zander, S., Kunkes, E. L., Schuster, M. E., Schumann, J., Weinberg, G., Teschner, D., Jacobsen, N., Schlögl, R. & Behrens, M. The role of the oxide component in the development of copper composite catalysts for methanol synthesis. *Angew. Chemie - Int. Ed.* **52,** 6536–6540 (2013).
9. Spencer, M. S. The role of zinc oxide in Cu/ZnO catalysts for methanol synthesis and the water-gas shift reaction. *Top. Catal.* **8,** 259–266 (1999).
10. Fujitani, T. & Nakamura, J. The effect of ZnO in methanol synthesis catalysts on Cu dispersion and the specific activity. *Catal. Letters* **56,** 119–124 (1998).
11. Kanai, Y., Watanab, T., Fujitani, T., Saito, M., Nakamura, K. & Uchijimi, T. Evidence for the migration of ZnO_x in a Cu/ZnO methanol synthesis catalyst. *Catal. Letters* **27,** 67–78 (1994).
12. Fujita, S., Usui, M., Ito, H., Takezawa, N. Mechanisms of methanol synthesis from carbon dioxide and from carbon monoxide at atmospheric pressure over Cu/ZnO. *J. Catal.* **157,** 403–413 (1995).
13. Choi, Y., Futagami, K., Fujitani, T. & Nakamura, J. Role of ZnO in Cu/ZnO methanol synthesis catalysts - morphology effect or active site model? *Appl. Catal. A Gen.* **208,** 163–167 (2001).
14. Hambrock, J., Schröter, M. K., Birkner, A., Wöll, C. & Fischer, R. A. Nano-brass: bimetallic copper/zinc colloids by a nonaqueous organometallic route using $[Cu(OCH(Me)CH_2NMe_2)_2]$ and Et_2Zn as precursors. *Chem. Mater.* **15,** 4217–4222 (2003).
15. Sanches, S. G., Flores, J. H., De Avillez, R. R. & Pais Da Silva, M. I. Influence of preparation methods and Zr and y promoters on Cu/ZnO catalysts used for methanol steam reforming. *Int. J. Hydrogen Energy* **37,** 6572–6579 (2012).
16. Derrouiche, S., Lauron-Pernot, H. & Louis, C. Synthesis and treatment parameters for controlling metal particle size and composition in Cu/ZnO materials-first evidence of Cu_3Zn alloy formation. *Chem. Mater.* **24,** 2282–2291 (2012).
17. Behrens, M., Studt, F., Kasatkin, I., Kühl, S., Hävecker, M., Abild-Pedersen, F., Zander, S., Girgsdies, F., Kurr, P., Kniep, B., Tovar, M., Fischer, R. W., Nørskov, J. K.& Schlögl, R. The active site of methanol synthesis over $Cu/ZnO/Al_2O_3$ industrial catalysts. *Science* **336,** 893–898 (2012).
18. Kattel, S., Ramírez, P. J., Chen, J. G., Rodriguez, J. A. & Liu, P. Active sites for CO_2 hydrogenation to methanol on Cu/ZnO catalysts. *Science* **355,** 1296–1299 (2017).
19. Arena, F., Barbera, K., Italiano, G., Bonura, G., Spadaro, L. & Frusteri, F. Synthesis, characterization and activity pattern of $Cu\text{-}ZnO/ZrO_2$ catalysts in the hydrogenation of carbon dioxide to methanol. *J. Catal.* **249,** 185–194 (2007).
20. Saito, M., Fujitani, T., Takeuchi, M. & Watanabe, T. Development of copper/zinc oxide-based multicomponent catalysts for methanol synthesis from carbon dioxide and hydrogen. *Appl. Catal. A Gen.* **138,** 311–318 (1996).
21. Kurtz, M., Wilmer, H., Genger, T., Hinrichsen, O. & Muhler, M. Deactivation of supported copper catalysts for methanol synthesis. *Catal. Letters* **86,** 77–80 (2003).

22. An, X., Li, J., Zuo, Y., Zhang, Q., Wang, D. & Wang, J. A Cu/Zn/Al/Zr fibrous catalyst that is an improved CO_2 hydrogenation to methanol catalyst. *Catal. Letters* **118,** 264–269 (2007).
23. Weigel, J., Koeppel, R. A., Baiker, A. & Wokaun, A. Surface species in CO and CO_2 hydrogenation over copper/zirconia: On the methanol synthesis mechanism. *Langmuir* **12,** 5319–5329 (1996).
24. Yu, K. M. K., Tong, W., West, A., Cheung, K., Li, T., Smith, G., Guo, Y. & Tsang, S. C. E. Non-syngas direct steam reforming of methanol to hydrogen and carbon dioxide at low temperature. *Nat. Commun.* **3,** 1230 (2012).
25. Tong, W., Cheung, K., West, A., Yu, K.-M. & Tsang, S. C. E. Direct methanol steam reforming to hydrogen over $CuZnGaO_x$ catalysts without CO post-treatment: mechanistic considerations. *Phys. Chem. Chem. Phys.* **15,** 7240–7248 (2013).
26. Tong, W., West, A., Cheung, K., Yu, K. M. & Tsang, S. C. E. Dramatic effects of gallium promotion on methanol steam reforming Cu-ZnO catalyst for hydrogen production: Formation of 5Å copper clusters from Cu-$ZnGaO_x$. *ACS Catal.* **3,** 1231–1244 (2013).
27. Schumann, J., Eichelbaum, M., Lunkenbein, T., Thomas, N., Galván, M. C. A., Schlögl, R. & Behrens, M. Promoting strong metal support interaction: Doping ZnO for enhanced activity of Cu/ZnO:M (M = Al, Ga, Mg) catalysts. *ACS Catal.* **5,** 3260–3270 (2015).
28. Toyir, J., Ramírez De La Piscina, P., Fierro, J. L. G. & Homs, N. Highly effective conversion of CO_2 to methanol over supported and promoted copper-based catalysts: Influence of support and promoter. *Appl. Catal. B Environ.* **29,** 207–215 (2001).
29. Li, M. M.-J., Zeng, Z., Liao, F., Hong, X. & Tsang, S. C. E. Enhanced CO_2 hydrogenation to methanol over CuZn nanoalloy in Ga modified Cu/ZnO catalysts. *J. Catal.* **343,** 157–167 (2016).
30. Jiao, Y. N. & Hou, W. G. Effects of structural charges on points of zero charge and intrinsic surface reaction equilibrium constants of Zn-Al and Zn-Al-Fe hydrotalcite-like compounds. *Colloids Surfaces A Physicochem. Eng. Asp.* **296,** 62–66 (2007).
31. Zhang, L., Li, F., Evans, D. G. & Duan, X. Structure and surface characteristics of Cu-based composite metal oxides derived from layered double hydroxides. *Mater. Chem. Phys.* **87,** 402–410 (2004).
32. Zhang, L. H., Zheng, C., Li, F., Evans, D. G. & Duan, X. Copper-containing mixed metal oxides derived from layered precursors: Control of their compositions and catalytic properties. *J. Mater. Sci.* **43,** 237–243 (2008).
33. Behrens, M., Kasatkin, I., Kühl, S. & Weinberg, G. Phase-pure Cu,Zn,Al hydrotalcite-like materials as precursors for copper rich $Cu/ZnO/Al_2O_3$ catalysts. *Chem. Mater.* **22,** 386–397 (2010).
34. Busca, G., Costantino, U., Marmottini, F., Montanari, T., Patrono, P., Pinzari, F., Ramis, G. Methanol steam reforming over ex-hydrotalcite Cu–Zn–Al catalysts. *Appl. Catal. A Gen.* **310,** 70–78 (2006).
35. Chen, C., Yang, M., Wang, Q., Buffet, J.-C. & O'Hare, D. Synthesis and characterisation of aqueous miscible organic-layered double hydroxides. *J. Mater. Chem. A* **2,** 15102–15110 (2014).
36. Li, M. M. J., J. Zheng, J., Q, J., Liao, F., Raine, E., Kuo, W. C., Su, S. S., Po, P., Yuan, Y. & Tsang, S. C. The remarkable activity and stability of a highly dispersive beta-brass Cu-Zn catalyst for the production of ethylene glycol. *Sci. Rep.* **6,** 4–11

(2016).
37. Gao, P., Zhong, L., Zhang, L., Wang, H., Zhao, N., Wei, W. & Sun, Y. Yttrium oxide modified Cu/ZnO/Al_2O_3 catalysts via hydrotalcite-like precursors for CO_2 hydrogenation to methanol. *Catal. Sci. Technol.* **5,** 4365–4377 (2015).
38. Cheng, J., Wang, X., Yu, J., Hao, Z. & Xu, Z. P. Sulfur-resistant NO decomposition catalysts derived from Co-Ca/Ti-Al hydrotalcite-like compounds. *J. Phys. Chem. C* **115,** 6651–6660 (2011).
39. Wang, Q. & O'Hare, D. Recent advances in the synthesis and application of layered double hydroxide (LDH) nanosheets. *Chem. Rev.* **112,** 4124–4155 (2012).
40. Fichtl, M. B., Schumann, J., Kasatkin, I., Jacobsen, N., Behrens, M., Schlögl, R., Muhler, M. & Hinrichsen, O. Counting of oxygen defects versus metal surface sites in methanol synthesis catalysts by different probe molecules. *Angew. Chemie - Int. Ed.* **53,** 7043–7047 (2014).
41. Kuld, S., Conradsen, C., Moses, P. G., Chorkendorff, I. & Sehested, J. Quantification of zinc atoms in a surface alloy on copper in an industrial-type methanol synthesis catalyst. *Angew. Chemie - Int. Ed.* **53,** 5941–5945 (2014).
42. Kuld, S., Thorhauge, M., Falsig, H., Elkjær, C. F., Helveg, S., Chorkendorff, I. & Sehested, J. Quantifying the promotion of Cu catalysts by ZnO for methanol synthesis. *Science* **352,** 969–974 (2016).
43. Van Den Berg, R., Prieto, G., Korpershoek, G., van der Wal, L. I., van Bunningen, A. J., Lægsgaard-Jørgensen, S., de Jongh P. E. & de Jong, K. P. Structure sensitivity of Cu and CuZn catalysts relevant to industrial methanol synthesis. *Nat. Commun.* **7,** 13057 (2016).
44. Van Helden, P., Ciobîcə, I. M. & Coetzer, R. L. J. The size-dependent site composition of FCC cobalt nanocrystals. *Catal. Today* **261,** 48–59 (2016).
45. Moudler, J. F., Stickle, W. F., Sobol, P. E. & Bomben, K. D. *Handbook of X-ray photoelectron spectroscopy: A reference book of standard spectra for identification and interpretation of XPS data*. (Physical Electronics Division, Perkin-Elmer Corporation, Eden Prairie, 1992).
46. Günter, M. M., Ressler, T., Bems, B., Büscher, C., Genger, T., Hinrichsen, O., Muhler, M. & Schlögl, R. Implication of the microstructure of binary Cu/ZnO catalysts for their catalytic activity in methanol synthesis. *Catal. Letters* **71,** 37–44 (2001).
47. Burch, R., Golunski, S. E. & Spencer, M. S. The role of copper and zinc oxide in methanol synthesis catalysts. *J. Chem. Soc. Faraday Trans.* **86,** 2683–2691 (1990).
48. Klier, K. Methanol Synthesis. *Adv. Catal.* **31,** 243–313 (1982).
49. Frost, J. C. Junction effect interactions in methanol synthesis catalysts. *Nature* **334,** 577–580 (1988).
50. Hansen, P. L., Wagner, J. B., Helveg, S., Rostrup-Nielsen, J. R., Clausen, B. S. & Topsøe, H. Atom-resolved imaging of dynamic shape changes in supported copper nanocrystals. *Science* **295,** 2053–2055 (2002).
51. Gao, P., Zhong, L., Zhang, L., Wang, H., Zhao, N., Wei, W. & Sun, Y. Effect of hydrotalcite-containing precursors on the performance of Cu/Zn/Al/Zr catalysts for CO_2 hydrogenation: Introduction of Cu^{2+} at different formation stages of precursors. *Catal. Today* **194,** 9–15 (2012).
52. Gao, P., Zhong, L., Zhang, L., Wang, H., Zhao, N., Wei, W. & Sun, Y. Influence of modifier (Mn, La, Ce, Zr and Y) on the performance of Cu/Zn/Al catalysts via hydrotalcite-like precursors for CO_2 hydrogenation to methanol. *Appl. Catal. A Gen.*

468, 442–452 (2013).

53. Kühl, S., Schumann, J., Kasatkin, I., Hävecker, M., Schlögl, R. & Behrens, M. Ternary and quaternary Cr or Ga-containing ex-LDH catalysts - Influence of the additional oxides onto the microstructure and activity of $Cu/ZnAl_2O_4$ catalysts. *Catal. Today* **246,** 92–100 (2015).
54. Saito, M. R&D activities in Japan on methanol synthesis from CO_2 and H_2. *Catal. Surv. From Japan* **2,** 175–184 (1998).
55. Martin, O., Martín, A. J., Mondelli, C., Mitchell, S., Segawa, T. F., Hauert, R., Drouilly, C., Curulla-Ferré, D. & Pérez-Ramírez, J. Indium oxide as a superior catalyst for methanol synthesis by CO_2 hydrogenation. *Angew. Chemie - Int. Ed.* **55,** 6261–6265 (2016).
56. Liao, F., Wu, X., Zheng, J., Li, M., Kroner, A., Zeng, Z., Hong, X., Yuan, Y., Gong, X. & Tsang, S. C. E. A promising low pressure methanol synthesis route from CO_2 hydrogenation over Pd@Zn core–shell catalysts. *Green Chem.* **19,** 270–280 (2017).

Chapter 6: Capturing renewable H_2 of biomass for convenient methanol synthesis at low H_2/CO_2 over Rh-In bimetallic catalyst

6.1 Chapter overview

Methanol has grown into one of the largest chemical synthesis feedstocks due to the fact that it can be the raw materials for many chemical products and can also be directly used as a fuel or fuel substitutes. Methanol is conventionally manufactured via the syngas process from fossil fuel feedstocks. To fulfil the global commitment for an environmentally friendly and sustainable development, there is a strong interest in capturing renewable hydrogen generated from renewables such as biomass or water decomposition from solar or wind powers with carbon dioxide released in combustion to produce green methanol. However, production of renewable hydrogen is currently rather expensive and is produced in limited quantity as compared to CO_2. Particularly, in the utilisation of biomass for methanol production via gasification faces the problem of a large excess CO_2 to limited H_2 in its reforming gas mixture, which is not favourable for the downstream CO_2 hydrogenation reaction to methanol due to water-gas shift equilibrium to produce CO as the main by-product over commercial Cu-based catalysts. In this chapter, we present that a new class of Rh-In bimetallic catalysts can dramatically inhibit water-gas shift reaction, which as far as we are aware, give the highest methanol weight time yield of about 21.3 $g_{MeOH} \cdot g_{active\ metal}^{-1} \cdot h^{-1}$ with methanol selectivity of over 85% under excess CO_2 ($H_2/CO_2 \leq 3$) at 4.5MPa than all reported catalysts in literature. This makes the utilisation of biomass a competitive alternative to methanol production from the economic and the energetic point of view.

6.2 Introduction

Due to the increase in fossil fuels combustion by the increasing population and human activities, the concentration of CO_2 in the atmosphere is growing year by year. The issue of environmental pollution and global warming has become an international concern that has encouraged people to search for new sources and alternatives to alleviate the CO_2 emission problem. It has been found that CO_2 capture, storage and utilisation can effectively result in net removal of the atmospheric CO_2[1]. In addition, the combination of renewable energy and biomass with CO_2 utilisation seems to be the potential options for carbon-neutral process and sustainable development. Therefore, the recycling of CO_2 using renewable hydrogen from biomass and decomposition of water from solar, tidal wave, and wind powers through its hydrogenation to methanol, as suggested in the "Methanol economy" strategy[2], appears to be a very attractive approach due to the fact that methanol has high energy density and it is easy to be stored/transported hence suitable for replacing fossil fuels. In addition, methanol can also be the raw materials to produce thousands of chemical products.

Nowadays, methanol is predominantly produced from syngas, which is a mixture of CO, CO_2 and hydrogen gas derived from fossil resources, in a high-pressure process using a $Cu/ZnO/Al_2O_3$ catalyst[3]. However, the rapid advances in hydrogen gas availability by utilising solar energy, wind power, hydropower and biomass as well as the low-cost capture and storage of CO_2 from combustion aid the development of the synthesis of renewable methanol from CO_2 hydrogenation reaction[1,4,5]. Among all the alternative resources, biomass has been found promising in generating a CO_2/H_2 mixture that can be coupling with the downstream CO_2 hydrogenation reaction, as recently demonstrated in the low-temperature aqueous phase reforming (APR) and the supercritical water gasification (SCW)[6,7]. However, the utilisation of biomass for methanol production faces the problem of

a large excess CO_2 in the gas production. Therefore the stoichiometric adjustment has to be applied either by adding hydrogen or CO_2 removal, which require burdensome equipment and high costs[8,9]. Similarly, the production of hydrogen from renewable means is rather expensive and is produced in limited quantity as compared to CO_2[10]. Thus, to achieve the synthesis of methanol from biomass, a catalyst that can efficiently catalyse CO_2 hydrogenation to methanol, $CO_2 + 3H_2 \rightarrow CH_3OH + H_2O$, under CO_2 excess/H_2 deficient conditions would be highly desirable.

It is known that bimetallic nanoparticles/alloys show the intimate contacts of the two elements which can modify their electronic properties and change the adsorption properties of the metal surfaces[11,12]. A good example can be found in the Cu-Zn system, which is reported that Zn modified Cu surface gives better methanol production rates than the unmodified Cu surface because the Zn-modified Cu surface has lower adsorption energies that result in a stronger binding of intermediates and lower energetic barriers to the methanol product[13–15]. Although the adsorption properties of the Cu surface can be improved by modifying with Zn species, Cu surface still possesses the drawbacks on the low activity for hydrogen activation, which leads to a low coverage of surface H and slows down the further hydrogenation of the intermediates into methanol[11]. Consequently, for the Cu-based catalysts, high methanol selectivity commonly requires an extreme reaction condition (high pressure of over 10 MPa, high ratios of H_2:$CO_2 \geq 3$) otherwise CO is favourably produced through the reverse water-gas shift reaction (RWGS) route ($CO_2 + H_2 \rightarrow CO + H_2O$)[16]. In addition, it has been reported that the methanol selectivity of Cu-based catalysts is limited according to thermodynamic calculations[11], which leads to significant CO production through the reverse water-gas shift reaction, therefore to explore non-Cu based catalysts for the synthesis of methanol from biomass-derived gas is needed to accomplish this

development. In this chapter, we report a novel Rh-In bimetallic catalyst that shows optimal adsorption properties to the intermediates of methanol product than unmodified rhodium surface and is proven experimentally to give a more superior methanol production under CO_2 excess/H_2 deficient conditions. Thus, we believe that a new convenient methanol synthesis based on the biomass with lower energy cost could be established over this new class of catalyst, as illustrated in Figure 6-1.

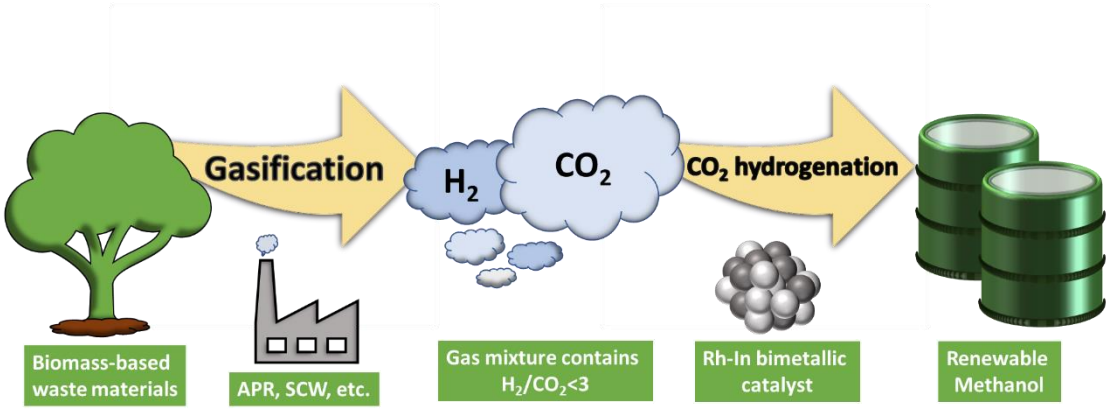

Figure 6-1. A renewable-based methanol production process via catalytic hydrogenation of CO_2 using biomass-derived CO_2/H_2 mixture over Rh-In bimetallic catalyst. (APR: Aqueous phase reforming; SCW: Supercritical water gasification.)

6.3 Results and discussion

6.3.1 Optimisation of catalyst composition

To find out the suitable support and optimise the chemical compositions of the Rh-containing catalysts for CO_2 hydrogenation to methanol, we prepared a series of binary metal oxides as the supports by co-precipitation method and loaded Rh on them using wet-impregnation method, then screened those catalysts for methanol production at relatively low pressure (4.5 MPa) and high gas hour space velocity of WHSV = 18,000 $mL \cdot g_{cat}^{-1} \cdot h^{-1}$); details on those binary oxides supported Rh samples can be found in Table 3-2, Synthesis procedure, Chapter 3. After thermal treatment in N_2 at 450 ^oC, the XRD patterns (Figure 6-2) of those binary metal oxides supported Rh samples showed broad diffraction peaks from the supports but no peaks from the Rh compounds could be detected, indicating that Rh species were well-dispersed in the small crystalline metal oxide particles. Figure 6-3 shows that all the binary oxides supported Rh samples synthesised in this study could catalyse CO_2 hydrogenation to form methanol, and the highest methanol selectivity is found in the Rh/InAlO sample (Rh/In on alumina). Moreover, the synthesis parameters of the indium-aluminium oxide supported Rh catalyst has been further studied with various temperatures of thermal treatment in N_2 as well as different Rh loadings, and it has been found that 450 ^oC thermal treatment and >3% loading are preferred for methanol production (Figure 6-4 and Figure 6-5).

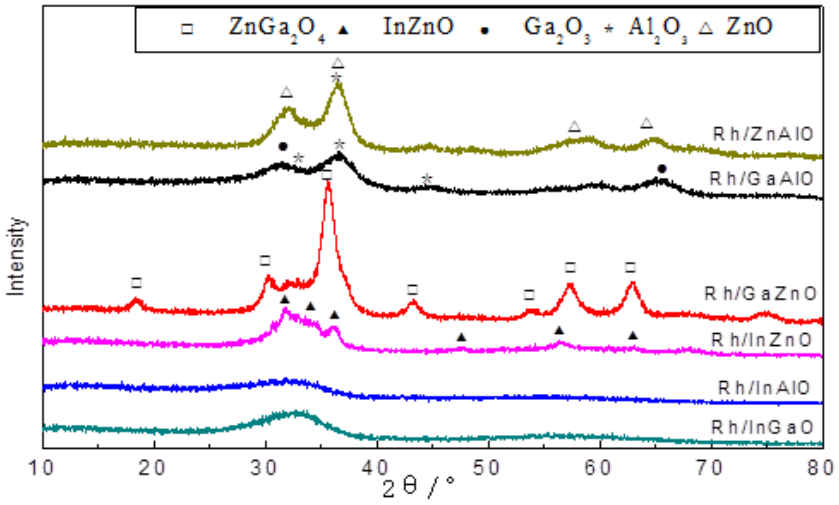

Figure 6-2. XRD patterns of the binary metal oxides supported Rh samples after 450 ºC thermal treatment in N_2.

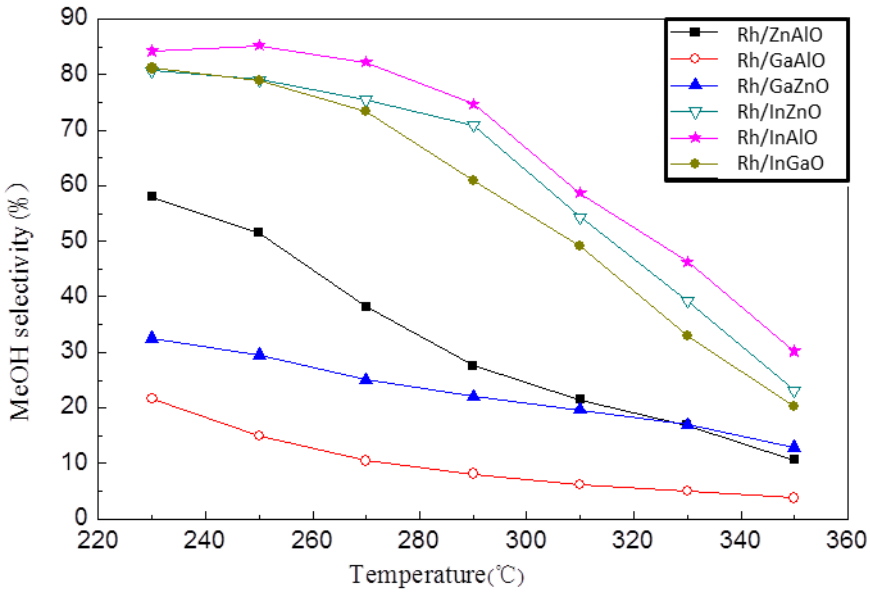

Figure 6-3. Methanol selectivities of the binary metal oxides supported Rh samples at 4.5 MPa, WHSV = 18,000 $mL \cdot g_{cat}^{-1} \cdot h^{-1}$, and H_2:CO_2 (molar) = 3:1 with different reaction temperatures.

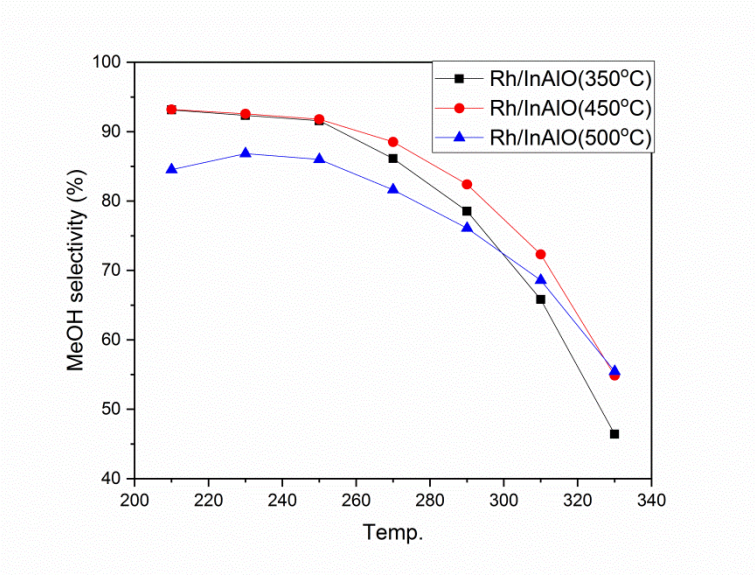

Figure 6-4. Methanol selectivities of Rh samples on the indium-aluminium oxides support with different N_2 heat treatment temperatures. Reaction conditions: 4.5 MPa, WHSV = 18,000 $mL \cdot g_{cat}^{-1} \cdot h^{-1}$, and H_2:CO_2 (molar) = 3:1.

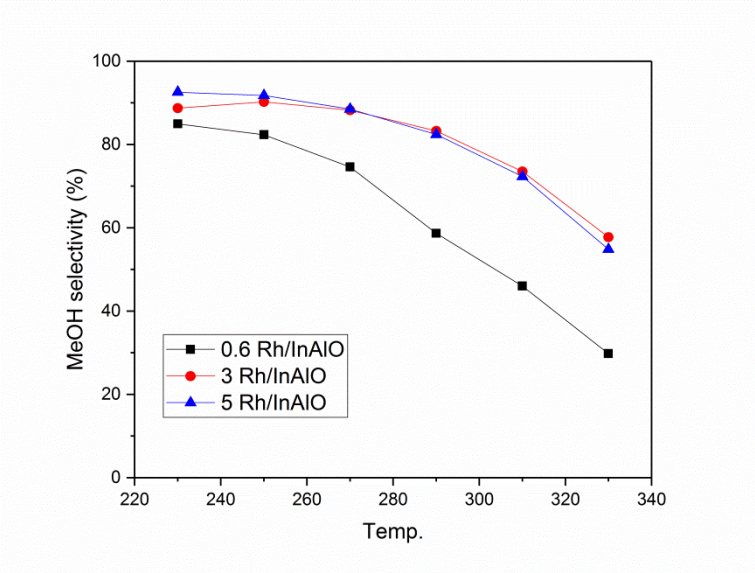

Figure 6-5. Methanol selectivities of indium-aluminium oxides supported Rh samples with different Rh loading. Reaction conditions: 4.5 MPa, WHSV = 18,000 $mL \cdot g_{cat}^{-1} \cdot h^{-1}$, and H_2:CO_2 (molar) = 3:1.

6.3.2 Catalytic performance of the catalysts

After optimising the synthesis conditions of the indium-aluminium oxide supported Rh samples, we then prepared a series of Rh-containing samples with different In/Al compositions (see the details on Table 3-3 of Chapter 3) and tested them for CO_2 hydrogenation reaction. As can be seen from Figure 6-6a that the samples with In/Al ratios from 0 to 1 give a diverse product compositions: The sample contains no indium (the Rh/(10Al)O sample) showed the total conversion of CO_2 to methane, then CO predominated the product phases when the Rh/(1In9Al)O was used. This clearly reflects the strong adsorption of CO_2 and H_2 on unmodified Rh surface to give total hydrogenation of CO_2 to mainly methane as the more favourable thermodynamic predicted product[17]. We can see that methanol emerged in the Rh/(1In9Al)O sample and then started surpassing other components in the Rh/(3In7Al)O before it becoming substantial (>85% selectivity) in the Rh/(5In5Al)O and the Rh/(10In)O samples. This suggests that the presence of indium in the vicinity of rhodium significantly attenuates the adsorption properties of rhodium sites from methanation to methanol production, and such modification of rhodium have not been reported in the literature. Similar modification of the catalytic properties of ruthenium, another well-known catalyst for catalytic methanation from CO_2 hydrogenation[17], can be found in the Ru/(5In5Al)O sample made by the identical synthesis process as the Rh/(5In5Al)O sample. Ruthenium is believed to be even more active in CO_2 methanation than rhodium[17], suggesting the modification of ruthenium should be more difficult to achieve than that of rhodium. As expected, the methanation of CO_2 over the Ru/(5In5Al)O sample cannot be excluded as a noticeable amount of methane still appeared in its product composition, suggesting the indium modification to ruthenium sites was not as extensive as it was to the rhodium sites. Along with the significant changes of the reaction products, we can also see that the CO_2 conversion dropped drastically when incorporating indium into

Rh-containing catalyst. However, according to Figure 6-6a, a decent CO_2 conversion (>10%) can still be achieved when using the Copre-Rh/(5In5Al)O sample which was made by co-precipitation of all three components, i.e., Rh, In and Al. Note that the "Copre" stands for co-precipitation. The specific surface areas and the rhodium surface areas shown in Table 6-1 reveal that adding rhodium together with indium and aluminium species in the co-precipitation process could greatly increase the specific surface area of the catalyst as well as the surface exposure of rhodium compared to the catalyst made by loading rhodium on the supports via wet-impregnation method. It is well-accepted that the active sites become abundant when the surface area of a catalyst increases, thus can enhance the conversion rate of the reactants. On the other hand, it has been recently reported that indium oxide can act as a superior catalyst for methanol production from CO_2 hydrogenation[18], therefore we also tested the indium-aluminium oxides support which was labelled as "(5In5Al)O support" in Figure 6-6a and we found that only 30% methanol selectivity with low CO_2 conversion can be achieved from the indium-aluminium oxides support without Rh loading under our conditions. This suggests that indium oxide does not contribute to the high methanol selectivity (>85%) in our indium-modified rhodium samples.

Table 6-1. Specific surface areas and rhodium surface areas of Rh/(5In5Al)O and Copre-Rh/(5In5Al)O) samples

Sample	**S_{BET} (m^2g^{-1})[a]**	**S_{Rh} (m^2g^{-1})[b]**
Rh/(5In5Al)O	32	17
Copre-Rh/(5In5Al)O)	280	133

[a]Specific surface areas determined by BET analysis.
[b]Rhodium surface areas determined by hydrogen/oxygen titration.

For the methanol synthesis from CO_2 hydrogenation reaction, the reverse water-gas shift (RWGS) reaction is the major competing reaction to the methanol production, therefore, high methanol selectivity in our indium-modified rhodium samples must possess the ability to inhibit the RWGS reaction so that to minimise the formation of CO. To get the reaction states according to the equilibrium thermodynamics of the CO_2 hydrogenation to methanol under our reaction conditions, theoretical calculations were thus performed to derive the equilibrium thermodynamics values (HSC Chemistry 5.11) where only the intrinsic properties of the gas species were considered. Here the reactant mixtures of 1 mole of CO_2(g) and 3 moles of H_2(g) were considered, and product species of H_2O(g), CO(g) and CH_3OH(g) were taken into account (experimentally identified). In CO_2 hydrogenation reaction to methanol, the use of higher CO_2: H_2 ratio is not thermodynamically favourable. Figure 6-6b shows the catalytic result of CO_2 hydrogenation with different CO_2:H_2 ratio (from 1:3 to 3:1) over our best Rh-containing sample, the Copre-Rh/(5In5Al)O. A commercial $Cu/ZnO/Al_2O_3$ catalyst (HiFUEL^{TM} R120, Johnson Matthey, plc) was also tested for the comparison. By increasing the CO_2 : H_2 ratios from 1 : 3 to 3 : 1, the methanol selectivities over the Copre-Rh/(5In5Al)O sample especially at the excess CO_2 were surprisingly achieved well beyond the thermodynamic predictions (indicated by the dotted line in Figure 6-6b), suggesting that the reaction rate of RWGS was suppressed on our indium-modified rhodium catalyst. In contrast, the methanol selectivity for the commercial $Cu/ZnO/Al_2O_3$ catalyst sharply decreased to below 10% at the conditions of CO_2 : H_2 = 3 : 1, indicating the decreasing trend of methanol selectivity in the commercial $Cu/ZnO/Al_2O_3$ catalyst was mainly governed by thermodynamics.

Figure 6-6c gives the methanol weight time yield ($g_{MeOH} \cdot g_{active\ metal}^{-1} \cdot h^{-1}$) of the Copre-Rh/(5In5Al)O as compared to the commercial HiFUEL^{TM} ($Cu/ZnO/Al_2O_3$) catalyst. We can clearly see that the methanol yields per $gram_{active\ metal}$ given by the commercial $Cu/ZnO/Al_2O_3$ catalyst compared to those in the Copre-Rh/(5In5Al)O sample were overwhelming, showing the outstanding activity of methanol production over our indium-modified rhodium catalyst. Moreover, as far as we are aware, this methanol weight time yield of 21.3 $g_{MeOH} \cdot g_{active\ metal}^{-1} \cdot h^{-1}$ obtained by the Copre-Rh/(5In5Al)O catalyst at $CO_2 : H_2 = 1 : 3$ under the typical reaction conditions is the highest value in all reported catalysts from the literature for CO_2 hydrogenation reaction[11]. The methanol selectivity as well as the weight time yield of the Copre-Rh/(5In5Al)O catalyst at $CO_2 : H_2 = 1 : 3$ can even be tuned by adjusting the WHSV to higher values. From Figure 6-7 the Copre-Rh/(5In5Al)O catalyst achieved nearly 100% CH_3OH selectivity with the weight time yield over 40 $g_{MeOH} \cdot g_{active\ metal}^{-1} \cdot h^{-1}$, proving its excellent ability to catalyse CO_2 hydrogenation to methanol with high yield. Noted that the Copre-Rh/(5In5Al)O catalyst still maintained this high methanol selectivity at superior methanol yields when it was applied to the excess $CO_2 : H_2$ conditions which were thermodynamically unfavourable for methanol production (Figure 6-6b). Consequently, with such high methanol production under excess CO_2 (H_2 deficient) reaction conditions, our new Copre-Rh/(5In5Al)O catalyst displays the major advantage to carry out CO_2 hydrogenation in capturing limited renewable hydrogen to methanol. It is particularly well suited for biomass-derived CO_2/H_2 mixtures via recently reported supercritical water gasification or aqueous phase reforming without any hydrogen admixture or CO_2 removal[6,7].

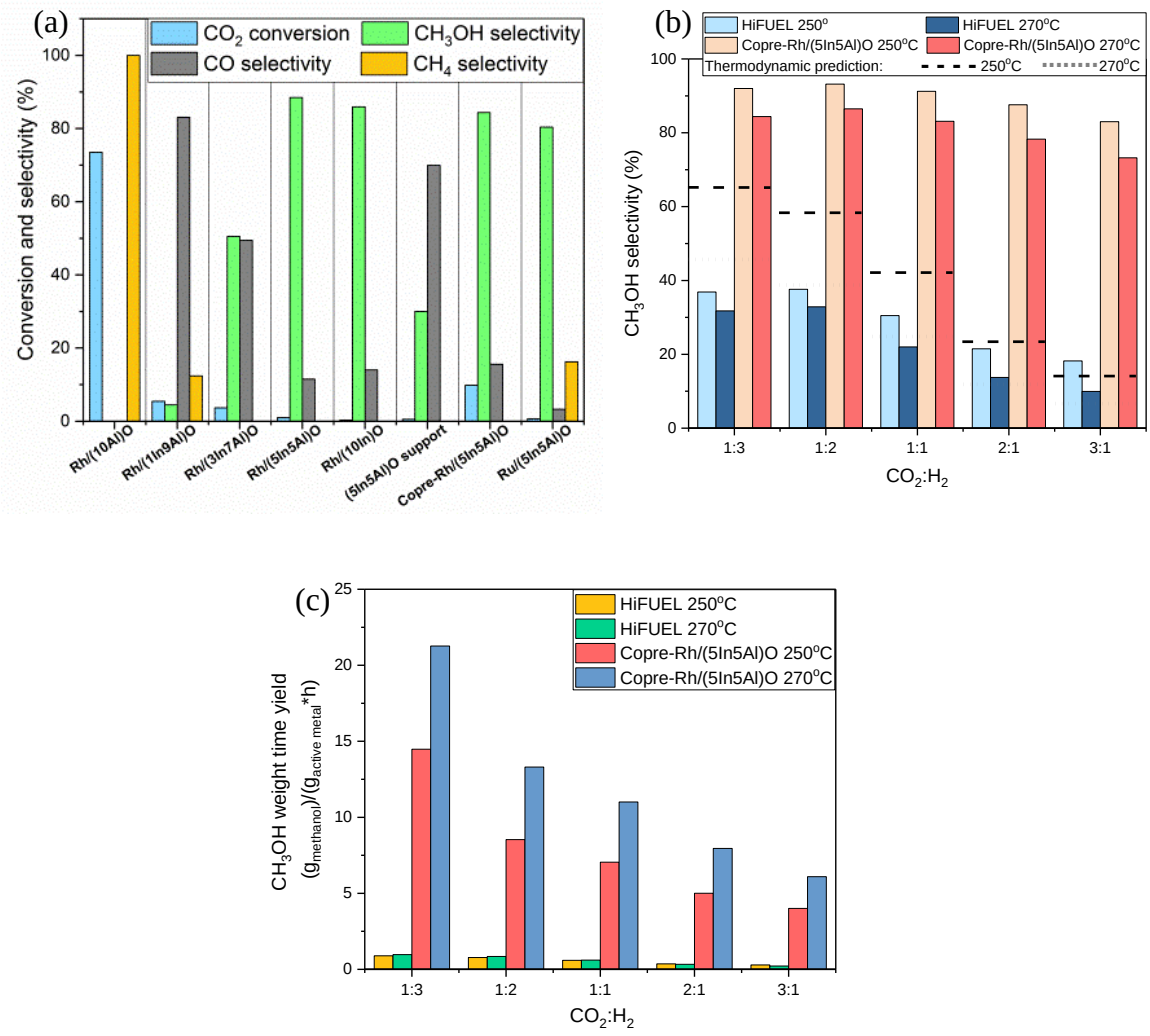

Figure 6-6. The catalytic performance of CO_2 hydrogenation to methanol at 4.5 MPa over the studied catalysts. (a) Methanol selectivities at 270 °C, CO_2:H_2=1:3 of Rh and Ru catalysts of different In/Al ratios and different synthesis methods. (b) Methanol selectivities at 250 °C and 270 °C of Copre-Rh/(5In5Al)O sample compared with commercial Cu/ZnO/Al_2O_3 catalyst under different CO_2:H_2 ratios. The dotted lines indicate the calculated methanol selectivities by taking both methanol synthesis and RWGS equilibria into account. (c) The weight time yield of methanol at 250 °C and 270 °C of Copre-Rh/(5In5Al)O sample compared with commercial Cu/ZnO/Al_2O_3 catalyst under different CO_2:H_2 ratios. The decreasing trend for both catalysts is according to the thermodynamic limits when higher CO_2: H_2 ratio is used.

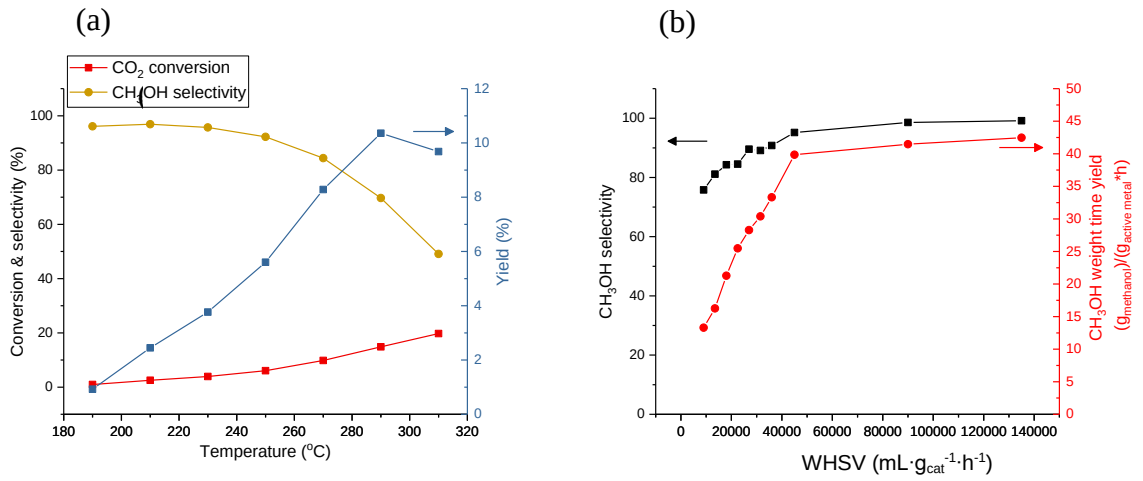

Figure 6-7. (a) CO_2 conversion, CH_3OH selectivity and yield of the Copre-Rh/(5In5Al)O catalyst under various reaction temperatures. Reaction conditions: 4.5 MPa of 75% H_2 and 25% CO_2, WHSV = 18,000 $mL \cdot g_{cat}^{-1} \cdot h^{-1}$). (b) CH_3OH selectivity and weight time yield of the Copre-Rh/(5In5Al)O catalyst under various WHSV. Reaction conditions: 4.5 MPa of 75% H_2 and 25% CO_2 at 270 °C .

6.3.3 The electronic properties of the indium-modified Rh catalyst

The change of the catalytic properties we have observed in our Rh-containing catalysts is believed to be induced by the indium incorporation. To further investigate, the electronic properties of the rhodium-containing catalysts were systematically studied by XPS. The characteristic photoemission from the Rh 3d, In 3d, Al 2p and O 1s core levels were recorded for each sample. For consistency, all the binding energies that are reported have been calibrated to the C 1s transition at 285.0 eV. The XPS of Rh 3d and In 3d of the reduced Rh-containing catalysts are shown in Figure 6-8. The Rh 3d XPS doublet peaks progressively shifted toward higher binding energy indicative of higher oxidation state of rhodium, as the indium content decreases to zero (from Rh(10In)O to Rh(10Al)O). It is known that small

rhodium particles supported on alumina are very vulnerable to oxidation[19], therefore our Rh-containing samples might have encountered a small degree of re-oxidation during their storage and transportation prior to the XPS analysis. Further investigations on the samples before/after H_2 reduction have been conducted by rhodium and indium L_3-edge XANES, see Figure 6-9. From Rh L_3-edge XANES of the Copre-Rh/(5In5Al)O catalyst, we can see the rhodium species turned metallic after H_2 reduction, but the reduced sample still contains oxidic rhodium, which implies that the sample could be re-oxidised during sample transport before performing the ex-situ XANES experiment. On the other hand, from In L_3-edge XANES spectra, we know that most indium species stay as indium oxide after H_2 reduction, but there was a slight decrease in the white line intensity, which means there might be a small degree of indium being reduced presumably when in direct contact with Rh. It is interesting to see that when having more indium content in the Rh-containing sample, less oxidic rhodium could be clearly observed through XPS analysis (Figure 6-8), which is also obtained by L_3-edge XANES analysis (Figure 6-9). This means the presence of indium can prevent the re-oxidation of rhodium species, suggesting the indium modification can change the properties of metallic rhodium and stabilise it from interaction with oxygen. On the other hand, from In 3d XPS spectra shown in Figure 6-8, there is no distinguishable shift observed, indicating that most indium species stayed as oxidic after reduction.

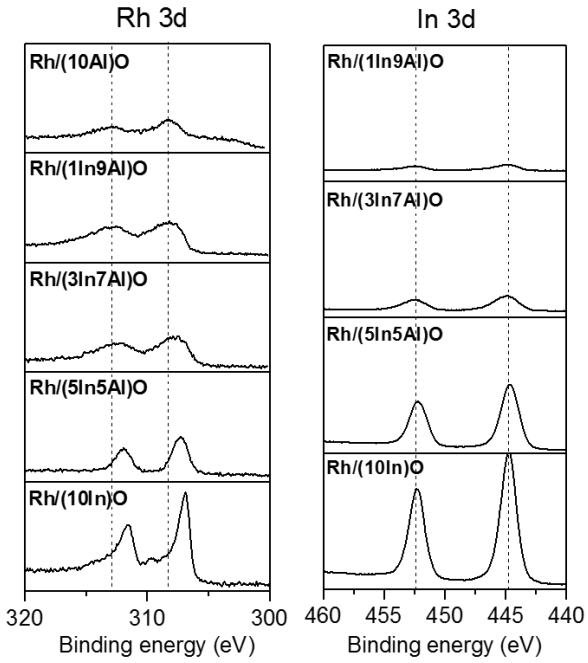

Figure 6-8. XPS Rh 3d and In 3d spectra of the reduced Rh-containing sample.

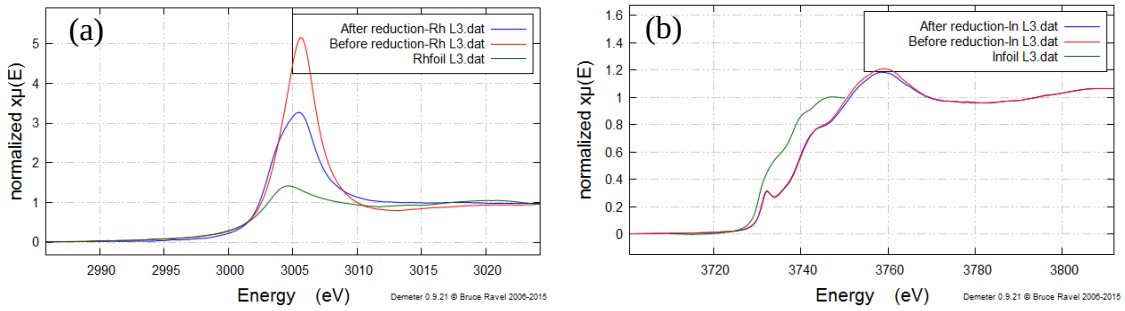

Figure 6-9. XANES spectra for the Copre-Rh/(5In5Al)O catalyst before and after H_2 reduction: (a) Rh L_3-edge XANES; (b) In L_3-edge XANES.

6.3.4 Structural characterisation of the indium-modified Rh catalyst

We then performed Rh K-edge XAS analysis, which gives the detailed information on oxidation state and local atomic structure of Rh over these samples. Figure 6-10a shows the normalised Rh K-edge XANES spectra of the reduced Rh-containing catalysts and the rhodium reference material. In agreement with the XPS result (Figure 6-8), the rhodium species of the samples containing less indium were more oxidised. The rhodium species in the Rh/(5In5Al)O, Rh/(10In)O and Copre-Rh/(5In5Al)O samples that have higher indium content showed metallic characteristic as the absorption edge positions of these samples were close to that of the rhodium foil. Figure 6-10b shows the Fourier-transform Rh K-edge EXAFS of the reduced Rh-containing samples. The k^3-weighted EXAFS and the corresponding fitting of the Rh-containing samples are shown in Figure 6-10c and the structural fitting parameters are detailed in Table 6-2. It can be seen from Figure 6-10b that in general, each Rh-containing sample contains two main shells, that is, a Rh-O shell at around 2Å and the Rh-metal shell at a longer distance. For the Rh/(In9Al)O sample, the observed distance of Rh-O at 2.04 Å along with the Rh-Rh at 2.66 Å and 3.05 Å indicate the first three Rh-(neighbour atoms) distances in a hexagonal (corundum) Rh_2O_3 structure[19]. The Rh/(3In7Al)O sample gives similar peak positions but the bond lengths and the coordination numbers that fit the experimental data are slightly different from the Rh/(1In9Al)O sample, as can be seen in Table 6-2. It is evident the Rh/(3In7Al)O sample contained a mixed structure including Rh_2O_3 and other rhodium species, i.e., metallic rhodium and Rh-In alloy, since those compounds have Rh-(neighbour atoms) bonds in the similar distance range. As the indium content further increased, the coordination number of Rh-O decreased as well as the distance of the Rh-Rh bond at around 2.66-2.70 Å increased, suggesting less oxidic rhodium existed in the system when the indium concentration was higher. Besides, in the Rh/(5In5Al)O and Copre-Rh/(5In5Al)O samples, there are three

distinctive bonds observed at the distances of 2.64, 2.82 and 3.07 Å, that are attributed to the Rh-In, Rh-In and Rh-Rh bonds, respectively, from the tetragonal $RhIn_3$ structure. The Rh/(10In)O sample gives even higher Rh-In alloy content due to its higher coordination number of the Rh-In bond. Besides, the Rh/(10In)O sample contains no oxidic rhodium species (no Rh-O bond detected). To show that the incorporation of the $RhIn_3$ alloy structure is necessary to achieve a satisfactory fitting, a comparison of the fit, both with and without $RhIn_3$ alloy structure is presented in Figure 6-11.

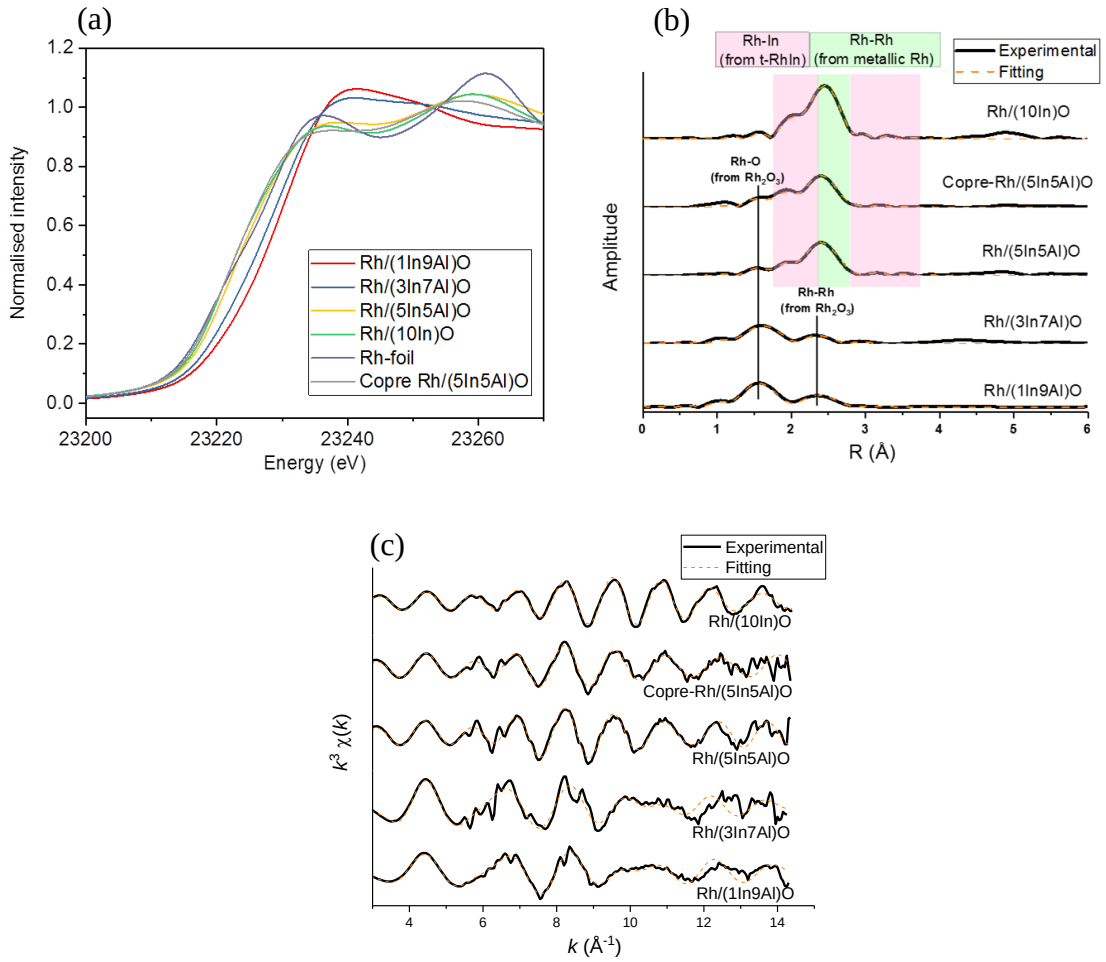

Figure 6-10. (a) normalised Rh K-edge XANES spectra of the reduced Rh-containing catalysts and the rhodium reference material; (b) k^3-weighted Rh K-edge Fourier transforms of the reduced Rh-containing samples; (c) k^3-weighted Rh K-edge EXAFS spectra for the reduced Rh-containing catalysts.

Table 6-2. The structural fitting parameters of the Rh K-edge EXAFS of the reduced Rh-containing samples.

Sample	Scatterer	R (Å)	C.N.	D-W	R factor
Rh/(1In9Al)O	O	2.04(1)	3.3(1)	0.004(1)	0.5%
	Rh	2.66(1)	2.3(1)	0.008(1)	
	Rh	3.05(3)	0.8(2)	0.015(2)	
Rh/(3In7Al)O	O	2.07(1)	2.9(2)	0.005(1)	1.9%
	Rh, In	2.68(1)	2.3(2)	0.011(1)	
	Rh, In	2.94(2)	1.0(2)	0.011(2)	
Rh/(5In5Al)O	O	2.04(2)	0.5(1)	0.006(2)	0.6%
	In	2.64(1)	3.3(1)	0.006(1)	
	Rh	2.71(1)	2.4(2)	0.005(1)	
	In	2.82(2)	2.1(2)	0.007(2)	
	Rh	3.07(2)	1.7(4)	0.007(2)	
Copre-Rh/(5In5Al)O	O	2.06(2)	0.6(2)	0.005(2)	1.4%
	In	2.62(2)	3.1(3)	0.004(2)	
	Rh	2.73(3)	1.9(2)	0.004(1)	
	In	2.83(1)	2.5(3)	0.010(2)	
	Rh	3.07(2)	2.3(4)	0.015(2)	
Rh/(10In)O	In	2.64(1)	4.4(1)	0.004(1)	0.4%
	Rh	2.73(1)	2.3(2)	0.004(1)	
	In	2.80(1)	1.4(3)	0.007(2)	
	Rh	3.03(1)	1.4(3)	0.006(2)	

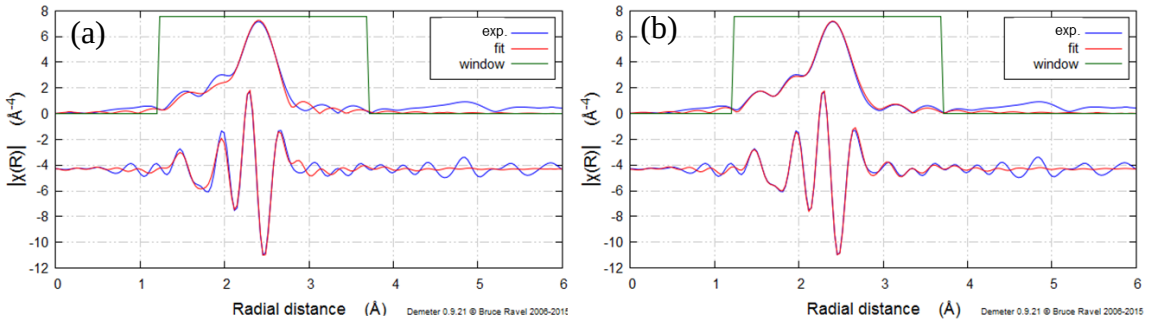

Figure 6-11. Fourier transforms of Rh K-edge EXAFS for the reduced Copre-Rh/(5In5Al)O sample: (a) fit without $RhIn_3$ structure and (b) fit with $RhIn_3$ structure.

H_2-TPR profiles of some of the Rh-containing catalysts, as well as the (5In5Al)O support, are presented in Figure 6-12. The profile for the Rh/(10Al)O catalyst showed peaks at 135 and 248 ºC, which are attributed to the reduction of well-dispersed Rh_2O_3 and of larger Rh_2O_3 particles[20], respectively. After indium incorporation, we can see that only the reduction peak of well-dispersed Rh_2O_3 can be observed in the Rh/(1In9Al)O sample, suggesting that indium addition can enhance the dispersion of rhodium species. As the indium content further increased, the reduction temperature of the well-dispersed Rh_2O_3 increased in the Rh/(3In7Al)O sample, and the reduction peak then became insignificant in the Rh/(5In5Al)O and Rh/(10In)O samples. It seems that the presence of indium species in the vicinity of rhodium had a very strong influence on the reduction of rhodium in the Rh-containing samples, that is, the indium species controlled the reduction of rhodium by slowing down the reduction reaction. On the other hand, it can be noted that the (5In5Al)O support sample started the hydrogen uptake at around 200 ºC, which is attributed to the reduction of the surface or the dispersed indium oxide phase with smaller particles sizes[21]. Therefore, under the reduction temperature of 290 ºC that we applied prior to the catalytic

testing, the reduction of rhodium species is likely to occur simultaneously with the reduction of the surface indium species to form Rh-In alloy as we observed from the Rh K-edge EXAFS analysis.

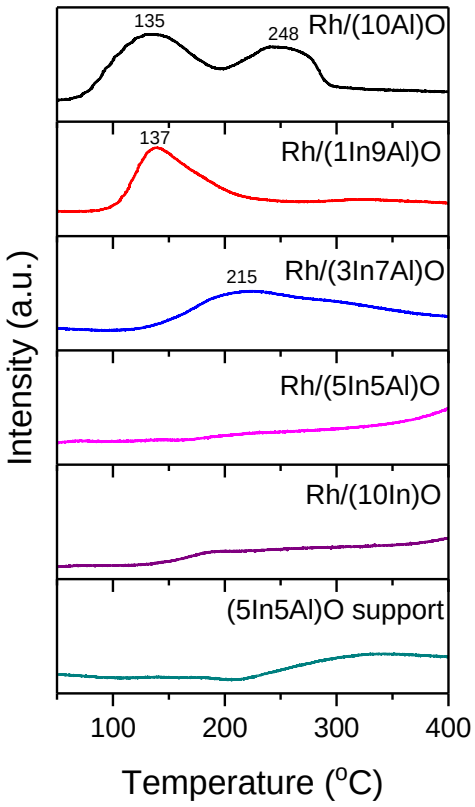

Figure 6-12. Temperature programmed reduction profiles of the Rh-containing samples.

The HR-TEM image of the reduced Copre/Rh(5In5Al)O sample and the corresponding fast-Fourier Transform (FFT) analyses of the selected area presented in Figure 6-13a reveal the existence of nano-clusters as a tetragonal $RhIn_3$ structure with the particle size of less than 5nm (the majority is 1-2nm). From the HR-TEM images, the hexagonal In_2O_3 appeared as the main light-contrast particles which were in the vicinity of the darker Rh-containing clusters that scattering electrons more strongly. This observation is in agreement with the

XRD patterns in Figure 6-13b that the hexagonal In_2O_3 phase is the predominant structure in the Copre/Rh(5In5Al)O sample either before or after catalytic testing. We cannot detect any rhodium containing phase from the XRD probably due to the low loading (~2.5 wt.%) of rhodium, and the absence of aluminium oxides phases from XRD patterns indicates that aluminium oxide species are in the form of amorphous structure.

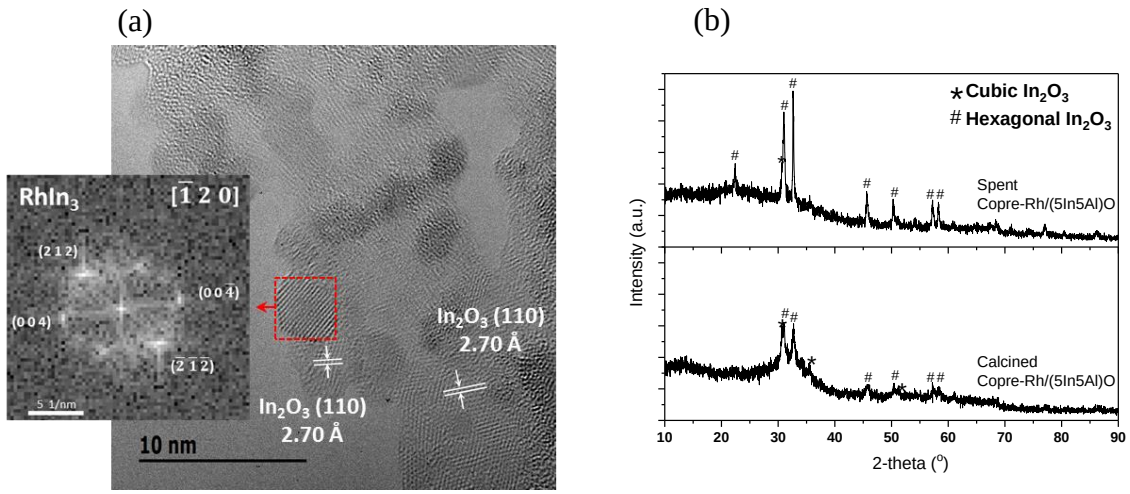

Figure 6-13. (a) HR-TEM images and the corresponding fast-Fourier Transform (FFT) analyses of the selected area of the reduced Copre/Rh(5In5Al)O sample; (b) XRD patterns of the calcined (in N_2) and spent Copre-Rh/(5In5Al)O samples.

6.3.5 Discussion

It is well-known that addition of foreign metal atoms even in a trace level to the metal catalyst to form bimetallic nanoparticles/alloys can significantly modify the electronic properties of the primary mono-metallic surface. This can alter its adsorption properties of the metallic phase (with foreign metal atom impurities) hence dictating product specificity. Many examples have been recently reported including Cu-Zn system[13–15], Pd@Zn core-shell

[11,12], Pd-Ga, Pd-In[22], Ni-Ga[23] catalysts, etc. for the selective CO/CO_2 hydrogenation. In this study, it is clear that the formation of Rh-In alloy in the reduced Rh-containing samples containing indium oxide can greatly modify their catalytic properties in the CO_2 hydrogenation reaction. According to the theoretical calculations[23–27], the catalytic activity of CO_2 hydrogenation to methanol is critically dependent on the overall adsorptivity of catalytic surfaces. Previous studies suggest that CO_2 hydrogenation involves two possible reaction pathways, i.e., the formate (HCOO) pathway and the hydrocarboxyl (COOH) pathway[28–30]. The thermodynamic preferable formation of surface HCOO (through M-O adsorption) over COOH (through M-C adsorption) from CO_2/H_2 adsorption as M moves towards right hand of the periodic table (weaker adsorption due to a decrease in metal d-band average energy and increase in electron filling) is given[26,27,31]. The selective formation of HCOO over COOH as the intermediate leads to enhanced methanol selectivity through further multi-steps hydrogenation. It is also noted that COOH is the chemical precursor of CO from reverse water-gas shift reaction[24].

In the case of unmodified rhodium, the metallic surface binds carbon dioxide and hydrogen strongly presumably through COOH so that the most thermodynamic stable product, methane, is produced from the subsequent extensive CO_2 hydrogenation. Alloying with indium on rhodium weakens the adsorption energy of the surface to favour the surface HCOO according to the literature[23,32], hence leads to methanol production. To probe the surface adsorption properties of the Rh-containing catalysts, we performed the in-situ FTIR measurement with the CO_2/H_2 flow at 50 ^oC to 290 ^oC. It can be seen from Figure 6-14a that for the Copre/Rh(10Al)O sample without indium addition, the $Rh(CO)_2$ gem-dicarbonyls species (through Rh-C interaction) were initially adsorbed on rhodium, giving the peaks at 1960-1990 cm^{-1} and 2030-2050 cm^{-1}, which are believed to be the key intermediate for the

methane formation due to strong dissociative H adsorption on Rh surface[33]. Other weakly adsorbed species, namely, linear CO, bridging CO, adsorbed H_2O, and mono-dentate formate[34,35], could also be observed in the temperature range from 50 ^oC to 290 ^oC, but the intensities of the adsorbed H_2O and mono-dentate formate greatly decreased as the increase of temperature. In contrast, the Copre/Rh(5In5Al)O sample displays different adsorbed species detected during the in-situ FTIR measurement. It can be seen from Figure 6-14b that at 50 ^oC, the prevalent intermediates including bi-dentate and poly-dentate carbonates as well as mono-dentate and bi-dentate formates (formed via adsorbed HCOO), which are regarded as the key intermediates for the methanol production[36,37], were prevalently observed. It can also be noted that a weak band attributed to the linear CO at around 2000-2010 cm^{-1} [38]. As the temperature was raised, this band was apparently increased. However, there was no formation of characteristic strong and broad bands of 2110 and 2180 cm^{-1} attributable to the gas-phase carbon monoxide[39]. Thus, this surface CO (and COOH) is expected to be in equilibrium with other surface species (i.e., HCOO) without the direct desorption of the gaseous CO.

Interestingly, it has been observed that surface HCOO is also formed preferentially over COOH on the Cu-Zn based surfaces. Behrens *et al*. have reported a similar stabilisation of adsorbed HCOO when Zn atoms are introduced on Cu step sites[13]. However, as in our case, the Cu-based surface in HiFUEL^{TM} catalyst exhibits much lower methanol selectivity at the expense of CO/H_2O via RWGS than Rh-In under identical conditions at the present pressure regime. It is noted that H adsorption energies on Cu (111) decorated by Zn is very low, which leads to low activity for H_2 dissociation on Cu-based surface[11]. This could lead to a low surface H coverage that slows down the further hydrogenation rate of HCOO into methanol. In addition, the decomposition of COOH to adsorbed CO and OH is less

dependent on the concentration of surface H according to reaction stoichiometry[11], which rapidly consumes the produced COOH to CO/H_2O via RWGS reaction and shifts the equilibrium between HCOO/COOH. The in-situ FTIR measurement of the commercial $Cu/ZnO/Al_2O_3$ sample shown in Figure 6-15, which gives the information that the surface of the commercial $Cu/ZnO/Al_2O_3$ catalyst showed predominantly the products of the RWGS reaction (CO and H_2O): It is shown that at low temperature the water species could be observed, and the small sharp peaks at around 2060-2080 cm^{-1} are the bands corresponding to the chemisorbed CO on a low Miller-index plane of Cu[37]. When the temperature increased, the vibrations of water vapour enhanced. In addition, two strong and broad bands at 2110 and 2180 cm^{-1} attributed to the gas-phase carbon monoxide demonstrated that the RWGS reaction had occurred[39]. Note that the absence of the surface adsorbed intermediates is showing a consequence of the low residence time as well as relatively weak adsorption of these species on the Cu surface. In contrast, our Rh-based surface is expected to show a more superior ability in activating H_2 than that of in Cu-based catalysts as indicated by its higher H adsorption energie[11,40]. As predicted by the theoretical model, H adsorption energy increases as one goes to the left from the group 11 metals (Cu, Ag, Au)[41,42]. Thus, we demonstrate that the higher H and HCOO surface coverages on RhIn due to optimal surface adsorptivity will favour the high methanol production rate as well as suppressing the surface COOH to inhibit the RWGS reaction. This result has clearly suggested the unique surface properties of bimetallic RhIn catalyst is better adapted to tackle low ratios of H_2/CO_2 mixtures from biomass to methanol at mild conditions compared to the commercial $Cu/ZnO/Al_2O_3$ catalysts.

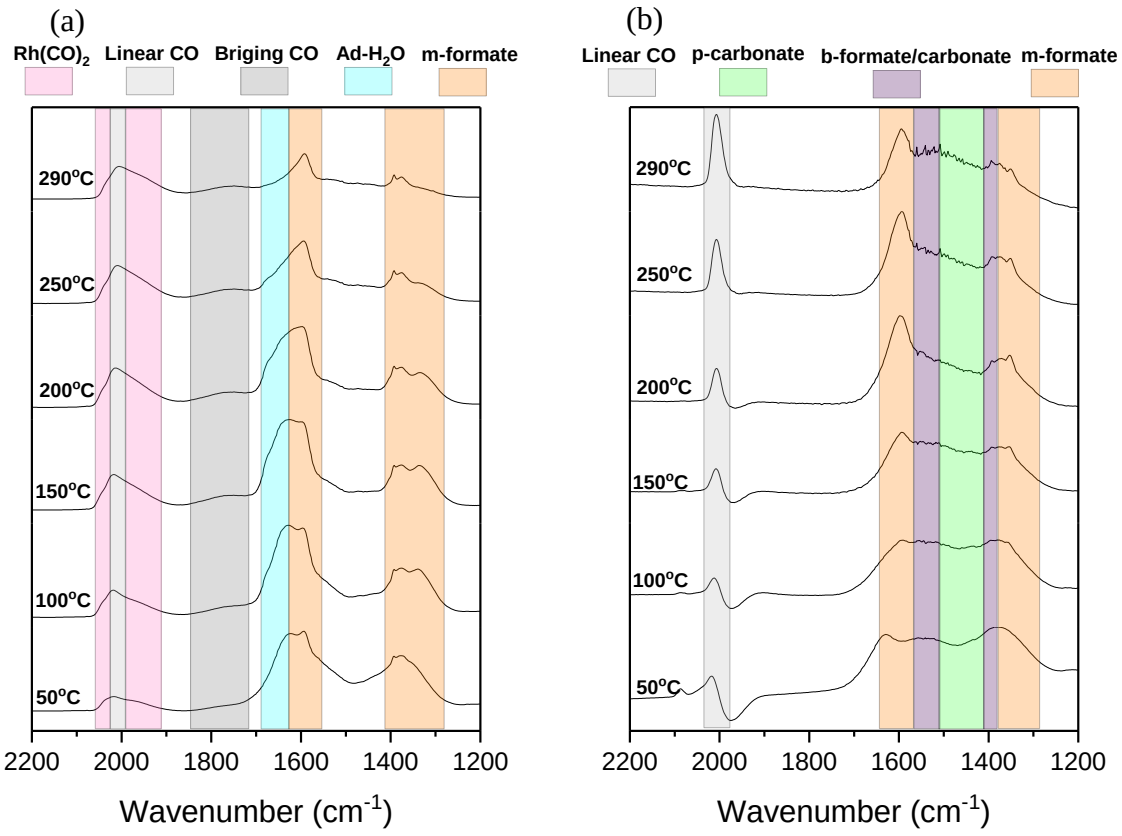

Figure 6-14. In-situ FTIR spectra of the adsorbed species on the reduced surface. (a) Copre/Rh(10Al)O sample; (b) Copre/Rh(5In5Al)O sample. The gas flow of 25% CO_2 and 75% H_2 was passed through the catalyst pellets made by 20 mg of samples at various temperatures.

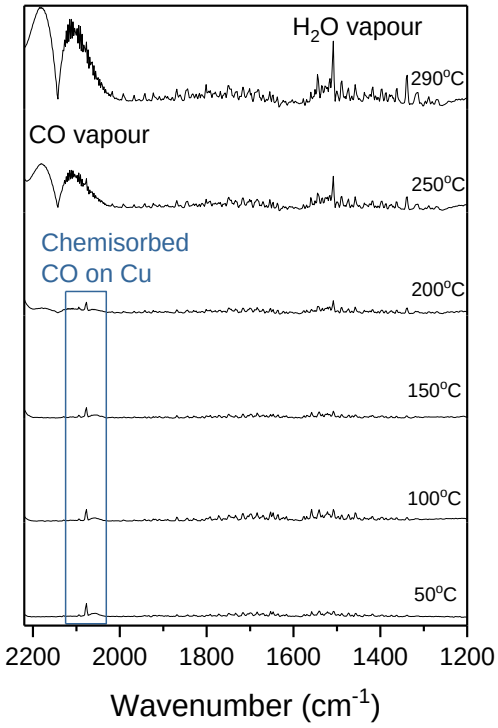

Figure 6-15. In-situ FTIR spectra of the adsorbed species on the reduced commercial $Cu/ZnO/Al_2O_3$ (HiFUEL^{TM}) surface. The gas flow of 25% CO_2 and 75% H_2 was passed through the catalyst pellets made by 20 mg of samples at various temperatures.

6.4 Chapter conclusion

It is reported that Rh-containing catalysts with indium oxide inclusion can generate Rh-In alloy surface which offers catalytically active sites for selective methanol synthesis from CO_2/H_2 mixtures. This Rh-In surface appears to stabilise surface HCOO-intermediates for superior methanol production with impressive weight time yield whereas suppressing the formation of COOH-adsorbed species for RWGS reaction at applied pressure. Moreover, the Rh-In catalysts can maintain high methanol selectivity of over 85% under practically low H_2/CO_2 conditions at a high flow rate, which is far from the thermodynamically

favourable regime for methanol production. With the increasing demands for the renewable methanol synthesis from biomass resources, we believe that the superior catalytic performance of this novel Rh-In catalyst under a diverse of CO_2/H_2 ratios allows a more efficient handling with the upstream CO_2/H_2 production from the current biomass gasification processes.

Reference

1. Yu, K. M. K., Curcic, I., Gabriel, J. & Tsang, S. C. E. Recent advances in CO_2 capture and utilization. *ChemSusChem* **1,** 893–899 (2008).
2. Olah, G. A., Goeppert, A. & Prakash, G. K. S. Beyond oil and gas: the methanol economy. *Angew. Chemie - Int. Ed.* **44,** 2636–2639 (2005).
3. Chinchen, G. C., Denny, P. J., Jennings, J. R., Spencer, M. S. & Waugh, K. C. Synthesis of methanol. Part 1. Catalysts and kinetics. *Appl. Catal.* **36,** 1–65 (1988).
4. Turner, J., Sverdrup, G., K. Mann, M. K., Maness, P. C., Kroposki, B., Ghirardi, M., Evans, R. J., Blake, D. Renewable hydrogen production. *Int. J. Energy Res.* **32,** 379–407 (2008).
5. Song, C. Global challenges and strategies for control, conversion and utilization of CO_2 for sustainable development involving energy, catalysis, adsorption and chemical processing. *Catal. Today* **115,** 2–32 (2006).
6. Huber, G. W., Shabaker, J. W. & Dumesic, J. A. Raney Ni-Sn catalyst for H_2 production from biomass-derived. *Science* **300,** 2075–2077 (2003).
7. Reddy, S. N., Nanda, S., Dalai, A. K. & Kozinski, J. A. Supercritical water gasification of biomass for hydrogen production. *Int. J. Hydrogen Energy* **39,** 6912–6926 (2014).
8. Specht, M., Bandi, A., Baumgart, F., Murray, C. N. & Gretz, J. Synthesis of methanol from biomass/CO_2 resources. *Greenh. Gas Control Technol.* **723,** 1–6 (1999).
9. Yin, X., Leung, D. Y. C., Chang, J., Wang, J., Fu, Y. & Wu, C. Characteristics of the synthesis of methanol using biomass-derived syngas. *Energy & Fuels* **19,** 305–310 (2005).
10. Götz, M., Lefebvre, J., Mörs, F., Koch, A. M. Graf, F., Bajohr, S., Reimert, R. & Kolb, T. Renewable power-to-gas: A technological and economic review. *Renew. Energy* **85,** 1371–1390 (2016).
11. Liao, F., Wu, X., Zheng, J., Li, M., Kroner, A., Zeng, Z., Hong, X., Yuan, Y., Gong, X. & Tsang, S. C. E. A promising low pressure methanol synthesis route from CO_2 hydrogenation over Pd@Zn core–shell catalysts. *Green Chem.* **19,** 270–280 (2017).
12. Liao, F., Wu, X., Zheng, J., Li, M., Zeng, Z., Hong, X., Kroner, A., Yuan, Y., Gong, X. & Tsang, S. C. E. Pd@Zn core–shell nanoparticles of controllable shell thickness for catalytic methanol production. *Catal. Sci. Technol.* **6,** 7698–7702 (2016).

13. Behrens, M., Studt, F., Kasatkin, I., Kühl, S., Hävecker, M., Abild-Pedersen, F., Zander, S., Girgsdies, F., Kurr, P., Kniep, B., Tovar, M., Fischer, R. W., Nørskov, J. K.& Schlögl, R. The active site of methanol synthesis over $Cu/ZnO/Al_2O_3$ industrial catalysts. *Science* **336,** 893–898 (2012).
14. Kuld, S., Thorhauge, M., Falsig, H., Elkjær, C. F., Helveg, S., Chorkendorff, I. & Sehested, J. Quantifying the promotion of Cu catalysts by ZnO for methanol synthesis. *Science* **352,** 969–974 (2016).
15. Li, M. M.-J., Zeng, Z., Liao, F., Hong, X. & Tsang, S. C. E. Enhanced CO_2 hydrogenation to methanol over CuZn nanoalloy in Ga modified Cu/ZnO catalysts. *J. Catal.* **343,** 157–167 (2016).
16. Saito, M. R&D activities in Japan on methanol synthesis from CO_2 and H_2. *Catal. Surv. From Japan* **2,** 175–184 (1998).
17. Frontera, P., Macario, A., Ferraro, M. & Antonucci, P. Supported catalysts for CO_2 methanation: A review. *Catalysts* **7,** 59 (2017).
18. Martin, O., Martín, A. J., Mondelli, C., Mitchell, S., Segawa, T. F., Hauert, R., Drouilly, C., Curulla-Ferré, D. & Pérez-Ramírez, J. Indium oxide as a superior catalyst for methanol synthesis by CO_2 hydrogenation. *Angew. Chemie - Int. Ed.* **55,** 6261–6265 (2016).
19. Kroner, A. B., Newton, M. A., Tromp, M., Russell, A. E., Dent, A. J. & Evans, J. Structural characterization of alumina-supported Rh catalysts: Effects of ceriation and zirconiation by using metal-organic precursors. *ChemPhysChem* **14,** 3606–3617 (2013).
20. Vis, J. C., van't Blik, H. F. J., Huizinga, T., van Grondelle, T. & Prins, R. The morphology of rhodium supported on TiO_2 and Al_2O_3 as studied by temperature-programmed and transmission electron microscopy. *J. Catal.* **95,** 333–345 (1985).
21. Chen, M., Xu, J., Liu, Y. M., Cao, Y., He, H. Y. & Zhuang, J. H. Supported indium oxide as novel efficient catalysts for dehydrogenation of propane with carbon dioxide. *Appl. Catal. A Gen.* **377,** 35–41 (2010).
22. Iwasa, N., Mayanagi, T., Ogawa, N., Sakata, K. & Takezawa, N. New catalytic functions of Pd-Zn, Pd-Ga, Pd-In, Pt-Zn, Pt-Ga and Pt-In alloys in the conversions of methanol. *Catal. Letters* **54,** 119–123 (1998).
23. Studt, F., Sharafutdinov, I., Abild-Pedersen, F., Elkjær, C. F., Hummelshøj, J. S., Dahl, S., Chorkendorff, I. & Nørskov, J. K. Discovery of a Ni-Ga catalyst for carbon dioxide reduction to methanol. *Nat. Chem.* **6,** 320–324 (2014).
24. Rodriguez, J. A., Evans, J., Feria, L., Vidala, A. B., Liu, P., Nakamura, K. & Illas. F. CO_2 hydrogenation on Au/TiC, Cu/TiC, and Ni/TiC catalysts: Production of CO, methanol, and methane. *J. Catal.* **307,** 162–169 (2013).
25. Herron, J. A., Scaranto, J., Ferrin, P., Li, S. & Mavrikakis, M. Trends in formic acid decomposition on model transition metal surfaces: A density functional theory study. *ACS Catal.* **4,** 4434–4445 (2014).
26. Liu, C., Cundari, T. R. & Wilson, A. K. CO_2 reduction on transition metal (Fe, Co, Ni, and Cu) surfaces: In comparison with homogeneous catalysis. *J. Phys. Chem. C* **116,** 5681–5688 (2012).
27. Dietz, L., Piccinin, S. & Maestri, M. Mechanistic insights into CO_2 activation via reverse water - Gas shift on metal surfaces. *J. Phys. Chem. C* **119,** 4959–4966 (2015).
28. Yang, Y., Mims, C. A., Mei, D. H., Peden, C. H. F. & Campbell, C. T. Mechanistic studies of methanol synthesis over Cu from $CO/CO_2/H_2/H_2O$ mixtures: The source of C in methanol and the role of water. *J. Catal.* **298,** 10–17 (2013).
29. Yang, Y., Evans, J., Rodriguez, J. A., White, M. G. & Liu, P. Fundamental studies

of methanol synthesis from CO_2 hydrogenation on Cu(111), Cu clusters, and Cu/ZnO(000$\bar{1}$). *Phys. Chem. Chem. Phys.* **12,** 9909–9917 (2010).
30. Zhao, Y.-F., Yang, Y., Mims, C. A., Peden, C. H. F., Li, J. & Mei, D. Insight into methanol synthesis from CO_2 hydrogenation on Cu(111): Complex reaction network and the effects of H_2O. *J. Catal.* **281,** 199–211 (2011).
31. Ruban, A., Hammer, B., Stoltze, P., Skriver, H. L. & Nørskov, J. K. Surface electronic structure and reactivity of transition and noble metals. *J. Mol. Catal. A Chem.* **115,** 421–429 (1997).
32. Pápai, I., Ushio, J. & Salahub, D. R. Chemisorption of formate and acetate on cluster models of Rh and bimetallic RhSn clusters. *Surf. Sci.* **282,** 262–272 (1993).
33. Beuls, A., Swalus, C., Jacquemin, M., Heyen, G., Karelovic, A. & Ruiz, P. Methanation of CO_2: Further insight into the mechanism over Rh/γ-Al_2O_3 catalyst. *Appl. Catal. B Environ.* **113–114,** 2–10 (2012).
34. Karelovic, A. & Ruiz, P. Improving the hydrogenation function of Pd/γ-Al_2O_3 catalyst by Rh/γ-Al_2O_3 addition in CO_2 methanation at low temperature. *ACS Catal.* **3,** 2799–2812 (2013).
35. Karelovic, A. & Ruiz, P. CO_2 hydrogenation at low temperature over Rh/γ-Al_2O_3 catalysts: Effect of the metal particle size on catalytic performances and reaction mechanism. *Appl. Catal. B Environ.* **113–114,** 237–249 (2012).
36. Collins, S., Baltanas, M. & Bonivardi, A. An infrared study of the intermediates of methanol synthesis from carbon dioxide over Pd/β-Ga_2O_3. *J. Catal.* **226,** 410–421 (2004).
37. Sun, Q., Liu, C.-W., Pan, W., Zhu, Q.-M. & Deng, J.-F. In situ IR studies on the mechanism of methanol synthesis over an ultrafine Cu/ZnO/Al_2O_3 catalyst. *Appl. Catal. A Gen.* **171,** 301–308 (1998).
38. Solymosi, F., Erdohelyi, A. & Bansagi, T. Infrared study of the surface interaction between H_2 and CO_2 over rhodium on various supports. *J. Chem. Soc. Faraday Trans. I* **77,** 2645–2657 (1981).
39. Millar, G. J., Rochester, C. H. & Waugh, K. C. An in situ high pressure FT-IR study of CO_2/H_2 interactions with model ZnO/SiO_2, Cu/SiO_2 and Cu/ZnO/SiO_2 methanol synthesis catalysts. *Catal. Letters* **14,** 289–295 (1992).
40. Ferrin, P., Kandoi, S., Nilekar, A. U. & Mavrikakis, M. Hydrogen adsorption, absorption and diffusion on and in transition metal surfaces: A DFT study. *Surf. Sci.* **606,** 679–689 (2012).
41. Nørskov, J. K. Chemisorption on metal surfaces. *Reports Prog. Phys.* **53,** 1253–1295 (1990).
42. Toyoshima, I. & Somorjai, G. A. Heats of chemisorption of O_2, H_2, CO, CO_2, and N_2 on polycrystalline and single crystal transition metal surfaces. *Catal. Rev.* **19,** 105–159 (1979).

Chapter 7: Importance of structural integrity of carbon conjugated mediator for photocatalytic hydrogen generation from water over CdS-carbon nanotube-MoS_2 composite

The work in this chapter has been adapted and reproduced in part with permission from: Molly Meng-Jung Li, Poppy Mills, Simon M Fairclough, Alex Robertson, Yung-Kang Peng, Jamie Warner, Chunyang Nie, Emmanuel Flahaut, Shik Chi Edman Tsang. *Chemical Communications*, 2016, 52, 13596-13599. Copyright 2016 Royal Society of Chemistry.

7.1 Chapter overview

Photocatalytic water splitting has a high potential for application as a clean and renewable way to generate hydrogen, because it is a process with negligible CO_2 emission: Decomposition of water directly into hydrogen and oxygen under sunlight irradiation with a semiconductor material. Recently, the composite photocatalysts are emerging as an extensively studied project. They are prepared by combining non-oxide materials with oxides or other non-oxides, which can lead to an efficient charge separation while expanding the absorption spectrum of the photocatalyst. In this chapter, we report that the incorporation of quantum dots, CdS, is shown to significantly promote photocatalytic hydrogen production from water over single-layer MoS_2 via dispersing the two materials on carbon nanotubes to form a three-component nanocomposite. In addition, the hydrogen evolution rate of this nanocomposite is found critically dependent on the content and structural integrity of carbon nanotube such that double-walled carbon nanotube shows more superior H_2 production to single-walled carbon nanotube because its inner carbon nanotubes survive from the structural damage during functionalisation.

7.2 Introduction

The depletion of fossil fuel reserves and the undeniable environmental harms caused by their overconsumption make photocatalytic H_2 production from water attractive as future renewable energy source[1,2]. Typically, the photocatalytic splitting of water requires semiconductors to capture a photon with energy equal to or greater than their band gap energy. The photons are absorbed by a semiconductor nanocrystal causing the generation of photo-excited electrons and holes in the conduction and valence bands, respectively. The excited electron-hole pairs, known as excitons, are then subject to two main competitive deactivation routes, namely excitons recombination and excitons separation followed by chemical reactions. The former route is undesirable in photocatalysis since this only emits heat or light with no chemical process involved whereas the latter is important for photocatalytic reduction of water to hydrogen gas.

Nanosize CdS is a quantum dot material for efficient capture and emit photons due to its characteristic band edges and band gap[3,4]. However, it displays very poor photocatalytic activity due to rapid exciton recombination[5,6]. On the other hand, molybdenum disulfide (MoS_2) is not an intrinsic active semiconductor to capture photons in photocatalysis but its conduction band (-0.12 eV vs NHE) and valence band (1.78 eV vs NHE) render it suitable for electrochemical water-splitting[7]. It has been reported that an intimate mixture of CdS/MoS_2 can catalyse photocatalytic H_2 evolution efficiently[8]. In addition, CdS supported on carbon materials is also proven to suppress charge recombination and provide active adsorption sites, which leads to the enhancement of photocatalytic activity[9–13]. Furthermore, the use of graphene to support CdS quantum dots and single layer MoS_2 (s-MoS_2) into nanosize appears to give higher hydrogen evolution rate[7]. However, it is not yet clear about the functional roles of each component in these composite mixtures and their synergistic

effect(s) for photocatalytic H_2 evolution. It is believed that by elucidating such materials interactions, rational design of composite materials for more efficient photocatalytic conversion to chemicals could be developed.

In this chapter, we report the systematic study of correlation of photocatalytic H_2 activity with structural and electronic properties of CdS and s-MoS_2 as well as their interactions with surface functionalised single, double and multi-walled carbon nanotubes (SWNT, DWNT and MWNT) in composites using a range of characterisation techniques including XRD, TEM, and Raman. Particularly, time-resolved photoluminescence (TRPL) technique is invoked to investigate the lifetime of excitons with reference to activity measured for this type of composite. It is found that the excitons recombination readily taken place on CdS upon light activation can be effectively quenched when it is mixed with carbon nanotubes (CNTs) due to the rapid transfer of the photo-excited electrons to carbon structure before the proton reduction from water for the hydrogen production over s-MoS_2. Thus, the light capturing sites (CdS) can be separated from hydrogen production sites (s-MoS_2) via CNTs as the electronic mediator. Higher hydrogen production rate is obtained over the two finely dispersed phases on the CNTs than those without the carbon mediator due to the higher electron conductivity and storage capacity of CNTs[14,15]. It is also found that typical acid functionalisation of CNTs for the immobilisation of CdS and MoS_2 can result in the destruction of surface graphitic conjugation and affect the essential process of electron transfer, which will lead to poor activity. As a result, DWNT with intact inner carbon nanotubes acts as an optimal electron mediator for photocatalytic hydrogen production.

7.3 Results and discussion

The powder XRD of the synthesised CdS quantum dots is shown in Figure 7-1a, which confirms the CdS cubic structure. In addition, the Scherrer-equation reveals an average particle size of 5 nm. The UV-visible absorption of CdS presented in Figure 7-1b features a broad absorption peak at 472 nm corresponding to the reported band gap of 2.63 eV[3,4]. The TEM image (Figure 7-1c) also reveals typical 4.32 nm CdS nanoparticles and their size distribution in Figure 7-1d, suggesting small and uniform CdS nanoparticle size. When mixing CdS and s-MoS_2 sheets together, Figure 7-2 clearly shows that CdS nanoparticles tend to aggregate on the basal and edge regions of restacked s-MoS_2 sheets with more than one monolayer thickness. The severe aggregation of CdS and s-MoS_2 at the materials interface indicates a poor dispersion of these components for light capture and charge (excitons) separation.

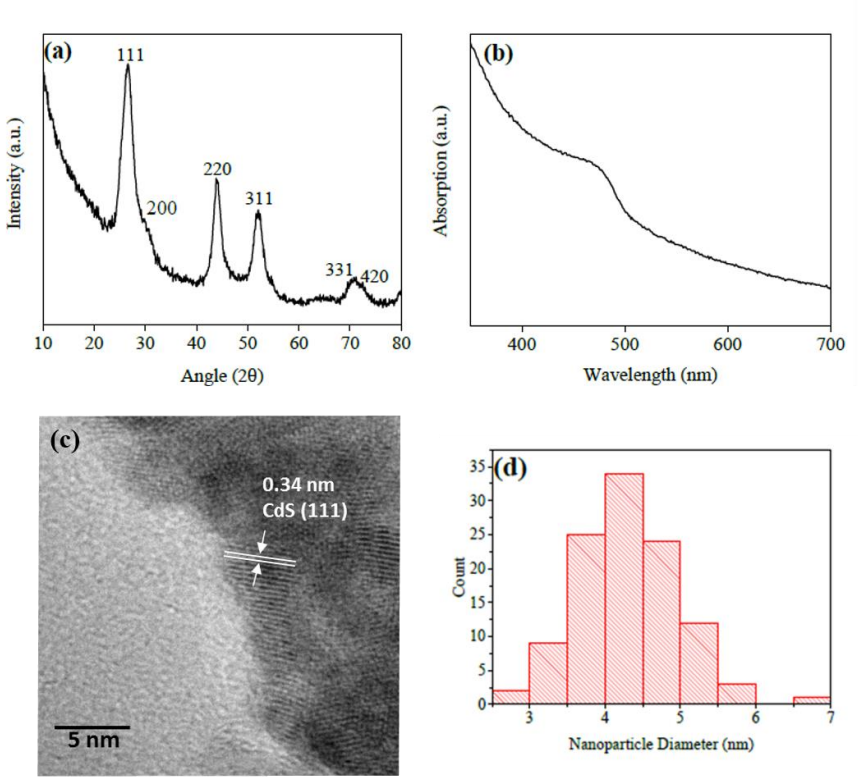

Figure 7-1. (a) X-ray diffraction pattern; (b) UV-visible absorption spectrum; (c) TEM image; (d) nanoparticle diameter size distribution of the synthesised CdS nanoparticles.

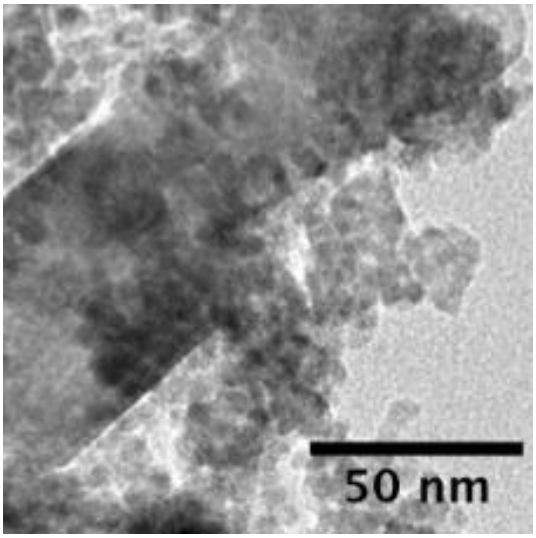

Figure 7-2. TEM image of CdS/s-MoS_2 nanocomposite, which reveals the aggregation of CdS nanoparticles on the basal planes and the edges of re-stacked s-MoS_2

It was envisaged that dispersion of CdS and s-MoS_2 on high surface area CNTs may overcome the aggregation problem. Typical HNO_3 acid pre-treatment on CNTs has been applied for the removal of contaminants (such as amorphous carbon and catalyst particles) as well as functionalising the outer carbon structure with terminal carboxyl and hydroxyl groups for the immobilisation and dispersion of solid phase in composite[16]. A detailed selection of acid treatments was reviewed by Flahaut *et al.*[17], which revealed that most of the treatments can effectively remove contaminants but also cause shortening of tube length and functionalise the carbon surface. Among various acids and concentrations applied, 3M HNO_3 was regarded as the optimum concentration and served as a compromise between the yield of the functional groups created on CNTs and the chemical damage to the CNTs structure. Therefore, the 3M HNO_3 treatment was chosen for the CNTs pre-treatment of the present study. The photocatalytic hydrogen production activity of the composite samples

with lactic acid as the sacrificial reagent was measured. Figure 7-3a shows that CdS or CdS/DWNTs are totally inert for the hydrogen production, implying that CdS and interface of CdS/DWNT cannot provide the sites for proton reduction despite the well-known light capture ability for excitons production over the CdS phase. In contrast, when s-MoS_2 is used, a significant quantity of H_2 is produced (137 μmol $h^{-1}g^{-1}$). Furthermore, the CdS/s-MoS_2 composite produces 1380 μmol $h^{-1}g^{-1}$ H_2, which is clearly higher than CdS or s-MoS_2 alone[7]. There is a further increase in the amount of evolved H_2 gas when DWNTs is added into the CdS/s-MoS_2 (see E, F, G). With the increased amount of DWNT added, a maximum of H_2 gas is evolved (5728 μmol $h^{-1}g^{-1}$) at 5 mg DWNT content. However, a further increase in the amount of DWNTs could impair the photocatalytic H_2 production, presumably due to masking of the active site, i.e., shield effect[4], when 7 mg of DWNT is used. Comparing different forms of CNTs (SWNT, DWNT and MWNT) with the same loading, see Figure7-3b, the DWNT composite gives the best activity per gram basis. Noticeably, SWNT composite gives only half H_2 production rate compared to the DWNT. Therefore, the functional roles for each component particularly the nature and quality of CNTs as support with respects to hydrogen production activity need to be investigated through careful material characterisations.

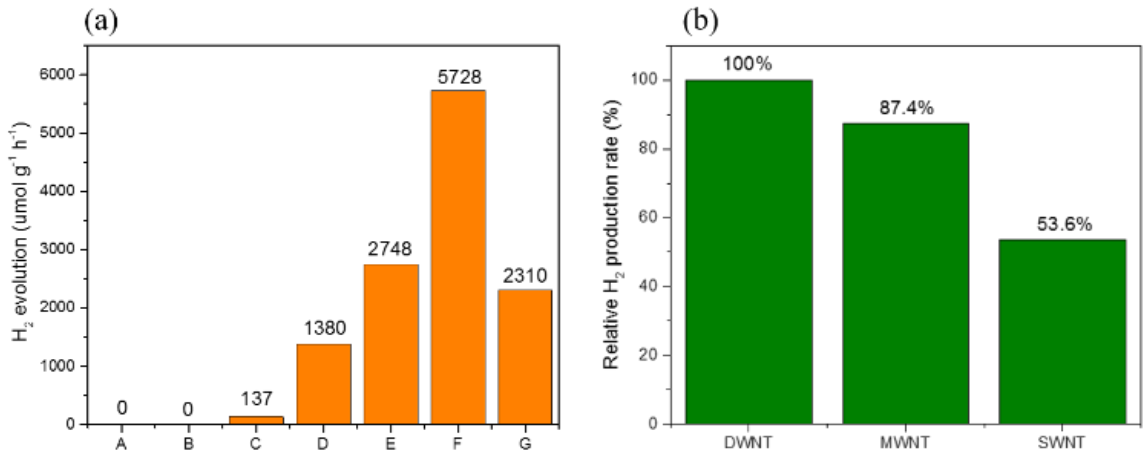

Figure 7-3. (a) Hydrogen evolution rate for 20 mg catalysts extracted from the mixture of **A**: CdS (100 mg); **B**: CdS/DWNT (100 mg CdS +0.4g DWNT); **C**: s-MoS_2; **D**: CdS/s-MoS_2 (100 mg CdS + 2 mg s-MoS_2); **E**: CdS/2mg DWNT/s-MoS_2 (100 mg CdS +2mg DWNT+ 2 mg s-MoS_2); **F**: CdS/5mg DWNT/s-MoS_2 (100 mg CdS +5mg DWNT+ 2 mg s-MoS_2); **G**: CdS/7mg DWNT/s-MoS_2 (100 mg CdS +7mg DWNT+ 2 mg s-MoS_2); (b) Hydrogen evolution rate for 5mg DWNT; MWNT and SWNT to support CdS and s-MoS_2.

To explore the charge (excitons) dynamics within the synthesised composites, the samples were examined using static and time-resolved photoluminescence spectroscopy (PL and TRPL). The steady-state PL spectra at an excitation wavelength of 405 nm shown in Figure 7-4a contain anticipated strong emission from CdS quantum dots centred at 750 nm by recombination of excitons from trap-state. However, CdS quantum dots when mixed with either CNTs or s-MoS_2 or CNTs/s-MoS_2 exhibit much smaller trap-state peaks compared with CdS alone, suggesting that the radiative recombination of excitons in CdS is minimised. CNTs appear to be more effective in quenching the PL than MoS_2 on the same weight basis but the mixture of CdS/DWNT/s-MoS_2 is the most effective. Figure 7-4b shows that DWNT,

MWNT and SWNT in quenching the trap-state emission PL. Figure 7-4c and 7-4d show the TRPL with decay monitored at 750 nm (excitation 405 nm) for samples with different components. An average lifetime (τ) for exciton recombination for each sample was derived and is shown in Table 7-1. The pristine CdS demonstrates an average lifetime of 13.00 ns; upon mixing with s-MoS_2 and DWNT, the photo-generated carriers are indeed significantly quenched, where the DWNT again shows better quenching ability compared to s-MoS_2. This indicates the photo-excited electrons collection/extraction from CdS to s-MoS_2 via DWNT is more efficient than that of CdS/s-MoS_2, presumably due to the high electron storage and mobility of DWNT. Among all the samples, CdS/DWNT/s-MoS_2 displays the lowest τ of 3.02 ns, implying it has a better carrier quenching (charge transfer) ability. Similar to the static PL, SWNT (4.53 ns) is less effective than MWNT (3.42 ns) and DWNT (3.02 ns) in quenching the excitons emission. As MoS_2 is the only component to provide active sites for proton reduction to hydrogen (see Figure 7-3a). it is likely that the photoelectrons generated by CdS upon light excitation are quickly taken up by the CNTs before passing to s-MoS_2. Apparently, the nature of CNTs appears to be critical for efficient transport and storage of photoelectrons from the CdS phase. It is well known that the electronic properties of the carbon nanotube are crucially depending on the diameter and chirality due to the distorted conjugated atomic tubular structure with partial overlap of P_z orbitals. The electronic properties of MWNT are quite complex, as each layer in MWNT can have different chiralities. Furthermore, MWNT shows considerably lower electronic conductivity than SWNT or DWNT due to the interactions between the layers within MWNT were found to disturb the electrical current along the tube axis[15]. The morphology of DWNT is very close to SWNT, but the inner carbon tubes may provide detainment of conjugation atomic pathway from aggressive mechanical or chemical damage to the outer tube surface[17].

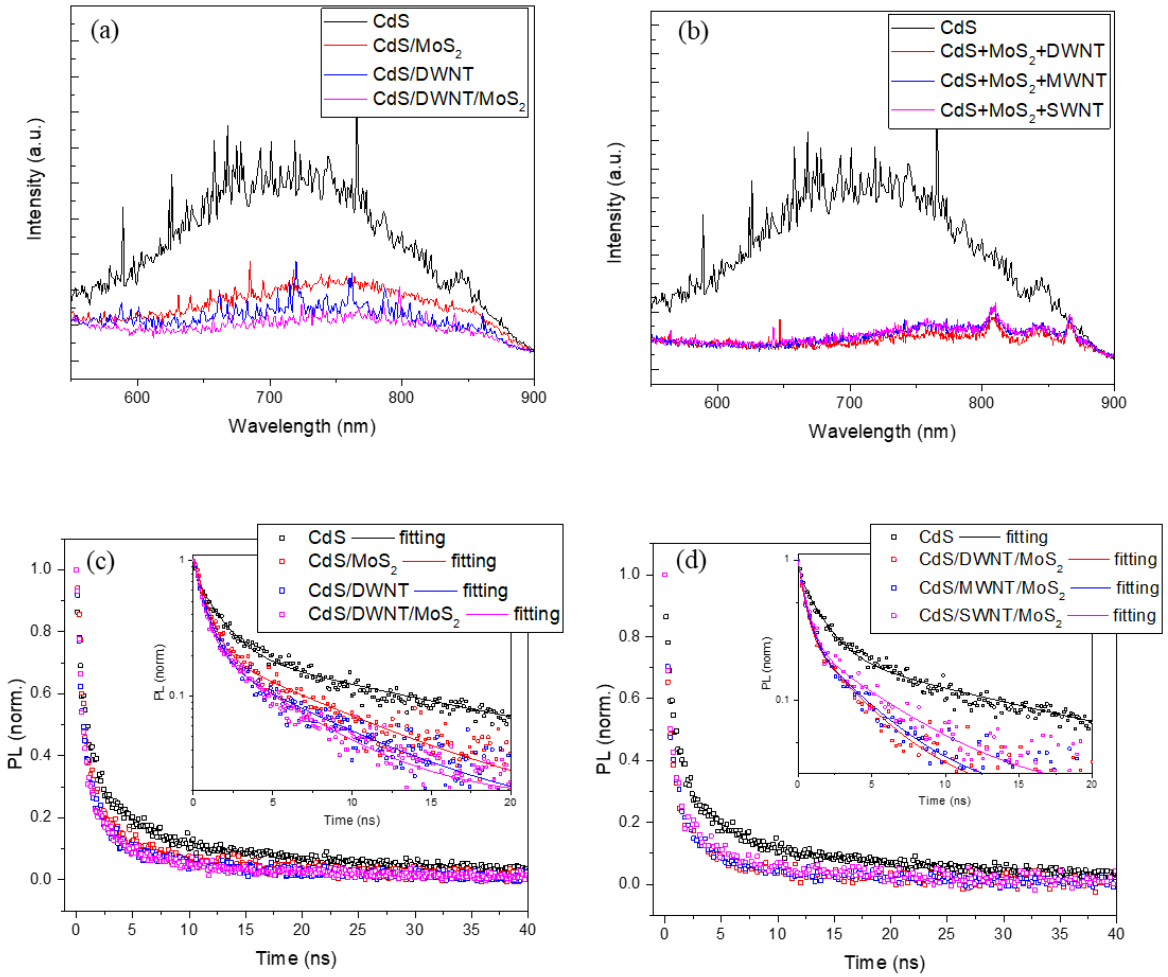

Figure 7-4. (a) and (b): steady state PL, excitation 405 nm for (a) CdS samples with different components (b) CdS and CdS/CNTs/s-MoS_2 samples. (c) and (d): time-resolved PL with decay monitored at 750 nm, excitation 405 nm for CdS samples with different components (d) CdS and CdS/CNTs/s-MoS_2 with different nature of CNTs.

Table 1. The fractional contribution (f_i) and lifetimes (τ_i) of each decay components & average lifetime (τ_{avg}) for various samples.

Material	f_1	τ_1	f_2	τ_2	τ_{avg}
CdS	20.8 %	1.45 ns	79.2 %	16.03 ns	13.00 ns
CdS/MoS_2	27.3 %	0.74 ns	72.7 %	7.82 ns	5.88 ns
CdS/DWNT	30.9 %	0.79 ns	69.1 %	6.83 ns	4.97 ns
CdS/DWNT/MoS_2	28.4 %	0.64 ns	71.6 %	3.96 ns	3.02 ns
CdS/MWNT/MoS_2	33.9 %	0.89 ns	66.1 %	4.72 ns	3.42 ns
CdS/SWNT/MoS_2	26.8 %	0.79 ns	73.2 %	5.90 ns	4.53 ns

High-resolution TEM (HR-TEM) images (Figure 7-5a and 7-5b) show the raw single and double-walled CNTs with the tubular graphene feature for the SWNT and DWNT, respectively. After 3M HNO_3 treatment, the majority of SWNTs by the typical acid treatment is converted to carbon sheets and amorphous carbon (the area of serious destruction of SWNT to amorphous carbon is shown in Figure 7-5c). But for DWNTs, many of them retain in the partial destructed tubular structure in amorphous carbon fragments (Figure 7-5d). Thus, the more fragile nature of SWNT leading to opening, unfolding, and destruction to carbon fragments is particularly noted.

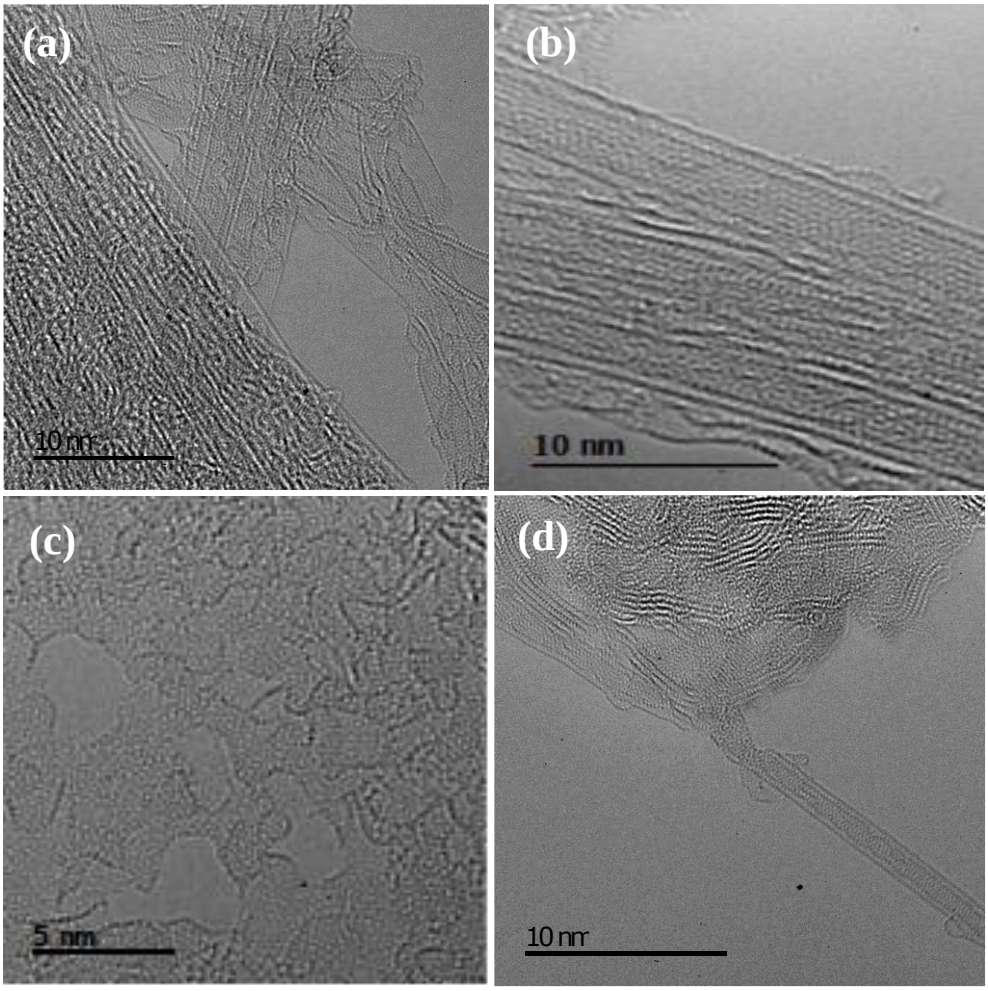

Figure 7-5. Typical HR-TEM images of (a) raw SWNT; (b) raw DWNT; (c) acid-treated SWNT; (d) acid-treated DWNT

To quantify the global structural change of the samples before and after the same acid treatment, Raman spectra of raw and HNO_3-treated CNTs are shown in Figure 7-6. The band located around 1315 cm^{-1} is assigned as the D-band which is commonly associated with the disordered, sp^3-hybridised carbon arising from defects and impurities, while the band located around 1580 cm^{-1} is assigned to the G-band which is associated with the crystalline graphitic structures[18]. The intensity ratio of D-band to G-band is commonly used to quantify the degree of disorder in graphene structure[19]. Table 7-2 gives the A_D/A_G and I_D/I_G ratios of

the raw and acid treated CNTs. Generally, HNO_3-treated CNTs showed a larger D-band to G-band ratios, indicating the destruction of graphene structure of CNTs during the acid treatment. Notably, the I_D/I_G ratio increases to 5.2 times in SWNT, followed by 4.9 times in DWNT and 2.1 times in MWNT sample. The increasing of D-band ratio in SWNT suggests that SWNTs indeed have undergone more severe damage after the identical acid treatment (particularly on the surface), which we believe to impair its charge transfer ability (giving rise to larger τ shown in Table 7-1), hence lower H_2 activity than DWNT (see Figure 7-3b).

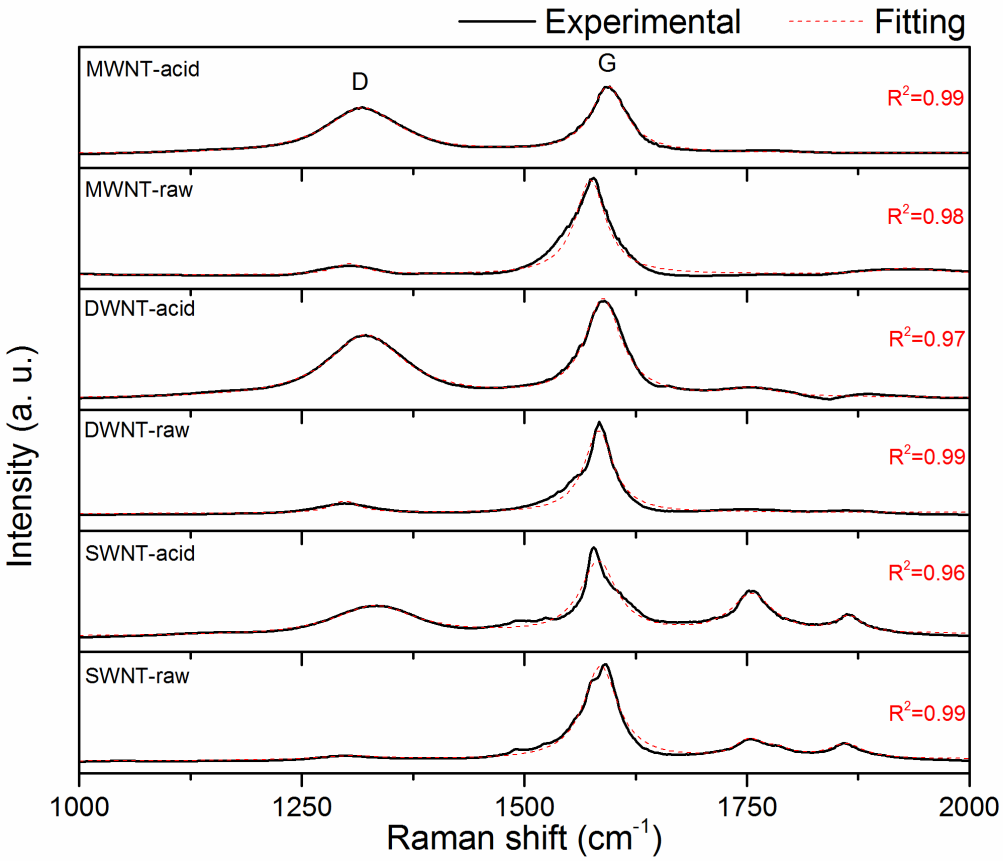

Figure 7-6. Raman spectra of raw CNTs and 3M HNO_3 treated CNTs.

Table 7-2. The A_D/A_G and I_D/I_G ratios of the raw and acid treated CNTs.

Sample	**A_D/A_G**	**I_D/I_G**
SWNT-raw	0.0261	0.0821
SWNT-Acid	1.431	0.4305
SWNT Ratio increment (acid/raw)	54.828	5.244
DWNT-raw	0.263	0.1404
DWNT-Acid	1.221	0.6894
DWNT Ratio increment (acid/raw)	4.643	4.910
MWNT-raw	0.0918	0.3490
MWNT-Acid	1.15	0.7265
MWNT Ratio increment (acid/raw)	12.527	2.082

Figure 7-7a shows that the image of the CdS/DWNT/s-MoS_2 composite. The regions of CdS nanoparticles and s-MoS_2 sheets dispersed on the partial tubular carbon structure can be differentiated through corresponding lattice fringe distances and fast-Fourier Transform (FFT) shown in Figure 7-7b. The intimate contact between CdS, s-MoS_2 and carbon nanotubes are clearly evidenced, which suggests that the CNTs remarkably decrease the aggregation of CdS and s-MoS_2 as they spread uniformly in the nanocomposite for superior H_2 activity than without the carbon support. Figure 7-8 illustrates the benefits of nano-composites of functional units for light capture, carrier transfer and catalysis in synergy for efficient photo-production of hydrogen from water. This indicates the future design of efficient photoactive composite for separation and optimisation of light capture nanomaterial from catalytic hydrogen production material via electron conductive mediator in a remote way. It is also clear from this study that the crucial maintenance of the integrity of the graphitic tubular structure with intact of conjugation of inner tubes is imperatively important for the charge transport and storage from light capture CdS phase to hydrogen production sites on s-MoS_2 for optimal photocatalysis.

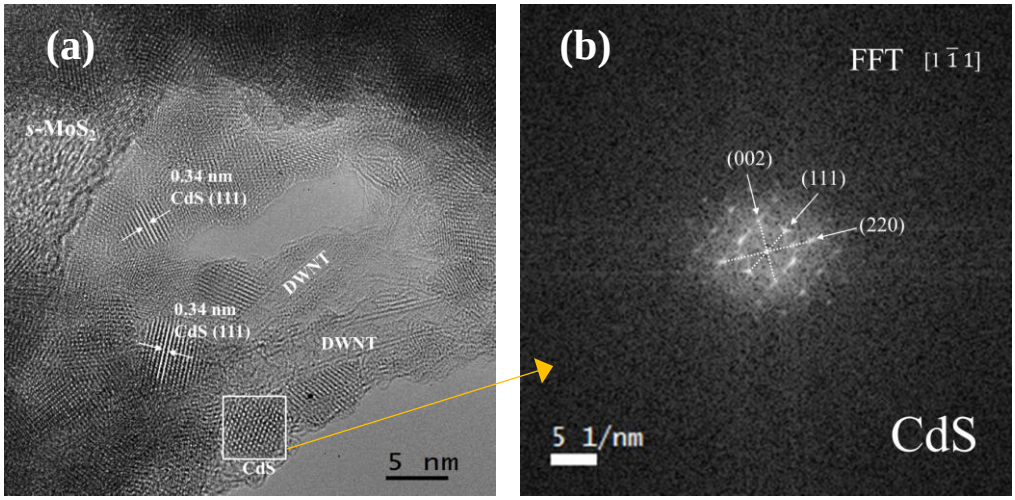

Figure 7-7. (a) A typical HR-TEM image of CdS/DWNT/s-MoS_2, the marked areas rich in compounds were confirmed by EDX; (b) Selected area of CdS nanoparticle with corresponding fast-Fourier Transform (FFT).

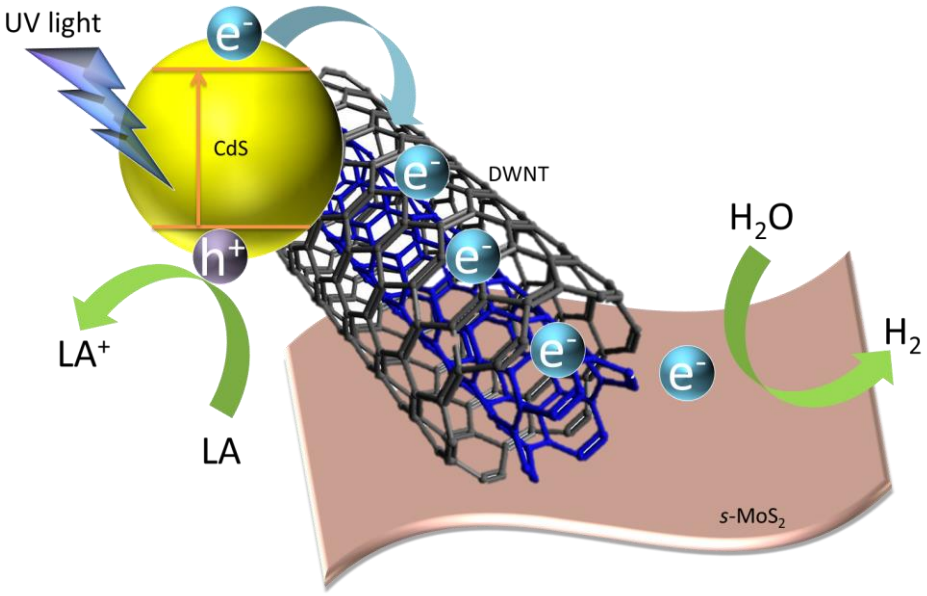

Figure 7-8. Schematic representation of the functions of nano-composites for light capture, carrier transfer and catalysis in synergy for efficient photo-production of hydrogen from water.

7.4 Chapter conclusion

In summary, photocatalytic hydrogen evolution activity through water splitting is greatly enhanced by the incorporation of carbon nanotubes and single-layered MoS_2 nano-sheets as cocatalysts into CdS system. CdS/DWNT/s-MoS_2 with the optimal amount of DWNT (mass ratio of CdS: DWNT: s-MoS_2 = 100: 5: 2) can provide a high hydrogen evolution rate of 5728 μmol g^{-1} h^{-1} and the unique roles of intact carbon nanotube as electron mediator are identified by the systematic TRPL study. In addition, DWNT shows the best performance compared to other forms of CNTs, due to its robust double-walled structure which can provide protection for the inner tube from surface damage during functionalisation/handling, while SWNT inevitably suffers from the destruction of conjugation. This study depicts the importance of fabrication of intimate heterojunctions demonstrating the benefits of nano-ensembles of functional units for light capture, carrier transfer and catalysis in synergy for efficient photo-production of hydrogen from water.

Reference

1. Ni, M., Leung, M. K. H., Leung, D. Y. C. & Sumathy, K. A review and recent developments in photocatalytic water-splitting using TiO_2 for hydrogen production. *Renew. Sustain. Energy Rev.* **11,** 401–425 (2007).
2. Kudo, A. & Miseki, Y. Heterogeneous photocatalyst materials for water splitting. *Chem. Soc. Rev.* **38,** 253–278 (2009).
3. Chen, X., Shen, S., Guo, L. & Mao, S. S. Semiconductor-based photocatalytic hydrogen generation. *Chem. Rev.* **110,** 6503–6570 (2010).
4. Li, Q., Guo, B., Yu, J., Ran, J., Zhang, B., Yan, H. & Gong, J. R. Highly efficient visible-light-driven photocatalytic hydrogen production of CdS-cluster-decorated graphene nanosheets. *J. Am. Chem. Soc.* **133,** 10878–10884 (2011).
5. Cao, A., Liu, Z., Chu, S., Wu, M., Ye, Z., Cai, Z., Chang, Y., Wang, S., Gong, Q. & Liu, Y. A facile one-step method to produce graphene-CdS quantum dot nanocomposites as promising optoelectronic materials. *Adv. Mater.* **22,** 103–106 (2010).
6. Fermín, D. J., Ponomarev, E. A. & Peter, L. M. Kinetic study of CdS photocorrosion by intensity modulated photocurrent and photoelectrochemical

impedance spectroscopy. *J. Electroanal. Chem.* **473,** 192–203 (1999).

7. Jia, T., Kolpin, A., Ma, C., Chan, R. C. T., Kwok, W. M. & Tsang, S. C. E. A graphene dispersed CdS–MoS_2 nanocrystal ensemble for cooperative photocatalytic hydrogen production from water. *Chem. Commun.* **50,** 1185–1188 (2014).
8. Zhang, J., Zhu, Z. & Feng, X. Construction of two-dimensional MoS_2/CdS p-n nanohybrids for highly efficient photocatalytic hydrogen evolution. *Chem. - A Eur. J.* **20,** 10632–10635 (2014).
9. Robel, I., Bunker, B. A. & Kamat, P. V. Single-walled carbon nanotube-CdS nanocomposites as light-harvesting assemblies: Photoinduced charge-transfer interactions. *Adv. Mater.* **17,** 2458–2463 (2005).
10. Lang, D., Shen, T. & Xiang, Q. Roles of MoS_2 and graphene as cocatalysts in the enhanced visible-light photocatalytic H_2 production activity of multiarmed CdS nanorods. *ChemCatChem* **7,** 943–951 (2015).
11. Pan, S. G. & Liu, X. H. CdS-Graphene nanocomposite: synthesis, adsorption kinetics and high photocatalytic performance under visible light irradiation. *New J. Chem.* **36,** 1781–1787 (2012).
12. Xiang, Q., Cheng, F. & Lang, D. Hierarchical Layered WS_2/Graphene-Modified CdS Nanorods for Efficient Photocatalytic Hydrogen Evolution. *ChemSusChem* **9,** 996–1002 (2016).
13. Ye, A., Fan, W., Zhang, Q., Deng, W. & Wang, Y. CdS–graphene and CdS–CNT nanocomposites as visible-light photocatalysts for hydrogen evolution and organic dye degradation. *Catal. Sci. Technol.* **2,** 969–978 (2012).
14. Baughman, R. H., Zakhidov, A. A. & De Heer, W. A. Carbon nanotubes - The route toward applications. *Science* **297,** 787–792 (2002).
15. Saito, R. & Dresselhaus, G. Tunneling conductance of connected carbon nanotubes. *Phys. Rev. B - Condens. Matter Mater. Phys.* **53,** 2044–2050 (1996).
16. Yao, Y., Li, G., Ciston, S., Lueptow, R. M. & Gray, K. A. Photoreactive TiO_2/carbon nanotube composites: Synthesis and reactivity. *Environ. Sci. Technol.* **42,** 4952–4957 (2008).
17. Bortolamiol, T., Lukanov, P., Galibert, A. M., Soula, B., Lonchambon, P., Datas, L. & Flahaut, E. Double-walled carbon nanotubes: Quantitative purification assessment, balance between purification and degradation and solution filling as an evidence of opening. *Carbon* **78,** 79–90 (2014).
18. Rosca, I. D., Watari, F., Uo, M. & Akasaka, T. Oxidation of multiwalled carbon nanotubes by nitric acid. *Carbon* **43,** 3124–3131 (2005).
19. Murphy, H., Papakonstantinou, P. & Okpalugo, T. I. T. Raman study of multiwalled carbon nanotubes functionalised with oxygen groups. *J. Vac. Sci. Technol. B Microelectron. Nanom. Struct.* **24,** 715–720 (2006).

Chapter 8: Conclusions and future perspectives

8.1 Conclusions

With the vast concerns about climate change and the actions for reducing fossil fuel usage, finding alternative renewable energy sources is of great interest. Numerous solutions have been proposed to alleviate the problems associated with the emission of CO_2. Among all the options, green methanol synthesis that consists of CO_2 capturing/recycling together with renewable hydrogen production, seems to be a promising way to achieve carbon neutral process and sustainable development. In this thesis, we put emphasis on the development of active bimetallic catalysts for the CO_2 hydrogenation reaction to produce methanol by increasing the number of active species (Cu-Zn alloy) through different synthesis methods as well as changing the adsorption properties of the bimetallic surfaces (In-modified Rh) to rationally dictate the reaction products. On the other hand, we also demonstrated the application of carbon nanotubes-promoted CdS-MoS_2 nanocomposites for photocatalytic green hydrogenation production from water. The main research achievements in this thesis are as follows:

In chapter 4, we report that the presence of a small amount of Ga^{3+} into Cu/ZnO system can lead to the formation of Ga-containing spinel, $ZnGa_2O_4$ structure, which creates electronic heterojunction with excess ZnO phase in the catalyst system. The result of time-resolved photoluminescence (TRPL) reveals that type-II heterojunction of ZnO-MGa_2O_4 (M = Zn, Cu) in the optimal sample (with 5 mole% Ga addition) promotes the spatial separation of excited electrons and holes across the interface which reduces the rapid instant recombination and prolongs their lifetime. This facilitates thermal deep reduction of ZnO

support to Zn atoms under hydrogen reduction condition. Therefore, a highly active CuZn bimetallic nanoparticle offering catalytic sites is generated. Furthermore, High-resolution transmission electron microscopy (HR-TEM), nano-diffraction and X-ray Absorption Spectroscopy (XAS) characterisation reveal the formation of a small *beta*-brass CuZn alloy phase (body-centred cubic, *bcc*). A correlation between Zn^0 concentration in the CuZn alloy nanoparticle to the catalytic performance is also clearly demonstrated, which shows that both CO_2 conversion and methanol selectivity are significantly improved by increasing the Zn^0 content in these hetero-junctioned catalysts.

In chapter 5, to further enhance the dispersion and specific surface area of the active species (Cu-Zn alloy) in the Cu/ZnO catalyst system, we have adopted a novel synthesis approach, i.e., aqueous miscible organic solvent method (AMOST), and synthesised an ultra-thin (1-3 cationic-layers) $(CuZn)_{1-x}Ga_x$-CO_3 layered double hydroxides (AMO-LDH) nanosheets as catalyst precursors for methanol production from CO_2 hydrogenation. We found that upon reduction, the AMO-LDH samples with appropriate Ga^{3+} composition give consistently and significantly higher surface areas and Cu-Zn dispersions than the catalysts prepared from conventional hydroxyl-carbonate phases (the catalysts introduced in Chapter 4). Owing to the distinctive local steric and electrostatic stabilization of the thin-layer LDH matrix, this discrete cationic layer can facilitate the formation of small (~4 nm) and homogeneous Cu particles decorated with trace Zn atoms with narrow size distribution which lead to higher CO_2 conversion and methanol production. We also discovered that the Cu-Zn catalysts derived from this novel AMO-LDH precursor not only displayed a better methanol production yield than the commercial Cu/ZnO-based HiFUEL^{TM} catalyst, but also outperforms those multi-doped LDHs as well as those recently-reported highly active catalysts in the literature.

In chapter 6, we present that Rh-containing catalysts with indium oxide inclusion can generate active and small Rh-In bimetallic nanoparticles which offers catalytically active sites for selective methanol synthesis from CO_2/H_2 mixtures. The electronic properties and structural information of Rh-In bimetallic alloys have been extensively investigated by XPS and XAS analyses. We found that this new class of Rh-In bimetallic catalysts can dramatically inhibit the reverse water-gas shift (RWGS) reaction by stabilising surface HCOO-intermediates and suppressing the formation of COOH-adsorbed species on the bimetallic surface. As far as we are aware, this new class of Rh-In catalyst gives the highest methanol weight time yield of about 21.3 $g_{MeOH} \cdot g_{active\ metal}^{-1} \cdot h^{-1}$ with methanol selectivity of over 85% under excess CO_2 ($H_2/CO_2 \leq 3$) conditions at 4.5MPa than all reported catalysts in literature. This makes the utilisation of biomass (the upstream feedstock generation process of CO_2 hydrogenation) a competitive alternative to methanol production from the economic and the energetic point of view.

In Chapter 7, we demonstrate that the incorporation of quantum dots, CdS, is shown to significantly promote photocatalytic hydrogen production from water over single-layer MoS_2 via dispersing the two materials on carbon nanotubes (CNTs) including single, double, and multi-walled CNTs (SWNT, DWNT, and MWNT) to form nanocomposite photocatalysts. CdS/DWNT/s-MoS_2 with the optimal amount of DWNT (mass ratio of CdS : DWNT : s-MoS_2 = 100 : 5 : 2) can provide a high hydrogen evolution rate of 5,728 μmol$\cdot g_{cat.}^{-1} \cdot h^{-1}$. The unique roles of intact carbon nanotube as electron mediator are identified by the systematic TRPL study, and the hydrogen evolution rate of the nanocomposite is found critically dependent on the content and structural integrity of CNTs. Compared to other forms of CNTs, DWNT shows more superior H_2 production, because its robust double-walled structure can provide protection for the inner tube from surface damage during

functionalization/handling. The fabrication of intimate CdS/DWNT/s-MoS_2 nanocomposite demonstrates the advantages of nano-ensembles of functional units for light capture, carrier transfer and catalysis in synergy for efficient photo-production of hydrogen from water.

8.2 Future perspectives

At present, the major challenges for renewable chemical synthesis routes from CO_2 and hydrogen are to develop economically viable and efficient catalysts. Therefore, the research efforts on catalyst preparation using a variety of material compositions with different preparation methods are being explored continuously. To make the green methanol production become economically attractive, from the feedstock side, the efficient and economical CO_2 capture, as well as hydrogen production technologies, need to be available. As for the catalyst systems of CO_2 hydrogenation to methanol, the commonly used Cu-based catalyst, especially Cu-Zn based catalysts, still at the benchmark position due to their superior activity and economic advantages, we have shown in this thesis that the catalytic performance of Cu-Zn catalysts can be further improved via controlled reduction in a suitable catalyst precursor to make small (c.a. 4nm), stable, and homogeneous Cu-Zn nanoparticles. However, the catalytic performance of the Cu-based catalysts is often governed by the thermodynamics which shows low methanol selectivity under low reaction pressure (<2 MPa) or low H_2/CO_2 (ratio <3) conditions. Therefore, the catalysts possessed of the qualities including low cost, good performance, stable, and most importantly, can be effectively coupling with the CO_2/H_2 feedstock generation processes or be applied on those thermodynamically and kinetically unfavourable conditions are highly desirable. Adding foreign atoms to an existing metal system has been shown to be an effective method in improving the catalytic performance of monometallic nanoparticles due to the fine adjustment of the adsorption properties while forming alloys. In this context, rational design

of novel bimetallic alloy system through computational molecular modelling, advanced characterisation on the bimetallic systems as well as developing new synthesis methods that can lead to unique structural properties and enhanced activity toward methanol synthesis are highly desirable for the quest of ultimate catalyst.